UNIVERSITÀ DEGLI STUDI DI PAVIA
DOTTORATO DI RICERCA IN FISICA – XXXIII CICLO

PARTICLE DETECTORS R&D: DUAL-READOUT CALORIMETRY FOR FUTURE COLLIDERS AND MICROMEGAS CHAMBERS FOR THE ATLAS NEW SMALL WHEEL UPGRADE

LORENZO PEZZOTTI

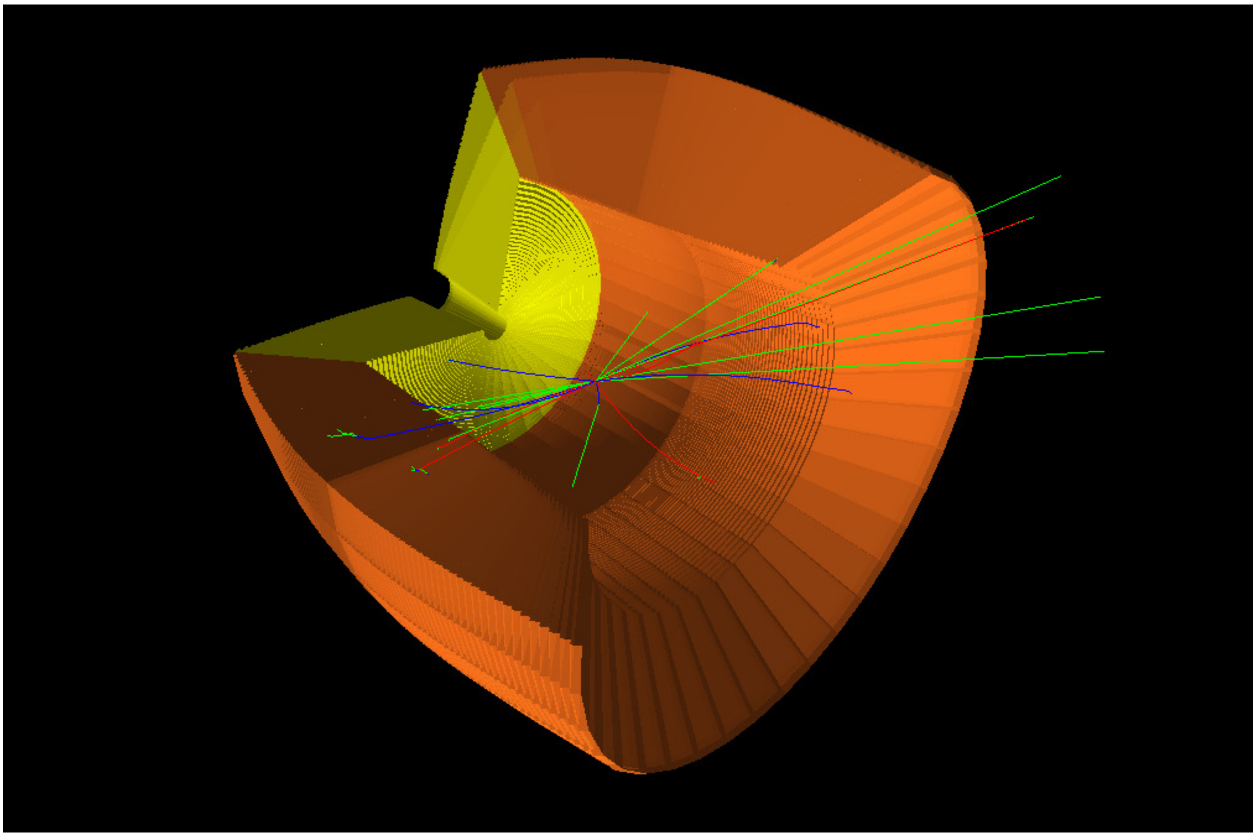

Tesi per il conseguimento del titolo

Università degli Studi di Pavia
Dottorato di Ricerca in Fisica - XXXIII Ciclo

Particle Detectors R&D: Dual-Readout Calorimetry for Future Colliders and MicroMegas Chambers for the ATLAS New Small Wheel Upgrade

Lorenzo Pezzotti

Submitted to the Graduate School of Physics in partial fulfillment
of the requirements for the degree of
Dottore di Ricerca in Fisica
Doctor of Philosophy in Physics
at the
University of Pavia

Supervisor: Dott. Roberto Ferrari
Internal Supervisor: Prof. Andrea Negri

Cover: Exploded view of a fully simulated $e^+e^- \rightarrow jj$ event showering in the IDEA dual-readout calorimeter.

Particle Detectors R&D: Dual-Readout Calorimetry for Future Colliders and MicroMegas Chambers for the ATLAS New Small Wheel Upgrade
Lorenzo Pezzotti
PhD thesis - University of Pavia
Pavia, Italy, April 2021

Contents

Introduction 7

I Feasibility studies of dual-readout calorimetry at future electron-positron circular colliders 9

1 Future electron-positron colliders and the IDEA Detector concept 11
- 1.1 The Large Hadron Collider 11
- 1.2 Post LHC Colliders 16
  - 1.2.1 The Future Circular Collider 17
  - 1.2.2 The Circular Electron Positron Collider 22
  - 1.2.3 The International Linear Collider 24
  - 1.2.4 The Compact Linear Collider 26
  - 1.2.5 The 2020 European Strategy for Particle Physics Update 29
- 1.3 The IDEA Detector concept 32
  - 1.3.1 Detector requirements 32
  - 1.3.2 Vertex detector 35
  - 1.3.3 Drift chamber 35
  - 1.3.4 Magnet system 39
  - 1.3.5 Preshower and muon chambers 39

2 Introduction to calorimetry 41
- 2.1 Calorimeters 41
- 2.2 Electromagnetic calorimetry 43
  - 2.2.1 Electromagnetic-particle cascades 43
  - 2.2.2 Electromagnetic calorimeters 45
    - 2.2.2.1 Fluctuations 46
  - 2.2.3 Electromagnetic showers and mips 49

2.3 Hadronic calorimetry 51
  2.3.1 Hadronic particle cascades 51
  2.3.2 Hadronic calorimeters 54
    2.3.2.1 Fluctuations 56
  2.3.3 Dual-readout method 59
  2.3.4 Compensation by neutrons signal boosting 62
  2.3.5 Towards the best hadronic energy resolution 63
  2.3.6 Jet energy measurements 64
  2.3.7 Catastrophic events 66
  2.3.8 Combined calorimetric systems 68
2.4 Calorimetry at future e^+e^- colliders 69
  2.4.1 Calorimetry requirements 69
  2.4.2 Drivers for the IDEA dual-readout calorimeter 72
  2.4.3 Dual-readout fiber calorimeters 73
  2.4.4 Particle Flow Analysis 81
  2.4.5 Particle Flow calorimeters 85

3 The IDEA calorimeter - full simulation studies 91
3.1 The detector 91
  3.1.1 Signal simulation 93
3.2 Calorimeter response and calibration 96
  3.2.1 Border effects 98
  3.2.2 Calibration 98
  3.2.3 On the correctness of the calibration approach 102
3.3 Electromagnetic performance 105
  3.3.1 Energy resolution and linearity 105
  3.3.2 Uniformity 107
3.4 Hadron performance 107
  3.4.1 Containment and calibration 107
  3.4.2 χ factor universality 114
  3.4.3 Energy resolution and linearity 116
  3.4.4 Calibrating with hadrons 117
3.5 Angle and position measurements 121
  3.5.1 Event displays 121
  3.5.2 Angular resolution 125
3.6 Physics benchmarks 128
  3.6.1 Jet reconstruction 129
  3.6.2 Jet calibration and resolution 135
  3.6.3 Analysis of physics events 137

4 Dual-readout calorimetry with SiPM light sensors 143
4.1 Silicon photomultipliers 143
4.1.1 Signal time evolution 146
4.1.2 Photon detection efficiency 146
4.1.3 Intrinsic noise sources 148
4.2 Tests of a dual-readout calorimeter prototype with SiPMs 150
4.2.1 Light readout system 152
4.2.2 Test-beam setup 154
4.2.3 Crosstalk results 156
4.2.4 Light yields results 157
4.2.5 Measuring electromagnetic shower profiles 160
4.2.6 Additional information from simulations 163
4.2.7 Restoring signal linearity 165
4.3 Conclusions and path towards the 2021 test beam 167

5 Axion like particles search with the FCC-ee IDEA Detector 171
5.1 Axion like particles search through 3-photon final states 171
5.2 The Delphes 3 software and the IDEA fast simulation 173
5.3 Analysis strategy 175
5.4 Results 180

II Construction and testing of the ATLAS New Small Wheel MicroMegas chambers 185

6 The ATLAS Experiment 187
6.1 The ATLAS Detector 187
6.2 Inner detector 189
6.3 Calorimeter system 191
6.4 Muon spectrometer 194
6.5 Trigger 196

7 The ATLAS New Small Wheel Micromegas chambers 197
7.1 The ATLAS New Small Wheel upgrade 197
7.2 The New Small Wheel layout 200
7.3 Micromegas chambers 202
7.4 Micromegas chambers construction and QA/QC 204
7.5 Micromegas chambers high-voltage testing 211
7.5.1 The CERN Gamma Irradiation Facility 211
7.5.2 Photon field mapping 215

7.5.3 Results 218

Conclusions **231**

Bibliography **233**

List of Figures **245**

List of Tables **259**

Acknowledgements **261**

Introduction

This thesis describes the work on particle detectors development, for both present and future high energy physics experiments, carried out in the three-years period, from October 2017 to October 2020, spent as a student of the XXXIII PhD Cycle in Physics of the University of Pavia and associate member of the National Institute of Nuclear Physics (INFN). To facilitate the framing of the topics presented, the thesis is divided into two parts, corresponding to the activities accomplished within two collaborations.

The first part concerns my activity as a member of the INFN RD_FCC Collaboration for the study of physics at future circular colliders. In this context, I worked on the development of dual-readout calorimetry and its applications to post-LHC electron-positron colliders. Chapter 1 is an introduction to the main proposed post-LHC colliders and is useful for presenting the IDEA Detector concept, where dual-readout calorimetry plays a central role. Chapter 2 describes the art of calorimetry, focusing on the different factors that affect the energy resolution and the requirements for future experiments. Chapter 3 reports the full-simulation description of the IDEA dual-readout calorimeter and the first results obtained in this regard. Chapter 4 concerns the research and development on the possibility of adopting Silicon PhotoMultipliers as light detectors for dual-readout calorimeters. Also in this case, the obtained results are original. Finally, Chapter 5 shows the physics reach of the IDEA Detector, coupled to the CERN future circular electron-positron collider, for axion-like-particles search.

The second part is about my work as a member of the ATLAS Experiment at CERN. I became a member of the Collaboration in November 2017 and author in December 2018. Together with the ATLAS-Pavia Group, I participated to the construction of micromegas chambers for the New Small Wheel upgrade, a new detector to be installed in the ATLAS forward muon spectrometer. In 2019, thanks to the award of an INFN Simil-Fellowship position, I joined the CERN New Small Wheel Integration Group and participated to the detector testing phase. Chapter 6 is a brief introduction to the ATLAS Detector, while Chapter 7 describes the New Small Wheel upgrade and the obtained results.

Part I

Feasibility studies of dual-readout calorimetry at future electron-positron circular colliders

Chapter 1

Future electron-positron colliders and the IDEA Detector concept

The chapter starts with an introduction to the main contemporary collider, the Large Hadron Collider, and continues with an assessment of the next big collider proposals. As stated by the 2020 European Strategy for Particle Physics Update, an electron-positron Higgs factory is the highest-priority next collider, and particular attention is spent on the Higgs measurement programs. Eventually, the IDEA Detector concept, targeting future circular e^+e^- colliders, is presented.

1.1 The Large Hadron Collider

In the coming decade, the Europe leading role in particle physics is guaranteed by the Large Hadron Collider (LHC) [1]. The LHC is a $\simeq$ 27 km long circular particle collider hosted at CERN, near Geneva. Its main goal is to accelerate and collide head-on two beams of protons with unprecedented center-of-mass energies. The LHC started its operation in 2009 with the run (Run 1) that ended in 2013. A second run, Run 2, started in 2015 and lasted until the end of 2018. Up to now, the LHC delivered proton-proton (pp) collisions at center-of-mass energies of 7, 8 and 13 TeV.

The LHC can also collide heavy ions at center-of-mass energies per nucleon of 2.76 TeV, 5.02 TeV ($Pb - Pb$), and 5.44 TeV ($Xe - Xe$), as well as $p - Pb$ at 5.02 TeV and 8.16 TeV.

The LHC is the latest of the CERN energy-frontier accelerators and its injection chain, sketched in Fig. 1.1, is dictated by the reuse of previous accelerators. The proton acceleration starts with the extraction of protons from hydrogen atoms through

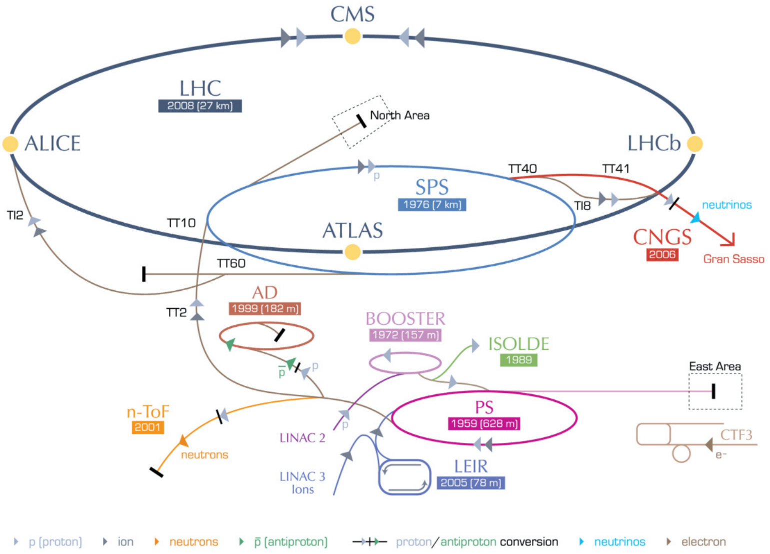

Figure 1.1: The CERN accelerator complex. Image from [2].

ionization, subsequently protons are accelerated by a linear accelerator (LINAC2) up to 50 MeV. The acceleration continues with a chain of injectors: the Proton Synchrotron Booster (PSB), the Proton Synchrotron (PS), and the Super Proton Synchrotron (SPS). At the end of the SPS acceleration, protons at 450 GeV are injected into the LHC via two transfer lines.

The LHC is a synchrotron-type accelerator, therefore, inside the LHC, protons are grouped in bunches separated in time by 25 ns. Bunch collisions happen at four Interaction Points (IPs), where four big experiments (ATLAS, CMS, LHCb and ALICE) are situated. Heavy ions follow a slightly different path as they are accelerated by the LINAC3 and by the Low Energy Ion Ring (LEIR) before entering in the PS.

The collider center-of-mass energy, also indicated by $\sqrt{s}$, is the maximal energy available in the collisions. It defines the phase-space accessible to the final state products of the interaction and limits the maximum mass of particles that can be produced. In a circular collider, the maximum momentum, a particle can be accelerated to, is dictated by the strength of the magnetic field induced by the accelerator dipoles. The relation between the beam momentum and the dipole field can be approximated to:

$$0.3B \simeq \frac{p}{r} \tag{1.1}$$

with B being the magnetic field expressed in units of Tesla, p the beam momentum expressed in terms of GeV/c and r the accelerator radius expressed in units of meter. The LHC effective radius is $r = (0.65 \times 27(\mathrm{km}))/2\pi = 2.8$ km, where the factor 0.65

takes into account the accelerator sections where dipoles are missing to leave room for the so-called straight sections (needed for the beam dump, accelerating cavities, detectors, . . .). The remaining sections are occupied by 1232, 15-meter-long, dipole magnets.

Eq. 1.1 defines the so called accelerator magnetic rigidity. For instance, the maximum center-of-mass energy envisaged for the LHC is 14 TeV, to accelerate proton beams to $7 \cdot 10^3$ GeV/c the nominal dipoles magnetic field will be 8.33 T. The field is generated by a current of $\simeq 12 \times 10^3$ A, circulating on NbTi superconducting filaments cooled down to 1.9 K.

The production cross sections, describing the likelihood of the different processes to happen, are function of the center-of-mass energy, as shown in Fig. 1.2. The actual maximum center-of-mass energy reached by the LHC is 13 TeV, achieved during Run 2.

In addition to the center-of-mass energy, the accelerator key parameter is the instantaneous luminosity ($\mathcal{L}$). It indicates the incident particle flow, i.e. the number of beam particles per unit area and unit time. Higher the luminosity, higher the probability for a beam particle to have a collision. For a synchrotron accelerator, $\mathcal{L}$ depends on the number of beam particles per bunch, the number of bunches, the bunch revolution frequency and the configuration of the focusing magnets (quadrupoles) in the proximity of the IP. For a proton-proton collider, the instantaneous luminosity is usually factored in independent terms as:

$$\mathcal{L} = \frac{n_b n_p^2 f}{4\pi\sigma_T^2} F \tag{1.2}$$

where n_b denotes the number of bunches, f is the revolution frequency and n_p the number of protons per bunch. Therefore, the numerator gives the number of possible interactions per second while, in the denominator, σ_T^2 indicates the beam transverse size at the IP. F is a factor, close to unity, taking into account geometric effects (like the beam-crossing angle) and dynamic effects (like beam-beam interactions). In the LHC design, the target for the instantaneous luminosity was about $\mathcal{L} = 10^{34}$ cm^{-2} s^{-1}. During Run 2 this goal was achieved and even exceeded, reaching about $\mathcal{L} = 2 \cdot 10^{34}$ cm^{-2} s^{-1}, as shown in Fig. 1.3.

The expected event rate of a given process (X), at the center-of-mass $\sqrt{s}$, is given by the product of its cross section (σ_X) and the instantaneous luminosity:

$$\frac{dN_X}{dt} = \mathcal{L} \cdot \sigma_X(\sqrt{s}) \tag{1.3}$$

To monitor the number of collisions delivered over time, a useful variable is the

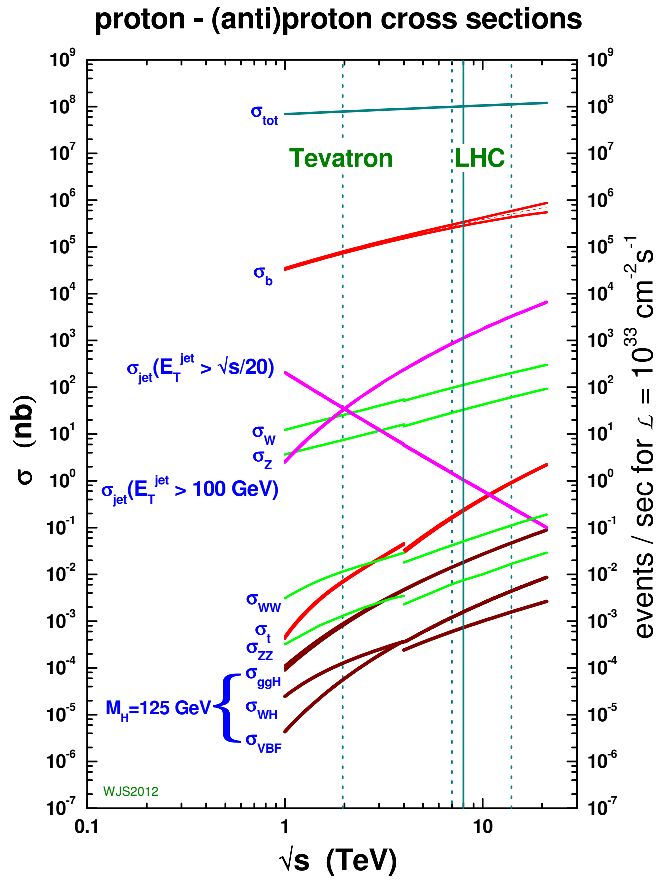

Figure 1.2: Production cross section for different processes as a function of the center-of-mass energy. Image from [3].

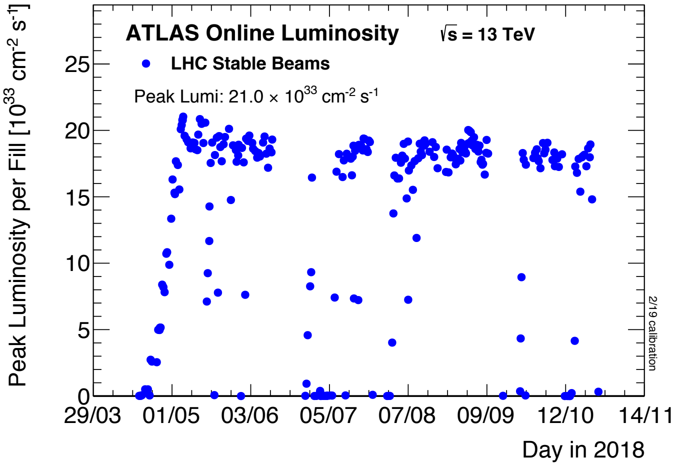

Figure 1.3: Peak instantaneous luminosity delivered to ATLAS for each LHC fill during stable beams for *pp* collisions at 13 TeV as a function of time in 2018. Image from [4].

integrated luminosity (L) defined as the integral of $\mathcal{L}$ over time. It is measured in units of inverse cross section. From Eq. 1.3, it follows that, for a process (X), the number of events N_X produced over a given period is directly proportional to L, $N_X = \sigma_X(\sqrt{s}) \cdot L$, which implies the general rule "the higher the integrated luminosity, the greater the discovery potential". The LHC integrated luminosity measured at the end of Run 2 by the ATLAS experiment (for physics analyses only) amounts to 139 fb^{-1} (3.2 fb^{-1} in 2015, 33.0 fb^{-1} in 2016, 44.3 fb^{-1} in 2017 and 58.5 fb^{-1} in 2018, Fig. 1.4).

Up to now, on top of the accurate measurement of many known SM processes, the LHC legacy consists of the Higgs boson discovery, the beginning of a new phase of detailed studies of its properties aimed at revealing the deep origin of the ElectroWeak (EW) symmetry breaking, and the indication that signals from new physics around the TeV scale are elusive, at best. The LHC future is dictated by its High-Luminosity upgrade (HL-LHC) approved by the CERN Council in 2016. The current schedule foresees the HL-LHC starting in 2027, providing an instantaneous luminosity 3-5 times higher than the one achieved in Run 2, and ending around 2040, after collecting an integrated luminosity of 3000 fb^{-1}. The HL-LHC will produce over 10^8 Higgs bosons, however, the precision on the Higgs properties measurements at the HL-LHC is limited by large theoretical and experimental uncertainties. For the majority of the Higgs couplings measurable at the HL-LHC, the resolution is estimated to be around 5-10%.

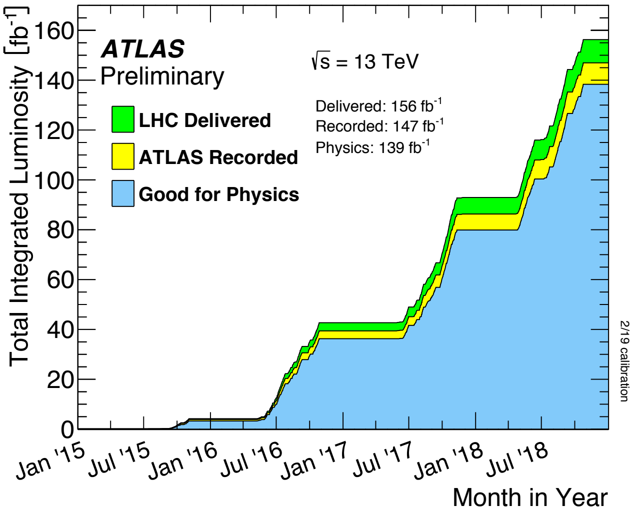

Figure 1.4: Integrated luminosity versus time delivered to ATLAS (green), recorded by ATLAS (yellow), and certified to be good quality data (blue) during stable beams for pp collisions at 13 TeV center-of-mass energy in 2015-2018. Image from [4].

1.2 Post LHC Colliders

The LHC experiments confirmed that the coupling with the Higgs boson is responsible for the masses of the W, Z, t, b and τ particles. However, several questions are still unanswered. The Higgs couplings are not universal, unlike gauge couplings, and their pattern, at the origin of the leptons and quarks masses, is not explained by the Standard Model (SM). The spontaneous symmetry breaking of the gauge symmetry $SU(2) \times U(1)$ is not explained by the SM as well. Moreover, the Higgs boson could couple to new particles and fields with no SM gauge interactions so that the only accessible production mechanism would be provided by the Higgs boson. The main goal of any post-LHC collider is studying the properties of the Higgs boson.

An electron-positron collider operating as an "Higgs factory" could produce Higgs bosons in a clean environment, guaranteeing a dramatic improvement in the measurement of the Higgs couplings to light particles. The main production mechanism would be the so-called Higgsstrahlung process in which the Higgs boson is produced in association with a Z boson ($e^+e^- \rightarrow Z^* \rightarrow ZH$) at a center-of-mass energy around 240 GeV. This center-of-mass energy is within the reach of both circular and linear e^+e^- colliders. On the other hand, in order to reach some sensible accuracy, hadron collisions at significantly higher center-of-mass energies than the LHC are needed to study the production of Higgs pairs, thus exploring the Higgs self-interaction mechanism. This process can be generated at high-energy linear e^+e^- colliders as well. Therefore, in the last 20 years, both circular and linear e^+e^- colliders have been proposed and, in the case of circular ones, they are intended to be followed by a high-energy $p-p$ collider. The following is a brief introduction to the main proposed colliders.

1.2.1 The Future Circular Collider

The CERN proposal for a post-LHC circular collider is the Future Circular Collider (FCC) project [5]. FCC is staged in a first lepton collider (FCC-ee) [6] phase followed by a hadron one (FCC-hh) [7]. Both colliders will be housed in the same tunnel with a length of about 100 km. The length is dictated by Eq. 1.1: to achieve a center-of-mass energy of about 100 TeV, exploiting the R&D work on Nb_3Sn superconducting dipoles targeting a magnetic dipole field of 16 T, one would need a radius of about 10 km, corresponding to a 100 km long circular collider, once you include the non-bending accelerator sections. Optionally, an electron-hadron collider could be housed in the same tunnel (FCC-eh), in order to collide 50 TeV proton beams with 60 GeV electrons from an energy-recovery linac. It would generate an integrated luminosity of about 2.5 ab^{-1} of 3.5 TeV electron-proton collisions.

The FCC-ee is designed to study with high precision the electroweak physics by producing $5{\cdot}10^{12}$ Z bosons, 10^8 W pairs, 10^6 Higgs bosons and 10^6 top quarks pairs. The collider will be operated in stages with center-of-mass energies ranging from 88 to 365 GeV.

The FCC-ee is a double ring collider where the luminosity is driven by the synchrotron radiation per electron. At low energies, with limited synchrotron radiation, a beam current of 1.39 A can be stored to achieve very high luminosities, whereas at the maximum beam energy the beam current has to be lowered to 5.4 mA, by changing the number of bunches. The fixed radiation power is 50 MW, compensated by the RF system. The injector chain makes use of a 6 GeV linac, a damping ring and the CERN SPS as a pre-booster. Fig. 1.8 shows the FCC-ee schematic view.

To achieve a statistical precision on a complete set of electroweak and Higgs observables by one or two orders of magnitude better than the current one, the data samples foreseen are divided as follows:

- 30 ab^{-1} at $\sqrt{s} \simeq 88$ and 94 GeV, for the direct measurement of the electromagnetic coupling constant at the Z mass scale.
- 100 ab^{-1} at the Z pole, for the measurement of the effective weak mixing angle and for the search of rare of forbidden Z decays.
- 10 ab^{-1} around the WW threshold, for the W mass and width measurement, shared between $\sqrt{s} \simeq 157.5$ and 162.5 GeV.

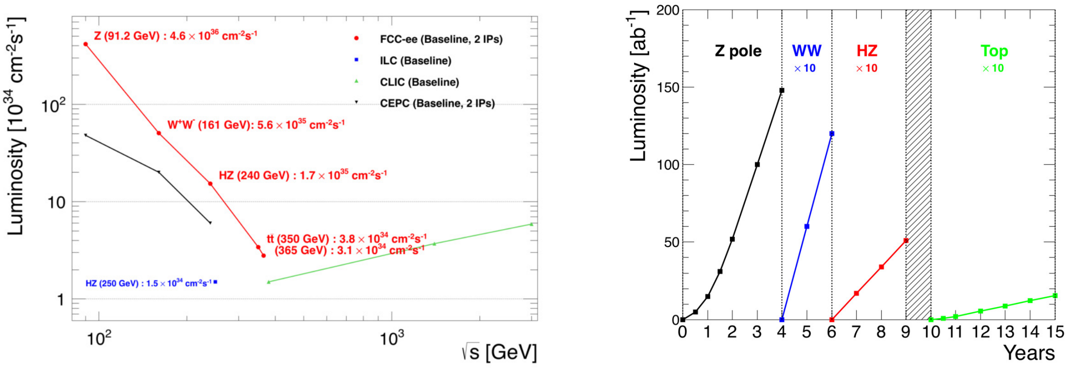

Figure 1.5: The FCC-ee baseline luminosity against $\sqrt{s}$ and compared to other e^+e^- colliders (left) and the integrated FCC-ee luminosity during 15 years of operation (right). Image from [6].

- 5 ab^{-1} at $\sqrt{s} = 240$ GeV, for an absolute measurement of the Higgs bosons couplings and decay width.
- $\simeq 0.2$ ab^{-1} in a 5 GeV window around the top quark threshold, $\sqrt{s} = 340-345$ GeV, for the measurement of the top-quark mass and width.
- 1.5 ab^{-1} above the top-pair threshold, $\sqrt{s} \simeq 365$ GeV, for the measurement of the top electroweak couplings.

Only circular colliders can achieve these luminosities in a reasonable amount of time. This is illustrated in Fig. 1.5 (left) showing the FCC-ee baseline luminosities summed over the two IPs against the center-of-mass energy ($\sqrt{s}$), and comparing it to the other e^+e^- colliders discussed here after.

Fig. 1.5 (right) shows the envisaged FCC-ee integrated luminosity accumulated during 15 years of operation. The baseline FCC-ee should improve the precision on all electroweak variables by a factor of 20 to 50 and up to 10 times the measurement of the Higgs couplings, in a model-independent way. The high-statistics samples will offer unique opportunities to test BSM signals as minute flavor-changing neutral currents, lepton-flavor-violating decays, dark matter production in Z and H decays or axion-like-particles produced in Z-boson decays (an example of the latter is studied in Chap. 5).

At $\sqrt{s} = 240$ GeV, the lab energy spectrum of the Z shows a clear peak at 125 GeV that corresponds to the Z recoil against the Higgs. Events under this peak tag the Higgs bosons independently of its decay mode. Therefore, the Higgsstrahlung process will allow the measurement of the Higgs coupling to the Z, which is the first step to the model-independent determination of its total width and thus of its couplings through branching ratio measurements. The leading Higgs couplings to

Collider	**HL-LHC**	**FCC-ee**			**FCC-eh**
Luminosity (ab^{-1})	3	5 @ 240 GeV	+1.5 @ 365 GeV	+HL-LHC	2
Years	25	3	4	-	20
$\delta\Gamma_H/\Gamma_H$ (%)	SM	2.7	1.3	1.1	SM
$\delta g_{HZZ}/g_{HZZ}$ (%)	1.3	0.2	0.17	0.16	0.43
$\delta g_{HWW}/g_{HWW}$ (%)	1.4	1.3	0.43	0.40	0.26
$\delta g_{Hbb}/g_{Hbb}$ (%)	2.9	1.3	0.61	0.55	0.74
$\delta g_{Hcc}/g_{Hcc}$ (%)	SM	1.7	1.21	1.18	1.35
$\delta g_{Hgg}/g_{Hgg}$ (%)	1.8	1.6	1.01	0.83	1.17
$\delta g_{H\tau\tau}/g_{H\tau\tau}$ (%)	1.7	1.4	0.74	0.64	1.10
$\delta g_{H\mu\mu}/g_{H\mu\mu}$ (%)	4.4	10.1	9.0	3.9	n.a.
$\delta g_{H\gamma\gamma}/g_{H\gamma\gamma}$ (%)	1.6	4.8	3.9	1.1	2.3
$\delta g_{Htt}/g_{Htt}$ (%)	2.5	–	–	2.4	1.7
BR_{EXO} (%)	SM (0.0)	<1.2	<1.0	<1.0	n.a.

Table 1.1: Precisions determined in the κ framework [8] on the Higgs boson couplings and total decay width, as expected from the FCC-ee data, and compared to those from the HL-LHC. All numbers indicate 68% C.L. sensitivities, except for the last line which gives the 95% C.L. sensitivity on the exotic branching fraction, accounting for final states that cannot be tagged as SM decays. The fit to the HL-LHC projections alone (first column) requires some assumptions: here, the branching ratios into $c\bar{c}$ and into exotic particles (and those not indicated in the table) are set to their SM values. The FCC-ee accuracies are subdivided in three categories: the first sub-column gives the results of the fit expected with 5 ab^{-1} at 240 GeV, the second sub-column in bold includes the additional 1.5 ab^{-1} at $\sqrt{s} = 365$ GeV, and the last sub-column shows the result of the combined fit with the HL-LHC. Similar to the HL-LHC, the fit to the FCC-eh projections alone requires an assumption to be made: here the total width is set to its SM value, but in practice will be taken to be the value measured by the FCC-ee.

SM particles (g_{hxx} for particle x) can be measured by the FCC-ee with a sub-percent precision as indicated in Tab. 1.1.

At energies of 500 GeV or higher, the FCC-ee would be able to further explore the Higgs properties by measuring the coupling to the top quark and its self-coupling as well. However, the top-Yukawa coupling will already be determined by the HL-LHC with a 2.4% precision, while the expected precision of 27% on the Higgs self-coupling that could be obtained from di-Higgs production at $\sqrt{s} = 500$ GeV and an integrated luminosity of 5 ab^{-1} is comparable with the model-independent precision of 34% from the measurement of the Higgs boson cross sections at 240 and 365 GeV. That is because the next-to-leading order graphs shown in Fig. 1.6 depend on the Higgs self-couplings and interfere with the leading order diagrams, impacting the Higgs production cross section. The center-of-mass dependence of this correction allows for a 3σ sensitivity to the Higgs self-coupling at the FCC-ee, as shown in

Observable	Parameter	Precision (stat.)	Precision (stat.+syst.+lumi.)
$\mu = \sigma(H) \times \mathrm{B}(H \to \gamma\gamma)$	$\delta\mu/\mu$	0.1%	1.45%
$\mu = \sigma(H) \times \mathrm{B}(H \to \mu\mu)$	$\delta\mu/\mu$	0.28%	1.22%
$\mu = \sigma(H) \times \mathrm{B}(H \to 4\mu)$	$\delta\mu/\mu$	0.18%	1.85%
$\mu = \sigma(H) \times \mathrm{B}(H \to \gamma\mu\mu)$	$\delta\mu/\mu$	0.55%	1.61%
$\mu = \sigma(HH) \times \mathrm{B}(H \to \gamma\gamma)\mathrm{B}(H \to b\bar{b})$	$\delta\lambda/\lambda$	5%	7.0%
$R = \mathrm{B}(H \to \mu\mu)/\mathrm{B}(H \to 4\mu)$	$\delta R/R$	0.33%	1.3%
$R = \mathrm{B}(H \to \gamma\gamma)/\mathrm{B}(H \to 2e2\mu)$	$\delta R/R$	0.17%	0.8%
$R = \mathrm{B}(H \to \gamma\gamma)/\mathrm{B}(H \to 2\mu)$	$\delta R/R$	0.29%	1.38%
$R = \mathrm{B}(H \to \mu\mu\gamma)/\mathrm{B}(H \to \mu\mu)$	$\delta R/R$	0.58%	1.82%
$R = \sigma(t\bar{t}H) \times \mathrm{B}(H \to b\bar{b})/\sigma(t\bar{t}Z) \times \mathrm{B}(Z \to b\bar{b})$	$\delta R/R$	1.05%	1.9%
$\mathrm{B}(H \to \text{invisible})$	B@95%CL	1×10^{-4}	2.5×10^{-4}

Table 1.2: Target precision, at the FCC-hh, for the parameters relative to the measurement of various Higgs decays, ratios thereof, and of the Higgs self-coupling. Notice that Lagrangian couplings have a precision that is typically half that of what is shown here, since all rates and branching ratios depend quadratically on the couplings.

Fig. 1.6. The 3σ evidence could be increased to 5σ, providing a discovery of the Higgs self-interaction, if the FCC-ee luminosity is increased by a factor two at high energies, for instance by adopting four IPs instead of the baseline choice of two. This upgrade is thus considered more viable than a 500 GeV FCC-ee upgrade.
It is worth noticing that the FCC-ee will also provide an unprecedented sample of isolated high-energy gluons through the $H \to gg$ decay.
Potentially after the FCC-ee operation, the FCC-hh could be built using as pre-accelerators the CERN Linac 4, PS, PSB, SPS and the LHC at 3.3 TeV. The FCC-hh could provide 20 ab^{-1} of 100 TeV proton-proton collisions, corresponding to the production of more than 10^{10} Higgs bosons. As a result of the model dependence being removed by the FCC-ee, a complementary Higgs measurement program would be achievable with the FCC-hh and eh. It includes the measurement to the percent level of rare Higgs decays such as $H \to \gamma\gamma$, $\mu\mu$, $Z\gamma$, the detection of the fully invisible $H \to 4\nu$, the measurement of the g_{Htt} coupling with percent precision and the measurement of the Higgs self-coupling to 5-7%, as summarized in Tab. 1.2. The Higgs couplings to all gauge bosons and to charged fermions of the second and third generations, with the only exception of the strange quark, will be measured with a precision ranging from few per mil to $\simeq 1\%$. The possibility to constrain the Higgs coupling to the lightest quarks and to the electron, by adding a special FCC-ee run at center-of-mass energy equal to the Higgs mass, is also under analysis.
The FCC integrated program should also study the EW phase transition, aiming at solving the matter-antimatter asymmetry problem. A possible explanation links this asymmetry to the EW symmetry breaking mechanism through which particles get masses. These models rely on a sufficiently violent transition to the broken-

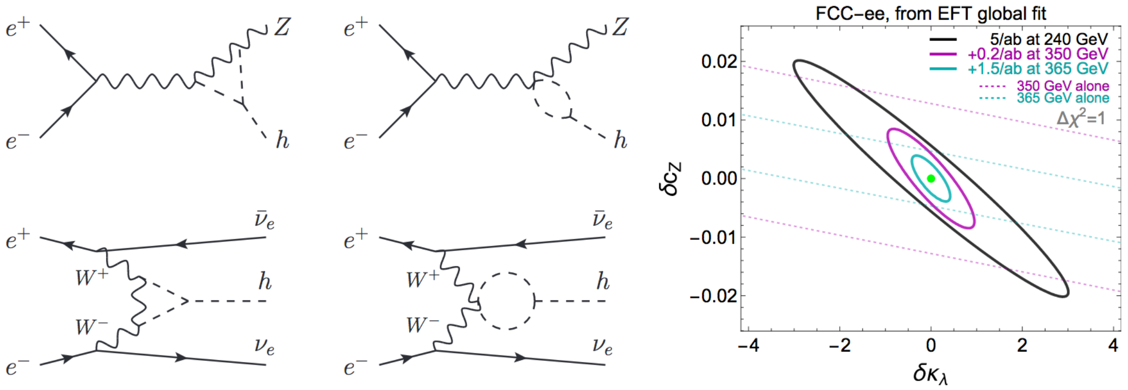

Figure 1.6: (Left) Sample diagrams illustrating the dependence on the Higgs self-coupling of single Higgs production at the FCC-ee.(Right) Standalone FCC-ee precision in the model-independent determination of the Higgs self-coupling ($\delta\kappa_\lambda$) and the HZZ coupling (δc_Z) deviations at 240 GeV (black), 350 GeV (purpled dashed), 365 GeV (green dashed) and by combining data at 240 and 350 GeV (purple), and at 240, 350 and 365 GeV (green). Image from [6].

symmetry phase, and the existence of adequate source of CP-violation. These conditions can be met in a large variety of Beyond Standard Model (BSM) scenarios. In particular, for a sufficiently strong phase-transition, there must be new particles with masses below one TeV that, interacting with the Higgs boson, modify the Higgs potential energy in the early universe. The production of these particles should be within the reach of FCC-hh. Another key search at the FCC is related to Dark Matter (DM). DM candidates masses can vary over several order of magnitudes and no experiment can probe the full range. However, for Weakly Interacting Massive Particles (WIMPs) DM candidates, the theory predicts masses ranging from few GeV to tens of TeV. The full energy and statistics of FCC-hh should be likely needed to search for these particles. Overall, the reach for the direct observation of new particles is driven by the FCC-hh. Examples of the FCC-hh discovery reach for the production of new particles are reported in Fig. 1.7. It includes, among others, Z' bosons decaying to various SM particles, excited quarks Q^* and massive gravitons G_{RS} from extra-dimensions theories.

Finally, we add that the FCC discovery potential is not limited to the very-high-mass domain. Thanks to the extremely high luminosity (of both FCC-ee and hh), it could reach an extraordinary sensitivity to very-weakly coupled particles, like axions and dark photons.

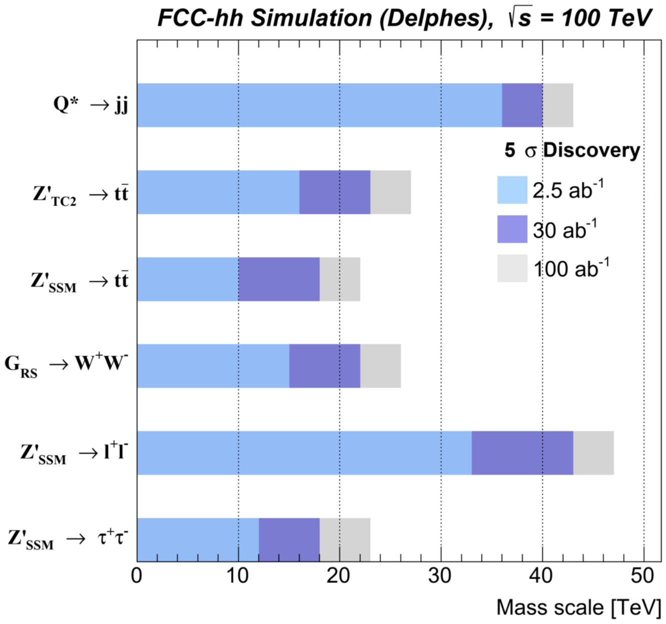

Figure 1.7: The FCC-hh mass discovery reach for several BSM s-channel resonances. Image from [5].

1.2.2 The Circular Electron Positron Collider

The Circular Electron Positron Collider (CEPC) is an international project initiated and hosted by China. It targets a circular collider operating at 91, 160 and 240 GeV, serving two multi-purpose detectors. The collider will be located in a 100-km long tunnel that could also host a Super Proton-Proton Collider (SPPC). The CEPC conceptual design report was published in 2018 [9, 10].

The main accelerator is a double-ring collider preceded by a linear accelerator, a damping ring and a booster. Fig. 1.9 shows the CEPC schematic view. The tunnel is designed to accommodate the SPPC without removing the CEPC, thus giving the possibility of electron-proton collisions. According to [11], the CEPC construction could be possibly start within few years and could be completed by 2030, by far the most aggressive time schedule among the big collider proposals.

The instantaneous luminosity envisaged is $3{\times}10^{34}$ cm^{-2}s^{-1} at the Higgs pole and $1{\times}10^{35}$ cm^{-2}s^{-1} at the W pole. At the Z pole the luminosity depends on the detector solenoidal field: it is limited to $1.7{\times}10^{35}$ cm^{-2}s^{-1} for 3 T solenoidal fields and reaches $3.2{\times}10^{35}$ cm^{-2}s^{-1} for 2 T ones. The CEPC baseline detector adopts a 3 T magnetic field, while the alternative detector presented in Sec. 1.3 uses a 2 T solenoid.

The CEPC physics program starts at $\sqrt{s}$ = 240 GeV where, in seven years of

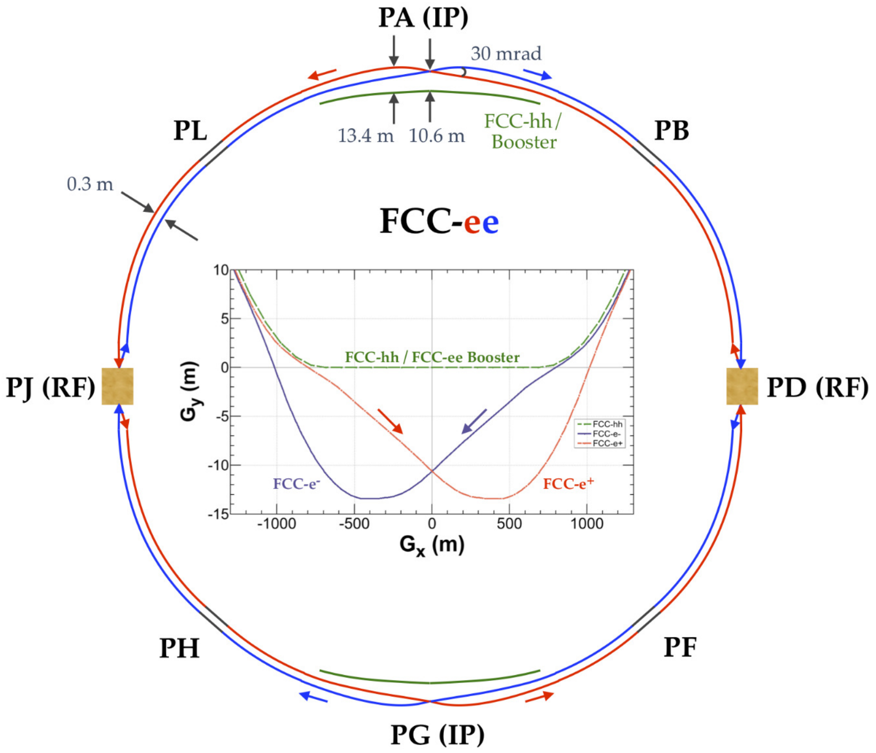

Figure 1.8: Schematic view of the FCC-ee. Image from [6].

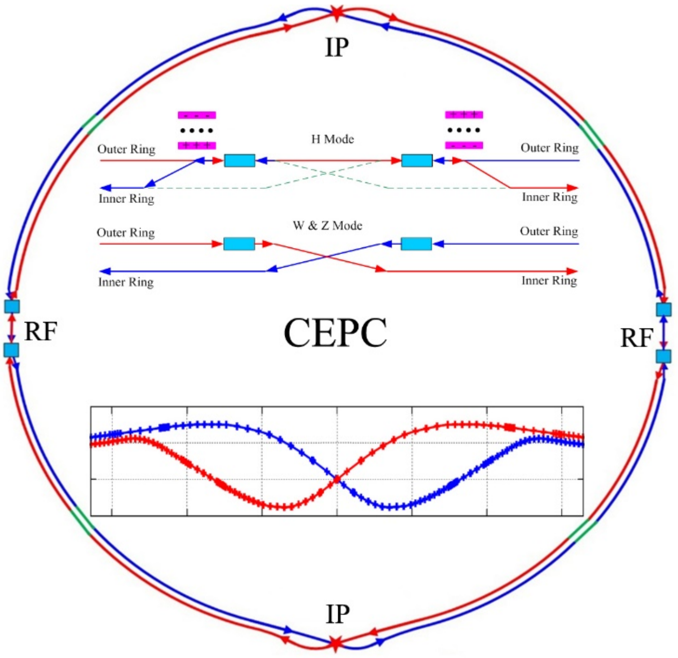

Figure 1.9: Schematic view of the CEPC. Image from [10].

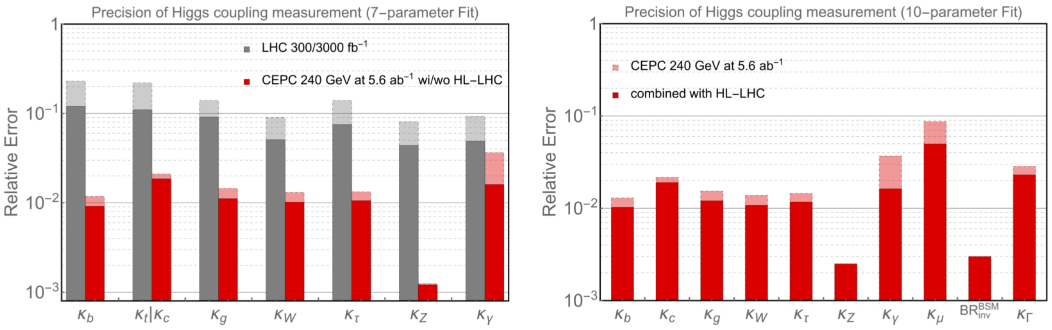

Figure 1.10: Expected relative precisions of the Higgs boson property measurements at the CEPC, with an integrated luminosity of 5.6 ab^{-1} at $\sqrt{s} = 240$ GeV, and the comparison with the LHC/HL-LHC. In the left panel, a constrained 7-parameter fit (chosen to facilitate a comparison with the LHC) in the $\kappa - framework$ is presented. In the right panel, a model-independent 10-parameter fit is presented. Image from [12].

operation, an integrated luminosity of 5.6 ab^{-1} will be collected, corresponding to $\simeq 10^6$ Higgs bosons. The center-of-mass energy will subsequently be reduced to 91.2 GeV for a two years run collecting 8 or 16 ab^{-1}, depending on the detector solenoidal field. In total, 10^{11}-10^{12} Z bosons will be produced. Eventually, a one year operation at the W threshold will be performed with $\sqrt{s}$ ranging from 158 to 172 GeV, providing 10^7 W bosons. The total Higgs width will be measured with a 3.1% precision. The measurement of the Higgs couplings can reach precisions of 0.1%-1%. This is approximately one order of magnitude better than the precision foreseen for the HL-LHC measurements as shown in Fig. 1.10. The CEPC has also great capability for precision measurement of most of the electroweak observables: it should improve the precision on the electroweak measurements by at least one order of magnitude.

1.2.3 The International Linear Collider

In its current version, the International Linear Collider (ILC) is a linear e^+e^- collider based on SuperConducting RadioFrequency (SCRF) cavities, whose technology is described in the 2013 Technical Design Report (TDR) [13]. Shortly after the Higgs boson discovery, it was established an initial center-of-mass energy of 250 GeV (ILC250). In its current form, the ILC250 [14] is a 250 GeV center-of-mass energy e^+e^- collider based on 1.3 GHz SCRF cavities. The accelerating cavities will provide a gradient of 31.5-35 MV/m, operating in a cryogenic infrastructure at 2 K. This technology is mature and is currently in use at the free-electron-laser facility at Desy, the XFEL, being an ILC demonstrator at a 10^{-1} scale. The design luminosity amounts to 1.35-1.5×10^{34}cm^{-2}s^{-1}, providing an integrated luminosity of 400 fb^{-1} in the first four operating years and 2 ab^{-1} in a little more than a decade. Two detectors will be used, ILD and SiD [15], operating under a push-pull configuration. The ILC candidate site is in the Kitakami region in northern Japan, chosen mostly for the absence of active seismic faults.

Fig. 1.12 shows the ILC250 schematic view. The ILC250 is 20.5 km long with two main arms, mostly occupied by the electron and positron linacs, at 14 mrad crossing angle. Electrons are produced by a polarized electron gun providing a 90% electron polarization at the source, resulting in more than 80% polarization at the IP. In the baseline configuration, positrons are produced by superconducting helical ondulators at the end of the electron main linac. They produce polarized photons further converted to positrons in a rotating target with a 30% longitudinal polarization. The drawback is the need of an operational electron linac working at the ILC250 nominal energy of 125 GeV. Alternatively, an electron accelerator providing a 3 GeV beam could be used to produce positrons by pair production. This configuration might not be able to provide positron polarization but could be used already during commissioning. Electrons and positrons are collected into the 3.2-km-long damping-ring complex to reduce their emittance to 20 nm in the vertical plane and 4 μm in the horizontal. The main linacs accelerate the beam thanks to SCRF cavities and eventually, the beams are focused to the size of 516 nm×7.7 nm. The ILC will operate using bunch trains where particles are grouped into sub-bunches and sub-bunches into bunches. The train repetition frequency is 5 Hz, and the sub-train bunch separation is 554 ns. This bunch train structure has deep impact on the detector design. It enables power pulsing of front-end electronics, resulting in a dramatically reduced power consumption, hence it eliminates the need for active cooling in many areas of the detectors resulting in a reduced material budget and an increased compactness. Similarly to the CEPC schedule, the ILC250 physics program, described in [16], will start with $e^+e^- \to ZH$ collision events (at $\sqrt{s} = 250$ GeV), from which the total Higgs width and the scale of the Higgs couplings can be determined. Individual couplings are later extracted from their branching ratio measurement. The ILC is upgradable in energy by making it longer or by increasing the acceleration gradient. At present, two energy upgrades are considered extending the center-of-mass energy to 500 GeV and 1 TeV. The higher-energy physics program includes the measurement of the top-quark mass with a precision of 40 MeV, the measurement of the top-quark electroweak couplings to the per-mil level, the measurement of the Higgs coupling to the top quark to a 2% accuracy, and measurement of the triple-Higgs coupling to a 10% accuracy. Fig. 1.11 shows the projected uncertainty on the Higgs couplings measurements.

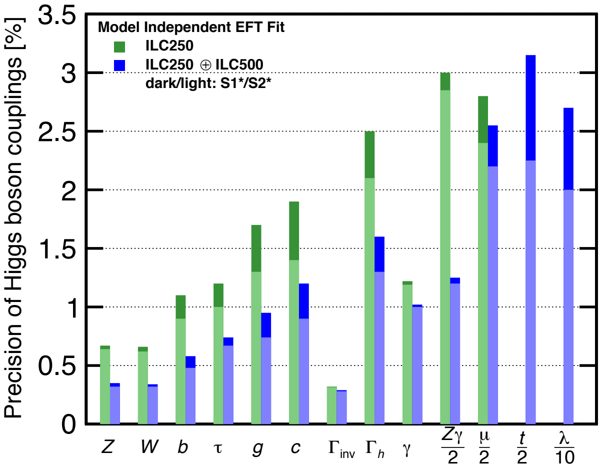

Figure 1.11: Expected ILC Higgs boson coupling uncertainties considering $\sqrt{s}$ = 250 GeV and an energy upgrade to 500 GeV, using the highly model-independent analysis presented in [17]. This analysis makes use of data of $e^+e^- \rightarrow W^+W^-$ in addition to Higgs boson observables and incorporates the projected LHC results. Results from integrated luminosities of 2 ab^{-1} at 250 GeV and 4 ab^{-1} at 500 GeV. The scenario S1* refers to analyses with the current detector understanding; the scenario S2* refers to more optimistic assumptions in which experimental errors decrease with experience. For a detailed explanation see [16]. Image from [16].

1.2.4 The Compact Linear Collider

The Compact Linear Collider (CLIC) is a multi-TeV linear e^+e^- collider to be located in the CERN area. The CLIC conceptual design report was published in 2012 [19, 20, 21]. The CLIC energy stages are $\sqrt{s}$ = 380 GeV, 1.5 TeV and 3.0 TeV, with corresponding instantaneous luminosities of 1.5, 3.7 and 5.9 × 10^{34} cm^{-2}s^{-1}, respectively. In about 7 years of operation at each energy stage, CLIC should provide an integrated luminosity of 1.0, 2.5 and 5.0 ab^{-1}, respectively for the 380 GeV, 1 TeV and 3 TeV stages.

A schematic layout of the CLIC complex is shown in Fig. 1.13. Electrons are created with a conventional radiofrequency (RF) injector, allowing ±80% polarization, while non-polarized positrons are created with electron beams accelerated to 5 GeV and sent into a crystal to produce energetic photons that, hitting a second target, convert into pairs. The emittance for both the electron and positron beams is reduced in two independent damping rings and they are sent into the main linac through a linear booster. The choice of having two independent beams through the whole chain is referred to as the two-beam acceleration scheme. The two main linacs accelerate beams exploiting normal conducting X-band cavities with an accelerating gradient

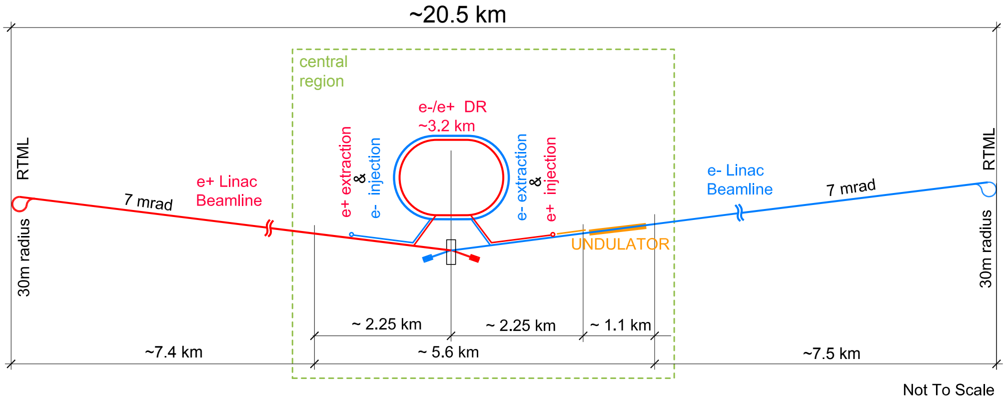

Figure 1.12: Schematic layout of the ILC250. Image from [16].

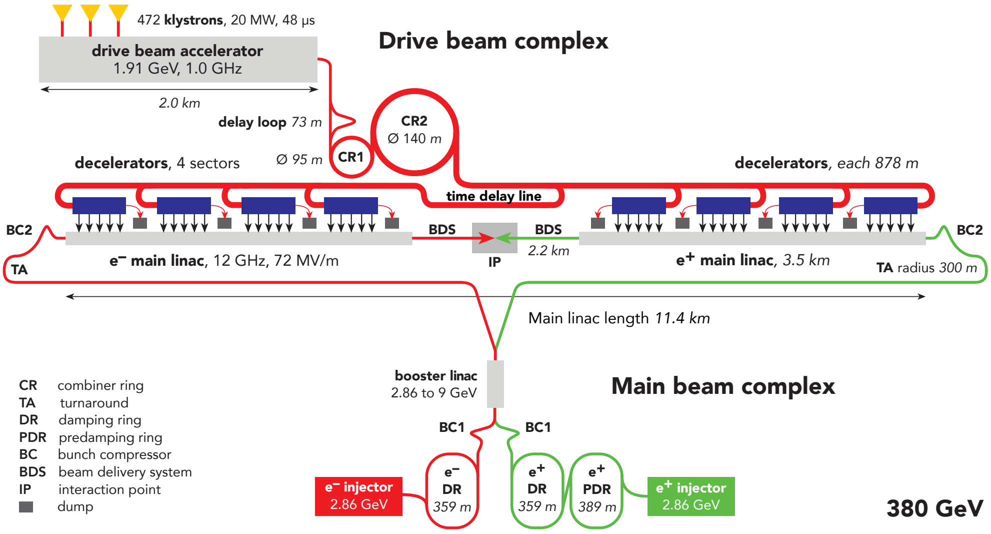

Figure 1.13: Schematic layout of the CLIC 380 GeV stage. Image from [18].

of 100 MV/m. For the first energy stage (380 GeV), a lower gradient of 72 MV/m is envisaged. Such extremely high gradient needs very short and high-power RF pulses that are difficult to generate at acceptable costs with traditional klystrons. To achieve that, CLIC exploits a novel drive-beam scheme that uses low-frequency klystrons to generate long RF pulses and stores their energy in a long, high-current, drive-beam pulse. This beam pulse is used to generate several short pulses distributed along the main linac. The CLIC upgrade to higher energy stages involves lengthening the main linacs. The main-linac tunnel length amounts to 11.4, 29.0 and 50.1 km for the three energy stages, respectively. The CLIC beam energy can be further adjusted if desired, for instance, a period of operation at 350 GeV is programmed to scan the top-quark pair-production threshold to measure the top-quark mass and width. Operation at much lower energy, *e.g.* the Z pole, are possible and a luminosity of 2.5 fb^{-1} per year can be achieved with an unmodified collider.

Similarly to the ILC, CLIC operates in bunch trains. The train repetition frequency is 50 Hz, and the sub-train bunch separation is 0.5 ns, independently from the center-of-mass energy. Again, this beam configuration impacts the detector design as in the ILC case previously described. To achieve the design instantaneous luminosity, CLIC requires very small beam sizes at the IP. The corresponding high-charge density leads to strong beam-beam effects, resulting in beamstrahlung emission and the subsequent production of background particles. To limit this background, CLIC would use flat beams which are much larger in the horizontal plane than in the vertical plane. For instance, the beam horizontal and vertical sizes at the 380 GeV energy stage could be $\sigma_x = 149$ nm and $\sigma_y = 2.9$ nm.

The CLIC physics program would start at 380 GeV, where the dominant Higgs production channel is the Higgsstrahlung process ($e^+e^- \to ZH$). 160×10^3 Higgs bosons would be produced during the first operation stage. At 1.5 and 3.0 TeV, the dominant Higgs production mechanism is W^+W^- fusion ($e^+e^- \to H\nu_e\overline{\nu_e}$), and in total 4.5×10^6 Higgs bosons would be produced. Additionally, the Higgs self-coupling could be measured thanks to $e^+e^- \to ZHH$ and $e^+e^- \to HH\nu_e\overline{\nu_e}$ events. As in the previous cases, the measurement of the Higgs boson production cross-section and decay branching ratios would be used to extract model-independent measurement of the Higgs couplings. The projected results for the three energy stages are shown in Fig. 1.14[1]. The g_{HZZ} could be measured with a 0.6% precision from the total ZH cross-section, and similar precisions are expected for other couplings such as g_{HWW} amd g_{Hbb}. The total Higgs width should be extracted with 2.5% accuracy. The 1.5 TeV energy stage would allow a 5σ observation of the double Higgsstrahlung process ($e^+e^- \to ZHH$) and provide evidence of the W^+W^- fu-

---

[1] As specified in [22], the projection for the Higgs couplings measurements were obtained assuming different energies of the first two stages: 350 GeV and 1.4 TeV.

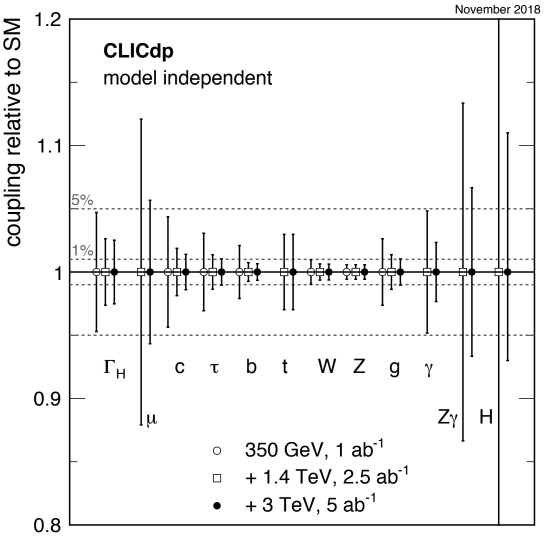

Figure 1.14: CLIC projection for the model-independent measurement of the Higgs coupling to SM particles [24, 25]. Image from [22].

sion process ($e^+e^- \to HH\nu_e\overline{\nu_e}$) that at 3 TeV should be the leading double-Higgs boson production mechanism. Combining the last two energy stages, the expected precision on the Higgs self-coupling is [-7%,+11%] [23].

1.2.5 The 2020 European Strategy for Particle Physics Update

The proposed timelines of post-LHC possible scenarios are shown in Fig. 1.15. Among them, the European Strategy for Particle Physics provides the European scientific vision and priorities of the field for the medium and long terms, charting the future of the field.

The 2020 European Strategy for Particle Physics Update [26] stated that “An electron-positron Higgs factory is the highest-priority next collider. For the longer term, the European particle physics community has the ambition to operate a proton-proton collider at the highest achievable energy.”. In the following the hadron collider target energy is identified as “at least 100 TeV”. The hadron collider calls for a $\simeq$ 100 km tunnel. Such a gigantic project would require decades and tens of billions of investments, therefore, in case the Higgs factory would be operated at CERN, it will be housed in the same tunnel. This is the FCC integrated program where the FCC-hh opens the possibility of an e^+e^- first stage.

However, the same document stated that “the timely realization of the electron-positron International Linear Collider (ILC) in Japan would be compatible with this strategy and, in that case, the European particle physics community would wish to collaborate". In a remarkable diplomacy exercise, the European Strategy Group aimed at the FCC-hh and binded the FCC-ee as a possible first stage, thus leaving open the possibility of a strong European participation to the ILC. Proponents of the FCC-ee program argued that the FCC-ee physics reach can be considered complementary to the ILC one and the possibility of building both e^+e^- colliders (FCC-ee and ILC) should be considered [27]. In any case, the integrated FCC project came out strengthened and its feasibility study should be completed on the timescale of the next Strategy Update.

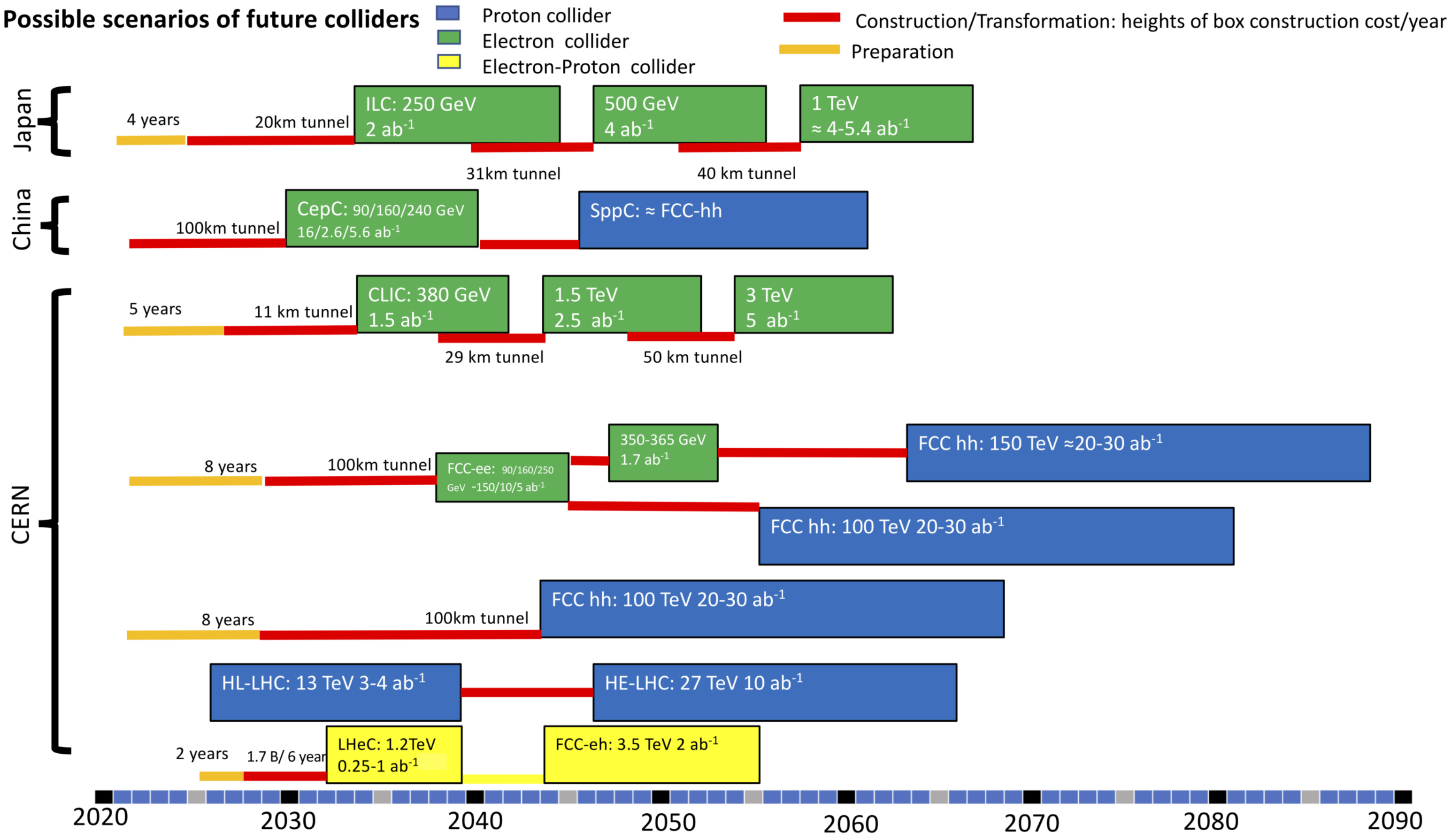

Figure 1.15: Possible timelines of future colliders including e^+e^- (ILC, CLIC, CEPC and FCC-ee), pp (FCC-hh and HE-LHC) and e^-p (LHeC and FCCeh) machines. Non discussed in the text is the HE-LHC, *i.e.* the possibility to extends the current energy frontier by almost a factor 2 by exploiting 16 T magnets while reusing the LHC tunnel [28]. Image from [29].

1.3 The IDEA Detector concept

In 2017 a new detector concept named IDEA (Innovative Detector for Electron-positron Accelerators) was proposed for operation at future circular e^+e^- colliders. In 2018 the IDEA concept was included in both the FCC-ee [6] and the CEPC [10] conceptual design reports.

Fig. 1.16 (left) shows an artistic view of the IDEA Detector. Fig. 1.16 (right) shows the IDEA structure and dimensions. IDEA exploits two main innovative sub-detectors: an ultra-light drift-chamber as main tracker, followed by a Dual-Readout (DR) fiber calorimeter. The drift chamber technology is based on the R&D work for the construction and operation of the MEG2 Ultra Light TIming Drift Chamber (MULTIDC), one of the key upgrade of MEG, an experiment hosted at the Paul Scherrer Institut (PSI), designed to search for the charged lepton flavor violating decay $\mu \to e^+\gamma$. The IDEA dual-readout calorimeter stands on the legacy of the DREAM/RD52 Collaboration, that demonstrated the feasibility of dual-readout optical-fibers calorimeters aiming at excellent, potentially unprecedented, resolution in single-hadron and jet energy measurements. Between the drift chamber and the calorimeter, there is another key element, an ultra-thin ($\simeq$ 30 cm thick) and low mass ($\simeq 0.7$ X_0 and $\simeq 0.16$ λ_{int}) solenoidal coil providing a magnetic field of 2 T. Tab. 1.3 summarizes the main parameters of the IDEA sub-detectors.

The following of this chapter is an introduction to the detector requirements at future e^+e^- circular colliders and the IDEA sub-detectors with the exception of the calorimeter. The calorimetry requirements at future e^+e^- colliders are reviewed in depth in Chap. 2, together with an introduction to the art of calorimetry and the related novel techniques. Chap. 3 and 4 summarize the main results on the IDEA dual-readout calorimeter design up to 2020.

1.3.1 Detector requirements

Most of the detector requirements for future electron-positron colliders can be extracted from Fig. 1.17, which shows the cross section (in fb), for several final states, as a function of the center-of-mass energy up to 3 TeV. The maximum cross section is located at the Z resonance, for which the $e^+e^- \to q\bar{q}$ process cross section amounts to $\simeq 2{\times}10^7$ fb. The process $Z \to q\bar{q}$ largely dominates the Z-boson decay modes with a branching ratio of $\simeq 70\%$. Considering the FCC-ee instantaneous luminosity at the Z pole ($4.6{\times}10^{36}$cm$^{-2}s^{-1}$), an event rate of $\simeq$ 100 kHz is expected equally shared among the two IPs. This is, by far, the highest event rate envisaged at future e^+e^- colliders, and is about four order of magnitudes lower than the LHC event rate

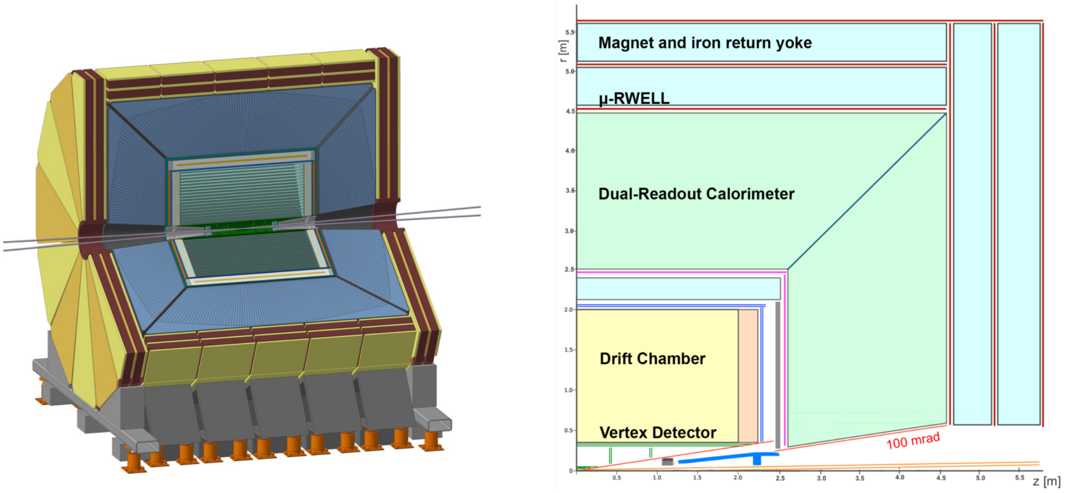

Figure 1.16: Artistic view of the IDEA detector concept (left). The structure and dimensions of the IDEA detector concept (right).

Vertex technology	Silicon
Vertex inner/outer radius (cm)	1.7/34
Tracker technology	Drift Chamber and Silicon Wrapper
Tracker half length (m)	2.0
Tracker outer radius (m)	2.0
Solenoid field (T)	2.0
Solenoid bore radius/half length (m)	2.1/3.0
Preshower absorber	Lead
Preshower R_{min}/R_{max} (m)	2.4/2.5
calorimeter absorber	Copper
calorimeter R_{min}/R_{max} (m)	2.5/4.5
Overall height/length (m)	11/13

Table 1.3: The IDEA sub-detectors main parameters.

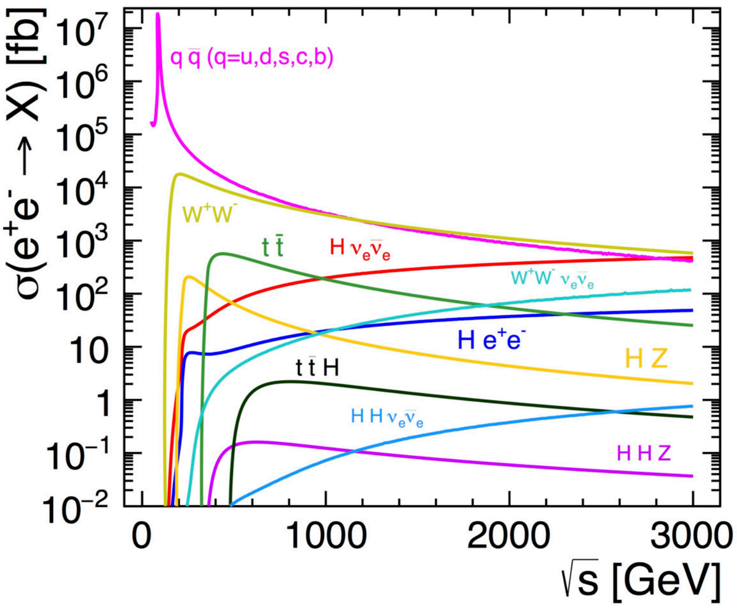

Figure 1.17: Cross-section (fb) for the $e^+e^- \to X$ process as a function of $\sqrt{s}$ (GeV). Image from [30].

in Run 2. Given the low event rate, the detectors need to collect every final state without loosing events. Thanks to the absence of background events, it is possible to design triggerless detectors. Hadronic final states dominate the decay modes of Z, W, H and top particles, therefore a precision jet identification and reconstruction is mandatory not to loose events. The requirements on jet, particle ID and momentum measurement largely dictate the calorimeter choice and design and are discussed in Chap. 2.

The requirement on the tracker is an excellent momentum resolution of about $\delta(1/p) = 2 - 3 \times 10^{-5}$ GeV^{-1}. The benchmark is the di-muon mass measurement in the process $e^+e^- \to HZ \to H\mu^+\mu^-$. This process allows the reconstruction of the Higgs mass, independently of the decay mode, using the leptons recoil mass and the (known) center-of-mass energy. Interestingly, the same is true for the process $e^+e^- \to HZ \to He^+e^-$, however the di-electron recoil mass resolution is limited by the fluctuations in the energy carried by electron/positron-radiated photons. The precise measurement of the radiated-photon energy sets a possible requirement for an excellent calorimetry-driven electromagnetic energy resolution and is discussed in Chap. 2.

Future e^+e^- colliders will produce billions of b-quarks, c-quarks, and τ-leptons, mostly from Z boson decays, making them, de-facto, B-factories and tau-charm factories. Several physics measurements, *e.g.* the Higgs coupling measurements, will depend on the identification of such heavy quarks and leptons and set stringent requirements on the vertex detectors. A common goal among the detector proposals is a resolution of 5 μm in the transverse impact parameter, d_0, for central tracks with p_T above few GeV. It severely limits the material thickness down to $\simeq 0.3\%\ X_0$ per vertex layer and requires a single hit position resolution of 3 μm in the vertex detector.

1.3.2 Vertex detector

The IDEA vertex detector, surrounding the 1.5 cm beam pipe, is based on monolithic pixel active sensors. The considered technologies are the fully depleted high-resistivity substrates, together with architectures implementing on-pixel sparsification and data driven, time stamped readout. The goal is a thickness of 0.15-0.30% X_0 per layer and a power dissipation below 20 mW/cm^2. This detector will significantly benefit from the electronic and mechanical work for the ALICE ITS [31], as well as of new ongoing developments, in the framework of the INFN ARCADIA R&D project.

1.3.3 Drift chamber

To match the momentum resolution requirement, IDEA adopts an ultra-light Drift CHamber (DCH). The main peculiarity is its high transparency, in terms of radiation lengths, following the work of the KLOE Experiment DCH [32] and the recent DCH for the MEG upgrade (MEG2) [33]. The design goal is a momentum resolution for charged particles of $\sigma(1/p_T) \simeq 3 \times 10^{-5}$ (GeV/c)$^{-1}$ and $\sigma(\theta, \phi) \simeq 0.1$ mrad for 45 GeV muons.

The DCH is a unique cylindrical volume, co-axial to the 2 T solenoid, with an inner radius of 0.35 m and an outer radius of 2 m, for a length of 4 m.

The DCH consists of 112 co-axial layers, at alternating sign stereo angles, ranging from 20 mrad to 180 mrad, arranged in 24 identical sectors. Fig. 1.18 shows the DCH structure and the readout printed circuit boards arrangement. Most of the material budget is located at the DCH end plates, therefore, to reduce the end plate amount of material, the gas containment structure is separated from the wire tension relief function. The wires are anchored to a self-sustaining light structure, the *wire cage*, surrounded by a very thin skin, the *gas envelope*, to compensate for the gas differential pressure with respect to outside. The wire cage is made of a set of 24 radial spokes, extending from the inner to the outer radius. The DCH is built by stacking radially in each sector printed circuit boards to which wires are soldered,

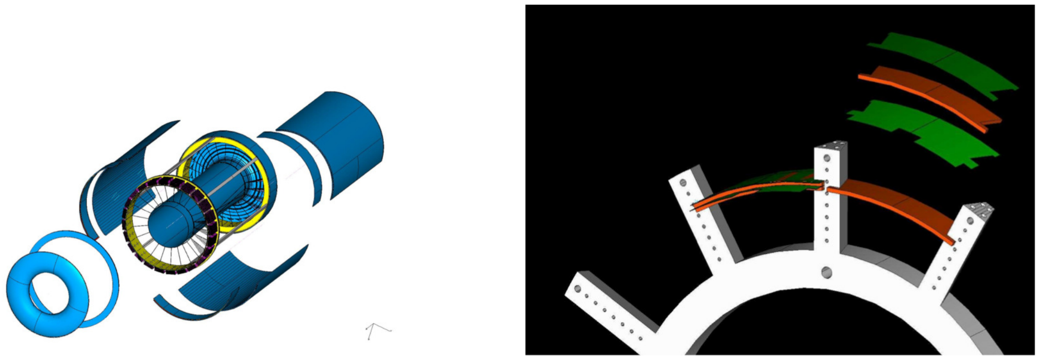

Figure 1.18: Schematic view of the DCH separation between gas containment and wire extension relief. In evidence the wire cage and the gas envelope (left). Schematic view from the MEG2 DCH: printed circuit boards (in green) to which wires are soldered, are stacked radially alternating with spacers (in red).

alternated with spacers for the proper cell width. Two carbon fiber domes, that are part of the gas envelope, enclose the gas volume. The total amount of material in the radial direction, towards the barrel calorimeter, is of the order of 1.6% of a radiation length, including inner and outer cylindrical walls and contributions from the gas mixture and the wires, as if they were uniformly distributed in the active volume. In the forward and backward direction, towards the end-cap calorimeters, the total amount of material is equivalent to about 5.0% X_0, including inner cylindrical walls and services endplates, instrumented with front-end electronics, signal and HV cables.

The innermost 8 layers, constituting the first super-layer, contain $N_1 = 192$ drift cells (8 per sector) each. In order to maintain an approximately constant cell size, the number of drift cells in each consecutive super-layer is incremented by 48 (2 in each sector): $N_i = 192 + (i - 1) \times 48$, up to $N_{14} = 816$ (34 drift cells per sector), for a total of 56448 drift cells. The width of the cell, approximately square, varies from about 12 mm at the innermost layer to about 14.5 mm at the outermost layer. For the chosen gas, He-iC_4H_{10} (90%-10%), this corresponds to about 350 ns maximum drift time for the largest cell size. The stereo angle is generated by stringing the wires between two points on the end plates at the same radius and mutually displaced by two sectors $(2\alpha - i = \pm 30^\circ)$, as sketched in Fig. 1.19 (left). Thus, the stereo angles increase linearly with the layer radius from 20 mrad to 180 mrad. Each layer consists of three wire sub-layers: an inner and an outer cathode sub-layers made of 40-μm-diameter Au-coated Al field wires and a middle anode sub-layer made of alternating sense (20-μm-diameter Au-coated W) and field shaping (50-μm-diameter Au-coated Al) wires. Two consecutive layers are oriented at opposite stereo angles. The outer cathode sub-layer of each layer lies at the same

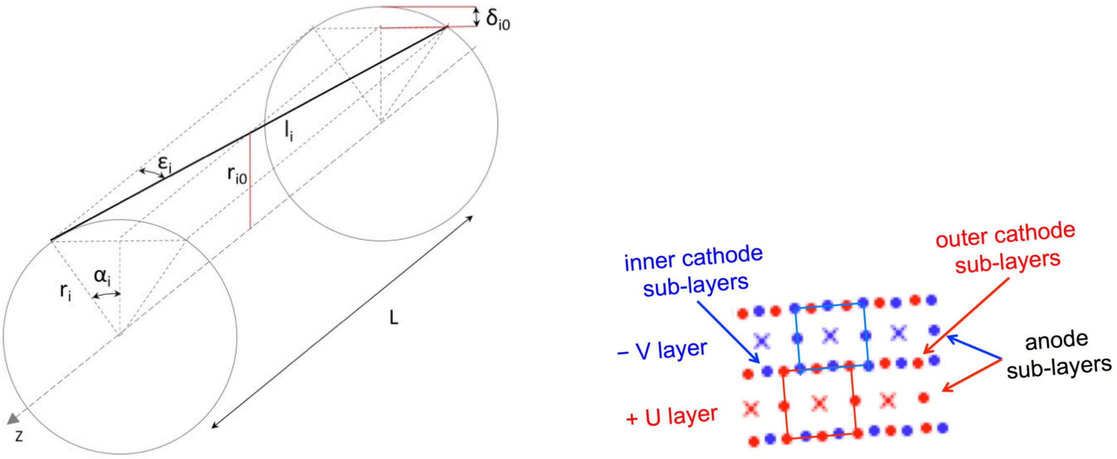

Figure 1.19: The arrangement of the DCH stereo wires.

radius as the inner cathode sub-layer of its radially adjacent layer, thus forming a dense equipotential mesh of cathode wire, see Fig. 1.19 (right). Its envelope in space forms a rotational hyperboloid surface.

A 100-μm drift-distance resolution has been measured with 7-mm-cell prototypes of the MEG2 drift chamber [34] using both a gas mixture and an electrostatic conditions very similar to the ones foreseen for the IDEA DCH. Analytical calculations, based exclusively on the DCH measured space points, for the momentum and angular resolution, are plotted in Fig. 1.20. Together with the excellent expected momentum resolution, the DCH can achieve superior particle identification capabilities thanks to the cluster-counting technique. The usual particle identification techniques based on the dE/dx measurements work by collecting the integrated charge over a single signal. This quantity is described by a Landau distribution. A large limitation of the dE/dx measurements is given by the need to truncate the largest dE/dx samples in order to get normally distributed values. On the other hand, the ionization process for which electrons are released follows a Poisson law, therefore by counting the total number of ionization clusters (N_{cl}) of a charged track one can reach a relative resolution on N_{cl} that follows $1/\sqrt{N_{cl}}$. The number of ionization clusters (dN_{cl}/cx) generated by a minimum ionizing particle in the DCH gas mixture is $\simeq 12.5$ cm^{-1}, corresponding to $(\sigma(dN_{cl}/cx)/(dN_{cl}/cx) \simeq 2\%)$. Based on this assumption, the expected performance relative to particle separation in terms of number of standard deviations is shown in Fig. 1.21 as a function of the particle momentum. The solid curves refer to the cluster-counting technique, while the dashed one refers to the expected identification power for the dE/dx method. For the whole range of momentum, particle separation by cluster counting outperforms the dE/dx technique.

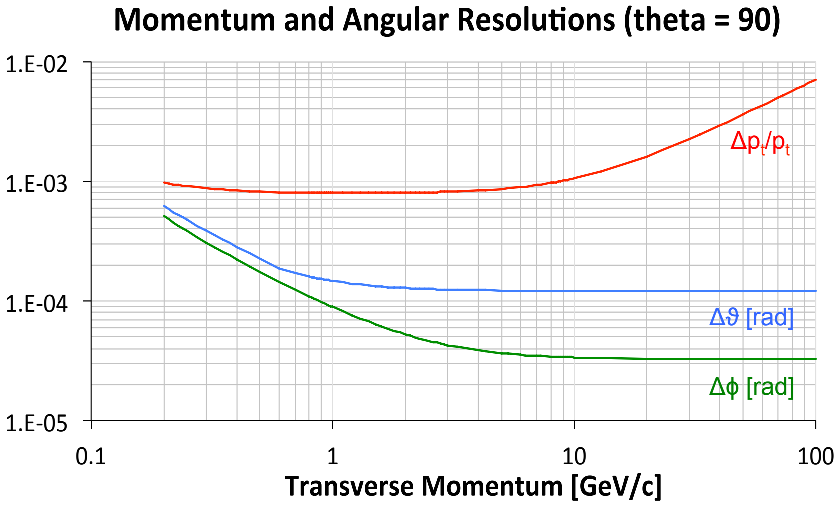

Figure 1.20: Momentum and angular resolution of the IDEA DCH as a function of the particle transverse momentum for $\theta = 90°$ assuming 100 μm spatial resolution.

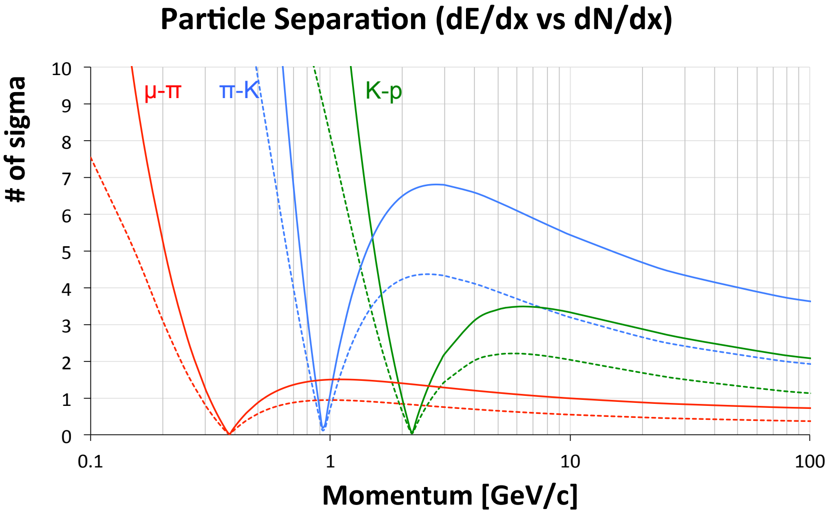

Figure 1.21: Particle type separation power of the IDEA DCH, in terms of number of standard deviations, as a function of the particle momentum.

1.3.4 Magnet system

A solenoidal magnet 5 m long and with an inner diameter of 4.2 m is considered. The relatively low field of 2 T guarantees that the magnet package thickness can be kept at 30 cm level. The flux return yoke scales with the square of the coil diameter, thus with the given dimensions a yoke thickness of less than 100 cm of iron is sufficient to contain the magnetic flux and to shield the muon chambers. The solenoid budget material amounts to 0.7 X_0 at 90°. Moreover, by positioning the coil inside the calorimeter volume, the stored energy is reduced by a factor four and the cost can be reduced by a factor two with respect to a coil surrounding the calorimeter.

1.3.5 Preshower and muon chambers

Both the IDEA preshower and the muon chambers are based on the micro-Resistive WELL (μ-RWELL) technology [35]. μ-RWELL chambers are compact Micro-Patter Gaseous Detector (MPGD), with a single amplification stage intrinsically spark protected. In the barrel region the magnet coil is used as a preshower and is followed by a layer of μ-RWELL chambers providing a very precise hit-level information immediately before the calorimeter. In the forward region, 1 X_0-lead-absorbers are placed in front of μ-RWELL chambers located immediately before the end-cap calorimeter. This allows to tag $\simeq$ 30% of the π^0 from their $\gamma\gamma$ decay and provides good acceptance for photons. Additional information for the π^0 identification is available from the calorimeter as explained in Chap. 3. The evaluation of the preshower performance and the single-hit-position resolution requirement are still in progress. MPGD, such as μ-RWELL chambers, will perfectly match also the requirements for the IDEA muon system, providing a good tracking efficiency, high-voltage stability, a space resolution for the coordinates of a muon track of 200-300 μm and a good time resolution thank to the fast charge amplification process.

Chapter 2

Introduction to calorimetry

The chapter is a non-exhaustive introduction to the art of calorimetry focused on detector response and energy measurements. Comprehensive references on the subject are [36, 37]. Eventually, calorimetry requirements for future electron-positron collider experiments are presented, together with the related calorimetric techniques.

2.1 Calorimeters

Calorimeters are particle detectors in which particles are (ideally) fully absorbed and their energy is translated into a measurable signal. Highly energetic interacting particles produce a shower of subsequent particles with progressively degraded energies. Charged particles within the shower interact with the detector active elements and their ionizing energy deposition is used to induce a signal in the form of charge or light pulses. The original information of the primary particle is inferred from the measured shower properties. In high-energy physics experiments, calorimeters are used to measure particles energy, momentum and type. In collider experiments with a 4π coverage, to ensure the best possible hermeticity, calorimeters are designed with cylindrical shapes around the beam axis. Every multi-purpose detector at colliders adopts a calorimetric system often combining two or more detectors. The calorimeter success in the particle physics experimental world is due to their unique features.

- In contrast to any other detector, calorimeters are sensitive to both charged and neutral particles, with the only exceptions of neutrinos for which, in most cases, they are completely transparent. Moreover, muons are not fully absorbed but, in most calorimeters, deposit energies of few GeV per meter (through both ionization and bremsstrahlung).

- They are fast detectors often used for triggering on events with interesting final states. For the case of photon triggering, they are the only detectors that can be used.

- The shower longitudinal development follows a logarithmic growth with the energy. Therefore, calorimeter dimensions barely depend on the collider center-of-mass energy. In contrast, dimensions of magnetic spectrometers (trackers immersed in a magnetic field) must linearly scale with the particle momentum not to degrade the momentum resolution for the highly energetic particles.

- The calorimeter energy (relative) resolution improves with the particle energy, scaling as $1/\sqrt{E}$. On the other hand, magnetic spectrometers can resolve particle momenta with a (relative) resolution linearly deteriorating with the momentum.

A calorimeter is an irreducible representation of the physics processes involved in the showering mechanism. While detecting electrons or photons, the showering mechanism only involves electromagnetic (em) processes that completely determine the calorimeter dimensions and response. While detecting hadrons, strong interactions with the detector nuclei occur, leading to huge differences in the shower dimensions and detector response.

Depending on the collision type (electron-positron or hadron-hadron), calorimeters operating at colliders detect particles with energies ranging from hundreds of MeV up to few TeV. However, their signals are largely produced by showering particles with much lower energies, ranging from the keV to the MeV scale. Processes happening at these energies dictate the calorimeter performance.

The calorimeter energy reconstruction depends on the calorimeter response and calibration. The calorimeter response is defined as the average signal produced per unit of deposited energy. Once the energy deposition is known, *e.g.* in data taking with test beams or in simulations, the calorimeter response can be measured. A calorimeter is said to be linear if it has a constant response. In a linear calorimeter, the response can be used as a calibration constant to reconstruct unknown energies. Differences in the calorimeter response while detecting different particle types introduce a further level of complication in the calibration procedure and they must be known and properly taken into account. The origins of the calorimeter response dependence on the particle type will be discussed all along this chapter.

2.2 Electromagnetic calorimetry

2.2.1 Electromagnetic-particle cascades

When an electron interacts with matter, its energy losses come from ionization and bremsstrahlung processes. For ionization, the stopping power, described by the Bethe-Bloch equation, decreases with the energy while the energy loss by the radiative process increases. Let us take lead ($Z = 82$) as an example. The energy loss for the two processes reaches the same intensity for electrons of $\simeq 7$ MeV, above it the radiative process starts dominating. Above 5 MeV the dominant interaction of the radiated photon with matter is via pair production. At higher energies (> 1 GeV), the cross section for both pair production and bremsstrahlung processes becomes nearly energy independent. As a result, an electron interacting with matter gives rise to a cascade of electrons, positrons and photons with progressively degrading energy, known as an em shower.

The particle multiplicity of the developing cascade keeps increasing up to a maximum until the average energy of the charged component falls below a critical energy point, below which the ionization process dominates over the radiative one. The critical energy, at which both processes play equally important roles, is roughly inversely proportional to the Z value of the absorbing medium:

$$\epsilon_c = \frac{610 \text{ MeV}}{Z + 1.24} \tag{2.1}$$

After the shower maximum, low energy photons (< 5 MeV) interact mostly via Compton scattering and photoelectric effect thus producing a greater abundance of electrons with respect to positrons. For instance, in lead only one quarter of the energy is deposited by positrons and the rest is entirely deposited by electrons.

When absorbed in a calorimeter, the low energy charged component of the em shower is responsible for most of the signal production. In lead, about 40% of the shower energy is deposited by particles below 1 MeV. The corresponding range is $\simeq 1$ mm or shorter and this length sets the scale for a proper sampling in electromagnetic calorimeters.

The shower maximum depth, *i.e.* the depth corresponding to the maximum number of particles produced in the showering process, logarithmically increases with the primary particle energy, as shown in Fig. 2.1 (a). The longitudinal shower development is described, for highly energetic em showers (> 1 GeV), by the *radiation length* (X_0), defined as the ratio of the electron energy and the specific energy loss by radiation. A high-energy electron loses on average 63% ($1 - e^{-1}$) of its energy by radiation traversing a 1 X_0 of material. When expressing the shower containment

in term of X_0, material-dependent effects are largely eliminated.
The angular distribution of the electrons produced by the photoelectric effect is almost isotropic and affects the lateral development of the shower beyond the shower maximum. The multiple scattering of electrons and positrons also contributes to the showering lateral development and is particularly relevant before the shower maximum. The result is an energy radial profile scaling exponentially with the radius and the scaling constants are different at the different stages of evolution of the shower. Two components are clearly recognizable in Fig. 2.1 (b) which shows the radial energy density for electrons in copper at three shower development depths. Another consequence of the almost isotropic angular distribution of the soft particles is that, after the first stages, particles have "forgotten" the direction of the primary particle.
For highly energetic em showers (> 1 GeV), the lateral development is described by the Molière Radius (ρ_M), defined as:

$$\rho_M = E_s \frac{X_0}{\epsilon_c} \tag{2.2}$$

where $E_s \sim 21.2$ MeV and ϵ_c is the critical energy. On average, 90% of the shower energy is deposited within a cylinder of 1 ρ_M, regardless the absorber material. The em shower lateral containment is largely independent of the primary particle energy. When expressed in g/cm^2, X_0 scales as A/Z^2 while ρ_M as A/Z, therefore the Molière radius is much less material dependent (copper and lead have approximately the same ρ_M but the X_0's differ by a factor of 3).
The radiation length is often used to describe the longitudinal shower development for both electron and photon induced showers. However, the shower development at the initial stages is fundamentally different for electron and photon events. While electrons start radiating immediately, photons must convert before releasing any energy inside the calorimeter. If they do, they can release even more energy than electron induced showers. This difference is evident in Fig. 2.2, showing the distribution of the energy fraction deposited in the first 5 X_0 by 10 GeV electrons and photons in lead.
The em shower profiles scale, in first approximation with X_0 and ρ_M, however this scaling is not perfect. It can be inferred from the fact that the particle multiplication continues down to lower energies in high-Z materials and decreases more slowly beyond the shower maximum. As a consequence, the shower maximum is located at a greater depth and one needs more X_0 to contain the same amount of energy. For instance, a given high-energy electron produces 3 times more positrons when showering in lead rather than in aluminum and one needs more X_0 of lead than of

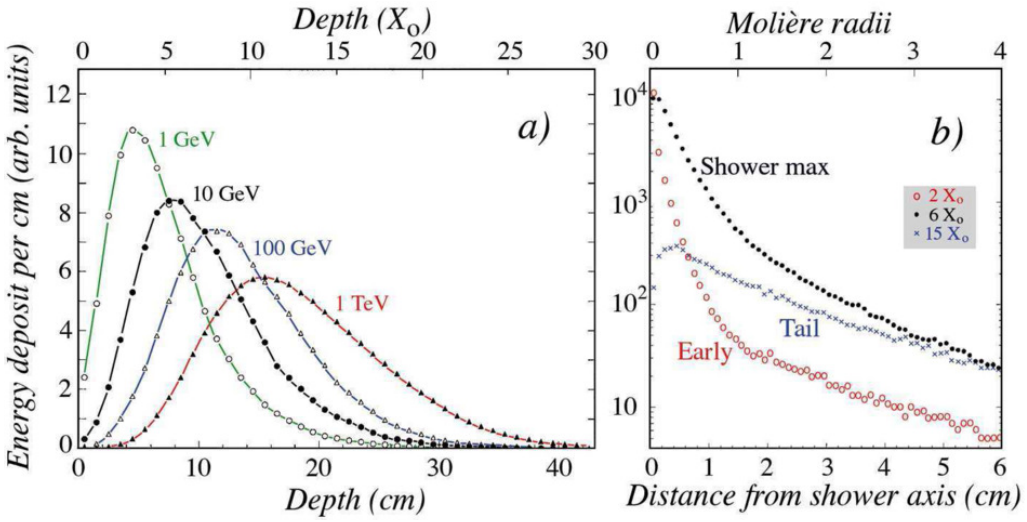

Figure 2.1: The energy deposited as a function of depth for 1, 10, 100 and 1000 GeV electron showers developing in a block of copper. The integral of the profiles has been normalized to the same value (a). The radial distributions of the energy deposited by 10 GeV electron showers in copper, at various depths (b). Results of EGS4 calculations. Image from [36].

aluminum to contain the shower at the 99% level, see Fig. 2.3.

2.2.2 Electromagnetic calorimeters

The prompt and compact em shower development allows to design relatively small calorimeters that are often used as electromagnetic compartments in complex calorimetric systems. Moreover, it also allows to design homogeneous calorimeters in which a unique material is used both as absorber and active element. Notable examples are crystal electromagnetic calorimeters. For instance, a single $PbWO_4$ crystal (X_0=0.89 cm, ρ_M=2.2 cm) contains approximately 90% of an electromagnetic shower within a 340 cm^3 volume (25 X_0, 1 ρ_M) corresponding to a weight of only 2.8 kg. To further reduce the detector dimensions, sampling electromagnetic calorimeters are built by alternating active and passive volumes, where active elements are substantially only able to generate a signal. The calorimeter X_0 and ρ_M are obtained as mass weighted combinations of the properties of the materials. Therefore, dense materials are used as absorbers to reduce the detector volume (typical materials for em calorimeters are lead, iron, copper, tungsten or depleted uranium).

Electromagnetic calorimeters are usually linear, as a consequence of the fact that,

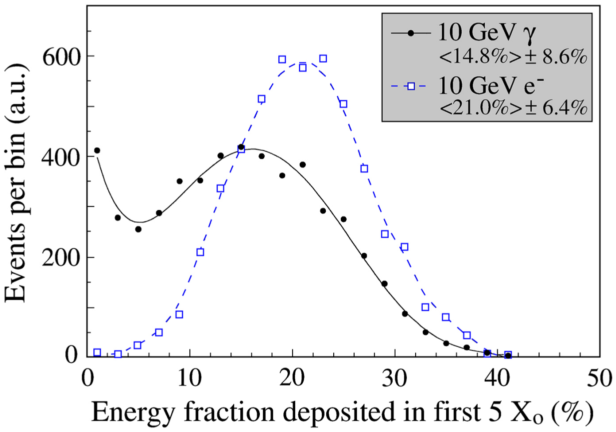

Figure 2.2: Distribution of the energy fraction deposited in the first 5 X_0 by 10 GeV electrons and photons showering in lead. Results of EGS4 calculations. Image from [38].

for fully contained showers, the entire primary energy is transferred to a very large number of shower particles (low-energy electrons and positrons that generate the signal), with an average energy that depends only on detector properties. Therefore the overall signal, *e.g. due to atom excitation or ionization*, is directly proportional to their number, which is in turn proportional to the primary energy. However, linearity may be lost if the active elements saturate for high (local) energy depositions. A non-constant response is typically a sign of readout electronics saturation or longitudinal shower leakage increasing with the energy. A remarkable exception comes from electromagnetic calorimeters coupled to digital active sensors. In this configuration a single active element provides the same signal when activated by 1 or n simultaneous particles. As the shower energy increases, so does the number of particles created and, given an almost constant shower volume, also the particle density increases. The result is a saturating signal leading to a non-constant response. Proportional active elements are usually preferred.

2.2.2.1 Fluctuations

In a linear em calorimeter, the calibration constant is used to reconstruct on average the primary electron and photon energies. Event-by-event fluctuations of the calorimeter response lead to energy fluctuations around the mean energy value. As a consequence, the calorimeter energy resolution depends on the response fluctuations and event-by-event corrections to it. What is normally quoted is the relative resolution, defined as the ratio of the energy-distribution standard deviation and its mean value (σ/E). Being dependent on E, this definition is valid only if the average

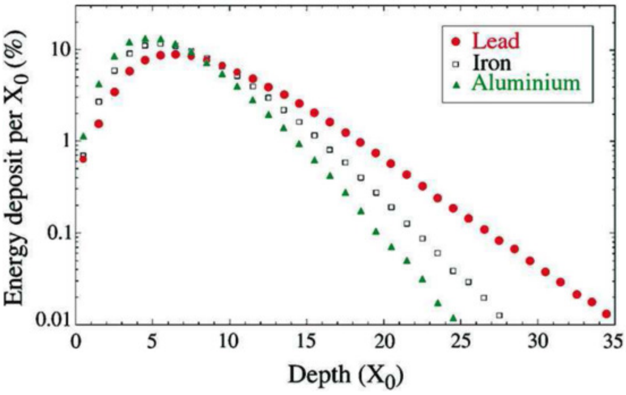

Figure 2.3: Longitudinal profiles of 10 GeV e^- showers developing in aluminum ($Z = 13$), iron ($Z = 26$) and lead ($Z = 82$). Image from [36].

energy E corresponds to the correct energy scale.
The response fluctuations are due to several effects with different dependencies on the energy. In em calorimeters common sources of response fluctuations are:

- sampling fluctuations, *i.e.* fluctuations in the energy deposited in active elements;
- signal quantum fluctuations, like photon statistics in light emitting active elements;
- instrumental effects, as, for instance, readout electronics noise, signal attenuation and geometrical inhomogeneities;
- fluctuations in shower containment.

Sampling fluctuations depend on the sampling fraction (the relative amount of active material) and the sampling frequency (thickness of the layers). The sampling fraction is usually defined on the basis of the energy lost by minimum ionizing particles (mip) as

$$f_{samp} = \frac{E_{active}}{E_{passive} + E_{active}} \tag{2.3}$$

where E_{active} and $E_{passive}$ indicate the energies deposited by an incident mip in the active and passive part, respectively. Sampling fluctuations follow the rules of Poisson statistics and contribute to the energy resolution with a term scaling as $1/\sqrt{E}$, *i.e.* $\sigma/E \sim E^{-1/2}$. In well designed electromagnetic sampling calorimeters, sampling fluctuations dominate over the other terms.

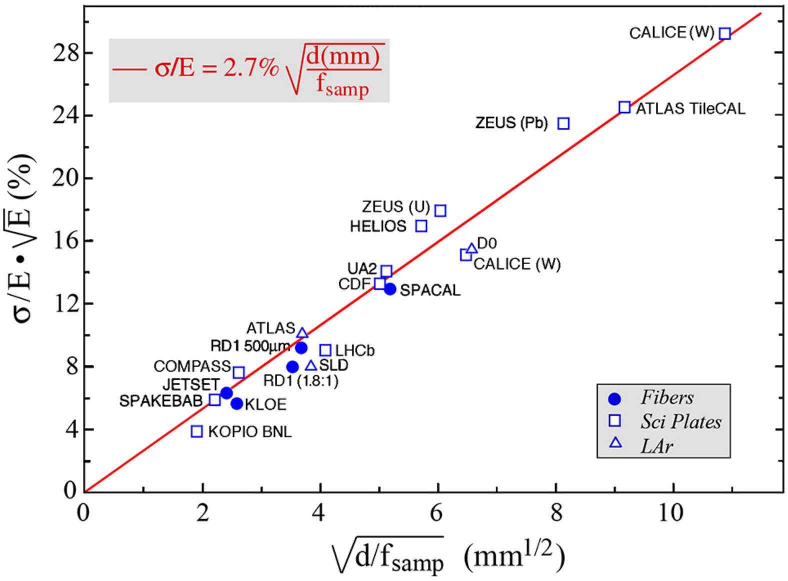

Figure 2.4: The em energy resolution of several sampling calorimeters as a function of $\sqrt{d/f_{samp}}$, where d is the thickness (in mm) of an active sampling layer and f_{samp} the sampling fraction for mips. The energy E is expressed in units of GeV. Image from [39].

In electromagnetic calorimeters with non-gaseous active media, sampling fluctuations are empirically described by the rule:

$$\frac{\sigma}{E} = \frac{2.7\%\sqrt{d/f_{samp}}}{\sqrt{E}} \tag{2.4}$$

where d is the thickness of the active elements (in mm) and f_{samp} is the sampling fraction for mips. Fig. 2.4 shows how Eq. 2.4 applies to several electromagnetic sampling calorimeters based on plastic scintillators or liquid argon. A better agreement is expected if the sampling fraction for electromagnetic showers is used in Eq. 2.4 instead of the mip one (see Sec. 2.2.3).

Also signal quantum fluctuations follow the rules of Poissonian statistics, as soon as the separate contributes are uncorrelated, and scale with $E^{-1/2}$. In homogeneous calorimeters they are usually the dominating term while in sampling calorimeters their contribution to the energy resolution is less than the sampling fluctuations.

Shower leakage fluctuations do not follow the Poissonian statistics and contribute to the calorimeter energy resolution with a term not scaling as $E^{-1/2}$. Detailed Monte Carlo simulations are often used to quantify leakage fluctuations and their dependence on the energy. For a given level of containment, longitudinal fluctuations are larger than lateral ones. This is due to the fact that the longitudinal development of a single shower fluctuates with the showering starting point, a feature for which only the primary particle is responsible. On the other hand, the lateral development is a collective phenomenon with several particles (typically thousands) involved.

The electronic noise contribution, being largely independent of the shower energy, is usually described with a (relative) term that scales with $1/E$. Response fluctuations induced by structural inhomogeneities depend on the shower position and, if located deep inside the calorimeter, might be energy dependent.

The calorimeter energy resolution is usually quoted by adding in quadrature each independent fluctuation term. While reducing sampling fluctuations is, in general, a good way to improve the energy resolution, it might be a waste of money. Indeed, due to the different energy scaling of the fluctuating terms, the relative contribution of each term changes with the energy. An example comes from the ATLAS em calorimeter for which an energy resolution of $\sigma/E = 10\%/\sqrt{E} \oplus 0.28/E \oplus 0.35\%$ is reported [40]. For energies below $\simeq$ 10 GeV, the electronic noise contribution to the energy resolution dominates over the others while, for energies above 1000 GeV, constant sources of fluctuations, such as the impact-point dependent response, completely determine the energy resolution. This behavior is sketched in Fig. 2.5.

Homogeneous calorimeters are not affected by sampling fluctuations, therefore they are chosen for high-energy-resolution applications. They can reach resolutions of few percent already at 1 GeV energies. The main drawbacks are wider shower volumes, leading to poorer shower-separation capabilities, and faster light yield deterioration with respect to plastic scintillators embedded in absorbing structures.

2.2.3 Electromagnetic showers and mips

Quite often the calorimeter response to mips is used as a gauge for electromagnetic shower energy reconstruction. This is fine only if differences in the response to electrons and mips are taken into account. Let consider the D0 calorimeter as an example. It was made of 3-mm-thick ^{238}U absorber plates interspersed with 4.6 mm liquid-argon-filled active gaps. The sampling fraction for mips, derived on the basis of the dE/dx values in active and passive materials, is 13.7%. However, the sampling fraction for electromagnetic showers was measured to be only 8.2%. The calorimeter e/mip ratio was 8.2/13.7=0.6. Hence, calibrating with mips and applying the calibration constants for em-shower energy reconstruction systematically led to an average underestimation of the electron energies.

As previously said, charged particles are responsible for the active element stimulation in electromagnetic showers, so one might expect the e/mip ratio to be 1. The origin of this discrepancy ($e/mip \neq 1$) is, again, due to the fact that the signal

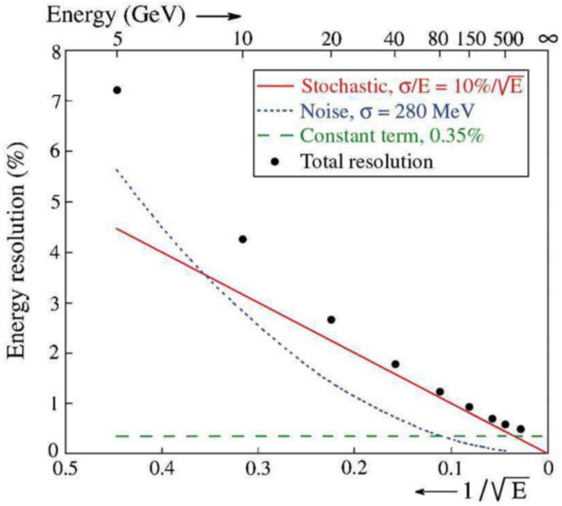

Figure 2.5: The em energy resolution and the separate contributions to it, for the ATLAS EM calorimeter as reported in [40].

is carried by (soft) particles at the MeV scale. Soft photons must produce a free electron to induce any signal, for which the photoelectric effect is the key process. The photoelectric effect has a Z^5 dependence on the absorber material and happens almost exclusively in the passive sections. Photoelectrons are produced in the absorber with energies of the order of 100 keV corresponding to typical ranges of 1 mm or shorter. Therefore, they can contribute to the calorimeter signal only if they are produced at the boundaries between the absorber and the next active element. In sampling calorimeters, the energy carried by the soft photons component is almost completely absorbed in the passive layers and its contribution to the signal is quenched. This is the origin of the e/mip problem. This also explains why e/mip amounts to $\simeq 1$ in homogeneous calorimeters.

To bring the e/mip ratio close to 1 in sampling calorimeters, two changes are effective: increasing the sampling frequency, to allow the photoelectrons to reach the active elements, and choosing active and passive elements with approximately the same Z. The latter can be achieved by adopting low Z absorbers. Copper ($Z = 29$) or copper-based alloys are good candidates. Fig. 2.6 confirms this idea. It shows the e/mip value of a uranium/PMMA (PolyMethyl MethAcrylate) and uranium/liquid-argon calorimeters as a function of the thickness of the absorber plates while keeping the same active-layer thickness.

The em shower soft component is not uniformly distributed among the shower volume and its contribution is more relevant at the shower (both lateral and longitudinal) tails, therefore the e/mip ratio changes with the shower shape and is minimal

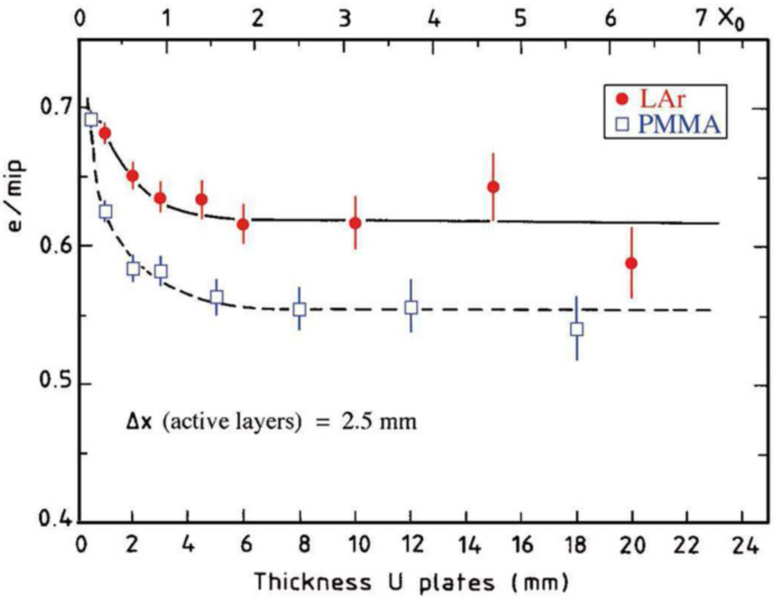

Figure 2.6: The e/mip ratio as a function of the thickness of the absorber layers, for uranium/PMMA and uranium/LAr calorimeters. The thickness of the active layers is 2.5 mm in all cases. Results from EGS4 simulations. Image from [36].

at its borders. Even though, to my knowledge, this effect has never been measured, good Monte Carlo tools easily predict it and an example will be given in Chap. 3 when calibrating the IDEA dual-readout calorimeter.

2.3 Hadronic calorimetry

Hadronic calorimeters are used to absorb and measure particle cascades induced by hadrons. Even if they can also be used to detect electromagnetic showers, it is most frequent and effective to use them in combination with an electromagnetic calorimeter section. Their response, dimensions and resolution are dictated by the properties of hadronic particle cascades in which strong interactions with the detector nuclei occur.

2.3.1 Hadronic particle cascades

While electromagnetic showers are governed by the interaction of electrons, positrons and photons with matter, showers induced by hadrons include a further great variety of particles (π, k, p, ...) arising from the strong interactions with the absorber nuclei. Pions are the most likely to be produced and amount to $\simeq 90\%$ of them.

Neutral pions (π^0) decay with a $\sim$ 99% branching ratio into two photons ($\pi^0 \rightarrow \gamma\gamma$). The other decay modes are $\pi^0 \rightarrow \gamma e^+e^-$, $\pi^0 \rightarrow e^+e^-e^+e^-$ and $\pi^0 \rightarrow e^+e^-$. Secondary particles from π^0 decays develop em showers. The fraction of energy carried by this em component is called the *electromagnetic fraction* (f_{em}). The conversion of part of the energy into an em shower is a one-way-only process because em showers cannot induce any nuclear interaction and behave as described in Sec. 2.2.1. Other processes contributing to the f_{em} are photon emission from excited nuclei and additional neutral meson decays (for instance the $\eta^0 \rightarrow \gamma\gamma$ process).

By increasing the primary-hadron energy, neutral pions start be produced by secondaries and high-order particles and the average f_{em} increases. The average electromagnetic fraction has been measured [41, 42] to increase with the primary energy following the power law:

$$\overline{f_{em}} = 1 - \left(\frac{E}{E_0}\right)^{k-1} \tag{2.5}$$

where E_0 is a material-dependent constant (it amounts to 0.7 GeV and 1.3 GeV for π^- induced showers in Cu and Pb, respectively), and $k \simeq 0.82$. Fig. 2.8 (a) shows this behavior for copper- and lead-based calorimeters. The average electromagnetic fraction roughly ranges from 30% to 50%, for charged-pion induced showers going from 10 GeV to 100 GeV. Eventually, extremely energetic hadronic showers resembles em showers ($f_{em} = 1$) leading to some particular effects. For instance, hadronic showers are on average more collimated at higher energies because em showers from π^0 decays develop closer to the shower axis. Fig. 2.7 (b) shows the f_{em} distribution for 150 GeV π^- showering in lead. The distribution is asymmetric, it fluctuates around a mean value with higher probabilities (tails) for larger values. This is expected. A large f_{em} arises when in the first nuclear reaction a large fraction of the primary energy is transferred to a π^0. If a similar large energy fraction is transferred to another particle, this does not lead necessarily to a small f_{em} because secondaries can produce energetic π^0's in the next reactions. The one-way-only mechanism describing the em component formation is responsible for asymmetric fluctuations of f_{em}.

When comparing charged-pion and proton induced showers, it is possible to notice that events with very high f_{em} values are suppressed for protons while admitted for pions. This is due to the baryon-number conservation law for which the total number of protons is conserved and processes where the leading proton yields a large fraction of its energy into f_{em} are suppressed. On the other hand, processes where the leading pion transfers a large fraction of its energy to one or more π^0 are possible like, for instance, the charge exchange process ($\pi^- + p \rightarrow \pi^0 + n$). We will see an example of this effect in Chap. 3 when studying the response of the IDEA

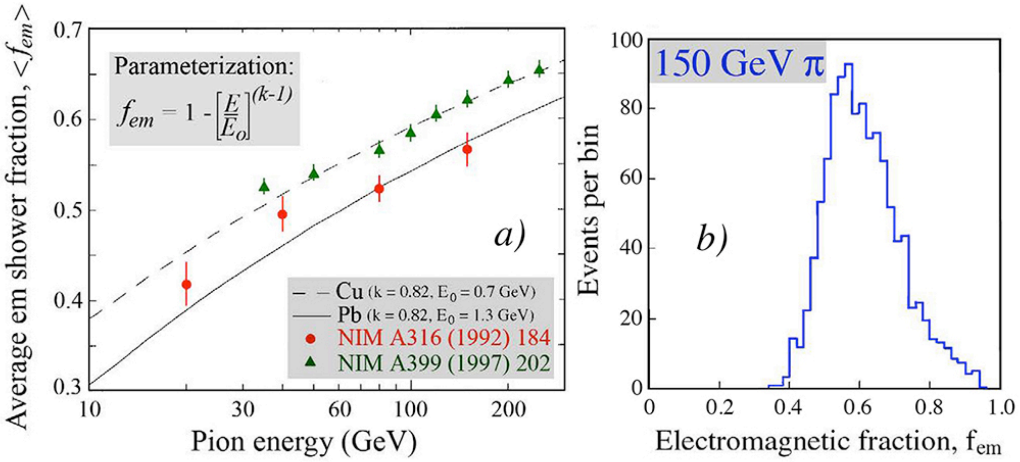

Figure 2.7: Measured average value of f_{em} as a function of energy, for showers developing in lead or copper (a), and the distribution of f_{em} values measured for 150 GeV, π^- showers developing in lead (b). The curves in graph (a) represent Eq. 2.5. Experimental data and images from [41, 42].

dual-readout calorimeter to pions and protons.
Moreover, protons and neutrons are released from atomic nuclei only if an energy, at least as high as their nuclear binding energy, is provided by the incident particle. The energy taken to release nucleons from nuclei does not contribute to the calorimeter signal and is known as the *invisible energy*. The invisible energy, the neutron component and the ionization component (mostly made of charged pions and protons) together form the non-electromagnetic (non-em) component, complementary to the em component. The energy sharing within the non-em component depends on the absorber element and detailed Monte Carlo simulations are needed for any quantitative study. For instance, in a typical hadron shower in lead, the non-em component is, on average, shared between ionizing particles (56%), two thirds of which are protons, neutrons (10%) and invisible energy (34%). Typical neutrons energies are few MeV while charged-particle energies range from tens to hundreds of MeV. At such energies the proton ionization power is much higher than the pion one, as stated by the Bethe-Bloch equation. The result is that protons travel for shorter ranges and contribute mostly to the signal in the core shower region. The range of such protons is typically few centimeters long and this sets the scale for a proper sampling in hadronic calorimeter. On the other hand, pions travel much longer distances, exiting the shower core, and contribute mostly to the signal at the shower tails. Examples will be shown in Chap. 3 when showing event displays from the IDEA dual-readout calorimeter. Neutrons contribute to the signal only if they

interact with the active elements nuclei and generate a sufficiently energetic charged product.

A useful quantity to describe hadronic shower profiles is the average distance high-energy hadrons travel before inducing a nuclear reaction, the *nuclear interaction length* (λ_{int}). When expressed in g/cm^2, λ_{int} scales with $\sqrt[3]{A}$. For the same material, the nuclear interaction length is much larger than the radiation length (for instance, in copper X_0 amounts to 1.4 cm and λ_{int} to 15 cm) and the difference is larger for high-Z materials. The amount of material to keep the longitudinal containment constant scales with the logarithm of the energy, as for em showers. Hadronic calorimeter dimensions scale accordingly, they typically are 7 to 10 λ_{int} deep for a longitudinal containment greater than 95%, depending on the energy scale, and, if shorter, their back is instrumented with auxiliary detectors, known as tail catchers, providing an event-by-event estimation of the shower longitudinal leakage. The hadronic shower shape fluctuates largely on an event-by-event basis, being affected by both the number of inelastic nuclear reactions and the number of π^0 produced. As opposed to em showers, there is not such a thing as a hadronic shower shape.

2.3.2 Hadronic calorimeters

Given the much larger dimensions of hadronic showers, hadronic calorimeters operating at collider experiments are always sampling calorimeters, to keep the experiment volume at manageable levels.

The calorimeter response to the em and the non-em components are indicated as e and h, respectively. We already explained why e is usually constant, *i.e.* calorimeters are linear for em shower detection. As described in [36], the non-em shower component is shared by mesons, spallation protons, evaporation neutrons, recoil target nuclei and is also partly used to release nuclear binding energy. There is no reason for the distribution of the non-em energy among these various components to be energy dependent. Therefore, the calorimeter response to the non-em component of hadronic showers (h) may be considered constant. A similar reasoning is reported in [43] concluding that h/e is a robust concept, independently of hadron energy and species. In Chap. 3 the h/e values of the IDEA dual-readout calorimeter are measured through simulations showing a good consistency with the above assumptions.

Calorimeters whose responses to the em and non-em components are identical ($e/h = 1$) are called compensating calorimeters. Most often, the invisible energy inside the non-em component conspires to reduce h with respect to e, and calorimeters for which $e/h > 1$ are called undercompensating calorimeters. Overcompensating calorimeters, for which $e/h < 1$, exist but are much rarer.

The calorimeter response to a hadronic shower is a combination of e and h, depend-

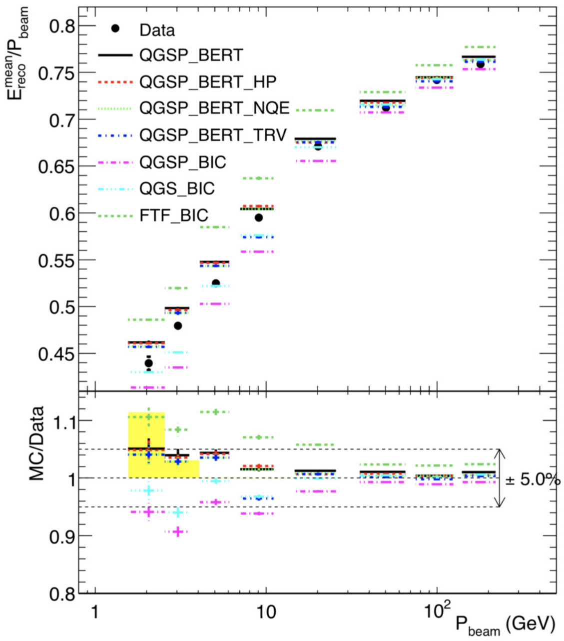

Figure 2.8: Mean energy for pions at beam momenta of 2–180 GeV showering in the ATLAS calorimeter. Result for both for data and Monte Carlo simulations. Image from [44].

ing on the average energy sharing between the em and the non-em component (the average f_{em} value). Indeed, the calorimeter response to charged pions (π) is given by:

$$\pi = ef_{em} + (1 - f_{em})h \tag{2.6}$$

Since the average f_{em} value increases with the energy, the response of non-compensating ($e/h \neq 1$) calorimeters is not constant and non-compensating calorimeters are intrinsically non-linear detectors for hadronic energy measurements. Most of the calorimeters operating at current collider experiments are undercompensating and their response increases with the energy. An example of non-linearity comes from the ATLAS calorimeter [44] and is reported in Fig. 2.8, showing the average reconstructed energy against the beam momentum. On the other hand, from Eq. 2.6 it follows that for compensating calorimeters $e = \pi$ and the detector is linear in hadron detection. This is the first benefit of compensation.

The calorimeter response to electrons (e) can be estimated by exposing the detector to an electron beam. To measure the calorimeter response to the non-em component (h) one would need to measure π and f_{em} over several events and, by using Eq. 2.6, calculating the h value at every event. Then, h would be the average value of the distribution. However, traditional calorimeters cannot measure f_{em} and this procedure is practically impossible.

If the dependence of the average f_{em} on the energy ($\overline{f_{em}(E)}$) is known, the e/h ratio can be measured using Eq. 2.6. Indeed, it follows that the ratio of the response to pions measured at two energies (E_1 and E_2) is given by:

$$\frac{\pi(E_1)}{\pi(E_2)} = \frac{\overline{f_{em}(E_1)} + [1 - \overline{f_{em}(E_1)}]h/e}{\overline{f_{em}(E_2)} + [1 - \overline{f_{em}(E_2)}]h/e} \tag{2.7}$$

By knowing the dependence of the average f_{em} on the energy ($\overline{f_{em}(E)}$), it is possible to estimate h/e. Note that this method only works if the calorimeter is linear for em shower detection, *i.e.* e is constant.

Even if the dependence of the average f_{em} on the energy, $\overline{f_{em}(E)}$, is assumed to be totally unknown, indications on the $\overline{f_{em}(E)}$ scaling can be derived from the π/e ratio. Indeed the terms $(1 - \pi/e)$ and $(1 - \overline{f_{em}})$ are directly proportional through the (constant) scale factor $(1 - h/e)$:

$$(1 - \pi/e) = (1 - h/e) \cdot (1 - \overline{f_{em}}) \tag{2.8}$$

e/π reduces to 1 if $e/h = 1$ or for hadronic showers dominated by the em-component ($f_{em} = 1$). In non-compensating calorimeters e/π tends to 1 with increasing energies. In the assumption that Eq. 2.5 holds, by measuring π/e as a function of energy, it is possible to extract the exponent k and the term $(1 - h/e)E_0^{1-k}$. As reported in [43], since $E_0 \sim 1$ for pion induced cascades and $1 - k$ is small, the term E_0^{1-k} is usually ignored and only h/e is reported.

In Sec. 2.3.1 we have seen that charged π tends to develop showers with higher f_{em} with respect to protons. In non-compensating calorimeters this leads to a different response to pions and protons. For instance, this difference amounts to $\simeq$ 5% for the ATLAS calorimeter [45] and exceeds 10% in the CMS Forward Calorimeter for energies below 100 GeV [46]. The compensating-calorimeter response is not affected by the f_{em} value therefore it is the same for different hadron types. This is the second benefit of compensation.

2.3.2.1 Fluctuations

We now turn our attention on event-by-event fluctuations in the calorimeter response to hadrons. All the sources of fluctuations affecting the calorimeter response to em showers (see Sec. 2.2.2.1) also contribute to the hadronic response. In particular, sampling fluctuations are usually larger for hadron showers than for em ones. This is due to the fact that the average number of particles contributing to the calorimeter signal is lower in hadronic showers with respect to same-energy em showers developing in the same calorimeter. In an em shower most of the signal is carried by $\simeq 1$ MeV electrons with ranges of few millimeters, therefore a single electron typically activates only one active element. On the other hand, most of the signal in hadronic showers is carried by 10-100 MeV protons/pions traveling longer distances. Such particles typically are thus sampled by more than one active element. Therefore, the number of different particles contributing to the signal is smaller for hadron showers. Fluctuations in this number are larger for hadron showers than for em showers and lead to higher sampling fluctuations.

Non-compensation is also responsible for event-by-event fluctuations in the calorimeter response to hadrons. Indeed, event-by-event fluctuations in the em component (f_{em}) affect the response of non-compensating calorimeters ($e/h \neq 1$). This non-Poissonian source of fluctuations is usually the dominant term in the energy resolution. It contributes to the energy resolution (σ/E) through an energy-dependent term, scaling as $cE^{-0.28}$ (for a detailed explanation see [36]). The term c depends on the calorimeter degree of non-compensation and the proper scaling of σ/E for a non-compensating calorimeter may be expressed as:

$$\frac{\sigma}{E} = \frac{a_1}{\sqrt{E}} \oplus cE^{-0.28} \tag{2.9}$$

An example of this energy resolution scaling is sketched in Fig. 2.9 (solid line). Interestingly, up to $\simeq 400$ GeV, it runs almost parallel to the (dashed) line corresponding to an energy resolution in which only the stochastic term is included ($\sigma/E = a/\sqrt{E}$).

This is the reason why often the energy resolution of non-compensating calorimeter is, with a good approximation, expressed as:

$$\frac{\sigma}{E} = \frac{a_2}{\sqrt{E}} + b. \tag{2.10}$$

Note that when expressing the energy resolution using Eq. 2.9 or Eq. 2.10, a_1 and a_2 assume different values and the stochastic terms cannot be directly compared.

In compensating calorimeters $c = 0$ and f_{em} fluctuations do not affect the energy resolution, thus the energy resolution is greatly improved. This is the third benefit of compensation.

As explained in Sec. 2.3.1, fluctuations of the em component are not symmetric. It follows directly that non-compensating calorimeters have a non-symmetric response to hadrons. Undercompensating calorimeters for which $e > h$ respond with an anomalously high signal in events with anomalously high f_{em} and their response distribution shape is dictated by the f_{em} distribution one (see Fig. 2.7). Several

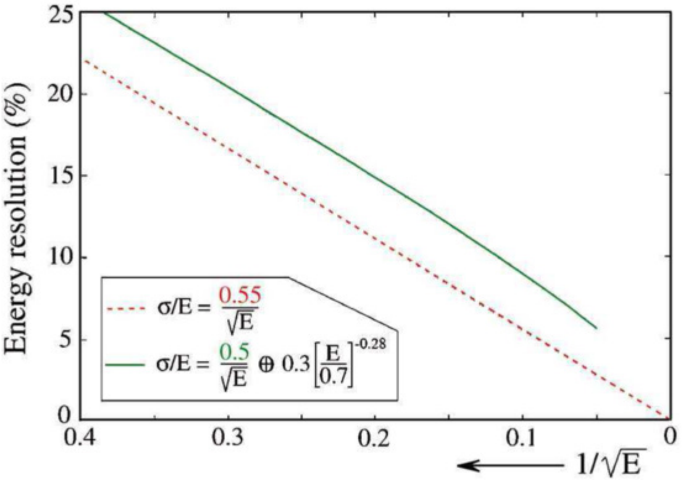

Figure 2.9: The hadronic energy resolution for a non-compensating calorimeter up to 400 GeV (solid line) and calculated with a sole stochastic term with a slightly larger scaling constant. Image from [36].

examples of this asymmetry are given in Sec. 2.4.3. Overcompensating calorimeters ($e < h$) are expected to have a non-symmetric response with anomalously small signals, although related examples are rare.

The compensating calorimeter response to hadrons, not being affected by f_{em} fluctuations, is symmetric. This is the fourth benefit of compensation.

Overimposed to f_{em} fluctuations, another source of fluctuations affects the calorimeter response to hadrons: the event-by-event fluctuation of the invisible energy fraction (f_{inv}).

To understand its impact on the fluctuation of the calorimeter response, the relation between f_{em} and f_{inv} must be known. For instance, under the assumption that they are uncorrelated, their contribution to the calorimeter response fluctuations have to be added in quadrature. Under the same hypothesis, the f_{inv} fluctuation forms the ultimate source of fluctuation spoiling the energy resolution, and affects both compensating and non-compensating calorimeters. Indeed, some publications state that "fluctuations in (in)visible energy play a role in all hadron calorimeters and form the ultimate limit to the achievable hadronic energy resolution . . . the resolution of compensating calorimeters is ultimately limited by fluctuations in the (in)visible energy" [47].

A 2018 study [48] shed light on the relation between f_{em} and f_{inv}, and on the role of invisible energy fluctuations on the energy resolution of hadronic calorimeters. We review this result while introducing two compensating techniques: dual-readout calorimetry and compensation by neutron signal boosting.

2.3.3 Dual-readout method

Compensating calorimeters sample the em component and the non-em component of a hadronic shower with the same response. To achieve the same result, the dual-readout method [49] works by measuring the f_{em} on an event-by-event basis and correcting the calorimeter signal for its value. To measure f_{em}, dual-readout calorimeters exploit the fact that the signal in the em component is carried by electrons and positrons that are relativistic down to 200 keV energies, while the signal in the non-em component is mostly carried by non-relativistic particles. Therefore, collecting the Cherenkov signal produced in a hadronic shower is almost equivalent to sampling the em component. A second signal (typically from scintillators) is used to measure the signal from ionization energy deposition, from which a first (non-compensated) estimation of the shower energy is inferred. Eventually, this value is corrected for the event f_{em} measured with the Cherenkov signal.

Let us consider a calorimeter sampling the Cherenkov and the scintillation signals of a hadronic shower. After the signal calibration at the electromagnetic scale, *i.e.* with electrons, the energies reconstructed with the two signals (S and C) are given by:

$$S = E[f_{em} + (h/e)_S(1 - f_{em})] \tag{2.11}$$

$$C = E[f_{em} + (h/e)_C(1 - f_{em})] \tag{2.12}$$

where the h/e values weight the different degree of non-compensation of the two signals. For a fully em event, both S and C equal E since they are both calibrated at the em scale. For a fully non-em event, they correspond to E scaled by their degree of non-compensation. Note that both h/e are constant and measurable quantities as explained in Sec. 2.3.2.

The event energy, corrected for the f_{em} value, is given by:

$$E = \frac{S - \chi C}{1 - \chi}, \tag{2.13}$$

with

$$\chi = \frac{1 - (h/e)_S}{1 - (h/e)_C}. \tag{2.14}$$

As long as the (h/e) values are constant, the χ factor is as well a detector constant (independent of energy and particle type) and can be straightforwardly estimated with test beam data. This feature is referred to as the χ factor universality. A quantitative example (from simulations) of the χ factor universality is given in Chap. 3 when describing the calibration of the IDEA dual-readout calorimeter.

The χ factor universality was demonstrated for the first time by the DREAM Collaboration [50], using a copper-fiber calorimeter described in Sec. 2.4.3. The Cherenkov light was collected in undoped quartz fibers, while the dE/dx induced signal was provided by scintillating plastic fibers. They found h/e ratios of 0.21 and 0.77 for the Cherenkov and the scintillating signals, respectively. An $(h/e)_C$ value greater than 0 indicates that the Cherenkov response to the non-em component is not completely suppressed and some relativistic charged particles (mostly charged pions) contribute to the calorimeter Cherenkov signal. In a ideal DR calorimeter, the Cherenkov signal would sample exclusively the em component ($h/e = 0$) being a direct measurement of f_{em}. On the other hand, if $(h/e)_C = (h/e)_S$ the two signals would sample the two components (em and non-em) with the same response and no information on the f_{em} could be extracted. Therefore, the best DR calorimeter is the one with the lower $(h/e)_C$ and the higher $(h/e)_S$ values possible, or equivalently, the lower χ factor. The χ factor depends both on the calorimeter materials and sampling fraction and, to my knowledge, its scaling with the material A and Z values is unknown.

Reconstructing hadron energies using Eq. 2.13 corrects for the event f_{em} value, leading to all the compensation benefits, such as a linear detector, an energy resolution not spoiled by f_{em} fluctuations and a symmetric response. Examples from test-beam data are given in Sec. 2.4.3.

The χ factor universality guarantees that compensation is achieved through Eq. 2.13 for every particles type (protons, pions, kaons, ...) and energy. An example from the IDEA dual-readout calorimeter simulation is given in Chap. 3.

The dual-readout method can be used in calorimeters with any kind of absorber and the calorimeter sampling fraction can be increased as desired. It is also possible to design homogeneous dual-readout calorimeters, as demonstrated by separating the scintillation and the Cherenkov light from BGO crystals [51]. For these reasons it has been defined as a flexible compensating technique [52]. These features are not available in compensating calorimeters exploiting neutrons signal boosting explained in Sec. 2.3.4.

We now consider the role of the f_{inv} fluctuation on the calorimeter response. Fig. 2.10 (a) shows a scatter plot correlating the nuclear binding energy losses, *i.e.* the invisible energy, and the f_{em} for 100 GeV π^- showering in lead (see [48] for details). It turned out that a strong (anti)correlation exists among the two variables. Fixing the event f_{em} constrains with great precision the f_{inv}, *i.e.* if f_{em} is measured on an event-by-event basis, the invisible energy inside the non-em components is determined in every event with great accuracy. However, small fluctuations in the invisible energy are still possible due to the non-perfect correlation between the two variables. Therefore, the ultimate resolution achievable with the dual-readout method depends on the strength of the correlation between the f_{em} and f_{inv}, rather than on the rms of the invisible energy distribution.

On the f_{em} measurements Let consider again Eqs. 2.11, 2.12. As soon as the h/e value of a signal (S or C) is known and E is known as well (for instance in a test-beam), it is possible to estimate f_{em} on an event-by-event basis by using any of the two signals. For instance, in the S case, f_{em} is given by:

$$f_{em} = \frac{S/E - h/e_S}{1 - h/e_S} \tag{2.15}$$

If both h/e values are known, it is possible to estimate f_{em} on an event-by-event basis regardless the E value, by exploiting the S/C ratio

$$\frac{S}{C} = \frac{f_{em} + h/e_S(1 - f_{em})}{f_{em} + h/e_C(1 - f_{em})} \tag{2.16}$$

If both h/e values are unknown it is not possible to measure the f_{em} using S and C. Note that the χ factor can be estimated as soon as E is known (for instance in a test-beam) and once χ and one of the two h/e values are known, the last missing h/e is constrained. Estimating at least one of the two h/e values is mandatory to measure f_{em}.

We propose here a new variable that could be used to further constrain the h/e values. It is possible to build the experimentally accessible variable

$$Z = \frac{1 - C/S}{1 - \chi \cdot C/S} \tag{2.17}$$

When $f_{em} = 1$, Z amounts to 0, while it reaches $1 - h/e_C$, for $f_{em} = 0$ events. Indeed:

$$Z = (1 - h/e_C) \cdot (1 - f_{em}) \tag{2.18}$$

i.e. Z provides an event-by-event estimate of f_{em} within an (unknown) constant scale factor. It is the dual-readout equivalent of Eqs. 2.8. Again, in the assumption that Eq. 2.5 holds, we get

$$< Z(E) >= (1 - h/e_C) \cdot \left(\frac{E}{E_0}\right)^{k-1} \tag{2.19}$$

and, as before, it is possible to extract the exponent k and the term $(1 - h/e_C) \cdot E_0^{1-k}$ and, if $E_0 \sim 1$ and $1 - k$ is small (as they are supposed to be for charged pions), h/e_C can be directly estimated.

Therefore, it is possible to experimentally verify the correctness of the f_{em} scaling

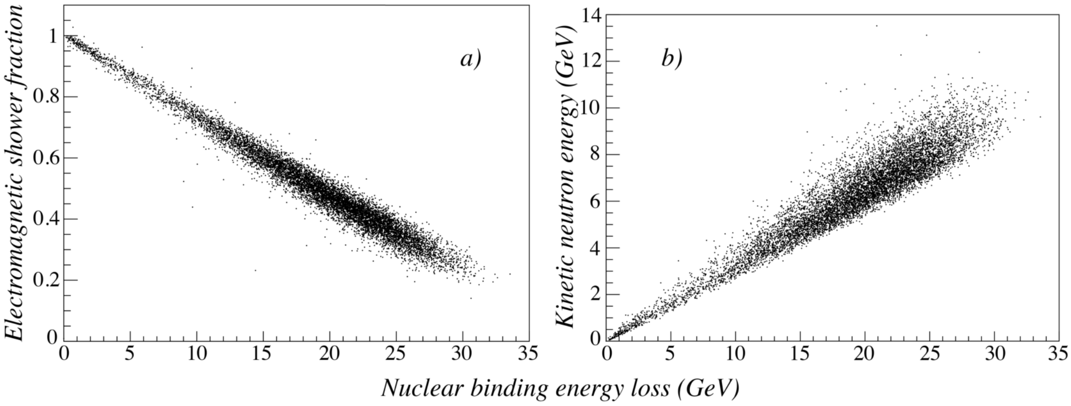

Figure 2.10: The f_{em} (a) and the total kinetic energy carried by neutrons (b) plotted *vs.* the total nuclear binding energy loss (invisible energy) when 100 GeV π^- are absorbed in lead. Results from GEANT Monte Carlo simulations. Image from [48].

with the energy (E). It is also possible to measure the k value and to experimentally measure f_{em} apart from a scaling factor.
Finally, h/e_C could be estimated with some educated guess. It must be understood the accuracy that can be reached.

2.3.4 Compensation by neutrons signal boosting

The (probably) most relevant source of non-compensation is the invisible energy affecting the non-em component. The dual-readout method measures f_{em} and constrains f_{inv} on an event-by-event basis. A second method to achieve compensation, historically developed first, measures f_{inv} through the neutron kinetic energy. It is known as compensation by neutrons signal boosting or by Signal Amplification through Neutron Detection (SAND).
Fig. 2.10 (b) shows a scatter plot correlating the energy fraction carried by neutrons (f_n) and f_{inv} for 100 GeV π^- showering in lead. It indicates a good correlation between the two. This opens the possibility to correct on an event-by-event basis the calorimeter response for the effect of the invisible energy by boosting the signal from neutrons.
Neutrons typically do not carry a large energy fraction ($f_n < 10\%$), nonetheless their contribution to the calorimeter signal can be much larger. At low energies the most likely process to occur for a neutron is elastic scattering on a nucleus target.

The transferred energy fraction is on average:

$$f_{elastic} = \frac{2A}{(A+1)^2}, \tag{2.20}$$

where A is the mass number of the target. This energy transfer increases as A decreases, reaching 50% for hydrogen. In lead it amounts to 0.024. For instance, in an alternating Pb/H structure, with the same amount of Pb and H nuclei, soft (MeV-type) neutrons would transfer $\simeq$ 98% of their energy to hydrogen, while a mip would release only 2.2% of the deposited energy in the hydrogen layers. It follows that signal amplification through neutron detection is a powerful technique to increase the calorimeter response to the non-em component.

By tuning the calorimeter sampling fraction, one can design a calorimeter for which $e = h$. The optimal samplings fraction to achieve compensation through SAND is $\simeq 10\%$ for U/plastic-scintillators and $\simeq 2-3\%$ for Pb/plastic scintillators. In short, compensation through SAND can be achieved in sampling calorimeters with active materials containing hydrogen and a precisely tuned sampling fraction.

SAND requires a fixed sampling fraction and it is not possible to deliberately increase it for a better energy resolution. Moreover, to collect signals from soft neutrons one needs to integrate the signal over large volumes ($\simeq$ m^3) and times ($50-100$ ns). An additional drawback is the need to adopt high-Z absorber materials to reduce the energy transfer to the nuclei through neutron elastic scattering, see Eq. 2.20. Lead and uranium are thus common choices.

We now consider fluctuation terms in such a calorimeter. Invisible energy fluctuations are ruled out by their correlation with the neutrons kinetic energy and, given $e/h = 1$, fluctuations in the f_{em} no longer affect the calorimeter response. It is not a surprise that calorimeters holding the best hadronic energy resolutions are of this type. Good examples are the ZEUS Calorimeter ($\sigma/E \simeq 35\%/\sqrt{E}$) [53] and the SPACAL calorimeter ($\sigma/E = 32\%/\sqrt{E} \oplus 1\%$) [54]. The ultimate resolution achievable with this technique is related to the strength of the correlation between the f_n and f_{inv}, rather than the rms of the invisible energy distribution.

2.3.5 Towards the best hadronic energy resolution

Compensating calorimeters are good candidates to achieve the best possible hadronic energy resolution. A legitimate question is which compensating technique leads to the best hadronic energy resolution. As the ultimate sources of fluctuations affecting them are known, it is possible to make assumptions on the answer. However, a full containment dual-readout hadronic calorimeter has not been built yet and the ultimate resolution achievable with this technique remains one of the main goals of future colliders strategic R&D.

Fig. 2.10 suggests that f_{em} is better (anti)correlated to the invisible energy than the kinetic energy of neutrons. Authors of [48] draw the conclusion that a full containment dual-readout calorimeter would likely measure hadrons energies with a better resolution than calorimeters compensating through SAND.

Hints of this better correlation were already obtained experimentally by the RD52 Collaboration. Fig. 2.11 shows that the Cherenkov signal from the DREAM fiber calorimeter is a superposition of several (more) Gaussian signal distributions obtained with subsamples with approximately the same f_{em}. It also shows that the same Cherenkov signal is also a superposition of Gaussian signal distributions with approximately the same neutron kinetic energy fraction (f_n). Comparing the two result it is evident how subsamples are wider when selected according to their neutron kinetic energy. This is a clear consequence of the poorer correlation binding f_n and f_{inv} with respect to the one with f_{em}.

To achieve the best hadronic energy resolution, it is possible to exploit both f_{em} and f_n to constrain simultaneously f_{inv}. This works because f_{em} and f_n are correlated to f_{inv} in different ways. The RD52 Collaboration showed that it is possible to measure f_n exploiting the timing information of the scintillation signals [55]. Indeed, dual-readout calorimeters measuring the f_n, known as triple-readout calorimeters, have been proposed as a natural R&D evolution (for instance in [56]).

2.3.6 Jet energy measurements

At multi-purpose collider experiments the key performance of hadronic calorimeters is the jet energy resolution, rather than the hadronic one. Jets are collimated sprays of particles. Within a single jet there are photons, from neutral pions decays, initiating em showers in the calorimeter, and a large variety of hadrons inducing hadronic showers. The non-compensating calorimeters response to jet is a mix of the responses to them. On the other hand, compensating calorimeters are not affected by the relative fraction of photons and hadrons inside jets. Since compensating calorimeters are linear for hadrons and electrons detection, one might expect them to be linear for jet detection. However, in calorimetry there is an exception for almost any intuition.

Fig. 2.12 shows the ratio of the responses to electrons and hadrons (e^+/p, e^-/π^- and e^+/π^+) of the (compensating) ZEUS calorimeter. It reaches 1 for hadron energies above 5 GeV, while it decreases of $\simeq 40\%$ at 0.5 GeV energies. Since the calorimeter response to electrons e is constant, this behavior is entirely ascribed to changes in the response to hadrons. For energies above 5 GeV almost every hadron induces at least one nuclear breakup and the shower development proceeds as de-

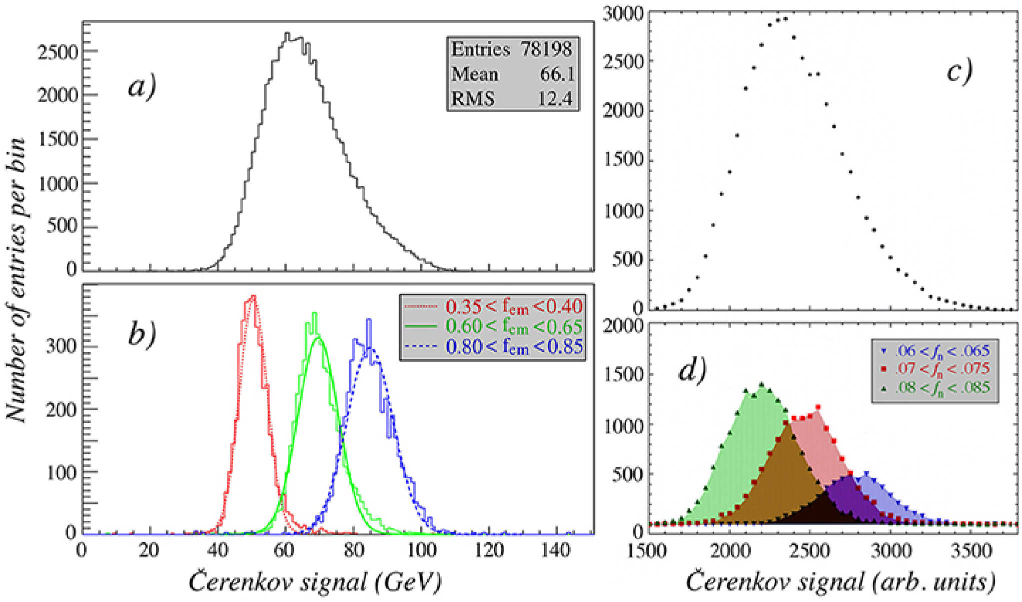

Figure 2.11: Distribution of the total Cherenkov signal for 100 GeV π^- (a) and the distributions for three subsets of events selected on the basis of the electromagnetic shower fraction (b). Data from [50]. Distribution of the total Cherenkov signal for 200 GeV multi-particle events (c) and the distributions for three subsets of events selected on the basis of the fractional contribution of neutrons to the scintillator signal (d). Data from [55]. Image from [39].

scribed in Sec. 2.3.1. The ZEUS calorimeter achieved compensation through SAND and, according to Eq. 2.8, $e/\pi = 1$. The probability for a hadron to induce a nuclear breakup reduces for lower energies. If a hadronic shower is not initiated, a charged hadron looses energy in the calorimeter exclusively by ionization, resembling the mip behavior. The calorimeter response to such a particle equals the mip response. Following what stated in Sec. 2.2.3, for a sampling calorimeter $e/mip < 1$ and the e/π ratio ranges from 1 to the e/mip calorimeter ratio.

This is an exception to the rule “a compensating calorimeter is linear for hadron detection”. Every compensating calorimeter is linear for hadron detection in the high-energy range. Or, every compensating calorimeter for which $e/mip = 1$ is linear for hadron detection.

An effective way to increase the e/mip value of a sampling calorimeter is to use low-Z absorber materials (see Sec. 2.2.3). For instance, keeping the same ZEUS calorimeter structure and replacing ^{238}U plates with copper, the e/mip value would become $\simeq 0.85$ as marked in Fig. 2.12.

It turned out this effect is particularly important for jet detection. Low energy jet

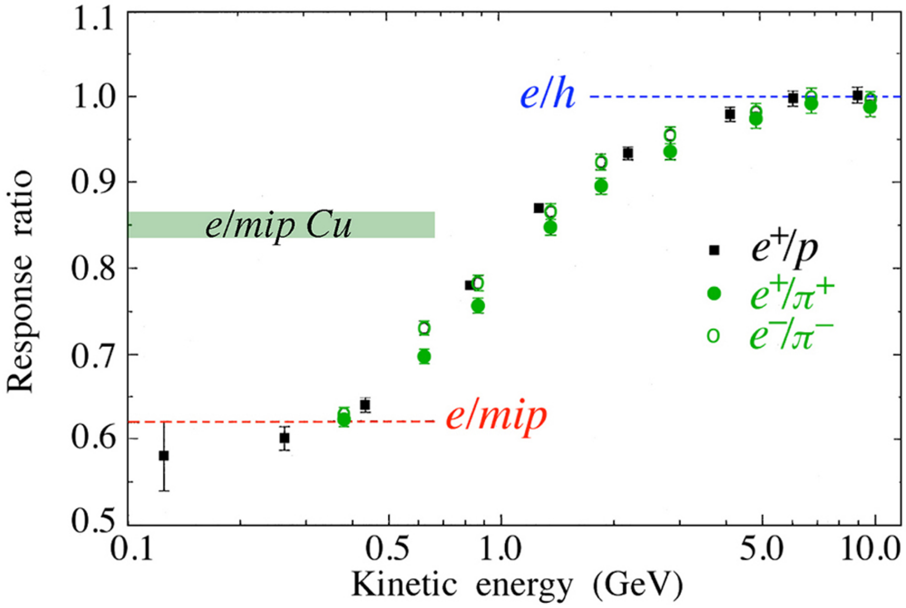

Figure 2.12: The ratio of the responses of the (compensating) ZEUS calorimeter to electrons and (low-energy) hadrons. Data from [57]. Image from [36].

fragments account for a non-negligible fraction of a jet energy. Fig. 2.13 shows the distribution of the energy carried by charged particles with a momentum smaller than 5 GeV/c, in $Z \to u\overline{u}$ and $H \to gg$ events with the Z and H bosons decaying at rest. In the Z decays, most probably, 21% of the boson invariant mass is carried by these particles and varies between 13% and 35% in a 1 σ_{rms} interval. For the Higgs decay, it amounts to 34% with rms variations between 23% and 45%. If the calorimeter response to low energy hadrons differs from the response to high energy hadrons, then this fluctuation directly translates into a fluctuation in the calorimeter response, spoiling the jet energy resolution. The ZEUS calorimeter energy resolution for intermediate vector bosons was sensibly worse than the one expected on the basis of its excellent single-pion energy resolution.

2.3.7 Catastrophic events

Other kinds of fluctuations, sometimes catastrophic, might happen regardless the calorimeter degree of compensation. One example is provided by calorimeters with a very small sampling fraction and linear (non-saturating) active elements, like the original CDF iron/gas forward calorimeter. In these calorimeters the sampling fraction can be reduced down to $\mathcal{O}(10^{-5})$. It means that a 100 GeV hadron deposits

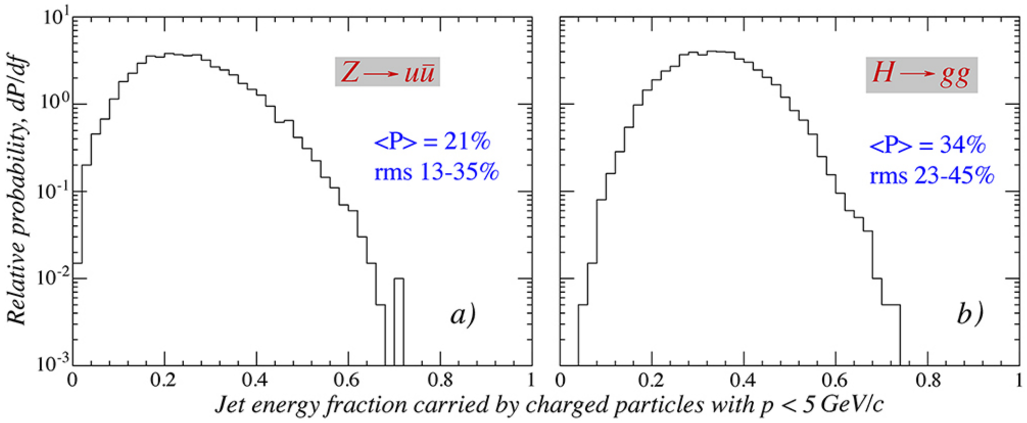

Figure 2.13: Distribution of the fraction of the energy released by hadronically decaying Z (a) and H (b) bosons at rest that is carried by charged final-state particles with a momentum less than 5 GeV/c. Image from [36].

only $\simeq$ 1 MeV in the active elements.

MeV-type neutrons may elastically scatter on a single hydrogen nucleus in the active element and the accelerated proton thus releases a comparable amount of energy ($\simeq$ MeV) in a single gas layer. Therefore, a single MeV neutron can resemble a 100 GeV hadron in such a calorimeter. This phenomenon, known as the Texas-tower effect, was observed by the CDF Collaboration as randomly generated signal spikes. Eventually, the detector was replaced by a plastic-scintillator one with a sampling fraction three order of magnitudes higher [58]. In a certain way, being replaced can be considered the most catastrophic fluctuation a calorimeter can experience.

The Texas tower effect might affect also compensating calorimeters. An example comes from the ^{238}U/gas L3 hadron calorimeter [59]. Fig. 2.14 shows signal distributions for 6 GeV electrons and pions when the wire chambers were filled with Ar/CO_2 or isobutane. For hadron detection isobutane led to a response roughly doubled and more asymmetric with respect to Ar/CO_2, a clear consequence of neutrons elastically scattering on the gas protons. Even when a compensating gas mixture was employed, signals distribution showed a high-side tail spoiling the energy resolution. This is another remarkable exception to the rule “compensating calorimeters always achieve superior hadronic energy resolutions”.

The Texas tower effect is the combined effect of a small sampling fraction coupled to non-saturating active elements. If the active element is non-saturating but the sampling fraction increased, a single MeV-type neutron can still induce a large signal but the corresponding energy would be reduced by the higher calorimeter response. On the other hand, keeping a very low sampling fraction but using saturating active

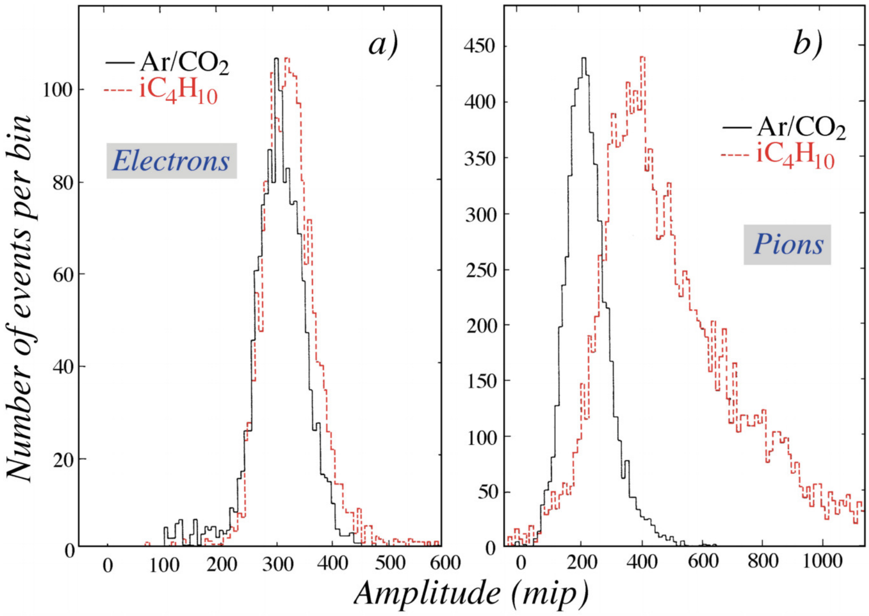

Figure 2.14: Signal distributions from the L3 ^{238}U/gas calorimeter, for 6 GeV electrons (a) and 6 GeV pions (b), using Ar/CO$_2$ or isobutane. Data from [59]. Image from [36].

elements prevents the possibility that a single particle creates very high ("spiking") signals.

Avoiding extremely small sampling fractions and using saturating active elements is a safe choice. An examples of how plastic scintillators saturate light emission for highly ionizing particles is discussed in Chap. 3, when presenting the IDEA calorimeter simulation.

2.3.8 Combined calorimetric systems

Typically, experiments at colliders combine an electromagnetic calorimeter followed by a hadronic one. This choice gives the possibility to separately design the two sections, optimizing the structure, the sampling fraction and the readout system according to the physics of interest and costing.

However, combining two calorimeters with different e/h values leads to an additional level of complication that might easily result in a spoiled energy resolution. An example is offered by the CMS calorimeter system where the hadronic section ($e/h = 1.3$) is preceded by crystals ($e/h = 2.4$) [55]. Fig. 2.15 shows the response to hadrons divided into two samples according to the showering starting point. At low energies, the response is more than 50% larger for the penetrating events. It follows

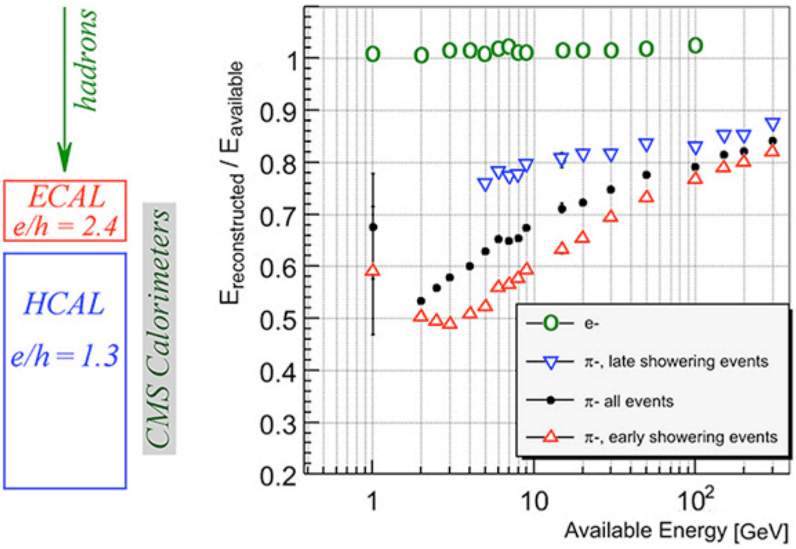

Figure 2.15: The CMS barrel calorimeter response to electrons and pions as a function of energy. The pion events are subdivided into two samples according to the starting point of the shower, and the pion response is also shown separately for these two samples. Image from [60].

that the calorimeter response to hadrons depends on the showering starting point and reaches its maximum for events entirely contained in the hadronic section. In an experiment, it is often hard to determine the shower starting point, especially if these pions are traveling in close proximity to other jet fragments which develop showers in the em section. If the showering starting point is unknown, its event-by-event fluctuations directly affects the hadronic energy resolution.

Note that a longitudinally unsegmented compensating calorimeter can be calibrated with electrons and the same calibration constants can be used to correctly reconstruct, on average, both em and hadronic showers. This is the fifth benefit of compensation.

2.4 Calorimetry at future e^+e^- colliders

2.4.1 Calorimetry requirements

Most final states at the FCC-ee come from Z/γ boson decays. At the Z pole ($E_{CM} \simeq$ 90 GeV) about 70% of the events are two-jet final states from the $Z \to q\bar{q}$ decay mode. A similar branching ratio ($\simeq$ 67%) determines the probability for a W boson to decay into quark pairs. Therefore, the most probable signatures for the process

$Z^*/\gamma^* \to W^+W^-$ at the W threshold ($E_{CM} \simeq 160$ GeV) are 2-jet and 4-jet final states.

At the top-quark threshold ($E_{CM} \simeq 360$ GeV) the signatures of the process $Z^* \to t\bar{t}$ are again governed by the $t \to W^+b$ and the $\bar{t} \to W^-\bar{b}$ decay modes. About 46% of the event final states are made of 6 jets and 45% are 4 jets plus one lepton and one neutrino.

The Higgs production at the Higgs threshold ($E_{CM} = 240$ GeV) is via the process $e^+e^- \to Z^* \to ZH$, the so called Higgsstrahlung mechanism. According to [61], the branching ratio for jet final states from this process are approximately:

- 32% for 2-jet final state including $Z \to qq$ and $H \to 0j$, $Z \to ll, \nu\nu$ and $H \to qq$, $Z \to ll, \nu\nu$ and $H \to WW/ZZ$(semileptonic),
- 55% for 4-jet final states including $Z \to qq$ and $H \to 2j$, and $Z \to ll, \nu\nu$ and $H \to WW/ZZ \to 4j$,
- 11% for 6-jet final states including $Z \to qq$ and $H \to WW/ZZ \to 4j$.

the remaining $\simeq 2\%$ are events with no jets ($Z \to ll, \nu\nu$ and $H \to 0j$).

A superior jet energy/momentum resolution is a globally accepted calorimetry requirement. The ultimate goal for the jet energy resolution is derived from the Higgsstrahlung process. By using the hadronic decay modes of the Z bosons, in addition to the e^+e^- and the $\mu^+\mu^-$ decays, an important gain in the event rate can be obtained. However, other processes such as $e^+e^- \to W^+W^-$ will obscure the signal unless the experiment is able to efficiently distinguish between hadronic decays of W and Z. This requires that 80-90 GeV jets are resolved with a resolution of $\simeq 3$ GeV. It is important to note that such an energy resolution has already been achieved for hadrons by compensating calorimeters but not for jets (see Sec. 2.3.6). This sets a severe requirement for hadronic calorimetry at future e^+e^- colliders.

The jet energy resolution is determined by fluctuations in the hadronic showers induced by the jet hadronic component. Therefore improving the calorimeter em energy resolution does not help for reaching excellent jet energy resolutions. Resolving photon energies with resolutions of $\sigma/E = 10\% - 15\%/\sqrt{E}$ is general satisfactory in this respect.

However, other processes ask for a better em energy resolution. An example is the radiative process $e^+e^- \to Z\gamma$ with subsequent Z decay into two Standard-Model neutrinos, which are invisible to the detector. The Feynman diagrams are sketched in Fig. 2.16 (top row). Such a process may be used to measure the Z coupling to the electron neutrino that is very poorly known. This is possible thanks to the presence of the t-channel W exchange in the $e^+e^- \to \overline{\nu_e}\nu_e\gamma$ channel which interferes with the process involving electron neutrino and deforms slightly the spectrum of the

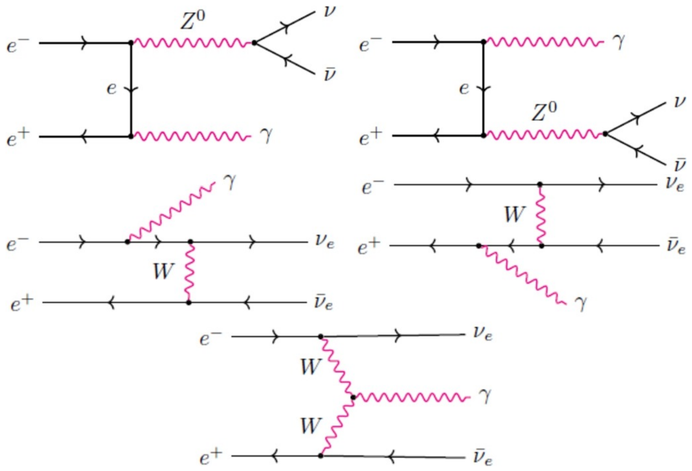

Figure 2.16: Production of flavor-untagged ν through the process $e^+e^- \to Z\gamma \to \nu\nu\gamma$ (top row). Production of flavor-tagged ν_e through the process $e^+e^- \to \overline{\nu_e}\nu_e\gamma$ with W exchange (middle and bottom rows). Image from [62].

tagged photon. The Feynman diagrams for the W exchange process are sketched in Fig. 2.16 (bottom row). The interference effect is shown in Fig. 2.17, which presents the differential cross section against the E_γ/E_{beam} variable when the interference is included or excluded. From the skewness of the distribution, it is possible to extract the Z-to-electron-neutrino coupling. In [62] it is shown how at the FCC-ee, at a center-of-mass energy of 161 GeV and an integrated luminosity of 10 ab^{-1}, a detector with an energy resolution of $\simeq 1\%$ for the photon energy measurement could measure the coupling with a precision of 1%. Such a photon energy resolution is within the reach of homogeneous crystal calorimeters.

Moreover, it was shown [63] that an excellent em energy resolution would lead to a better final-state radiation recovery for electrons, that is beneficial for the Higgs recoil mass measurements through the $Z(ee)H$ final states. For instance, a $3\%/\sqrt{E}$ energy resolution would lead to a Higgs mass resolution only 20% larger than the one measured through the $Z(\mu\mu)H$ process.

Related to rare or forbidden signatures, an excellent em energy resolution is beneficial to reach the best possible sensitivity to processes like $Z \to \tau e$, $Z \to \mu e$ and $\tau \to \mu\gamma$. An example for which a good em energy resolution improves the detector sensitivity to beyond-the-standard-model axion-like-particles will be discussed in Chap. 5.

It is being discussed, among the calorimeter requirements, if at least one experiment should achieve an excellent electromagnetic energy resolution as it can be provided by homogeneous crystal calorimeters. This will very likely be the case, if the option

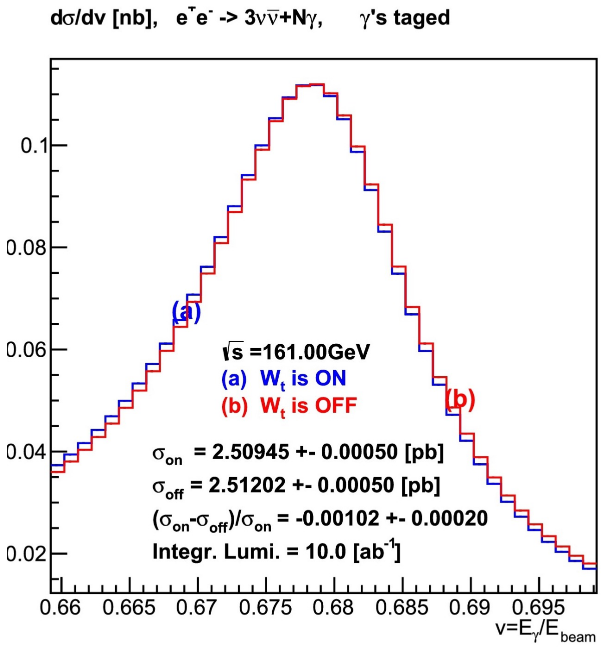

Figure 2.17: Examining difference of the photon spectrum for the electron neutrino and muon neutrino channels due to the t-channel W exchange (see text for details). Result considering 10 ab^{-1} at 161 GeV center-of-mass energy. Image from [62].

to have four IPs for the FCC-ee, instead of two, will gain consensus.

2.4.2 Drivers for the IDEA dual-readout calorimeter

To match the hadronic requirements, the IDEA Experiment adopted a dual-readout fully projective (and modular) fiber calorimeter. The goal is a calorimeter system with approximately the same response to any particle type. By exploiting the dual-readout method (Sec. 2.3.3), it is possible to achieve the same response for electrons and hard hadrons ($e/h = 1$), *i.e.* hadrons producing hadronic showers mainly through nuclear interactions. The response to the soft hadron components, *i.e.* hadrons loosing their energy mainly by ionization, is kept as close as possible to e by using low-Z absorber materials (like copper) and a high sampling frequency. In a dual-readout fiber calorimeter, the high sampling frequency can be achieved by reducing the fiber pitch. This is a great advantage with respect to calorimeters compensating by SAND, for which the fixed sampling fraction limits the sampling frequency. Eventually, signal fluctuations due to the calorimeter longitudinal segmentation (discussed in Sec. 2.3.8) are ruled out by designing a longitudinally unsegmented calorimeter with an overall constant sampling fraction. This is possible thaks to the fact that a dual-readout calorimeter exploits, at least at the leading order, a single calibration with electrons for any energy measurement. In Chap. 3 we present the calorimeter geometry and performance as designed and studied with the Geant4 toolkit [64].

The drawback of a single unsegmented calorimeter for both hadron and electron detection is limiting the electromagnetic energy resolution to what is achievable with a sampling calorimeter. To achieve an excellent electromagnetic energy resolution, an IDEA crystal option was recently suggested [63]. It exploits an homogeneous crystal electromagnetic section, 25 X_0 deep, in front of the IDEA fiber-sampling calorimeter. The drawbacks of this crystal option are easily predictable. Crystals are non-compensating calorimeters with high e/h values. For hadrons starting showering inside the electromagnetic section, the energy carried by the non-electromagnetic component will be highly underestimated. Hence, fluctuations in the showering starting point would induce fluctuations on the combined-calorimeter-system response to hadrons. This sets another important requirement for IDEA: every electromagnetic section must use a dual-readout calorimeter. The possibility to simultaneously extract the Cherenkov and the scintillation light from crystals was demonstrated by the RD52 Collaboration [51]. At present, an R&D is being proposed for fully understanding and optimizing the extraction of the two signals [63].

2.4.3 Dual-readout fiber calorimeters

In the last 20 years dual-readout fiber calorimeters have been built and tested by the DREAM/RD52 Collaboration[1]. The DREAM (Dual-REAdout Module) calorimeter consisted of plastic scintillating fibers for the visible (ionizing) energy measurement, and clear undoped fibers for the collection of the Cherenkov light. Fibers where inserted in a 2.5 mm diameter extruded hole. The absorber material chosen is copper. A basic unit of the calorimeter is sketched in Fig. 2.18. In each hole 7 optical fibers, 3 scintillating and 4 Cherenkov, were inserted. Fibers have a diameter of 0.8 mm and both quartz fibers (in the central region) and PMMA clear fibers (in the peripheral regions) were used for the Cherenkov light detection. The instrumented cross section has a radius of 16.2 cm and a length of 2 m corresponding to 10 λ_{int}. Fig. 2.19 shows the calorimeter front face and the fibers at its rear end.

Considering only the scintillation signal, the sampling fraction for mips is 2.1%. The calorimeter was divided into 19 hexagonal towers, and fibers from each tower were divided into two bunches, one for scintillation fibers and one for Cherenkov fibers. Each bunch was readout by a PMT, see again Fig. 2.19.

---

[1] All the DREAM/RD52 publications are available at http://www.phys.ttu.edu/∼dream/results/publications/publications.html

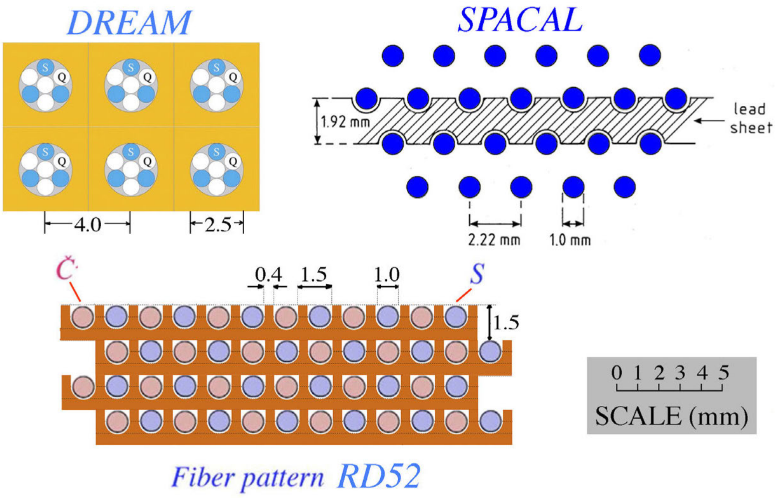

Figure 2.18: The structure of the DREAM calorimeter, the RD52 calorimeter and, for comparison, the SPACAL calorimeter. Image from [65].

The merit of this calorimeter is to have demonstrated the applicability of the dual-readout method described in Sec. 2.3.3. Fig. 2.20 shows the signals distribution for 100 GeV π^-. Both calibration constants were estimated with electrons, therefore, they follow Eqs. 2.11, 2.12. As expected, both energies are on average underestimated and this is much more evident for the Cherenkov signal given its higher degree of non-compensation. Both distributions also show the typical asymmetric shape that reflects the asymmetric f_{em} distribution explained in Sec. 2.3.1. As both signals are undercompensating, they are correlated.

Once the two signals behave as expected, all the benefits of compensation can be achieved by applying Eq. 2.13. The last missing part is how to extract the two h/e values. By dividing the sample in subsets of f_{em}, it is possible to plot the S and C signals as a function of f_{em}. From Eqs. 2.11, 2.12, it is then possible to extract the h/e values from a linear fit to data. Fig. 2.21 shows the results for the Cherenkov and scintillation signals when the calorimeter was exposed to high-particle-multiplicity events (to possibly emulate “jets”), created by pions interacting in a target upstream of the calorimeter. According to Eqs. 2.11, 2.12, the average signal would reconstruct the total amount of energy (200 GeV) for $f_{em} = 1$. However, in this calorimeter, a non-negligible average energy leakage for hadronic shower was present and this certainly invalidates the previous statement. Moreover, it is impossible to exclude that, on average, some particles produced in the upstream target do not reach the calorimeter front face. Under the assumption that the detected energy was, on average, 188 GeV instead of 200 GeV, the authors of [50] concluded that the calorimeter

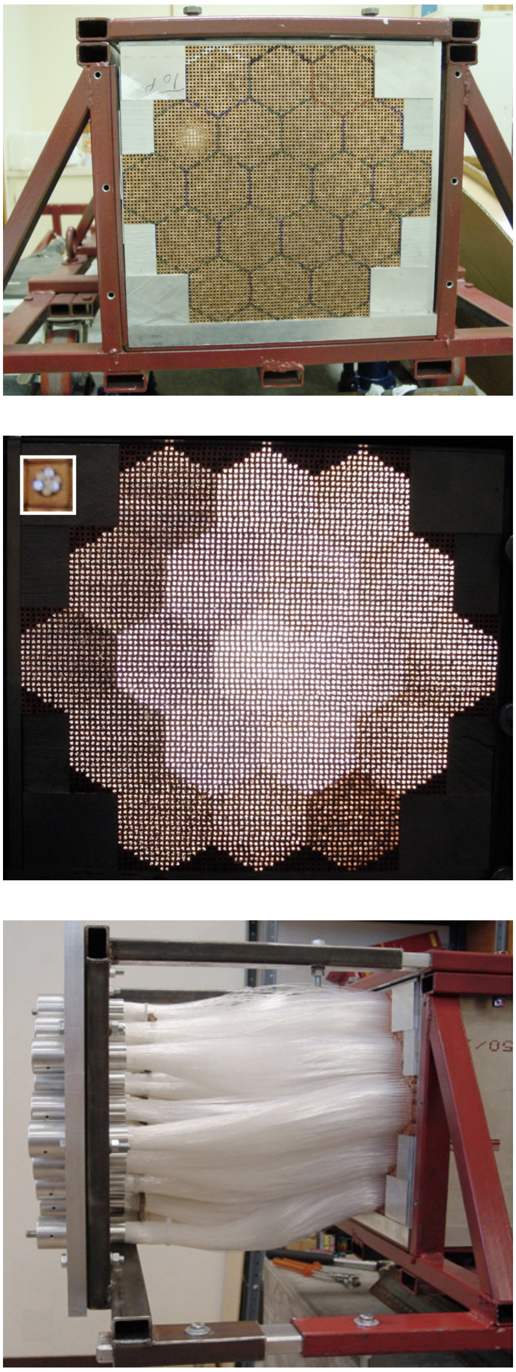

Figure 2.19: The DREAM calorimeter front face (top). The DREAM calorimeter front face when fibers were illuminated from the rear end (middle). The DREAM calorimeter fibers grouped into bunches readout by PMTs (bottom).

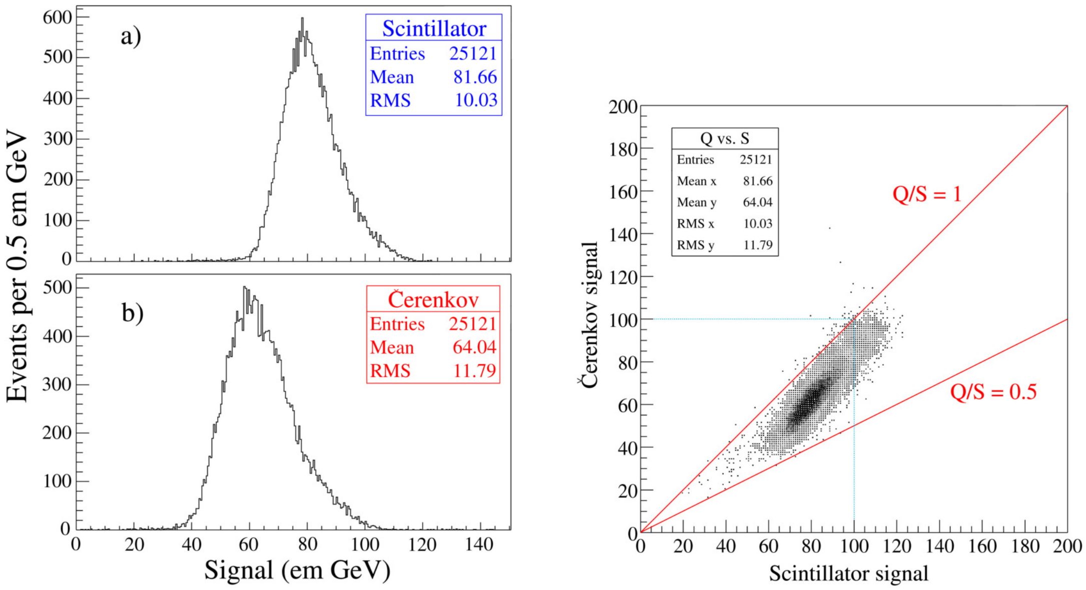

Figure 2.20: Signal distribution for 100 GeV π^- for the scintillation (a) and the Cherenkov (b) signals of the DREAM calorimeter. Both signals are calibrated with electrons. Scatter plot correlating the two signals. Image from [50].

χ factor was $\simeq 0.3$. At present, a big uncertainty on this number should be considered.

The last missing piece is describing how the event sample was divided in subsamples of f_{em} since the h/e values were originally unknown and therefore the f_{em} measurement not possible. What has been used is a recursive method described here after. Starting from tentative h/e values (both for S and C) the events were classified on the basis of their preliminary f_{em} values and plots similar to the ones in Fig. 2.21 were created. From those plots, new h/e values were obtained from a linear fit to data. The event sample was re-divided in subsamples of f_{em} and new plots were created from which new h/e values were found. The exercise was stopped as soon as the h/e values converged to a constant value. What probably happens with this method is that the h/e values converge to a pair of values that satisfies the relation $\chi = (1 - h/e_S)/(1 - h/e_C)$. We note again that χ is a fix and measurable quantity. Likely, a full containment hadronic dual-readout calorimeter should easily provide a measurement of this key parameter. Building such a detector is one of the main goal of the IDEA project.

Once the electromagnetic fraction was measured on an event-by-event basis using the ratio of Eqs. 2.11, 2.12, the signals distribution from 100 GeV π^- was divided into f_{em} subsamples obtaining the result already shown in Fig. 2.11. This is one of

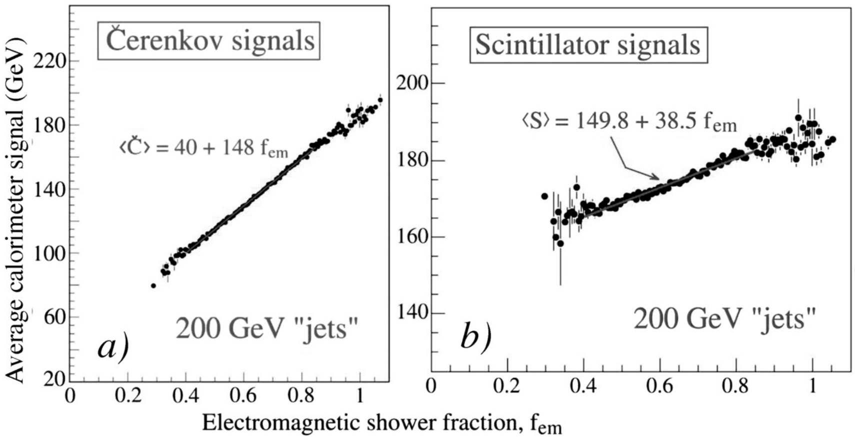

Figure 2.21: The average reconstructed energy for several subsamples of f_{em}. Results from 200 GeV multi-particle events (see text for details), for the scintillation (a) and the Cherenkov (b) signals. Image from [50].

the most evident demonstration of the benefit of the dual-readout method on the hadronic energy resolution.

Even if the uncertainty on the χ factor was not negligible and the energy measurements were affected by leakage, the dual-readout method improved the calorimeter performance in terms of signal linearity, signal distribution symmetry and energy resolution. By using Eq. 2.13, the results shown in Fig. 2.22 were obtained for 200 GeV multi-particle events ("jets"). Fig. 2.22 (a) and (b) show the energy distribution obtained with the Cherenkov signal and the dual-readout combination of the two signals, respectively. It is remarkable how the dual-readout method correctly reconstructs the jet energy within a few percent (with respect to $\simeq$ 188 GeV of contained energy) with a detector calibrated with electrons. Also, the corresponding distribution has a Gaussian shape and the energy resolution was significantly improved (Fig. 2.22 (c)), even if highly affected by leakage fluctuations. Hadronic signal linearity was more or less restored as well (Fig. 2.22 (d)).

The success of the DREAM project led to the formation of the RD52 Collaboration, that was part of the CERN detector R&D program. The aim of the collaboration was to overcome the limiting factors affecting the energy resolution of the DREAM fiber calorimeter. Three limiting factors were identified: the lateral side leakage, photostatistical fluctuations in the number of detected Cherenkov photons and a small sampling fraction. To limit fluctuations in the number of detected Cherenkov photons, the Cherenkov light yield must be increased. To achieve that, several changes were applied simultaneously: the numerical aperture of the Cherenkov fibers was

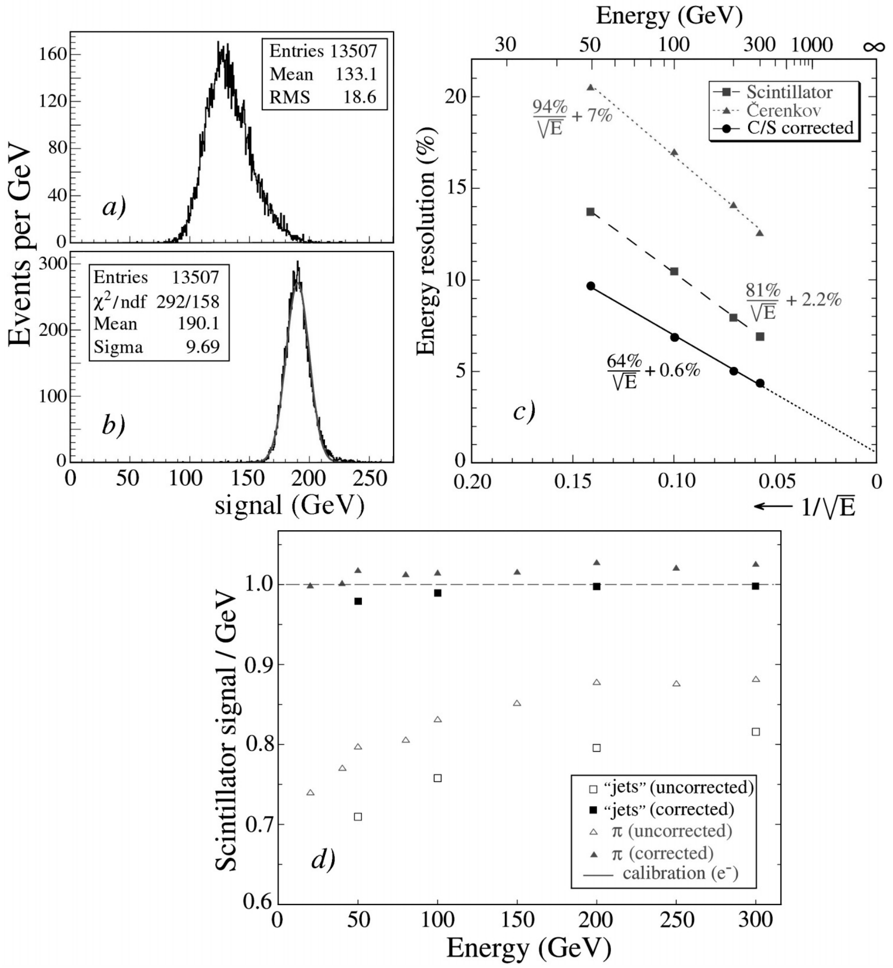

Figure 2.22: Energy distribution for the Cherenkov signal (a) and the dual-readout combination of the two signals (b) for 200 GeV multi-particle jets. The DREAM energy resolution (c) for multi-particle jets and linearity in the $10 - 300$ GeV range (d) for multi-particle jets and single-charged-pion events. Image from [50].

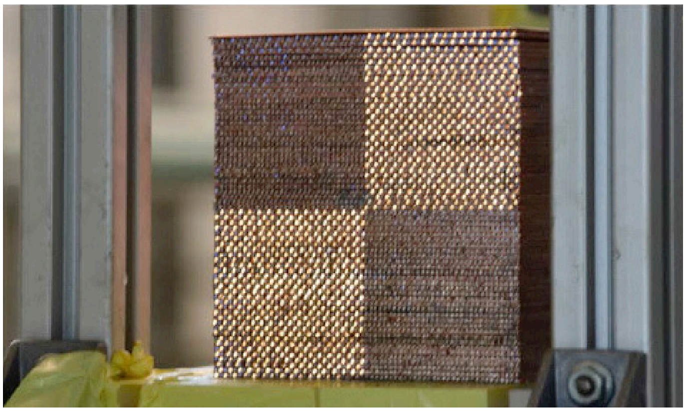

Figure 2.23: Front face of a single RD52 copper module. Scintillating fibers from two of the four towers were illuminated at the calorimeter rear end.

increased by replacing quartz fibers with PMMA fibers (the numerical aperture is 0.50 and 0.33 for PMMA and quartz fibers, respectively), the upstream tip of the fibers was aluminized to reflect the trapped light and the PMT quantum efficiency was increased (using a super bialkali photocathode). To achieve a higher sampling fraction and sampling frequency, fibers were individually inserted in the absorber and the relative fraction of volume occupied by active elements was roughly doubled with respect to the DREAM calorimeter, see Fig. 2.18.

With this configuration in mind, several copper-based modules with dimensions of $9.2 \times 9.2 \times 250$ cm^3 were built. Each module was divided into four towers and fibers from each tower were grouped in a Cherenkov bunch and a scintillation bunch individually readout by a PMT. Fig. 2.23 shows the front face of a copper module. The fiber pattern is sketched in Fig. 2.18.

The Cherenkov light yield was measured by integrating the PMT charge after having estimated the PMT gain. It reached 33 photoelectrons per GeV deposited at the em scale while, for the DREAM calorimeter, it amounted to (only!) 8 photoelectrons per GeV. In Chap. 4 we describe how a new Silicon PhotoMultiplier (SiPM) readout doubled the Cherenkov light yield with respect to the RD52 copper modules.

One of the main advantage of the new fiber pattern is that the two signals represent independent sampling structures. Therefore, they can be combined for a better energy resolution. On the other hand, in the original DREAM configuration the two signals were sampling showers in the same way, thus exhibiting a strong correlation [66]. Fig. 2.24 shows the em energy resolution of the RD52 copper modules for electrons with energies ranging from 6 to 80 GeV.

Interestingly, the scintillation signal exhibits an energy resolution deviating from $E^{-1/2}$ as if a constant fluctuation term is present. This term seems to be much

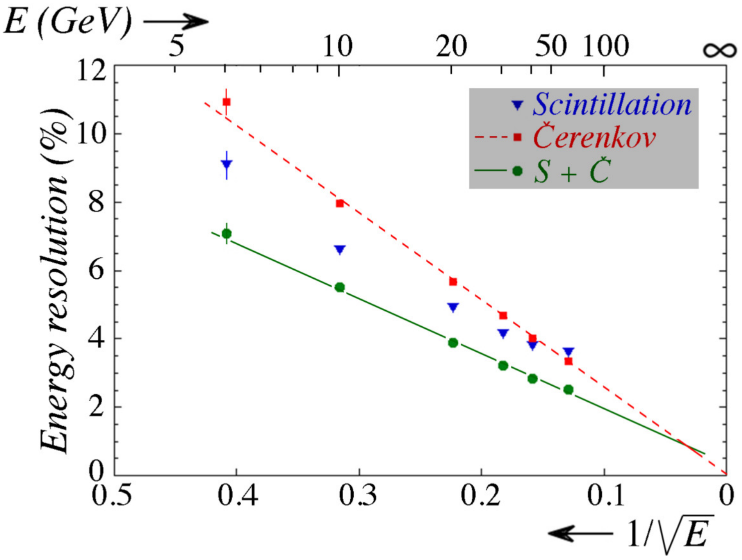

Figure 2.24: The em energy resolution of the RD52 copper calorimeter. Results for the scintillation and Cherenkov signals and for the linear combination of the two. Image from [67].

smaller in the Cherenkov channel and therefore also in the linear combination of the two. The origin of this behavior is the dependence of the response on the impact point. If an electron starts showering close to a fiber, the resulting signal is slightly higher than a shower induced farther from the fiber. Since em-shower lateral dimensions do not change with the primary particle energy, this effect does not depend on the energy and is a constant term of fluctuations. In the Cherenkov channel this effect is largely suppressed because the Cherenkov signal does not sample the initial stage of the shower development, as the photons emitted there have a direction strongly correlated with the primary particle direction and fall outside the numerical aperture of the fibers. Evidence of this effect was observed when measuring the radial shower shape with a sub-millimetric precision, and the results are reported in Chap. 4.

The constant term of the combined resolution was less than 1% and future measurements at higher energies will help constraining it with a better precision. The stochastic term amounted to $13.9\%/\sqrt{E}$ due to both sampling fluctuations and photo-statistic fluctuations [67].

Another important lesson from the copper modules is that the production of copper plates with precise holes is very difficult and time consuming due to the hardness of the material. To overcome the structural limitations given by copper, the RD52 Collaboration built nine modules using lead, that is much easier to extrude. Fig. 2.25

shows the 9-module front face, arranged in a 3×3 geometry, and the entire calorimeter at the CERN SPS H8 beam line. The detector dimensions are $27.6 \times 27.6 \times 250$ cm^3 (about 10 λ_{int}). Each module was divided into four towers and each tower was readout by 2 PMTs, one for the scintillating fibers and one for the Cherenkov fibers. In total 72 PMTs were used.

Each tower was independently calibrated with electrons, later pions were sent at the detector central region. Fig. 2.26 shows the scintillation and Cherenkov signals distribution for 20, 60 and 100 GeV π^- and the corresponding energy distribution obtained by applying Eq. 2.13. All the benefits of the dual-readout method are well reproduced also in this calorimeter. The χ factor used is 0.45; it was estimated as the one corresponding to the minimal rms of the corrected energy distribution (details are given in [68]). The energy resolution obtained is compatible with $\sigma/E = 70\%/\sqrt{E}$ and a subsequent publication confirmed this scaling [68]. This resolution is not much different from the DREAM one, as in both cases lateral leakage fluctuations were the dominant source of fluctuations. Detailed Monte Carlo simulations were performed to confirm it (see [69] and [36] (Sec. 8.2.6.5)) and showed that a same-structure calorimeter with a lateral cross section of 65×65 cm^2 could reach, for 100 GeV pions, an energy resolution of σ/E of 4.6% or 3.2%, if the FTFP_BERT or the FTFP_BERT_HP physics lists are used, respectively. The ultimate resolution achievable with this technique is still to be experimentally demonstrated and this sets the main goal of the IDEA dual-readout calorimetry R&D.

The DREAM/RD52 Collaboration reached several other remarkable results and an extensive discussion on the subject goes beyond the scope of this introduction. Nevertheless, they are certainly relevant for calorimetry at future colliders. Among them, we cite:

- The good particle identification capabilities of a dual-readout fiber calorimeter exploiting the ratio of the two signals, the shower shape, the shower timing information and the signals digitized shapes [70].
- The possibility to measure the neutron component of hadronic showers by exploiting the timing information of the signals [55].
- The possibility to extract scintillation and Cherenkov signals in homogeneous crystal calorimeters [51].

2.4.4 Particle Flow Analysis

To match the jet requirements at future e^+e^- colliders a lot of effort has been spent in the last decades on a completely different approach that, to some extent, can be

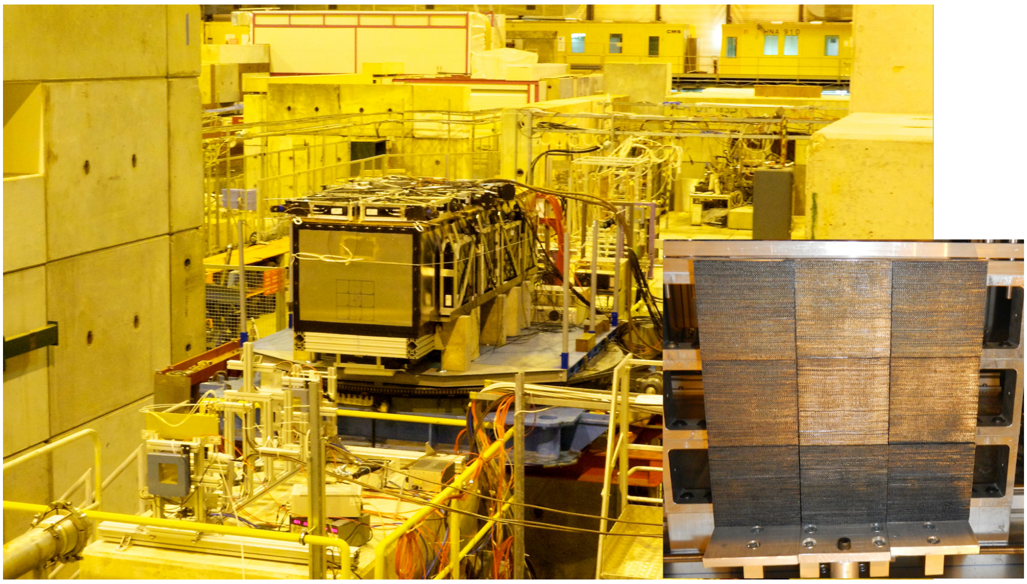

Figure 2.25: The RD52 lead calorimeter at the CERN SPS H8 beam line and the calorimeter front face made of 3×3 modules.

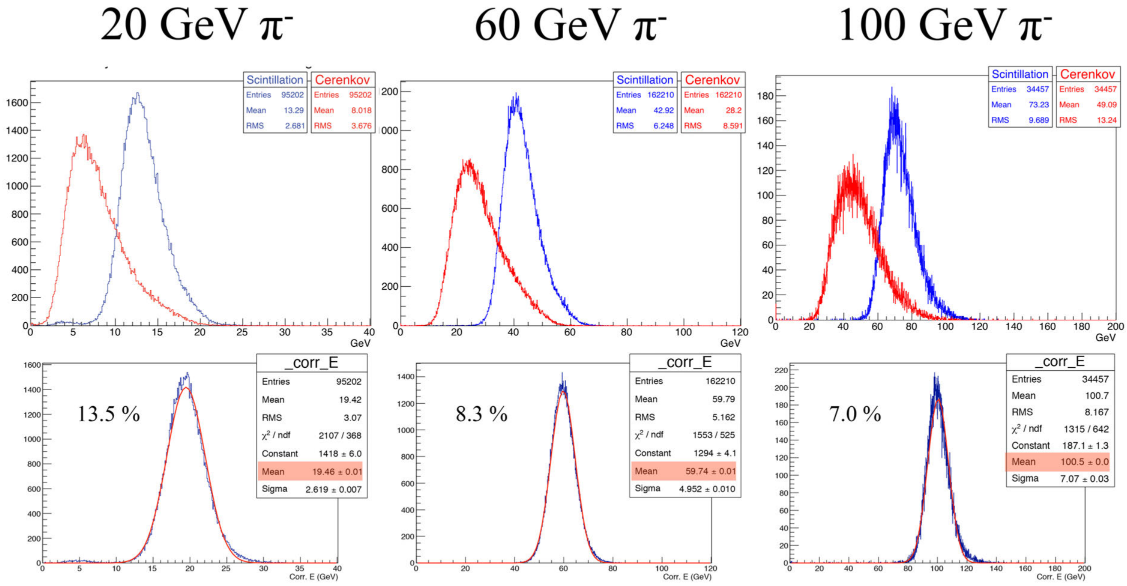

Figure 2.26: The RD52 lead calorimeter scintillation and Cherenkov signal distributions for 20, 60 and 100 GeV π^- (top row). The corresponding energy distributions obtained with Eq. 2.13 (bottom row). Image from [65].

considered orthogonal to the dual-readout method. It is based on the combination of the tracker and a highly-granular calorimeter system. It relies on the fact that charged-particle momenta are better resolved with the tracker rather than with the calorimeter, while neutral particles energies and momenta can only be measured with the calorimeter.

The required jet energy resolution can only be achieved if every particle momentum is properly measured and clustered. This implies that the calorimeter signals induced by charged particles must be accurately selected, linked to the original track and subtracted from the calorimeter energy computation. From this requirement it follows the need to design highly granular calorimeters that efficiently cluster signals induced by charged particles. The idea of following the particle tracks deep inside the calorimeter gives the method its name: Particle Flow Analysis (PFA).

To my knowledge, the first experiment that applied PFA is ALEPH [71] at the Large Electron Positron collider (LEP). The ALEPH experiment used PFA to achieve an energy resolution of 6.2 GeV on the products of hadronically decaying subsamples of Z bosons. It roughly corresponds to an improvement of 25% with respect to the reported hadronic energy resolution of the standalone calorimeter system.

Also experiment at hadron colliders successfully used PFA. An example is the CDF experiment at the Tevatron. Fig. 2.27 shows the effect of including the tracker and the shower-max detector information on the jet energy measurement, for jets detected in the barrel region [72]. More recently, the CMS Experiment at the LHC improved the jet energy resolution using PFA (see, for instance, [73]). Fig. 2.28 shows the (simulated) improvement on the jet energy resolution.

It should be noted that, in the above examples, PFA improved the jet energy resolution at experiments using calorimeters with poor energy resolutions and its effect on better calorimeters will likely be more modest. In any case, combining tracks with the calorimeter information has proven to be beneficial in pile-up suppression, as demonstrated by the ATLAS Experiment [74]. Recently, the CMS Experiment embarked in a gigantic Phase-II upgrade project to build a highly granular calorimeter for the forward regions, the High-Granularity CALorimeter (HGCAL) [75]. The project is dictated by the need to replace the current detector ($PbWO_4$ followed by brass/plastic-scintillators) that is expected to become ineffective by around 2025 due to radiation damage. The new detector will consists of an electromagnetic section of 28 sampling layers with silicon active cells of 0.5-1.0 cm^2, depending on the expected flux, followed by a less granular hadronic section exploiting both silicon and plastic scintillator active elements. The detector will comprise about 6 million electronic channels and will both mitigate the radiation damage and the pile-up effects.

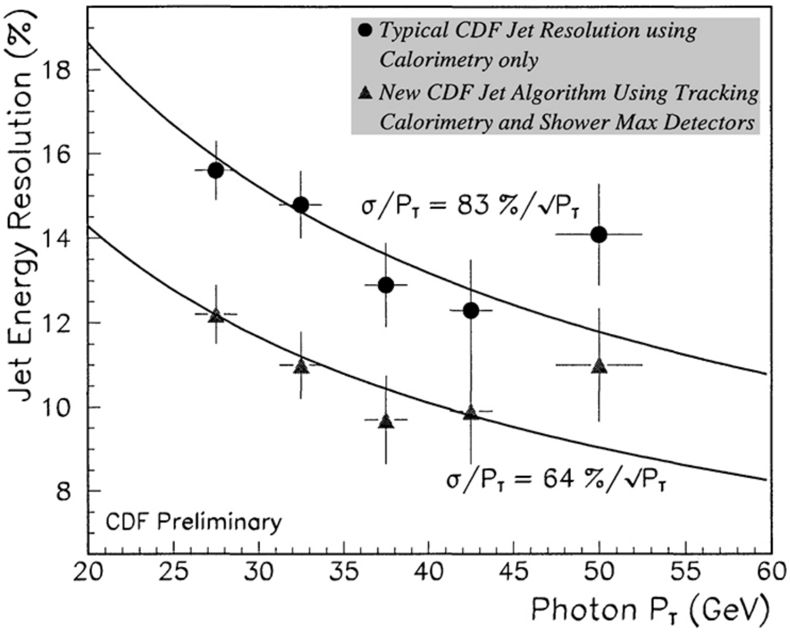

Figure 2.27: The effect of including the tracker and the shower max detector information on the jet energy measurement, for jets detected in the CDF barrel region. Image from [72].

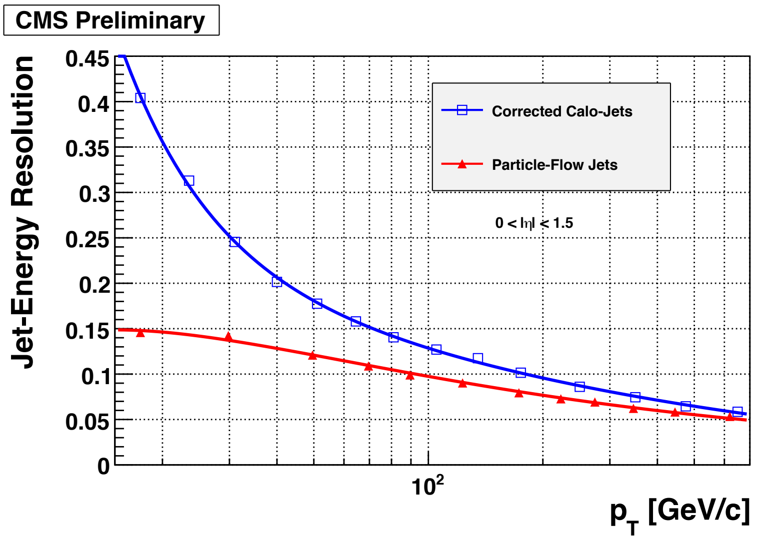

Figure 2.28: The effect of including the tracker information on the jet energy measurement, for jets detected in the CMS barrel region. Results from CMS simulation. Image from [73].

2.4.5 Particle Flow calorimeters

Almost every detector concept for future e^+e^- colliders exploits PFA. The two detectors proposed for the ILC, ILD and SiD [15], and the CLIC detector [20], also rely on a strong solenoidal field magnet of 4-5 T. This helps the shower separation at the calorimeter level because a strong magnetic field spreads to a larger extent collimated beams of (charged) particles. The porting of such detector concepts to future circular e^+e^- colliders, *i.e.* CLD, the CLIC detector tailoring for FCC-ee [76], and the CEPC baseline detector [10], cannot rely on such strong magnetic fields because the need of a low beam emittance at the Z luminosity requires magnetic field intensities not greater than 3 T.

The detector R&D of particle flow calorimeters for e^+e^- colliders is driven by the CALICE Collaboration. In the last 15 years several highly granular prototypes, both for em and hadronic showers detection, were built [77]. Active elements used are silicon pads (typically $\simeq$ 1 cm^2), scintillator strips, small Resistive Plate Chambers (RPCs), operating in the saturated mode, or alternatively Micromegas and GEMs. Usually they adopt tungsten for the em compartment given its small Molière radius (9.3 mm) to minimize the lateral shower development as much as possible. For the hadronic compartment, iron or stainless steel are often used.

Among the em prototypes, the largest one is a tungsten/silicon detector [78] with an active surface area of 18×18 cm^2 and 30 layers for a length of 20 cm. The total thickness corresponds to 24 X_0, divided into 10 first layers, 0.4 X_0 thick, followed by other 10 layers, 0.8 X_0 thick, and other final 10 layers, 1.2 X_0 thick. The active medium is silicon divided into 1×1 cm^2 diodes. There are 324 cells per layer for a total of 9720 readout elements. The reported em energy resolution is $16.5/\sqrt{E} \oplus 1.1\%$ [79] and is obtained with 525 μm thick silicon sensors.

CALICE also built sampling calorimeters for hadron detection. A sandwich calorimeter used 38 layers of 5 mm plastic scintillators spaced by either 17 mm thick steel plates or 10 mm thick tungsten plates [80]. In both cases the instrumented volume was $\simeq$ 5.3 λ_{int} deep. The transverse dimension is 90×90 cm^2. The active layers are subdivided into tiles with dimensions of 3×3 cm^2 or larger. Each tile adopts a wavelength shifting fiber to collect and absorb the scintillation light and re-emit it at a longer wavelength. Fibers are readout by SiPMs. The related R&D pioneered the large-scale usage of SiPMs in calorimetry. In Fig. 2.29 a picture of the plastic-scintillator layer is shown. The hadronic energy resolution was reported to be $57.6\%\sqrt{E} \oplus 1.6\%$ [81] (details on the sample selection and correction applied to the containment are not discussed here).

Another CALICE calorimeter has a lateral cross section of $\simeq$ 1 m^2 and the effective depth can be chosen by changing the absorber material and the thickness of

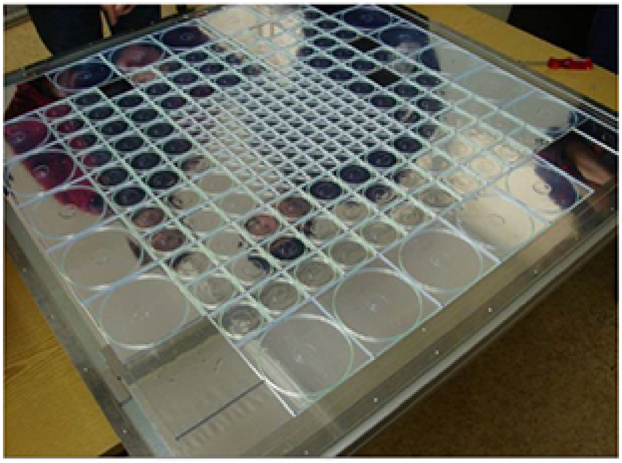

Figure 2.29: A plastic-scintillatior plane of the scintillator-based CALICE hadron calorimeter. The active tiles featuring different sizes are visible. Image from [80].

the absorber plates [82]. Active elements are 1×1 cm^2 RPC cells. In total, about 500×10^3 readout elements are present. The RPCs are operated in a saturated mode, therefore this detector is often referred to as a digital calorimeter. The device produced spectacular 3-dimensional images of hadronic showers, as the one depicted in Fig. 2.30.

A common problem of the CALICE calorimeters is a more or less evident non-linearity. In the case of the em Si/W calorimeter, the average signal measured per unit deposited energy increased by $\simeq$ 5% in the energy range 6-45 GeV [79], see Fig. 2.31. The fact that the calorimeter response increases with the energy is very curious, as most often signal non-linearity implies a response decreasing with the energy. The origin of this non-linearity is probably the calibration at the mip scale that is used to calibrate all the CALICE detectors. Such a calorimeter would correctly sample, on average, energies from a collection of mips regardless of the energy deposited. However, not only the response to electrons differs from the mip one in sampling calorimeters ($e/mip \neq 1$), but it also changes with the shower development. At the em shower tails (both longitudinal and lateral) the response to electrons becomes smaller and calibration constants estimated at the mip level lead to a systematic underestimation of the primary energy. To correct for this effect, corrections to the calibration constants must be applied and the knowledge of the showering profile is required. Therefore, the stage of the shower development must be known for every energy deposition. It should be reminded that the longitudinal profile of an em shower changes with the energy. For instance, a 100 GeV em shower has a highly energetic phase in the first steps that resembles a collection of mips.

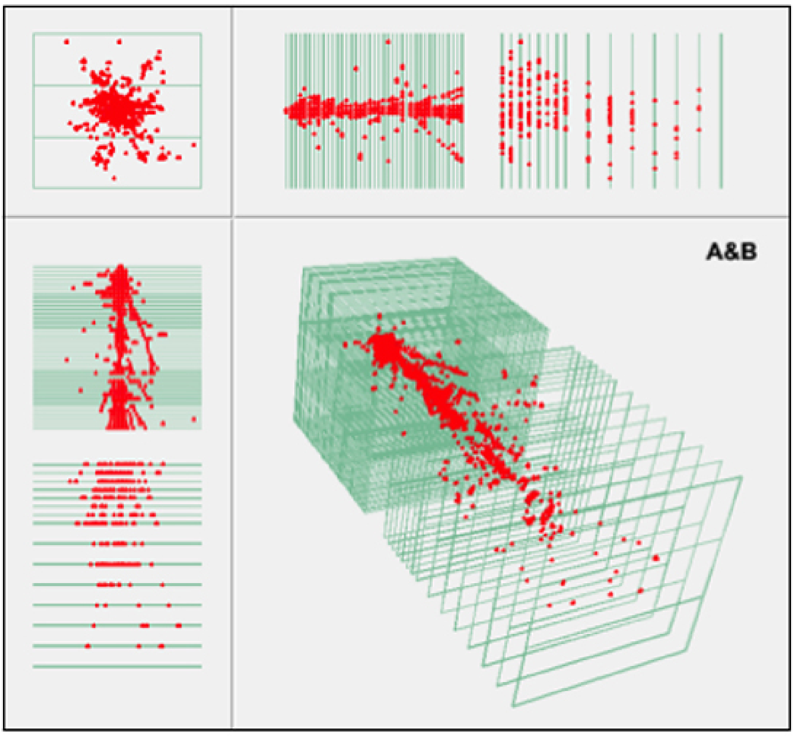

Figure 2.30: Recorded event display from the CALICE digital calorimeter detecting 120 GeV π^-. Image from [77, 83].

This stage is largely absent in a 10 GeV em shower. While longitudinal leakage increases with the energy, the shower tail, exhibiting the minimal response, is more and more leaking out of the calorimeter. Therefore, the overall correction to the energy reconstructed at the mip scale changes with the primary electron energy. The author of [36] suggests that, "if CALICE applied the same overall correction factor to account for the average difference between the em scale and the MIP scale at all energies, (it) might explain the response non-linearity observed for positrons in the W/Si calorimeter". A detailed explanation on how to achieve linearity in longitudinally segmented calorimeter is reported in [36].

Signal non-linearity for hadronic detection was reported for both the iron/plastic-scintillator and the digital calorimeters [84, 85]. The origin of this behavior is less clear and, for the SiPM readout calorimeter, it could be ascribed to a light read-out saturation. For the digital calorimeter the signal non-linearity is so large that the Collaboration decided to equip RPCs with a 2-bit readout system to divide the signals into three categories on the basis of different threshold levels. This upgrade is the so called semi-digital calorimeter [86]. Note that RPCs are still operated in avalanche mode so the signal threshold is only related to the number of (charged)

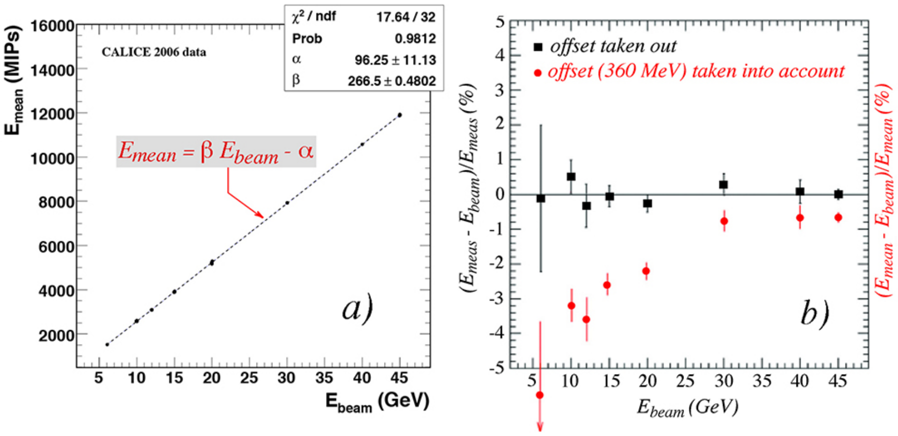

Figure 2.31: Average signal as a function of electron energy for the W/Si ECAL built by CALICE (a). Residual signals from this detector, before and after taking out a 360 MeV offset (b). Image from [79].

particles passing through the RPC and is not related to the energy deposited. Experimental results for this configuration were reported in [87]. The energy of primary particles was reconstructed by means of three (different) calibration constants weighting the number of cells above each threshold. It turned out that such calibrations constants must change with the primary energy and the particle type to properly reconstruct, on average, the primary energy. Fig. 2.32 shows the reconstructed energy distribution for the semi-digital CALICE calorimeter superimposed to the purely digital measurement, at 20 and 70 GeV π^-. The improvement is significant at the highest energy.

It is also important to remember that highly granular calorimeters at future e^+e^- colliders will crucially depend on the software reconstruction tools. The need to correctly identify energy depositions from charged particles and subtract them from the calorimeter contribution, demands for sophisticated software applications as the PandoraPFA software [88]. Every error in this respect leads either to a double counting of charged particle contributions or to an underestimation of the energy deposition from neutral particles. The double-counting happens when the contribution of charged tracks is not entirely subtracted from the calorimeter signal, and the underestimation of the energy from neutral particles happens whenever part of their signals is confused as the one of a charged induced shower and eventually subtracted. Event-by-event fluctuations between the two effects are largely non-symmetric, with a tendency to underestimate the energy deposition from neutral particles. They are treated as an additional source of fluctuations on the jet energy resolution, often referred to as the "confusion term". The impact of the confusion term on the energy

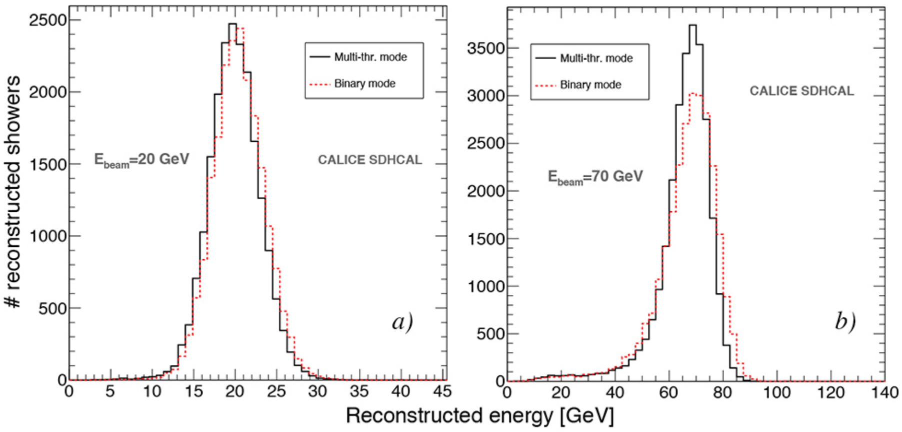

Figure 2.32: Reconstructed energy distribution with the binary mode (red dashed line) and the three-threshold mode (solid black line), for pions of 20 GeV (a) and 70 GeV (b), in the CALICE semi-digital hadron calorimeter. Image from [87].

resolution, as opposed to all the other fluctuations, increases with the energy. At the ILC, it starts dominating the jet energy resolution above $\simeq$ 300 GeV (see, for instance, [88]).

Chapter 3

The IDEA calorimeter - full simulation studies

The chapter outlines the work of fully simulating the IDEA dual-readout calorimeter carried out during 2019 and 2020. The aim of the work is to provide a from scratch implementation of the detector simulation code and to address its main performance while detecting final states from e^+e^- events. Several fundamental steps have been performed, from the geometry design to the calibration, from the single particle studies to the jet reconstruction. Selected results have been published in [89, 90]. Important aspects remain to be studied, among them the most important one is the integration with the other sub-detectors. What we learned here opened the path for any future investigation. The author of the thesis is the main author of this work.

3.1 The detector

IDEA, Innovative Detector for Electron–positron Accelerators, is a multi-purpose detector concept designed for high-luminosity electron-positron circular colliders. The calorimetric section adopts a dual-readout, longitudinally unsegmented and fully projective, fiber calorimeter. Following the lessons from [36] on high-resolution compensating fiber calorimeters, such as the SPACAL [54] and the RD52 calorimeters [49], the geometry is dictated by the following ideas.

The segmentation of the calorimeter is chosen in such a way that the volume in which a shower develops always corresponds to a small number of cells and most of the energy is deposited in a single cell. This highly simplifies the calibration procedures for which each cell response can be equalized as a single entity. This type of segmentation can be achieved in accelerator-based experiments where all the particles to be measured come, with a good approximation, from the Interaction Point (IP), with a tower-based structure. The detector volumes are divided into towers and the signal produced in each tower is integrated along the tower length. Active volumes are optical fibers running all along the tower volume. As demonstrated in [91], the possibility to independently readout each fiber with a dedicated Silicon PhotoMultiplier (SiPM) makes possible to not limit the spatial and angular resolution of the calorimeter to the tower dimension, and potentially leads to an unprecedented spatial and angular resolution. This also guarantees that two particles showering inside a single tower still can be identified on the basis of the signals produced inside the tower itself. A detailed description of a first dedicated SiPM readout is given in Chap. 4.

The main quantities provided by a calorimeter are the three-momentum vectors, from the shower positions and energies, and the nature of the incident particles, from topological information. To provide that, the likely best configuration is a projective tower structure where towers are truncated pyramids pointing to the IP. The inner face of each tower is projected at the outer surface where its area is roughly quadrupled. In such a geometry, signals directly identify a well defined interval for the production angle of the detected particle, as each tower corresponds to a certain region in θ and ϕ.

Following this reasoning, the IDEA calorimeter is made of 36 rotations around the beam axis corresponding to a segmentation of $\Delta\phi = 10.0°$. Each rotation is referred to as a slice. Each slice contains both barrel and end-cap towers with a θ coverage up to $\simeq 0.1$ rad. Towers are 2 m long.

The calorimeter barrel-region of a single slice is made of 80 towers while each slice end-cap region consists of 35 towers. Each tower has a θ segmentation of $\Delta\theta = 1.125°$. The barrel geometry is perfectly symmetrical with respect to the plane perpendicular to the beam, *i.e.* the first right-tower is identical to the first-left tower, and so on. Each slice is identical so that each tower (both end-cap and barrel ones) is repeated $2 \times 36 = 72$ times.

The calorimeter active elements are scintillating (polystyrene) and clear-plastic fibers (PolyMethyl MethAcrylate (PMMA)) embedded in copper. Fibers are placed in a chess-board like geometry with a 1.5 mm pitch. The fiber diameter is 1 mm thick (core + cladding) so that each fiber is separated from the closest ones by 0.5 mm of absorber material.

This complex geometry has been reproduced within the GEANT4 simulation toolkit [64] and all results in this chapter are obtained with it. Fig 3.1 and 3.2 shows respectively a slice of the IDEA calorimeter and sketches of the full calorimeter and of a single end cap.

Fig 3.3 shows the energy containment of each tower when 40 GeV electrons enter

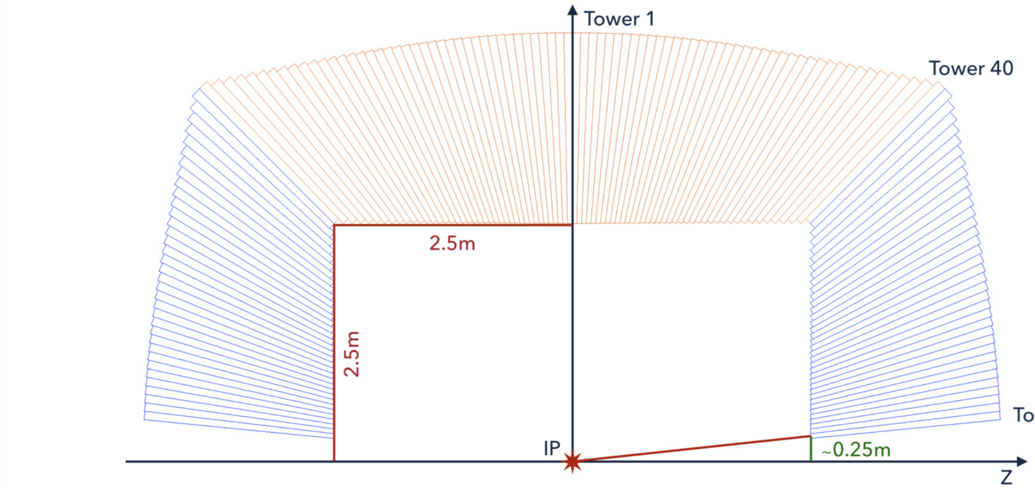

Figure 3.1: Sketch of a single slice of the IDEA calorimeter.

the calorimeter at the center of the tower inner face. As towers in the end-cap region shrink going towards the beam pipe, the energy containment decreases. With the exception of the seven towers closest to the beam pipe, the average containment is above 90%. This feature is at the basis of the calibration procedure explained in the following.

3.1.1 Signal simulation

The goal of the full simulation is to propagate each showering particle through the calorimeter, taking into account its interactions with the active elements, up to the formation of a signal that can be acquired in a real-life experiment (photoelectrons (p.e.), charge, ADC counts, ...). The following procedures are adopted to simulate the scintillation and Cherenkov signals.

Scintillation light production Every time a charged particle passes through a scintillating fiber, our GEANT4 application computes the ionization energy deposited inside that volume. This energy deposition is the seed for the scintillation light production. To translate this energy into light (photons) the Birks' saturation law must be included, stating that the light output per unit path length is related to the specific ionization by the relation

$$\frac{dL}{dx} = A\frac{dE/dx}{1 + k_b \cdot dE/dx} \tag{3.1}$$

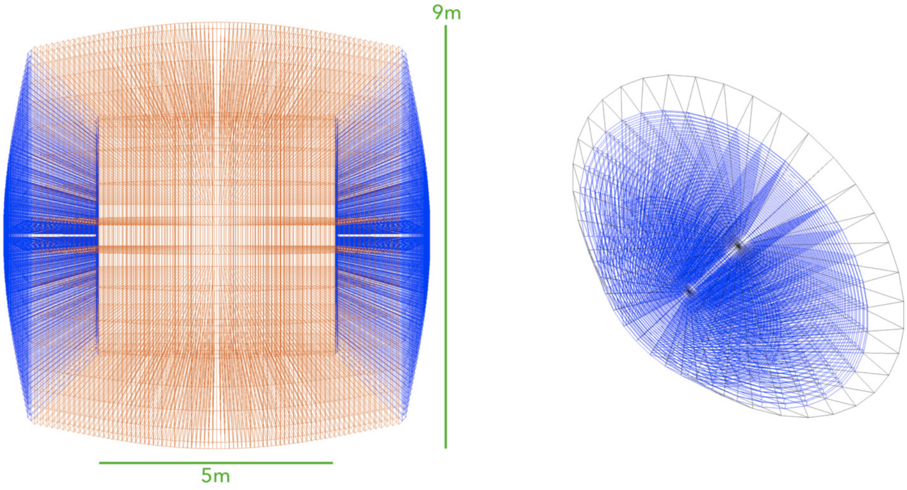

Figure 3.2: Sketch of the IDEA calorimeter (left) and end-cap geometry (right).

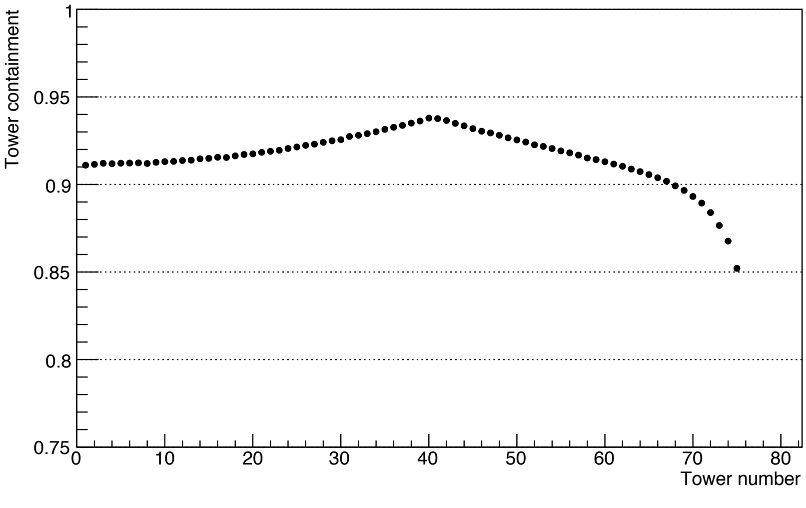

Figure 3.3: Energy containment of single tower (E_{cont}/E_{tot}) for 40 GeV electrons entering at the geometrical center of each tower, from tower 1 (first tower of the barrel region) to tower 75 (last tower of the end-cap region).

where dE/dx is the specific ionization and dL/dx is the corresponding specific light produced, k_b is the Birks' constant and A is the scintillation efficiency.
Eq. 3.1 reduces to a linear relationship for small dE/dx,

$$\frac{dL}{dX} \simeq A\frac{dE}{dx} \tag{3.2}$$

as observed experimentally, *e.g.* with electrons at energies above 125 keV. However, for large dE/dx values, it predicts a saturation of the light output to

$$\frac{dL}{dX} \simeq \frac{A}{k_b} \tag{3.3}$$

so that the light output becomes proportional to the range of the particle in the scintillator, ($R(E)$):

$$L \simeq \frac{A}{k_b}R(E) \tag{3.4}$$

The constant k_b amounts to 0.126 mm MeV^{-1} in polystyrene-based scintillators, or 0.013 g MeV^{-1} cm^{-2}. In a hadronic shower, more than half of the energy of the non-electromagnetic component is carried by charged particles where roughly two thirds are protons with typical energies of $\simeq 50 - 100$ MeV each. Such particles experience a ionization loss up to a factor 100 higher than the one of equally charged *mips* ($\simeq 1$ MeV cm^2 g^{-1}) thus resulting in a light production reduced by a factor 2 at most.
Eventually, the light produced on a step-by-step basis is smeared by a Poissonian distribution according to the statistical nature of the light production mechanism. This approach correctly reproduces photo-statistic fluctuations in scintillation light production and allows to reproduce within simulations the scintillating light yield (p.e./GeV) desired. Thanks to the Poissonian smearing, the simulation is tuned to $\simeq$ 400 scintillation p.e. per GeV deposited at the electromagnetic scale, *i.e.* with electrons.

Cherenkov light production The Cherenkov process has been added among the physics processes to be simulated, the Physics List, and is applied to every charged particle passing through clear-plastic fibers. The light seed is the number of Cherenkov photons trapped inside the fiber, *e.g.* emitted inside the fiber numerical aperture, produced in a single step. Each light seed is smeared by a Poissonian distribution. Similarly to what is done for the scintillation light, this smearing reproduces on average the desired light yield and the statistical fluctuations in Cherenkov light emission. The simulation is tuned to $\simeq$ 100 p.e. per GeV deposited at the electromagnetic scale.

Optical fibers offer two main benefits. They allow to select at will the calorimeter sampling fraction, by changing the fibers pitch, and they allow to achieve a constant response to electrons throughout the whole calorimeter. This second feature is crucial for dual-readout calorimeters for which calibration constants estimated with electrons are used to calibrate signals from hadronic showers developed much deeper and wider inside the calorimeter. To achieve it, two ingredients are needed:

- the sampling fraction must be constant throughout the whole calorimeter, and

- signals must be integrated all along the shower development.

The first requirement is achieved by inserting new staggered fibers as soon as they fit in along the tower development. The sampling fraction needs to be constant at the level of 1%, likely at the scale of the em shower dimensions, in order to keep the constant term of the energy resolution at that level. The second requirement is needed because the response to electrons changes with the shower development, hence in a longitudinally segmented calorimeter active elements in different positions with respect to the incident electron have different calibrations. Therefore, to correctly determine the deposited energy that corresponds to a given signal measured in a layer, the stage of the shower development when the signal was produced must be known. This cannot be solved with an overall depth dependence of the calibration constants because hadron showers may contain electromagnetic components that penetrate very deep into the calorimeter. To get calibration constants that can be used at any point of the calorimeter geometry, signals must be integrated over all the shower development. Fibers offers a simple solution by longitudinally integrating the signals.

3.2 Calorimeter response and calibration

Fig. 3.4, 3.5 show the scintillation and Cherenkov response, respectively, when 40 GeV electrons enter the calorimeter at the geometrical center of each tower, from tower 1 to tower 75, with a beam inclination of ($\theta = 0.125°$, $\phi = 1.5°$). The average tower response is indicated by the red line corresponding to 407 p.e./GeV for the scintillation signal and 103 p.e./GeV for the Cherenkov signal. Color bans represents deviation of ±1% to the mean response. Clearly GEANT4 indicates that differently-shaped towers can achieve a uniform response if the fiber pitch is kept identical for any tower.

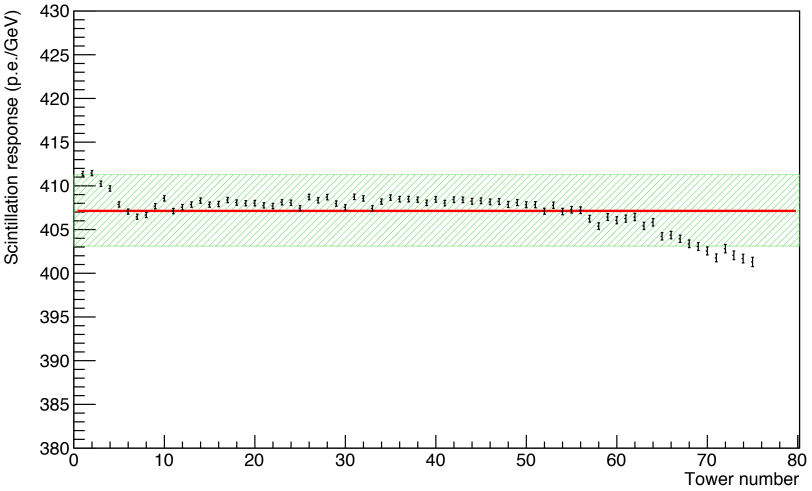

Figure 3.4: Scintillation response of the IDEA Calorimeter when 40 GeV electrons enter the calorimeter at the geometrical center of the tower inner face, from tower 1 to tower 75. Color bans represents deviation of ±1% to the mean response.

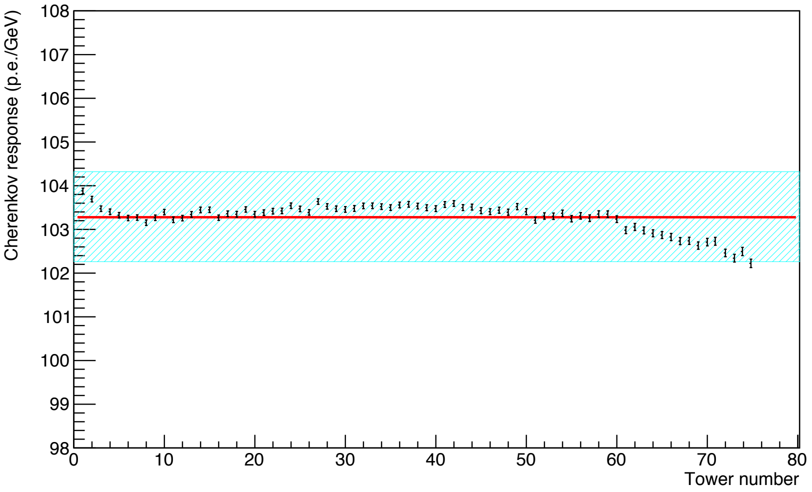

Figure 3.5: Cherenkov response of the IDEA Calorimeter when 40 GeV electrons enter the calorimeter at the geometrical center of the tower inner face, from tower 1 to tower 75. Color bans represents deviation of ±1% to the mean response.

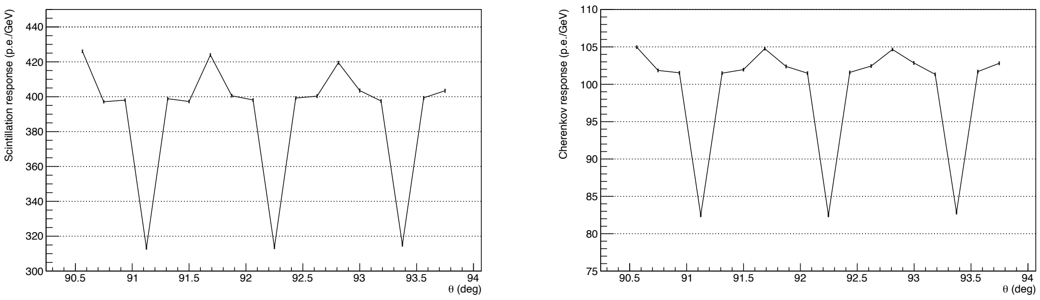

Figure 3.6: Response of the IDEA Calorimeter for 40 GeV electrons as a function of θ, scintillation signal (left) and Cherenkov signal (right). The highest points correspond to electrons entering the calorimeter at the geometrical center of the first three towers with no beam inclination.

3.2.1 Border effects

The situation changes when the electromagnetic shower energy is shared between two adjacent towers with similar intensities. This effect is due to the extremely collimated nature of electromagnetic showers for which about 10% of the signal is deposited within 1 mm from the shower axis (this feature has been measured with test-beam data, details are given in Chap. 4). At the border between two towers the shower sampling is performed by staggered fibers that start as soon as the tower opening allows for a new fiber placement. This results in a local smaller sampling fraction and a calorimeter response decrease. We studied this effect with 40 GeV electrons changing the θ angle with steps of $\Delta\theta/6 = 0.1875^\circ$ starting from the first tower geometrical center. The calorimeter response scan is shown in Fig. 3.6. The lowest response happens when electrons interact with the calorimeter exactly at the border between two adjacent towers. On the other hand, the highest response happens when the electron enters exactly at the tower geometrical center with no beam inclination. From the highest to the lowest response there is a loss of $\simeq$ 20% for the Cherenkov signal and $\simeq$ 25% for the scintillation signal. The discrepancy is explained by the more collimated nature of the scintillation signal with respect to the Cherenkov one.

3.2.2 Calibration

Dual-readout calorimeters are calibrated at the electromagnetic scale for single hadron, jet and electromagnetic event reconstruction. This is a great advantage. Thanks to the easy access to isolated electrons (positrons) in a circular electron-positron collider, the calibration constants estimation and monitoring are possible with great precision all the experiment life long. In the IDEA detector, electrons originating from the IP will traverse only $\sim 1\ X_0$ of budget material before interacting with the calorimeter, therefore their energy loss before the calorimeter interaction is expected to be largely marginal. Moreover, thanks to the chosen geometry the calibration constants can be estimated in a straightforward way.

The first step is to steer electrons of known energy at the center of each tower individually. We included a beam inclination of ($\theta = 0.125°$, $\phi = 1.5°$) with respect to each tower center. Fig 3.7, 3.8 show the average signal divided by the tower-contained energy for the scintillation and Cherenkov signals, respectively. These quantities are referred to as *equalization constants* as they are used to equalize the towers responses to the actual energy deposition. For instance, they could be used in a real experiment to factorize the tower-by-tower differences in the light readout chain.

It is important to notice that the average equalization constant is 410 p.e./GeV for the scintillation signal and 105 p.e./GeV for the Cherenkov one. These values are, respectively, 0.7% and 2% higher than the corresponding average response values. This is due to the fact that electromagnetic showers tails, being detected in the neighbouring towers, are sampled with a lower response with respect to the core showering in the central tower. This is a well known feature of electromagnetic calorimetry: *an electromagnetic shower is not a collection of mips.*

This effect makes the calibration of the electromagnetic calorimeter more subtle than what might be thought. Indeed, it might lead to a mis-reconstruction of the primary electron energy. If we sum the signals over all stimulated towers and apply the equalization constants, the primary electron energy is never correctly reconstructed. Fig 3.9, 3.10 show the reconstructed energies divided by the energy deposited in the calorimeter for the scintillation and the Cherenkov signal, respectively. It is evident how this mis-reconstruction is worse in the Cherenkov channel where the relative difference between the average response and the average equalization constant is greater. Also, this effect is higher in the end-cap towers where the energy containment of the mostly stimulated tower is lower. On the other hand, the mis-reconstruction is lower at tower 40 that exhibits the maximum shower containment.

To fix this mis-calibration, each equalization constant is scaled up in order to reconstruct, on average, the correct energy deposited. It is important to stress that each equalization constant is corrected independently from the others. What we find after the correction are the calibration constants. Fig 3.11, 3.12 show the reconstructed energy divided by the energy contained *vs.* the tower number, when the signal in each tower is multiplied by its own (corrected) calibration constant and the energies

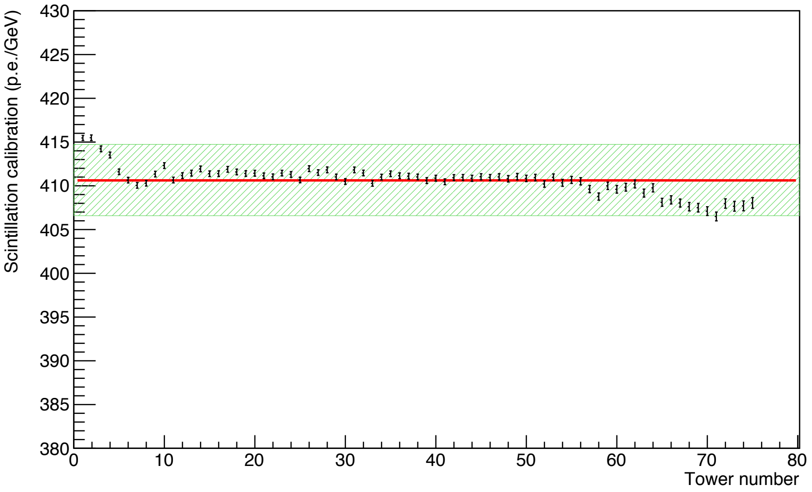

Figure 3.7: Equalization constants *vs.* tower number for the scintillation signal. See text for details. Color bans represents deviation of ±1% to the mean value.

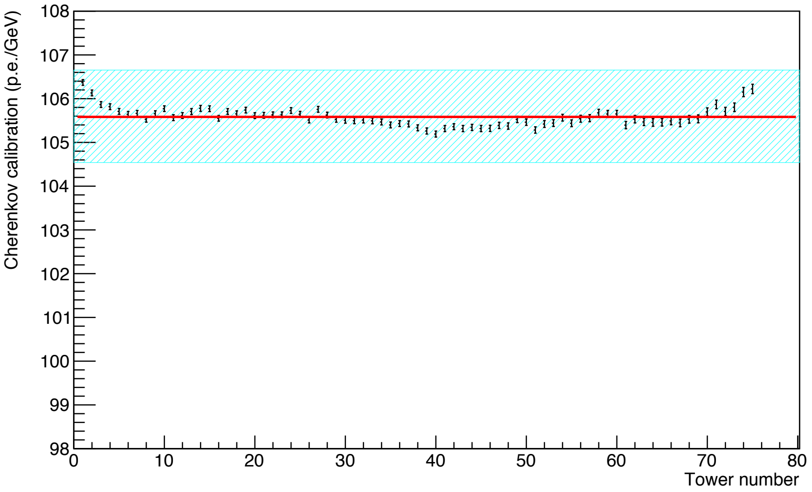

Figure 3.8: Equalization constants *vs.* tower number for the Cherenkov signal. See text for details. Color bans represents deviation of ±1% to the mean value.

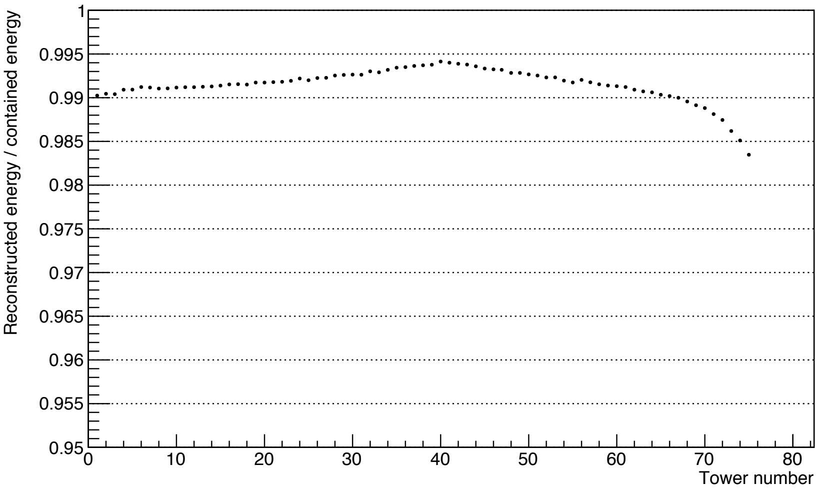

Figure 3.9: Reconstructed electron energy divided by the energy deposited *vs.* tower number for scintillation signal. See text for details.

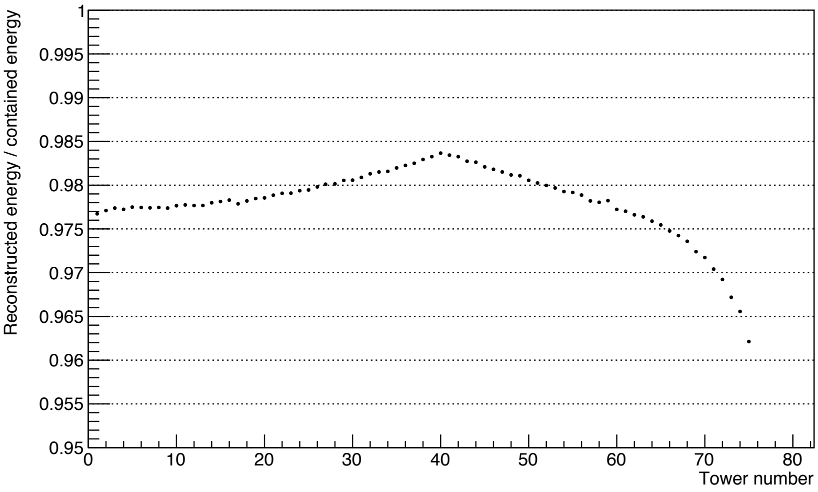

Figure 3.10: Reconstructed electron energy divided by the energy deposited *vs.* tower number for Cherenkov signal. See text for details.

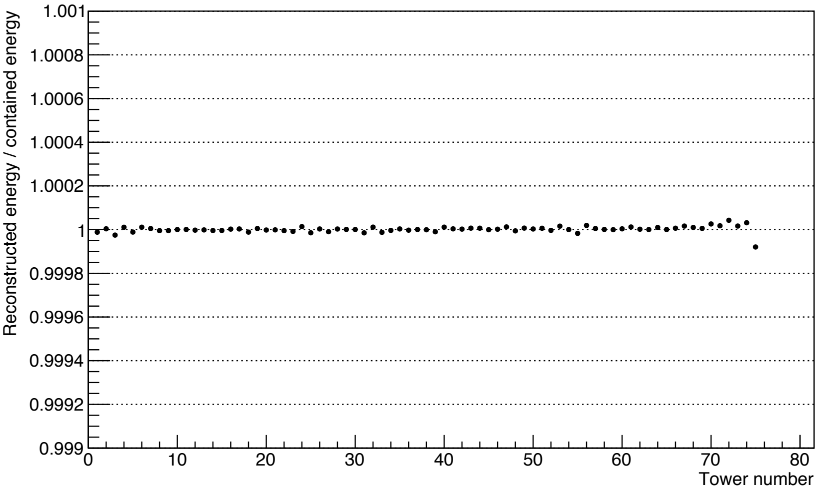

Figure 3.11: Reconstructed 40 GeV electron energy divided by the contained energy *vs.* tower number for the scintillation signal after the application of the calibration constants. See text for details.

found are summed over all the towers.

The average energy containment for electrons in the barrel region is 99.4%. To reconstruct the beam energy, instead of the contained energy, calibration constants of each towers are eventually scaled up to take into account on average the energy containment.

3.2.3 On the correctness of the calibration approach

The fact that is possible to estimate calibration constants independently for each tower, even if some energy sharing between towers is present, might lead to confusion, therefore we report here a brief recap of the calibration procedure.

The calibration approach is based on the following assumptions:

- The calorimeter is designed in such a way that a given em shower deposits on average always a certain energy E_{tot} and, regardless the impact point, the number of photons released N_{tot} is on average constant. It follows that the ratio E_{tot}/N_{tot} is constant.
- The calorimeter cells (towers) are identical (that is roughly the case for the IDEA calorimeter, at least in the barrel region) so that, when an electron interacts at the center of a tower, it releases, on average, the same energy E_c inside the tower and the number of photons created in the tower N_c is,

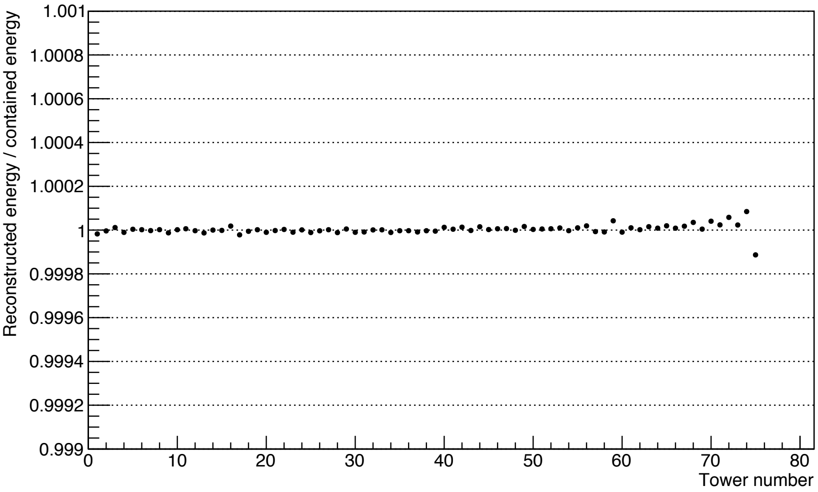

Figure 3.12: Reconstructed 40 GeV electron energy divided by the contained energy *vs.* tower number for the Cherenkov signal after the application of the calibration constants. See text for details.

on average, constant. So the ratio E_c/N_c is constant as well, but different from E_{tot}/N_{tot}. The reason why they differ is that the em shower tails have a different composition with respect to the shower core.

- Even if N_c is constant, each cell (tower) will give a different signal, in response to a given N_c, due to the cell-to-cell differences in the light collection and detection efficiency. These differences are absorbed in the equalization constants. The scale of the equalization constants is arbitrary, the only relevant thing is that via equalization constants the same signal is obtained from the same E_c and N_c.
- For every cell, the average response is measured (in arbitrary units) and the equalization constants are extracted.
- Once equalization constants are extracted, the sum of every cell signal is used to to calculate the calibration constant that (under the above assumptions) will be unique. The only additional input needed is the total energy contained in the calorimeter.

The following is a demonstration of the correctness of this approach. We want to calibrate a longitudinally unsegmented calorimeter divided into cells. Let assume that all calorimeter cells are equal so that the energy contained in each cell, when

the beam is impinging on its centre, is $E_c = f \cdot E_{tot}$.
E_{tot} is not the beam energy but the total contained energy, in general estimated with Monte Carlo simulations. $E_{nc} = E_{tot} - E_c$ is the total energy contained in the cells surrounding the centered cell. Then, for each calorimeter cell J, we can measure

$$\beta_j = \frac{E_c}{(S_j)_c} \tag{3.5}$$

where $(S_j)_c$ is the signal measured on cell J when beam is centered on it and E_c is, again, estimated from simulation.
On the other hand the signal is always proportional to the number of primary photons

$$S_j = \alpha_j \cdot (\gamma_p)_j \tag{3.6}$$

Where α_j is the efficiency of the cell J for collecting and converting photons. The fact that light production and transportation can have some variation from cell to cell is factorized into α_j.
When the beam is centered on J, the number of primary photons is independent of J so

$$(S_j)_c = \alpha_j \cdot (\gamma_p)_c \tag{3.7}$$

and

$$E_c = \beta_j \cdot (S_j)_c = \beta_j \cdot \alpha_j \cdot (\gamma_p)_c \tag{3.8}$$

Let define a parameter λ_c

$$\lambda_c = \frac{E_c}{(\gamma_p)_C} = \alpha_j \cdot \beta_j \tag{3.9}$$

that is independent of J and is the ratio between the contained energy and the number of the primary photons in the centered cell.
Let consider the case when the beam is centered on cell 2 and the shower is leaking in just two neighbouring cells, with label 1 and 3. There are three energy deposits E_1, E_2, E_3 and three signals S_1, S_2 and S_3. By definition, E_2 is equal to E_c. We can compute the sum

$$\begin{align}
E_{sum} =& \beta_1 \cdot S_1 + \beta_2 \cdot S_2 + \beta_3 \cdot S_3 = \tag{3.10}\\
& \beta_1 \cdot (S_1)_{nc} + \beta_2 \cdot (S_2)_c + \beta_3 \cdot (S_3)_{nc} = \tag{3.11}\\
& \beta_1 \cdot \alpha_1 \cdot (\gamma_p)_{1nc} + \beta_2 \cdot \alpha_2 \cdot (\gamma_p)_{2c} + \beta_3 \cdot \alpha_3 \cdot (\gamma_p)_{3nc} = \tag{3.12}\\
& \lambda_c (\gamma_p)_{1nc} + \lambda_c \cdot (\gamma_p)_{2c} + \lambda_c \cdot (\gamma_p)_{3nc} = \tag{3.13}\\
& \lambda_c \cdot (\gamma_p)_{tot} \tag{3.14}
\end{align}$$

but the total number of photons does not depend on anything except the shower energy, so let define a parameter λ_{tot}

$$\lambda_{tot} = \frac{E_{tot}}{(\gamma_p)_{tot}} \tag{3.15}$$

Finally

$$E_{sum} = \lambda_c \cdot \frac{E_{tot}}{\lambda_{tot}} = k \cdot E_{tot} \tag{3.16}$$

To conclude, by knowing E_c, all the β_j parameters are estimated by centering the beam on each cell. Then, the sum

$$E_{sum} = \sum_j (\beta_j \cdot S_j) \tag{3.17}$$

is built and, by knowing E_{tot}, it is possible to estimate the parameter k as

$$k = \frac{E_{sum}}{E_{tot}} \tag{3.18}$$

that is the calorimeter calibration constant. For a measurement, E is reconstructed as

$$E = \frac{1}{k} \cdot \sum_j (\beta_j \cdot S_j) \tag{3.19}$$

This result really depends only on the assumption of the uniformity of the cell energy containment. The only relevant point is to equalize all the cell responses since any constant normalisation factor is then re-adsorbed in the k factor. For the same reason, you only need to estimate E_{tot} (E_c is not necessary). You may equalize to any arbitrary value the cell responses, then build the equalized sum and finally calculate the calibration constant k.

3.3 Electromagnetic performance

3.3.1 Energy resolution and linearity

A dual-readout calorimeter samples electromagnetic showers independently with, typically, scintillation and Cherenkov signals. The two signals can further be recombined to get the best electromagnetic energy resolution possible.

Fig. 3.13 shows the scatter plot of the reconstructed energies when 50 GeV electrons enter the calorimeter at the center of tower 1 with a beam inclination of ($\theta = 0.125°$, $\phi = 1.5°$). Both distributions have a Gaussian shape and are centered on the cor-

rect beam energy. The two signals act as independent samplings of showers induced by electrons. This opens the possibility to combine the two signals to improve the overall calorimeter electromagnetic performances.
By fitting σ/E values in the energy range 10-250 GeV, as shown in Fig. 3.15 (blue and red lines for the scintillation and the Cherenkov signals respectively), we find that the energy resolutions are well fitted by:

$$\frac{\sigma}{E} = \frac{17.7\%}{\sqrt{E}} + 0.6\% \text{ or, } \frac{19.6\%}{\sqrt{E}} \oplus 1.3\% \tag{3.20}$$

for the scintillation signal, and

$$\frac{\sigma}{E} = \frac{19.4\%}{\sqrt{E}} + 0.1\% \text{ or, } \frac{20.0}{\sqrt{E}} \oplus 0.5\% \tag{3.21}$$

for the Cherenkov signal, with E expressed in GeV unit.
The constant term of the scintillation signal is larger due to the more collimated nature of ionizing energy deposition in electromagnetic showers with respect to the Cherenkov light signal. This makes the scintillation signal more sensitive to the impact point of the primary electron on the calorimeter face (the closer to a fiber the higher the signal). The best way to combine signals is the one that maximize the component with the minimum standard deviation, on an event-by-event basis,

$$E = \frac{E_s/\sigma_s^2 + E_c/\sigma_c^2}{1/\sigma_s^2 + 1/\sigma_c^2} \tag{3.22}$$

with σ_s and σ_c being calculated with Eqs. 3.20, 3.21. The energy resolution obtained, shown in Fig. 3.15 (black line), is well fitted by,

$$\frac{\sigma}{E} = \frac{13.0\%}{\sqrt{E}} + 0.2\% \text{ or, } \frac{14.0\%}{\sqrt{E}} \oplus 0.6\% \tag{3.23}$$

with E expressed in GeV units. The stochastic term greatly improved with respect to individual signals and the constant term got really close to the one obtained with the Cherenkov signal only.
Energy distributions for 50 GeV electrons sampled by the scintillation, the Cherenkov and the combined signals are shown in Fig. 3.14.
We investigated also the signal linearity. Fig. 3.16 shows the average reconstructed energy *vs.* the true beam energy in the energy range 10-250 GeV. The results were obtained with the same beam setup used for resolution studies. The calorimeter is linear for electron energy reconstruction in the energy range $10 - 250$ GeV within $\pm 1\%$.

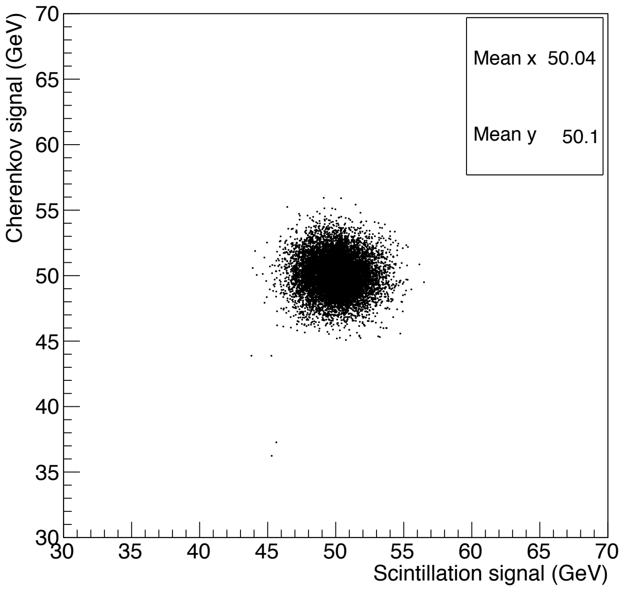

Figure 3.13: Reconstructed 50 GeV electron energy with the scintillation signal (X-axis) and the Cherenkov signal (Y-axis).

3.3.2 Uniformity

In a 4π calorimeter it is of great importance studying the performance uniformity across the whole detector. We studied it with 40 GeV electrons events simulated with the beam setup used to calibrate the detector. No event selection is applied. Fig. 3.17 (left) shows the mean reconstructed energy divided by the beam energy, *vs.* the tower number. Considering all the 75 towers, the maximum discrepancy from 1 is smaller than 0.5%. Fig. 3.17 (right) shows the corresponding energy resolution. Indeed a good uniformity of the energy resolution is found with the only exception of the tower closest to the beam pipe.

3.4 Hadron performance

3.4.1 Containment and calibration

To investigate the hadronic performance we simulated single π^- events in the energy range 10-150 GeV. It is important to notice here that we adopt the 10.5.p01 GEANT4 version and the FTFP_BERT Physics List (PL) and we assume this PL as the default one in the following.

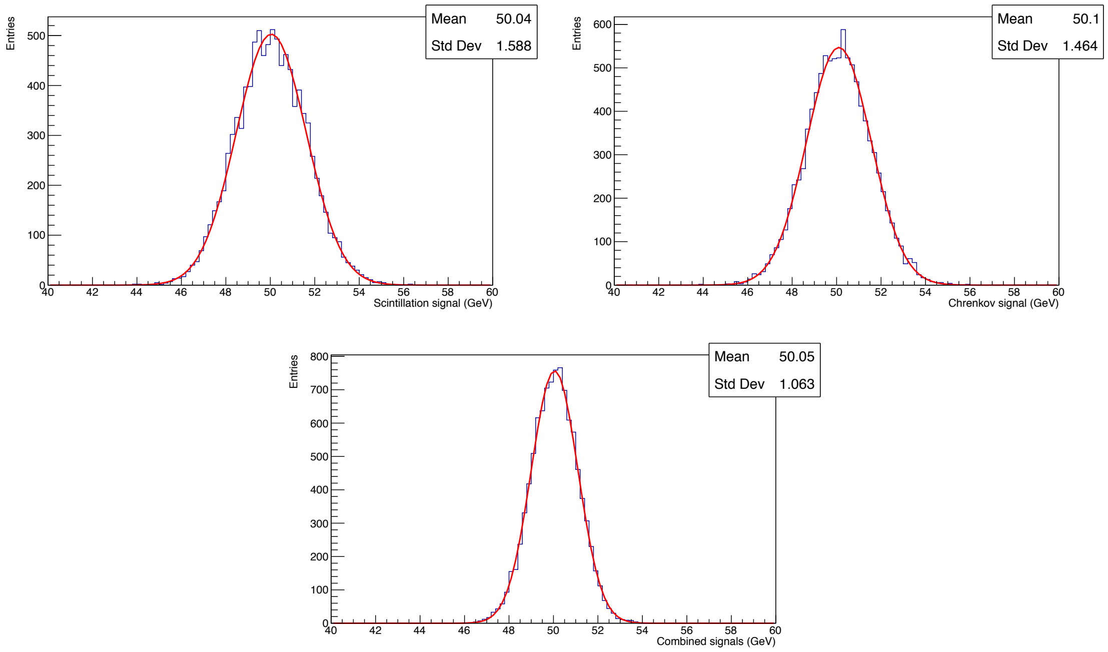

Figure 3.14: Reconstructed 50 GeV electron energy with the scintillation signal (top-left), the Cherenkov signal (top-right) and the combined signals (bottom).

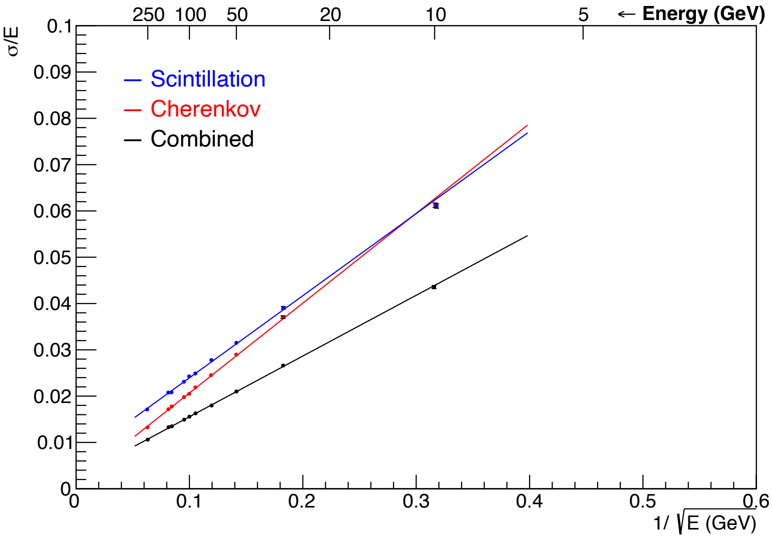

Figure 3.15: Electromagnetic energy resolutions of the IDEA dual-readout Calorimeter. See text for details.

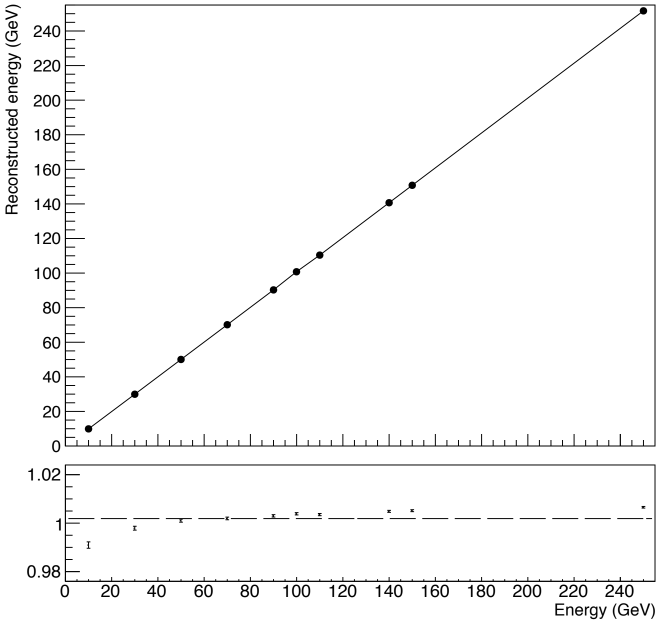

Figure 3.16: Reconstructed energy for electrons in the 10-250 GeV energy range *vs.* the beam energy.

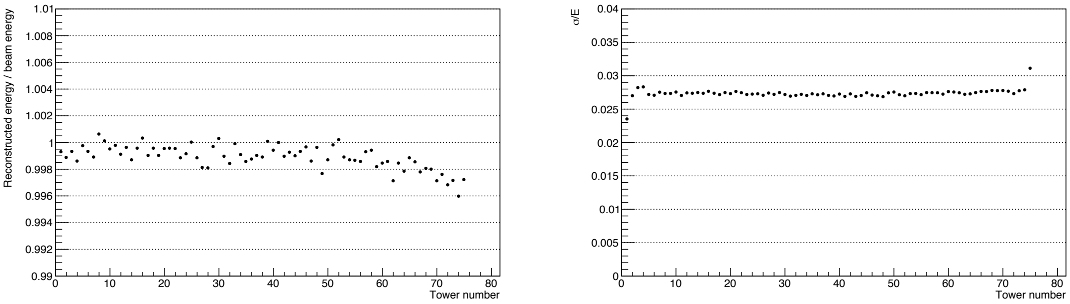

Figure 3.17: Average reconstructed energy, for 40 GeV electrons, divided by the beam energy *vs.* the tower number (left) and corresponding resolution *vs.* the tower number (right).

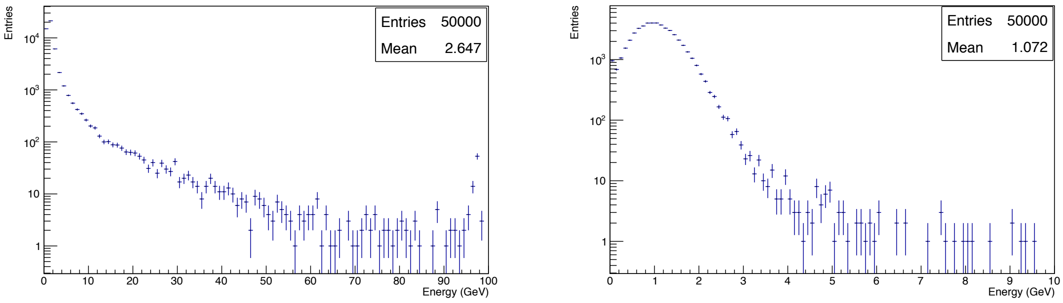

Figure 3.18: Kinetic energy of particles escaping the calorimeter outer surface. All particles (left) and neutrino particles only (right).

The first step is to study the containment. Fig. 3.18 shows the kinetic energy distribution of all particles escaping the calorimeter outer surface (left) and the contribution from neutrinos (right) for 100 GeV primary particles. The long tail, belonging to high-leakage events, ends with a peak that corresponds roughly to the total amount of energy. This punch-through events arise from primary pions travelling all the calorimeter long without inducing any nuclear reaction, hence they resemble *mips*.

To study the calorimeter performance for charged hadrons, we selected events with a kinetic energy carried by escaping particles below the cuts given in Tab. 3.1. They lead to an average energy containment of $\simeq 98.8\%$ almost independent of the primary particle energy in the energy range considered. The cut leads to a rejection of $\simeq 10 - 15\%$ of the events depending on the primary particle energy considered.

Fig. 3.19 shows the reconstructed energy for 100 GeV π^- when the calibration described in Sec. 3.2 is applied to the scintillation and the Cherenkov signals, left and right plots respectively.

Primary particle energy (GeV)	Cut (GeV)
$E \leq 12$	0.5
$12 < E \leq 50$	1.0
$E > 50$	3.0

Table 3.1: Cuts applied for hadron event selection.

They follow Eqs. 3.24, 3.25 with (h/e) weighting the different degree of non com-

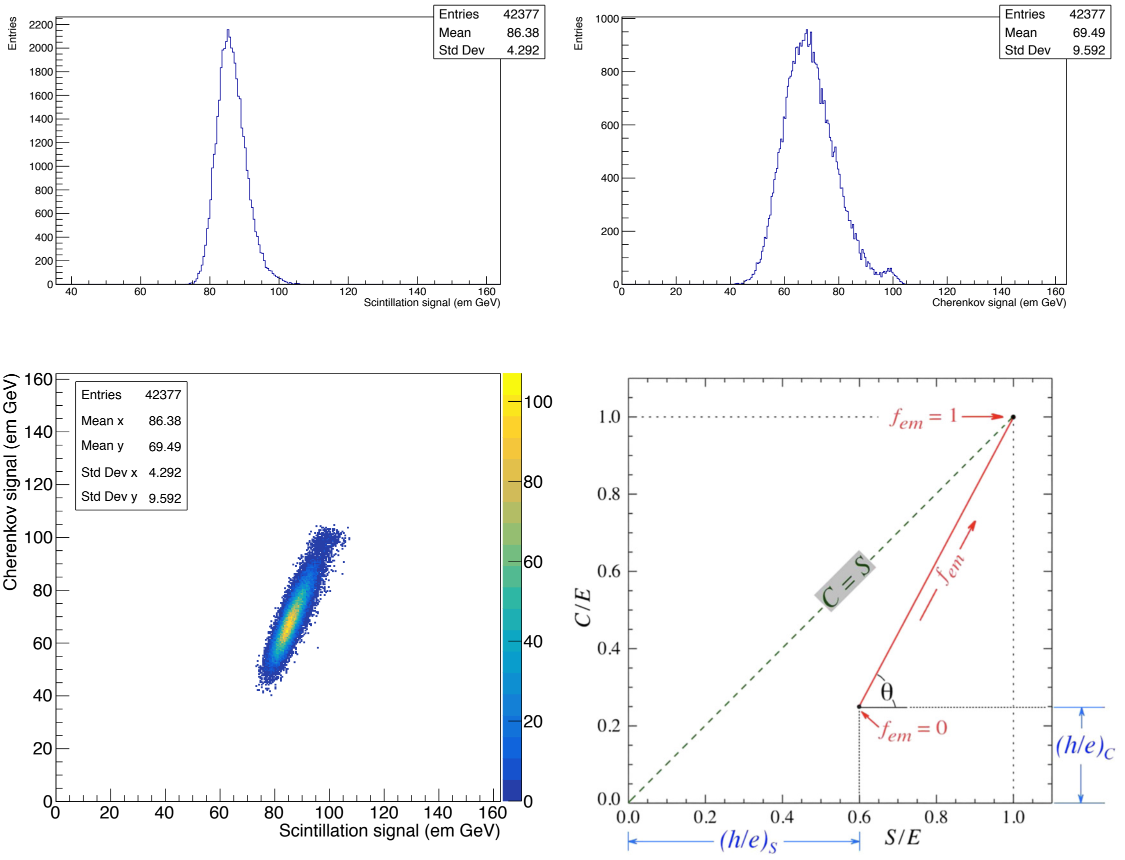

Figure 3.19: Reconstructed energy for 100 GeV π^- when the calibration at the electromagnetic scale is applied to the scintillation (up left) and the Cherenkov signal (up right). Scatter plot of the two variables (bottom left). Graphical representation of Eqs. 3.24, 3.25 (bottom right).

pensation of the two signals.

$$S = E[f_{em} + \big(h/e\big)_S \cdot (1 - f_{em})] \tag{3.24}$$

$$C = E[f_{em} + \big(h/e\big)_C \cdot (1 - f_{em})] \tag{3.25}$$

Both $\big(h/e\big)$ values are < 1, hence the two signals are undercompensating and the average reconstructed energy is below the true one. This also explains the signal correlation. The intrinsic asymmetric shape of the f_{em} distribution is the origin of the asymmetric reconstructed energies. Especially for the Cherenkov signal, it is possible to notice a bump around 100 GeV in the reconstructed energy distributions. In our understanding, it corresponds to events with very-high f_{em} values such as the events undergoing the charge exchange process ($\pi^- + p \rightarrow \pi^0 + n$).

As explained in Chap. 2, the correct energy is given by

$$E = \frac{S - \chi C}{1 - \chi} \tag{3.26}$$

with

$$\chi = \frac{1 - (h/e)_s}{1 - (h/e)_c} \tag{3.27}$$

Let now estimate the χ factor with simulations. By using Eq. 3.26 and knowing E it is possible to estimate χ on an event-by-event basis. Fig. 3.20 shows the χ factor distribution for 100 GeV π^-. We estimate the χ factor as the distribution most probable value.

A second method to estimate the χ factor is based on the estimation of both h/e values. For an overview of the methods to measure the the h/e values see Chap. 2. In our case, we accessed the f_{em} value on an event-by-event basis via the Monte Carlo truth information, and by selecting events belonging to given f_{em} values, we plotted S/E and C/E as a function of the electromagnetic fraction. Then, h/e values are then the only free, unknown, parameters of Eqs. 3.28, 3.29 and can be extracted with a fit to data.

$$S/E = f_{em} \cdot (1 - \left(h/e\right)_S) + \left(h/e\right)_S \tag{3.28}$$

$$C/E = f_{em} \cdot (1 - \left(h/e\right)_C) + \left(h/e\right)_C \tag{3.29}$$

Fig. 3.21 shows the profile of S/E and C/E as a function of f_{em} for 100 GeV π^-. As expected, the fitted functions cross at $f_{em} = 1$ for which they both correspond to 1 (a clear consequence of the calibration at the electromagnetic scale).

We report in Tab. 3.2 the χ factor values estimated with the two methods. It is important to underline that both methods estimate the χ factor as the one that gives on average the correct contained energy for hadrons and they do not rely on any energy resolution optimization. The two methods are consistent and show a further important feature of dual-readout calorimetry: *the χ factor is independent on the primary particle energy.* This is one of the two requirements for the χ factor universality. It is important to notice that for a proper validation of the hadronic results a full-containment dual-readout calorimeter, possibly copper-based and with a sampling fraction at least compatible with the one simulated here, is needed. As said in Chap. 2, building such a detector is one of the main goals of the IDEA Collaboration.

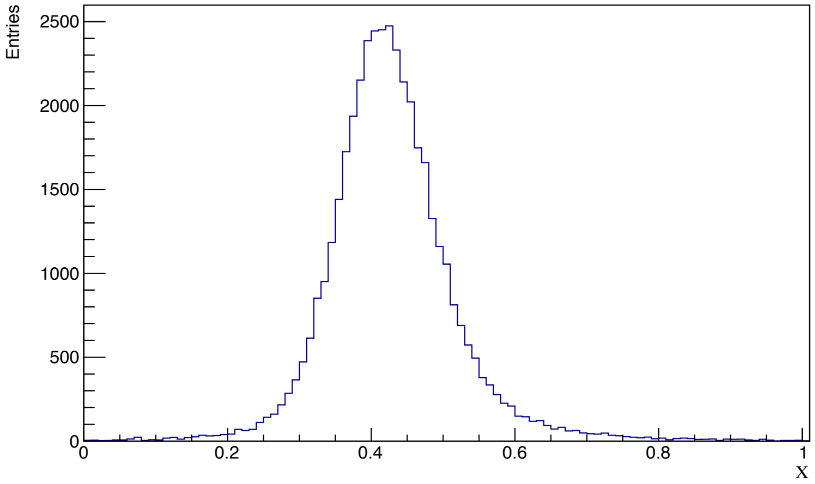

Figure 3.20: χ factor distribution for 100 GeV π^-.

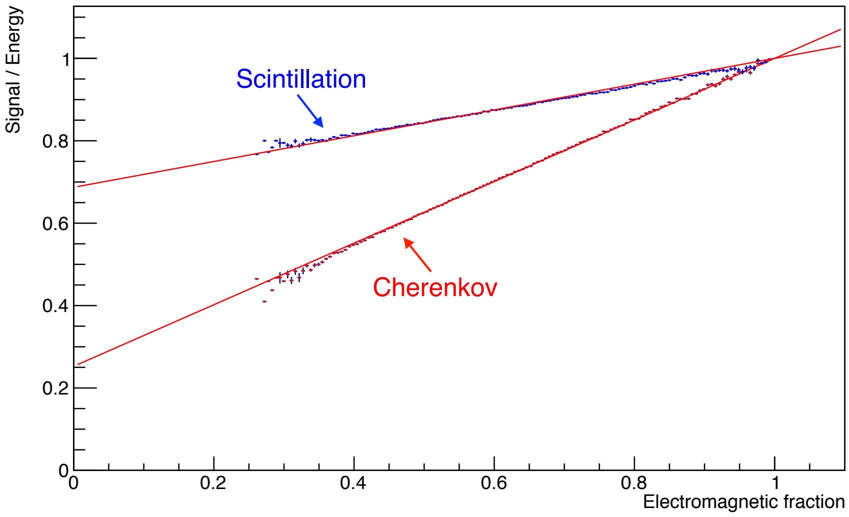

Figure 3.21: Profile of S/E (blue dots) and C/E (red dots) as a function of f_{em}, result for 100 GeV π^-.

	Method 2				Method 1	
Energy (GeV)	$(h/e)_S \pm 0.001$	$(h/e)_C \pm 0.001$	χ	δ	χ	δ
10	0.706	0.257	0.396	± 0.002	0.40	± 0.03
30	0.696	0.253	0.401	± 0.002	0.41	± 0.03
50	0.689	0.251	0.415	± 0.002	0.41	± 0.03
70	0.690	0.253	0.415	± 0.002	0.41	± 0.03
100	0.687	0.252	0.419	± 0.002	0.43	± 0.03
120	0.685	0.252	0.421	± 0.002	0.42	± 0.03
140	0.684	0.252	0.422	± 0.002	0.44	± 0.03
150	0.683	0.252	0.424	± 0.002	0.43	± 0.03

Table 3.2: χ factor values estimated with π^- simulations ranging from 10 to 150 GeV.

3.4.2 χ factor universality

The attractiveness of the dual-readout method relies on the universality of Eq. 3.26, meaning that it is possible to reconstruct energies in hadronic events, overcoming the non-compensation limits, *regardless* the hadron type and energy. It is a mandatory aspect to properly reconstruct jet energies for which several types of hadrons are simultaneously absorbed in a longitudinally unsegmented calorimeter. This feature is usually referred to as the χ factor universality.

We already saw that the χ factor does not depends on the π^- energies. Let now investigate the hadron-to-hadron differences. The best way is to look at the two signals, S and C, as in Fig. 3.19, because the χ factor is given by $\cot\theta$ of the fitted profile and any difference in the χ value would be spotted as a different inclination of the scatter plot profiles. Fig. 3.22 shows the scatter plot profiles for 100 GeV π^- (blue dots) and compares it to same energy k^- (pink dots), neutrons (green dots) and protons (red dots). It is evident how GEANT4 supports the assumption of a χ factor universality against the hadron type. This is a mandatory feature to any future simulation work. As a consequence, a single χ factor correctly gives, on average, the primary energy (excluding the leakage) for 100 GeV π^-, k^-, protons and neutrons, as plotted in Fig. 3.23.

Fig. 3.22 also shows an interesting feature. The events for which $f_{em} \simeq 1$ are highly suppressed for protons and neutrons with respect to the π^- ones. This is due to the baryon number conservation mechanism for which the possibility to exchange the close totality of the energy to a π^0 is forbidden (an explanation is given in Chap. 2).

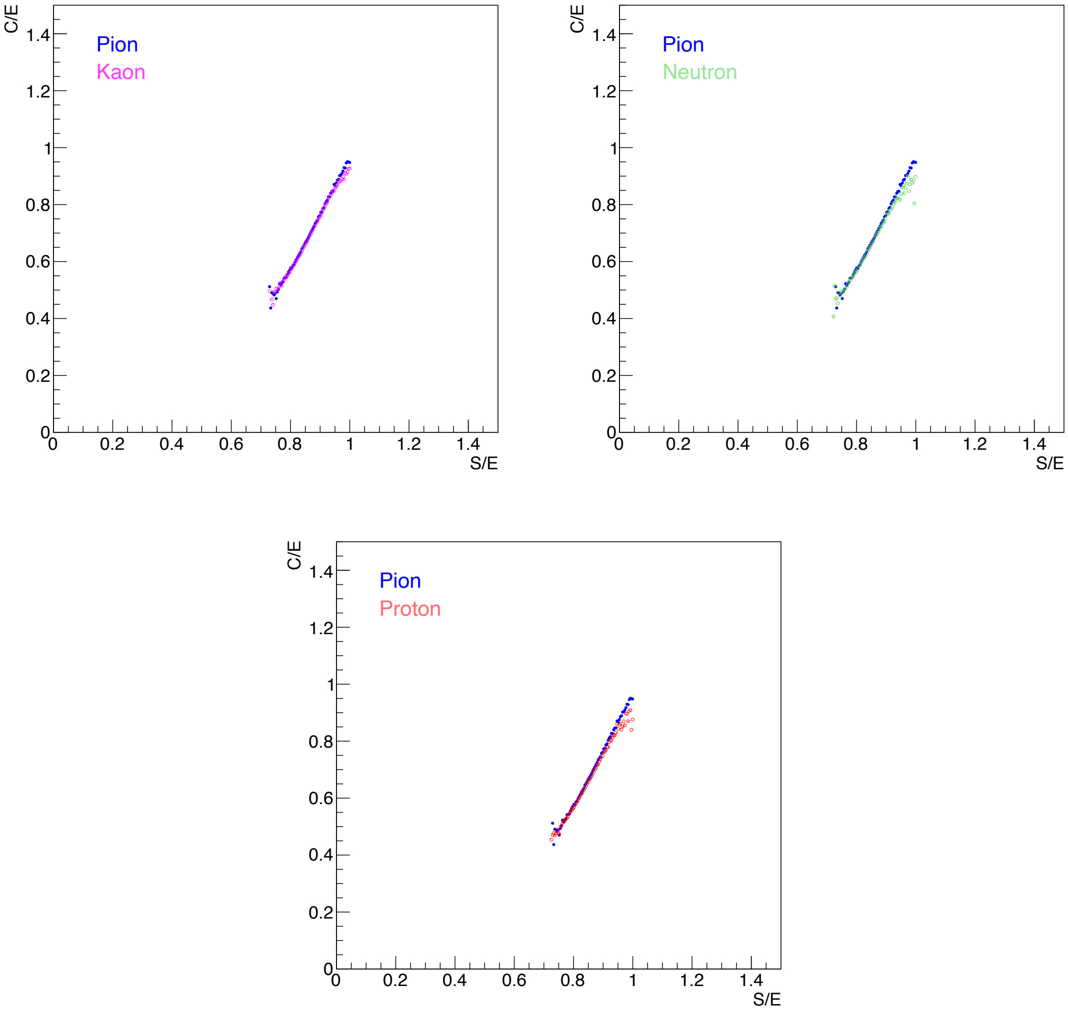

Figure 3.22: S/E *vs.* C/E scatter plots for 100 GeV π^- (blue dots), k^- (pink dots), neutrons (green dots) and protons (red dots).

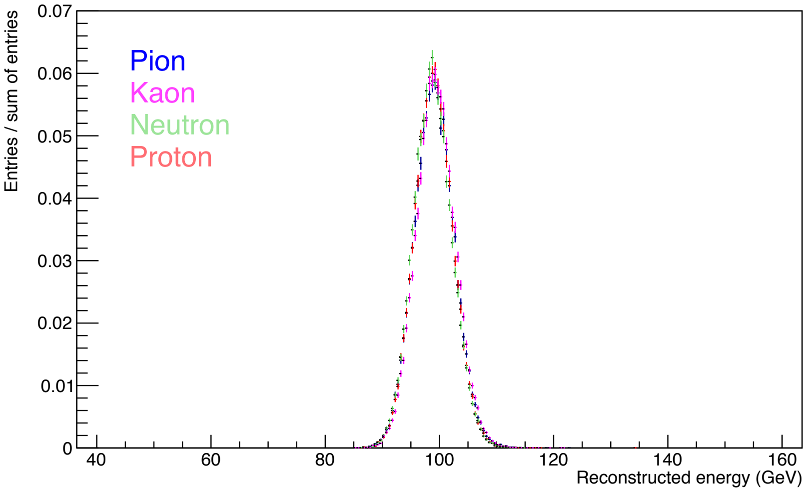

Figure 3.23: Reconstructed energy distribution with the same χ factor for 100 GeV π^- (blue), k^- (pink), neutrons (green) and protons (red). The energy has not been corrected for the hadronic energy containment of $\simeq 98.8\%$.

3.4.3 Energy resolution and linearity

We studied the hadron performance of the IDEA calorimeter by using the χ factor obtained as the one that correctly reconstruct on average the primary particle energy, $\chi = 0.41$. To take into account, on average, the energy loss by leakage, the reconstructed energies are boosted by 1%.
Fig. 3.24 shows the energy distribution for 100 GeV π^- (up) and the corresponding energy resolution in the range 10-150 GeV (bottom, black line). Here and in the following, pions are steered at the center of tower 1. The energy distribution asymmetric shape is completely restored by the dual-readout correction leading to a Gaussian distribution. When combining the signals we find an energy resolution for single hadrons of

$$\frac{\sigma}{E} = \frac{31\%}{\sqrt{E}} + 0.4\% \text{ or, } \frac{32\%}{\sqrt{E}} \oplus 1.3\% \tag{3.30}$$

with E expressed in GeV units.
Fig. 3.24 (bottom) also shows the energy resolution (σ/E) for the Cherenkov signal (red line) and the scintillation signal (blue line), a sensible improvement in the resolution is found above 10 GeV when the dual-readout method is applied. When comparing the resolutions it should be kept in mind that the average reconstructed signal in the S and C channels is always underestimated with respect to the dual-

readout corrected one and this has an impact on the σ/E values.

Another relevant advantage of the dual-readout method is the calorimeter linearity for hadron detection. Fig. 3.25 shows the average reconstructed energy *vs.* the true energy for charged π^- in the energy range $10-150$ GeV. By using a fixed χ factor it is indeed possible to reach a 1% linearity for hadron detection with no further corrections. This is another great advantage with respect to non-compensating calorimeters.

Tuning the χ factor We saw that GEANT4 reproduces all the main features of a dual-readout compensating calorimeter, *i.e.* a Gaussian response, a linear calorimeter for hadron detection and an excellent resolution. We investigated the impact of the χ factor on these features.

Fig. 3.26 shows the average reconstructed energy for 100 GeV π^- *vs.* the χ factor, the resolution *vs.* the χ factor and the reduced χ^2 of a Gaussian fit to the energy distribution *vs.* the χ factor. As previously found, the value that correctly returns on average the true energy with respect to the simulations is $\chi \simeq 0.41$. This is also close to the value leading to the most symmetrical distribution as confirmed by the minimal reduced χ^2 from a Gaussian fit to data.

Interestingly, the resolution (σ/E) reaches a minimum around $\chi \simeq 0.3$ where it is $\simeq 10\%$ smaller than the one found at $\chi = 0.41$. This feature must be confirmed by (new) test-beam data and, if confirmed, would leave room for improvement in the energy resolution by using a lower χ factor at the price of an average energy shifted towards lower values and a less symmetrical distribution.

3.4.4 Calibrating with hadrons

The method described before relies on signal calibration at the electromagnetic scale. We also explored the possibility of calibrating the dual-readout calorimeter with hadrons. The goal is to properly combine the C and S raw signals (p.e.), from π^- events, to reconstruct the primary energy. To do that, we used a Neural Network (NN) in which the input is a 2-nodes layer being fed with the S and C signals and the output is a single node layer outputting the primary particle energy. It is a regression problem.

The NN was built with the Keras library [92] and the optimal NN hyper-parameters have been selected with the Keras tuner. Tab. 3.3 summarizes the hyper-parameters defining the NN.

The training set was obtained by simulating 20k π^- events with the same beam setup described in Sec. 3.4.3 and a primary energy uniformly distributed in the range $3-200$ GeV. The events were selected according to cuts given in Tab. 3.1

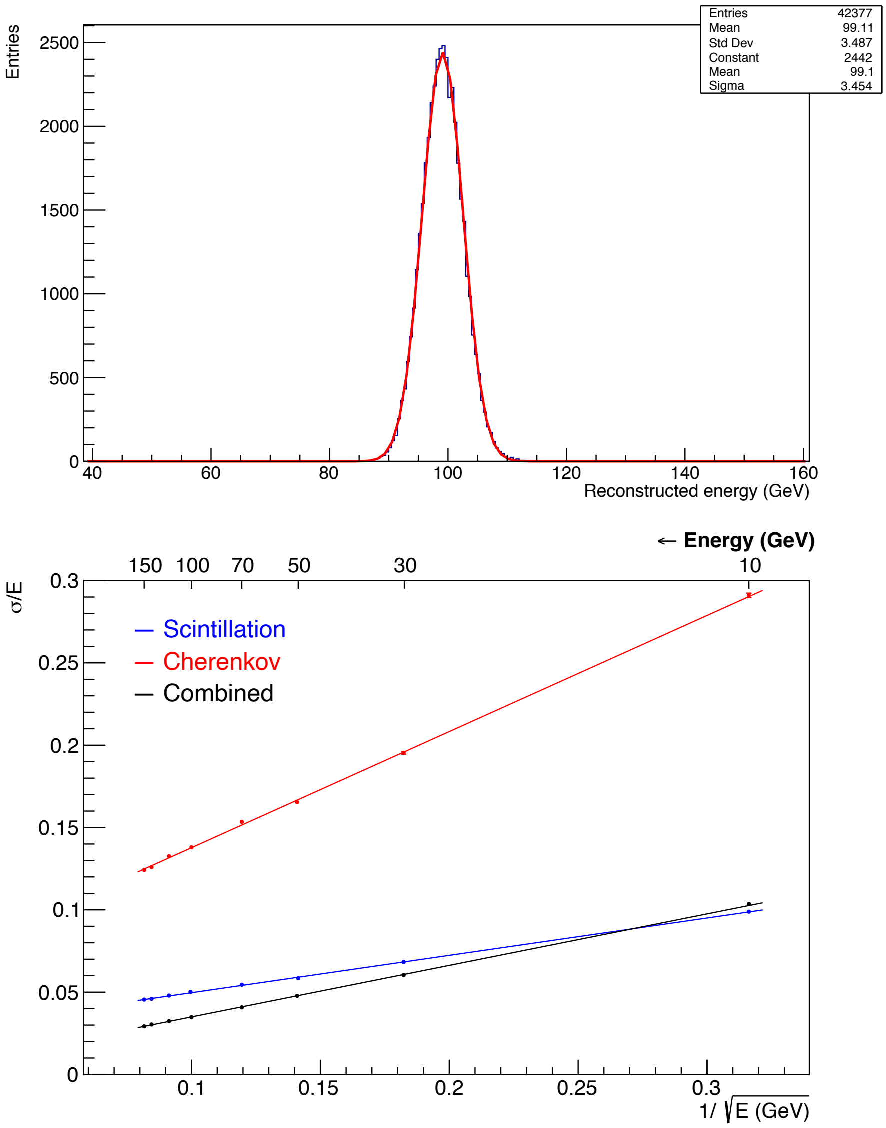

Figure 3.24: Reconstructed energy distribution for 100 GeV π^- (up) and fit to energy resolution points from 10 to 150 GeV (down).

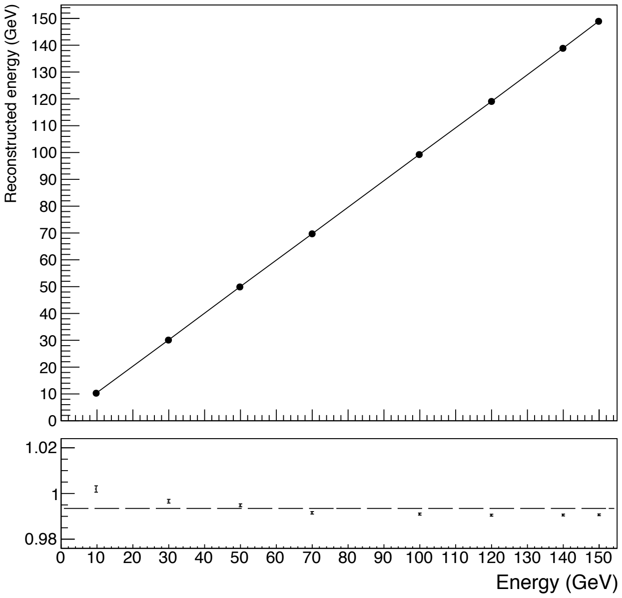

Figure 3.25: Linearity plot for 10 − 150 GeV π^- energies reconstructed with the dual-readout method.

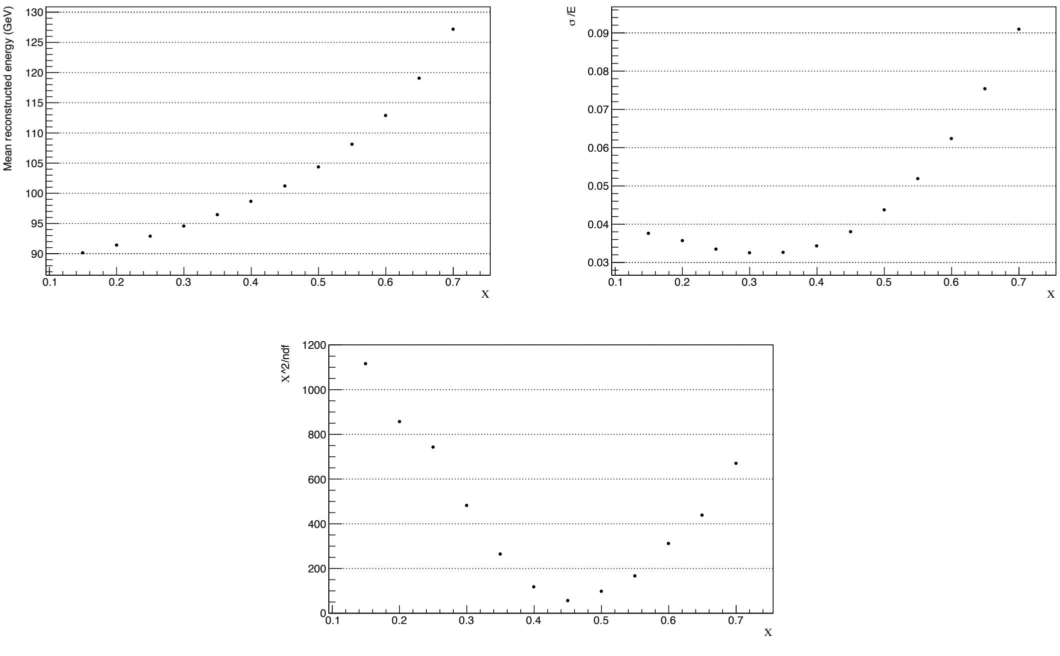

Figure 3.26: Average reconstructed energy *vs.* the χ factor, the resolution *vs.* the χ factor and the reduced χ^2 of the Gaussian fit to the energy distribution *vs.* the χ factor, for 100 GeV π^-.

Hidden layers (HL)	3
Nodes per HL	8
Activation function	Relu
Loss	Mean average error (MAE)
Optimizer	Adam
Learning rate	10^{-4}

Table 3.3: Hyper-parameters of the NN to reconstruct hadrons energies.

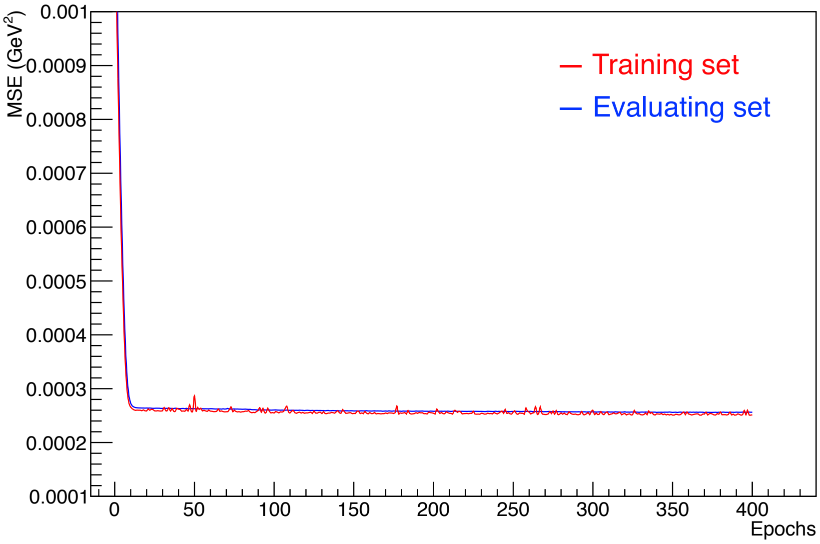

Figure 3.27: MSE of the NN prediction evaluated on the training set (red line) and the evaluating set (blue line) *vs.* the epochs.

and the resulting dataset was divided in a training set and an evaluating set equally populated. The NN was trained on the training set for 400 epochs and at each epoch its performance was evaluated on both the training and the evaluating set by means of the Mean Squared Error (MSE). Fig. 3.27 illustrates the MSE value per each training epoch for the training set (red line) and the evaluating set (blue line), showing no sign of overtraining. Fig. 3.28 shows the scatter plot of the fully trained NN prediction on the training set and the true energy values.

We evaluated the calorimeter hadronic performance when coupled to the NN. The same events described in Sec. 3.4.3 where used to feed the NN and the estimated energy was recorded at every event. Fig. 3.29 reports the reconstructed energy distribution for 100 GeV π^-. It can be directly compared to Fig. 3.24 as they belong to the same events. It is important to note that no calibration and no χ

factor has been used in the deep learning approach. Fig. 3.30 shows that with this new approach a 1% linearity for hadron detection is achieved with an energy resolution of

$$\frac{\sigma}{E} = \frac{26\%}{\sqrt{E}} + 0.6\% \text{ or, } \frac{28\%}{\sqrt{E}} \oplus 1.5\%, \tag{3.31}$$

with E expressed in GeV units. It turns out to be slightly better than the one obtained with the analytical approach.

3.5 Angle and position measurements

3.5.1 Event displays

One of the advantages of fibers is the possibility to increase the number of active elements up to very high values. In this simulated geometry we included $\sim 130 \times 10^6$ optical fibers equally divided in scintillating fibers and clear (Cherenkov) fibers. In the actual design of the IDEA concept each fiber is coupled to a dedicated SiPM. At the moment no signals grouping is considered but it might be added in future.

We investigated the average number of activated elements for e^- and π^- events at several energies. Fig. 3.31 shows the result for e^- and π^- (up and down, respectively) for the scintillating and Cherenkov signals (left and right, respectively). Results are shown for three cases: when all SiPMs are readout (black line), when a 1 p.e. threshold is applied, *i.e.* only SiPM with more than 1 p.e. are readout (blue line) and when a 2 p.e. threshold is applied (red line).

For both e^- and π^- the number of activated clear fibers is about half of the scintillation one, and for π^- the activated elements are roughly doubled with respect to e^-. Also, when applying a 1-p.e.-threshold readout the number of activated elements is reduced by $\simeq 30\%$.

This very high transverse granularity gives the possibility to sample showers with an unprecedented spatial resolution leading to some spectacular results. Fig. 3.32 shows the fiber-by-fiber event displays for the scintillation and Cherenkov signals (left and right, respectively), for 40 GeV e^-, π^0 and π^-. Few features should be noted here:

- In e^- induced events, very few fibers, typically 1 or 2, close to the shower axis, carry a large fraction of the integrated signal. This is true for both the scintillation and the Cherenkov signals and is more pronounced for the S channel.

  Electromagnetic showers are dictated by few processes that occur at every event with compatible intensities, hence they exhibit a typical common shape.

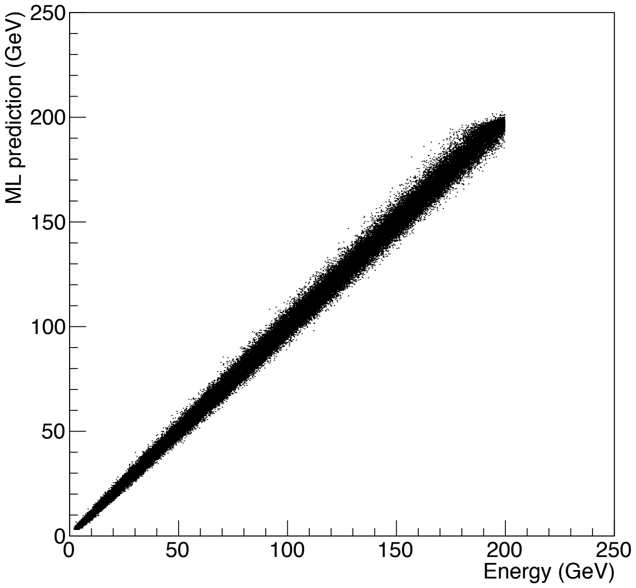

Figure 3.28: ML prediction *vs.* true energy for the evaluating set after 400 training epochs.

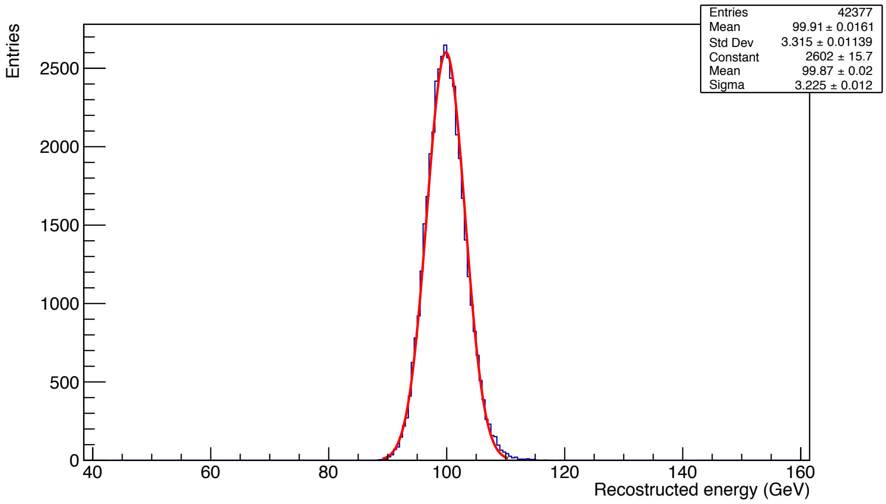

Figure 3.29: 100 GeV π^- energy distribution obtained with the NN.

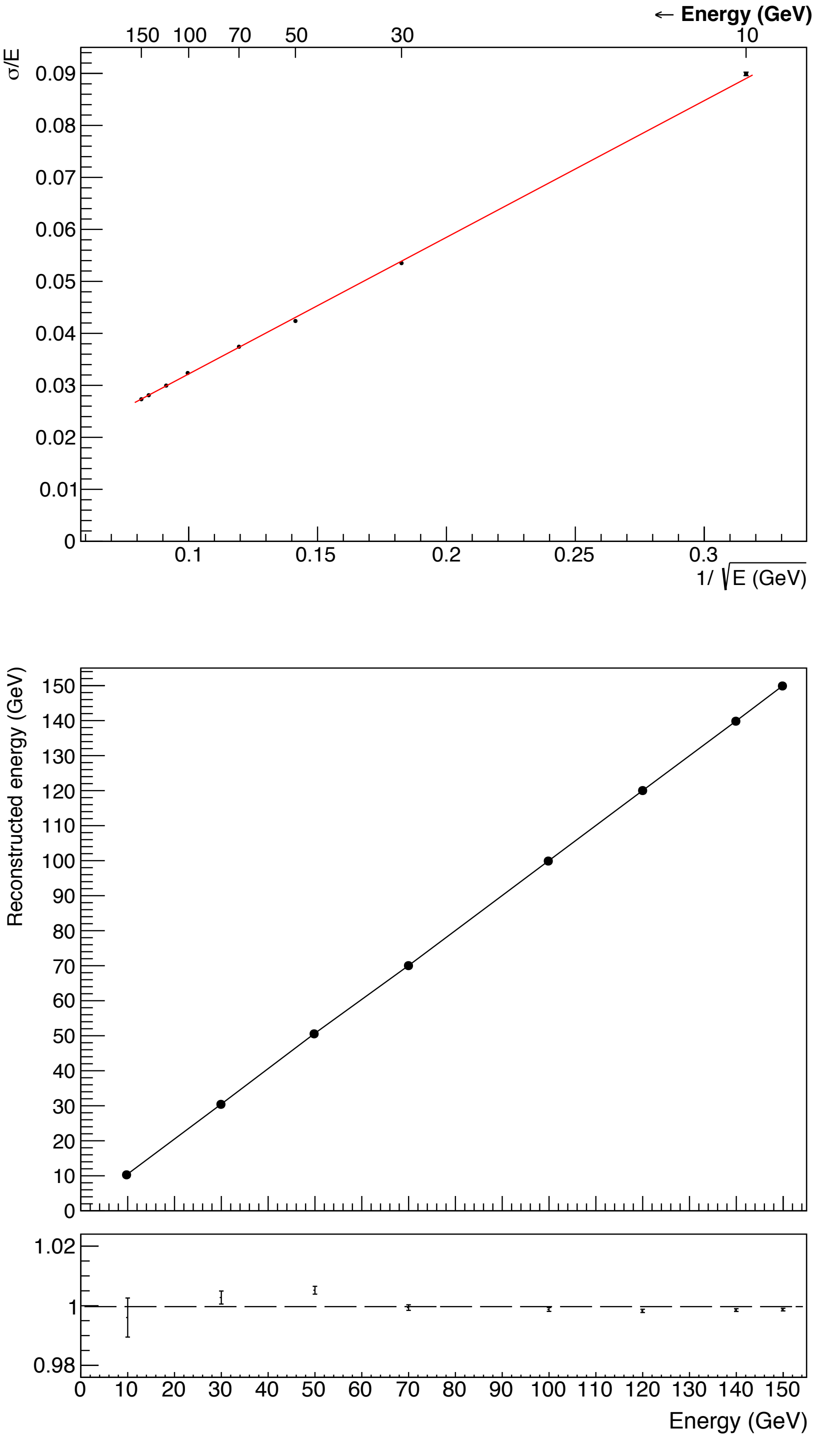

Figure 3.30: Energy resolution for 100 GeV π^- reconstructed with the deep learning approach (up) and corresponding linearity in the energy range 10-150 GeV (bottom).

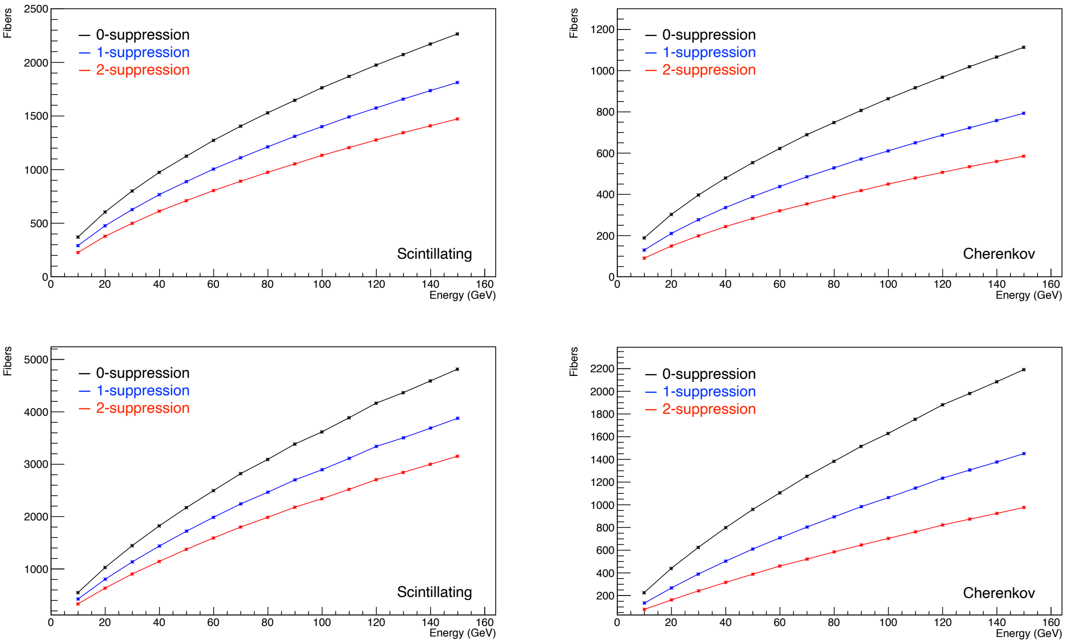

Figure 3.31: Average number of activated elements for e^- and π^- at several energies. Results for e^- and π^- (up and down, respectively), for the scintillating and Cherenkov signals, (left and right, respectively).

We investigated the electromagnetic shower containment by integrating signals within cones of changing ΔR. Fig. 3.33 shows the result for the scintillation and Cherenkov signals, left and right respectively, for 30 GeV (blue points) and 150 GeV (red points) e^-. As expected, the Molière radius, *i.e.* the radius integrating 90% of the energy deposit, does not depend on the particle energy and the average shower containment is almost identical at 30 and 150 GeV. Also, the scintillation signal exhibits a more peaked shower shape with respect to the Cherenkov signal: a cone with $\Delta R = 0.001$ integrates $\simeq 25\%$ of the S signals and $\simeq 20\%$ of the C signal. We will see in the next chapter how this feature has been verified on test-beam data.

- The extremely collimated nature of electromagnetic showers, coupled to this highly granular readout, opens the possibility to identify π^0 events by detecting two separated peaks inside the same shower.

- When sampling π^- induced showers, few straight lines arising from the central core and travelling towards the outer area are clearly detectable. Those signals come from low energy charged pions for which the probability of inducing a nuclear reaction is highly suppressed or impossible, hence they loose energy primarily by ionization. Relatively high energy deposits at the end of those tracks are also detectable as a result of the Bragg peak effect.

3.5.2 Angular resolution

This high traverse shower sampling is beneficial to resolve the shower barycenter position with great precision. In this fully projective calorimeter the X, Y and Z barycenter coordinates directly reveal the production angles of the primary particles, θ and ϕ. We studied the resolution on the angle measurements for e^- and π^- events, starting from the IP with a beam inclination of ($\theta = 91°$, $\phi = 1°$). Primary particles had energies ranging from 10 to 150 GeV.
Each fiber was linked to a (θ,ϕ) value and the barycenter coordinates were calculated as

$$\theta = \frac{\sum_i \theta_i S_i}{\sum_i S_i} \tag{3.32}$$

$$\phi = \frac{\sum_i \phi_i S_i}{\sum_i S_i} \tag{3.33}$$

with S_i being the signal (S or C). In this geometry the same strategy can be used to measure the shower barycenter position (x, y, z), for instance for the barycenter x position we have

$$x = \frac{\sum_i x_i S_i}{\sum_i S_i} \tag{3.34}$$

Let suppose to have a longitudinally unsegmented calorimeter divided in cells. Each cell energy deposit E_i has a relative precision σ_i/E_i. Given showers of energy E, this relative precision improves with $1/\sqrt{E}$, if the average shower profile is constant over E. Under this assumptions, all the terms in Eq. 3.34 have a relative precision that scales with $1/\sqrt{E}$ and the relative contributions of the individual terms to the sum are energy independent. Then it is fair to expect the position and angular resolution (σ) to scale with $1/\sqrt{E}$.
GEANT4 simulation are in good agreement with the expected prediction. Fig. 3.34 (left) shows the resolution on the θ angle for e^- events, expressed in mrad, *vs.* the energy. Fig. 3.34 (right) shows the resolution obtained when combining the signals ($\frac{C+S}{2}$). A fit scaling with $1/\sqrt{E}$ is in good agreement with data and suggests the

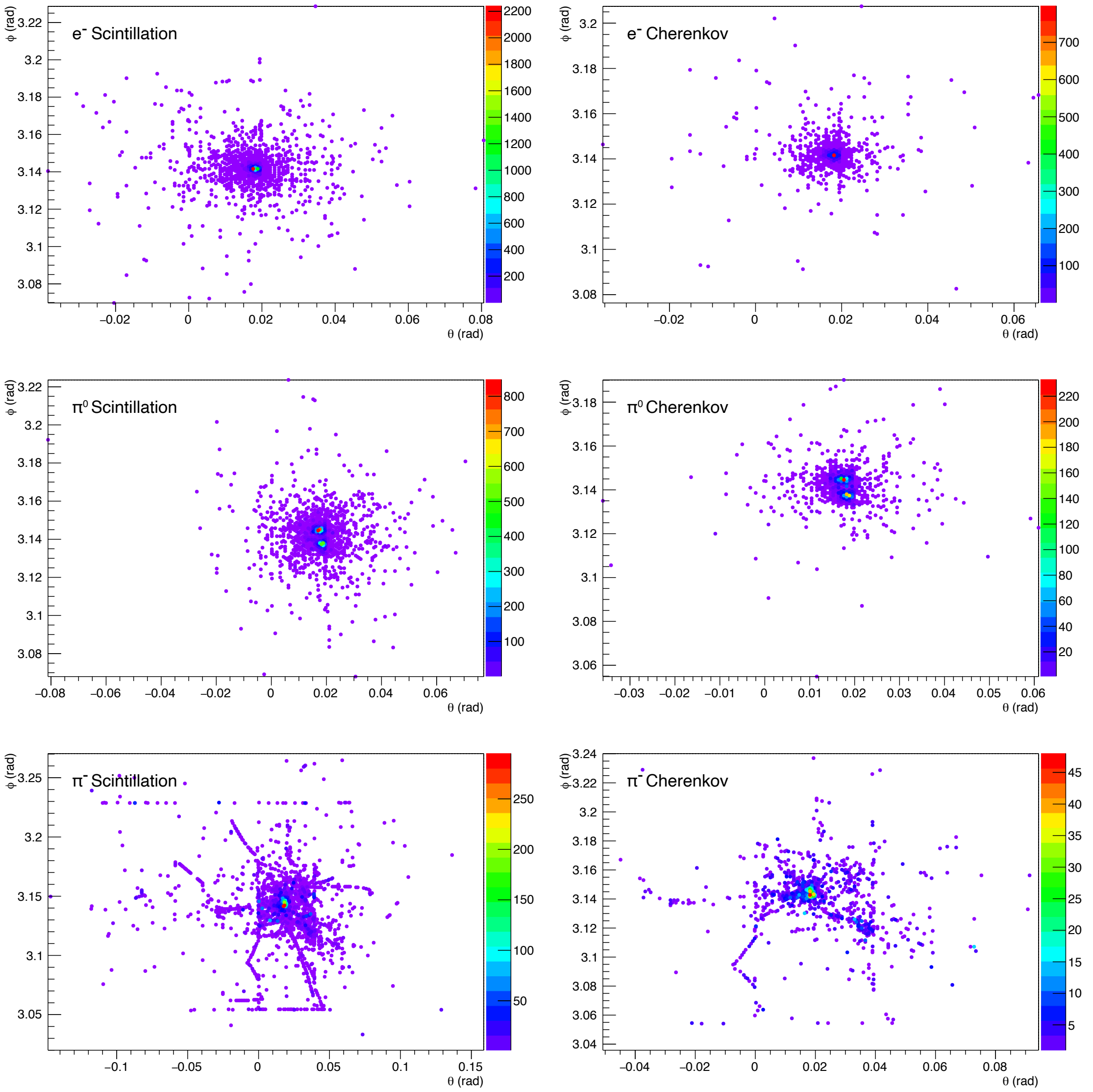

Figure 3.32: Event displays for 40 GeV e^- (upper plots), π^0 (central plots) and π^- (lower plots). Results for the scintillation and the Cherenkov signals, left and right, respectively. See text for details.

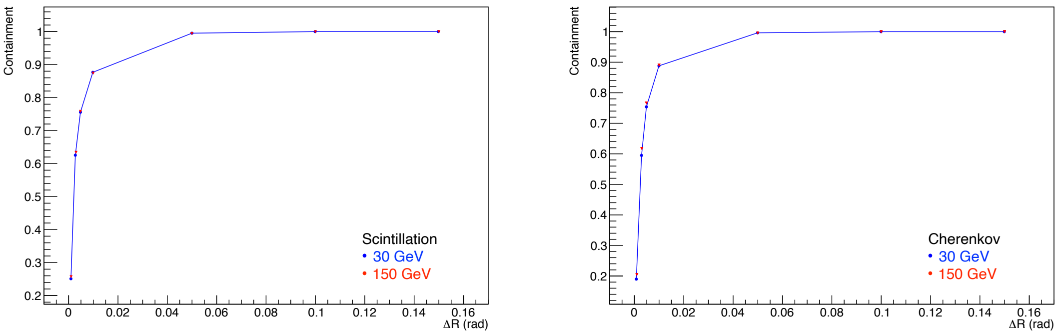

Figure 3.33: Signal containment *vs.* cone ΔR for showers induced by 30 GeV (blue points) and 150 GeV (red points) e^-. Results for scintillation and Cherenkov signals, left and right respectively. Results obtained with the beam setup described in Sec. 3.5.2.

following resolutions

$$\textbf{scintillation: } \sigma(\text{mrad}) = \frac{1.15}{\sqrt{E}} + 2.2\% \text{ or, } \frac{1.22}{\sqrt{E}} \oplus 6.1\% \tag{3.35}$$

$$\textbf{Cherenkov: } \sigma(\text{mrad}) = \frac{1.45}{\sqrt{E}} + 1.2\% \text{ or, } \frac{1.48}{\sqrt{E}} \oplus 4.9\% \tag{3.36}$$

$$\textbf{combined: } \sigma(\text{mrad}) = \frac{1.17}{\sqrt{E}} + 1.7\% \text{ or, } \frac{1.23}{\sqrt{E}} \oplus 5.4\% \tag{3.37}$$

with E expressed in GeV units. This exceptional resolution guarantees to resolve angles within $\simeq$ 1 mrad for e^- events already at 1 GeV energies. A compatible resolution is achievable for the ϕ angle. A very close performance is also predicted for γ events.

The combination of the signals does not lead to a sensible improvement in the resolution term with respect to the scintillation signal alone. This is due to a strong, expected, correlation between the two signals as they are sampling, on an event-by-event basis, the same shower shape, as confirmed by Fig. 3.35.

Hadronic shower shapes are unpredictable: *there is no such a thing as an hadronic shower shape*. The angular resolution on their barycenter is dominated by event-by-event fluctuations in the shower shape leading to an event-by-event barycenter shift. Fig. 3.36 (left) shows the angular resolution for π^- events for the barycenter θ angle obtained with the scintillation signal (blue points) and the Cherenkov signal (red points). For the Cherenkov signal the $1/\sqrt{E}$ scaling is not perfect and, at low energies, the S channel resolves better the shower position, while at 150 GeV the two

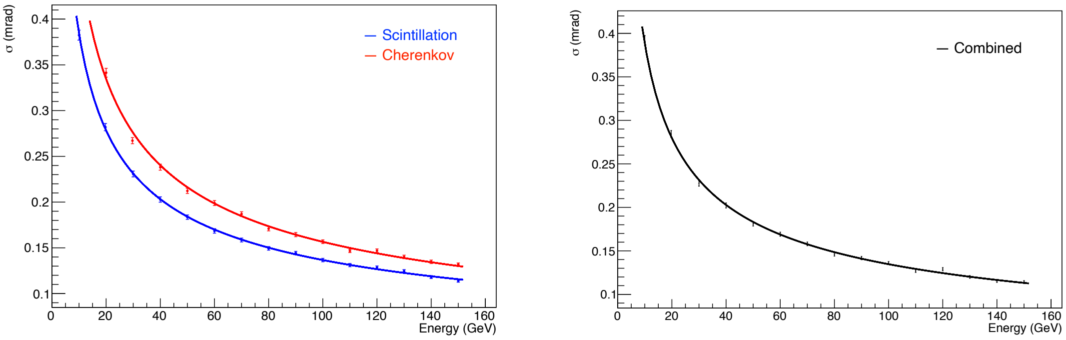

Figure 3.34: Angular resolution, σ (mrad), for e^- events in the energy range $10-150$ GeV. Result for the Cherenkov signal (red points), the scintillation signal (blue points) and their combination (black line).

resolutions become compatible. A possible explanation comes from the evolution of the shower composition with the energy. As the energy increases so does the f_{em}. Energy deposits of the electromagnetic component tend to be more collimated and close to shower axis with respect to the non-electromagnetic component. This has two effects: event-by-event fluctuations in the shower shapes are more and more suppressed and a greater fraction of the energy is localized close to the shower axis. Both effects improves the angular resolution. For the Cherenkov channel, being more sensitive to the f_{em}, this improvement is enhanced with respect to the scintillation channel. Fig. 3.36 (right) suggests the following angular resolution for π^- for the combined signals

$$\textbf{combined: } \sigma(\text{mrad}) = \frac{11.6}{\sqrt{E}} \tag{3.38}$$

with E expressed in GeV units.

3.6 Physics benchmarks

Detector requirements at future electron-positron circular colliders are dictated by the precision physics program envisaged at the high statistics Z pole, or while studying the final states opening up at the WW, ZH and $t\bar{t}$ thresholds. In Chap. 2 we showed the abundance of hadronic final states at future e^+e^- colliders. A hadronic jet consists (mostly) of pions, kaons, photons and protons. To properly reconstruct the four-momentum of the fragmenting parton each particle four-momentum must be accurately measured. The IDEA detector strategy to cope with this physic re-

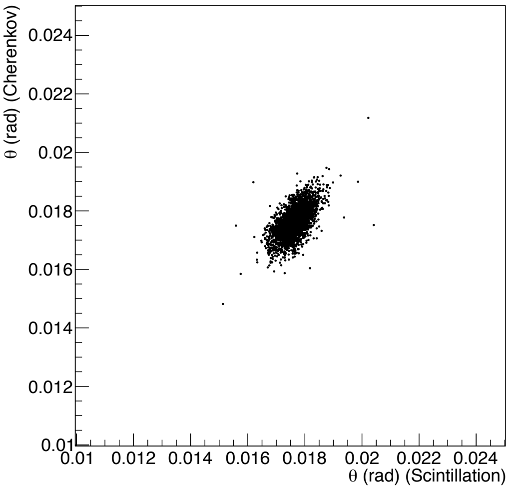

Figure 3.35: Scatter plot for the θ angle barycenter for 10 GeV e^- induced events measured with the scintillation and the Cherenkov signals independently.

quest is to fully absorb all the Standard-Model particles (but muons and neutrinos) in a device with an energy response approximately equal for all particle species.

This study represents the first attempt to investigate the IDEA calorimeter performance while reconstructing jet-final-states events, starting from the calibration at the electromagnetic scale till the reconstruction of heavy-boson invariant masses. To tackle all the steps for the first time, in a clear and viable way, the exercise is performed in a simplified setup with no budget material upstream the calorimeter and no magnetic field included. At present, jets are entirely reconstructed by means of the calorimeter information only and the potential gain of the combination with the IDEA tracker system is the first goal of future studies. We refer at these studies as the *calo only* results.

Events in the following are generated with the PYTHIA8 Monte Carlo generator [93], version 8.2. The quark hadronization is simulated according to the *tune-3* built-in option for which the jet substructure is parameterized on LEP data. Stable final states are used to feed the GEANT4 simulation described before through a dedicated (HEPMC format) event reader.

3.6.1 Jet reconstruction

Future circular electron-positron colliders will provide high statistics samples of $e^+e^- \rightarrow Z^*/\gamma \rightarrow jj$ events at several center-of-mass-energies (E_{CM}), resulting in

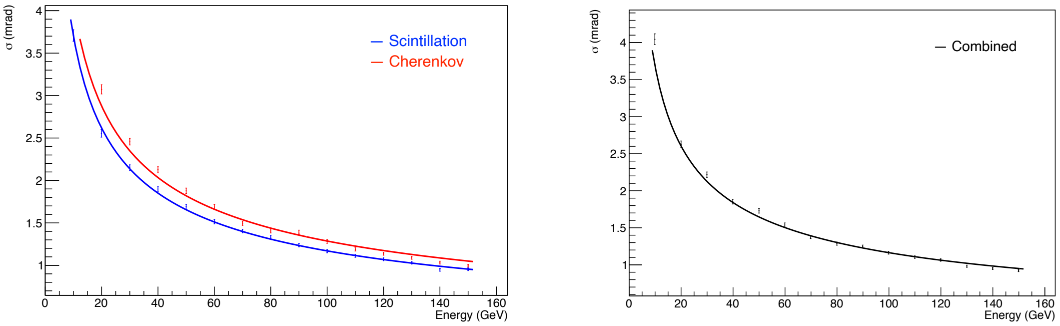

Figure 3.36: Angular resolution, σ (mrad), for π^- events in the energy range $10-150$ GeV. Results for the Cherenkov signal (red points), the scintillation signal (blue points) and their combination (black line).

events with two back-to-back jets with energy approximately equal to $E_{CM}/2 = E_{nom}$. We started from this process. Fig. 3.37 shows a display for such an event at $E_{CM} = 90$ GeV, depicted are the raw signals (*p.e.*) for the scintillation and the Cherenkov channels, left and right respectively. The up plots are event displays considering the calorimeter tower granularity, *i.e.* each entry corresponds to the (θ, ϕ) region of a single tower. The bottom plots show the same event display while sampled with the fiber granularity, *i.e.* each entry corresponds to the signal carried by a single fiber. In the following, we will consider jets as reconstructed with the tower granularity only and room for improvement is left for a more complex reconstruction dealing with the fiber-by-fiber information.

For each tower, we build a 4-vector with the direction obtained by linking the geometrical center of the tower to the IP, the energy is the one provided by the signal calibrated at the electromagnetic scale and the mass is set to zero. We neglected towers for which the energy deposition measured at the electromagnetic scale is below 10 MeV. The 4-vectors are used as input to the FASTJET package [94], version 3.3.2. The role of FASTJET is to provide a set of methods to cluster the input and return the 4-momentum of the primary parton(s). It provides implementation of clustering algorithms in spherical coordinates specifically for e^+e^- collisions. In particular, for the generalized k_t algorithm for e^+e^- collisions (*eegen_kt*), for each 4-momentum pair (i,j), it defines two distances

$$d_{ij} = \min\left(E_i^{2p}, E_j^{2p}\right)\frac{1-\cos\theta}{1-\cos R} \tag{3.39}$$

$$d_{iB} = E_i^{2p} \tag{3.40}$$

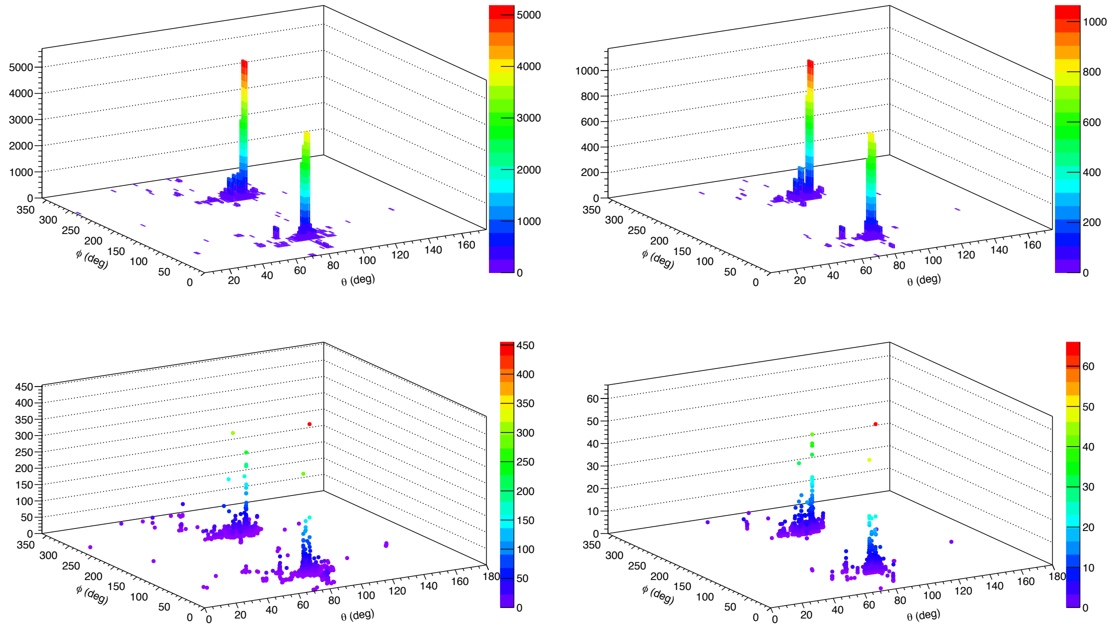

Figure 3.37: $e^+e^- \to Z^*/\gamma \to jj$ at $E_{CM} = 90$ GeV event display from the IDEA calorimeter. Depicted are raw signals (p.e.) for the scintillation signal (left) and the Cherenkov signal (right). Results obtained with the tower granularity (up) and the fiber granularity (down).

for p general value and $0 < R < 3\pi$. At any point in the clustering process, one identifies the smallest of d_{ij} and d_{iB}. In the *inclusive* version the clustering proceeds as follows.

- In case the smallest is a d_{ij}, one replaces i and j with a new object with momentum $p_i + p_j$, otherwise, if it is a d_{iB}, i is classified as inclusive jet and removed from the 4-momentum list. The clustering then continues until no 4-momenta remain. Of the final jets, generally only those above a given E value are actually used as the event jets. For values of $R < \pi$ and $p = -1$, the inclusive algorithm provides an infrared and collinear safe way of obtaining a cone-like algorithm for e^+e^- events, because hard separated jets have a circular profile on a sphere, with opening angle R. For $R > \pi$, the denominator of Eq. 3.39 $(1 - \cos R)$ is replaced with $(3 + \cos R)$. The only time a d_{ib} is relevant then is when there is only a single 4-vector in the event and the algorithm would return a single jet consisting of all particles in the event.

The *exclusive* version of the algorithm proceeds instead as follows.

- Again, if the smallest distance is a d_{ij}, i and j are replaced by a new object with momentum $p_i + p_j$. In the case the smallest distance is instead a d_{iB}, i is classified as part of the "beam" jet and discarded. The process continues until all d_{ij} and d_{iB} are above a certain threshold or, alternatively, until it reaches a configuration with a predetermined number of final jets. Also for the exclusive algorithm, if $R > \pi$, the denominator of Eq. 3.39 is replaced with $(3 + \cos R)$. In this way, the exclusive algorithm does not classify any 4-momentum as part of the "beam" jet, since the smallest distance is always a d_{ij}. Unlike the inclusive one, the exclusive algorithm provides non trivial information also in this case, since the clustering stops when all the d_ij are above a certain d_{cut} or an *ad hoc* number of jets is found, avoiding that all the 4-momenta in the event are clustered in a single jet.

We use the generalized k_t algorithm with $R = 2\pi$ and $p = 1$ and force the number of jets to two. Note that with these parameters the clustering sequence is identical to the one often referred to as the Durham algorithm, for which a single distance between 4-momentum pairs is calculate as $d_{ij} = 2\min\left(E_i^2, E_j^2\right)(1 - \cos\theta)$ and exclusive jets are extracted. The normalization of d_{ij}, however, remains different.
When reconstructing jets with a dual-readout calorimeter, an additional level of information is provided. The calorimeter produces, for each jet, two independent set of 4-momenta, one for the scintillation signal and one for the Cherenkov signal. After the clustering process on the signals induced by a single jet, two reconstructed jets are thus obtained, j_s and j_c, respectively for the scintillation and the Cherenkov signals. To exploit the dual-readout method, one has to properly match the j_s and j_c coming from the same jet. We developed from scratch two methods to perform the jet matching, as explained in the following. To estimate the impact of the detector energy resolution on the jet measurements, the two methods also perform (in different ways) the association of the reconstructed jets, j_r, after the jet matching, with the "truth" jets, j_t, *i.e.* the jets obtained by clustering the 4-momenta from stable particles provided by the event generator.

Method 1 Jets are built separately on the scintillation and the Cherenkov signals. Scintillation and Cherenkov jets are later associated by means of the minimal ΔR. Matched jets are merged to form a single reconstructed jet, j_r, according to Eq. 3.26, *i.e.*

$$P_x^r = \frac{P_x^s + \chi \cdot P_x^c}{1 - \chi} \tag{3.41}$$

$$P_y^r = \frac{P_y^s + \chi \cdot P_y^c}{1 - \chi} \tag{3.42}$$

$$P_z^r = \frac{P_z^s + \chi \cdot P_z^c}{1 - \chi} \tag{3.43}$$

$$E^r = \frac{E^s + \chi \cdot E^c}{1 - \chi} \tag{3.44}$$

Truth jets (j_t) are built by applying the same jet reconstruction algorithm on the truth particles which are fully absorbed in the calorimeter (*i.e.* excluding muons and neutrinos) and are within $|\eta| < 5$. To couple the reconstructed jets to the truth jets, we use again a nearest ΔR algorithm.

Method 2 Both the calibrated scintillator cells and the calibrated Cherenkov cells are added to the FASTJET input vector, with a label allowing the separation *a posteriori* of the two types of cells. In addition, all of the truth particles fully depositing their energy in the calorimeter are added to the input vector, but as *ghost particles*, *i.e.* particles which are geometrically associated to the jet, but do not influence the association algorithm. The clustering algorithm is run knowing that, for each jet, FASTJET allows the user to access the list of components which are the elements of the input vector associated to the jet. A loop is performed on the components of each jet, and we separately sum the 4-vectors of the scintillator, Cherenkov and truth components. Out of each jet in output from FASTJET, we build three jets, a scintillator jet, a Cherenkov jet and a truth jet. Eventually, the reconstructed jet (j_r) is built by combining each of the components of the scintillator and the Cherenkov jet using Eqs. 3.41-3.44.

Event cleaning Before studying the jet calibration and the calorimeter energy reconstruction performance, we need to select jets such that all of the particles contributing to the jets are fully or, at least, largely absorbed in the calorimeter. We define therefore the following cleaning cuts:

- reject events containing muons or neutrinos among the final states passed to GEANT4,
- require that the pseudorapidity of each of the two jets is within $|\eta| < 2$ to ensure a good lateral containment,

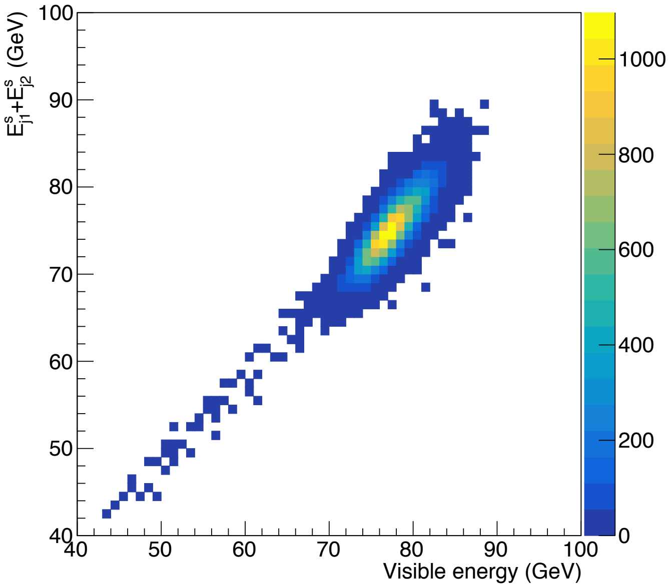

Figure 3.38: Correlation between the energy deposition in the calorimeter (from GEANT4), and the sum of the energies measured in the scintillating fibers at $E_{CM} =$ 90 GeV. E^s_{j1} and E^c_{j2} refer to the energy measured with the scintillation signal only for the first and the second reconstructed jets, respectively.

- reject events in which the kinetic energy carried by escaping particles (except neutrinos) from the back of the calorimeter is in excess of 0.1 GeV. The cut value was chosen by studying the spectrum of the particles escaping the calorimeter from the back as provided by GEANT4,
- reject events where the sum of the energies measured by the scintillating fibers is below a fixed value, dependent on the center-of-mass energy.

The last cut is justified by the fact that we want to exclude the small fraction of events where the total visible energy deposited into the calorimeter is too small compared to the sum of the energies of the particles being absorbed into it. The visible energy deposited in the calorimeter is provided as an output of the GEANT simulation, and it is found to have a very good correlation with the total energy as measured by the scintillating fibers calibrated at the electromagnetic scale, as shown in Fig. 3.38. The value of the cut on the total energy measured in the scintillating fibers is evaluated by visual inspection of the distribution for each of the benchmark energies, and is located at approximately 5 sigmas below the peak in the distribution.

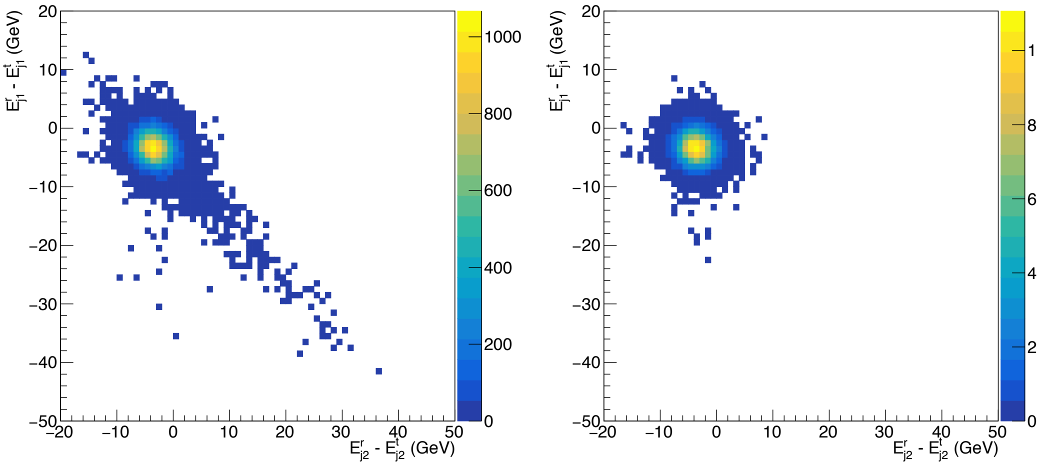

Figure 3.39: Difference between reconstructed and true energy for the first jet, versus the same difference for the second jet. Left side: first reconstruction method, right side: second reconstruction method. See text for details.

To compare the two methods and, in particular, their capability of matching truth jets with reconstructed jets, we evaluated the quantity $(E^r_{j2} - E^t_{j2})$ *vs.* $(E^r_{j1} - E^t_{j1})$ at $E_{CM} = 90$ GeV. Fig. 3.39 shows the result for the first method (left) and the second method (right). For the first method, a non negligible population of events is observed where the assignment of energy between jets is different for calorimeter and truth particles, pointing to a problem with the algorithm for associating truth jets to reconstructed jets. The second algorithm solves this issue and we will use it in the following as default for jet reconstruction.

3.6.2 Jet calibration and resolution

The calibration ansatz for jet energy measurements is Eq. 3.44. With the appropriate choice of χ, it allows the correct reconstruction of jet energies, by compensating for the fluctuations in the electromagnetic component of jet induced showering. To evaluate the jet calibration, six benchmark samples are used, each comprising 60k events, by requiring the production of a Z^*/γ decaying into two quarks with flavors u, d, s, c, for six different values of the center-of-mass energy of the accelerator: 30, 50, 70, 90, 150 and 250 GeV. For each energy, we build the distribution $E^r_j - E^t_j$, on both jets, for all the events passing the cleaning cuts. This is done for different values of χ ($\chi = 0.2, 0.3, 0.41, 0.42, 0.43, 0.445, 0.5$). We perform a gaussian fit on the distribution and take the mean value of the fit. This will be in general different from zero, except for a value of χ, and dependent on E_{nom}, half of the center-of-mass

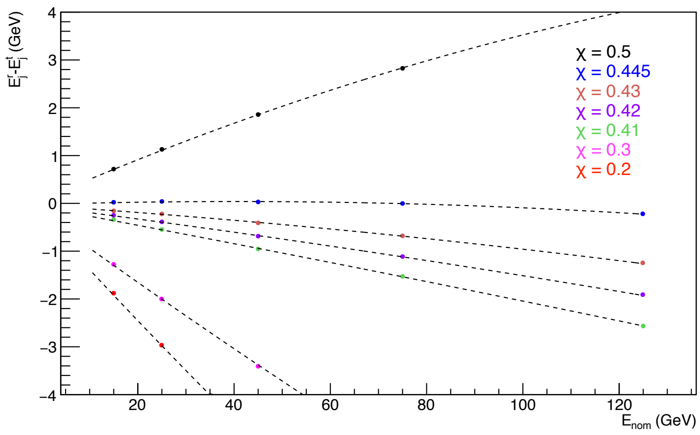

Figure 3.40: Gaussian means of the difference between the measured jet energy E_j^r and the true jet energy E_j^t as a function E_{nom} for different values of χ.

energy. The gaussian means as a function of E_{nom} are shown for the seven values of χ in Fig. 3.40.
We observe that in the range of $\chi = 0.41 - 0.43$, the one obtained with single π^-, the calorimeter exhibits a linear response for jet energy measurements, whereas it overestimates the energy for higher values and it underestimates it for lower values. In particular, for $\chi = 0.43$ it achieves a 1% linearity for jet detection in the jet energy range $10 - 125$ GeV. The best jet linearity is obtained with $\chi = 0.445$ for which the calorimeter is 0.2% linear in the energy range considered. This is only possible thanks to two things:

- the χ factor universality for which the dual-readout correction is the same for any hadron type and,
- the compensation for the electromagnetic fraction of the jet showers.

That is the beauty of dual-readout calorimetry, making possible to calibrate the calorimeter cells with electrons and estimating the χ factor with single π^-, both things that can be done at test-beam level, and yet correctly reconstruct the jet energies while compensating for the main source of energy fluctuation and non-linearity.
To evaluate the energy resolution, we build the distribution of $(E_j^r - E_j^t)/E_j^t$, obtained with $\chi = 0.43$, and we perform a gaussian fit on it. The sigma of the fitted gaussian is taken as an estimator of the jet energy resolution. The measured relative resolution as a function of the reciprocal of the square root of the jet nominal energy is shown

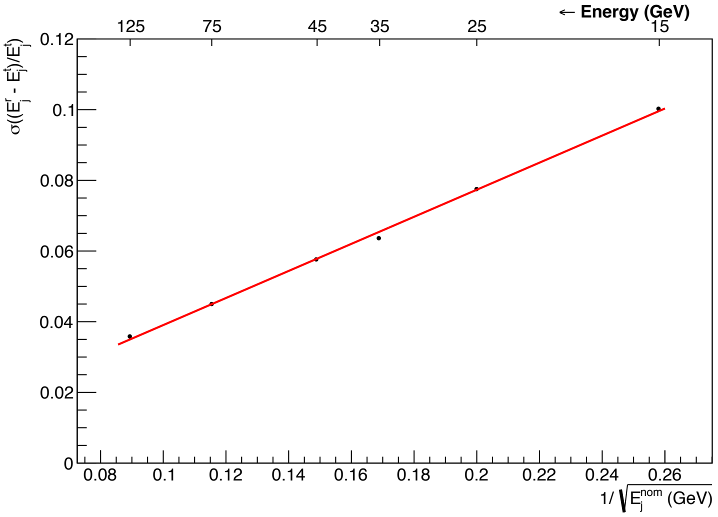

Figure 3.41: Energy resolution on the 2-jet energy measurement as a function of the reciprocal of the square root of the nominal jet energy.

in Fig. 3.41. A linear fit to data suggests a resolution compatible with

$$\frac{\sigma}{E} = \frac{38\%}{\sqrt{E}} \tag{3.45}$$

with E expressed in GeV units.

Another great benefit of the dual-readout correction is evident if we look at the distributions of $(E_j^r - E_j^t)/E_j^t$ for the six center-of-mass energies considered, Fig. 3.42. Namely the fact that jet energy distributions are well fitted with a symmetrical function with negligible non-symmetrical tails.

3.6.3 Analysis of physics events

The calibration procedure developed in the previous sections was applied to physics events where bosonic resonances decade into two jets, and the beam energy constraints cannot be used to constrain the energy of the jets.

Three different benchmark processes were addressed, each providing a final state signature with one boson decaying into a final state either invisible, or releasing minimal energy into the calorimeter, and the other boson decaying into two hadronic jets. The same reconstruction tools and jet calibration, using $\chi = 0.445$ for the best linearity possible, are adopted here and no further correction is applied. The processes are:

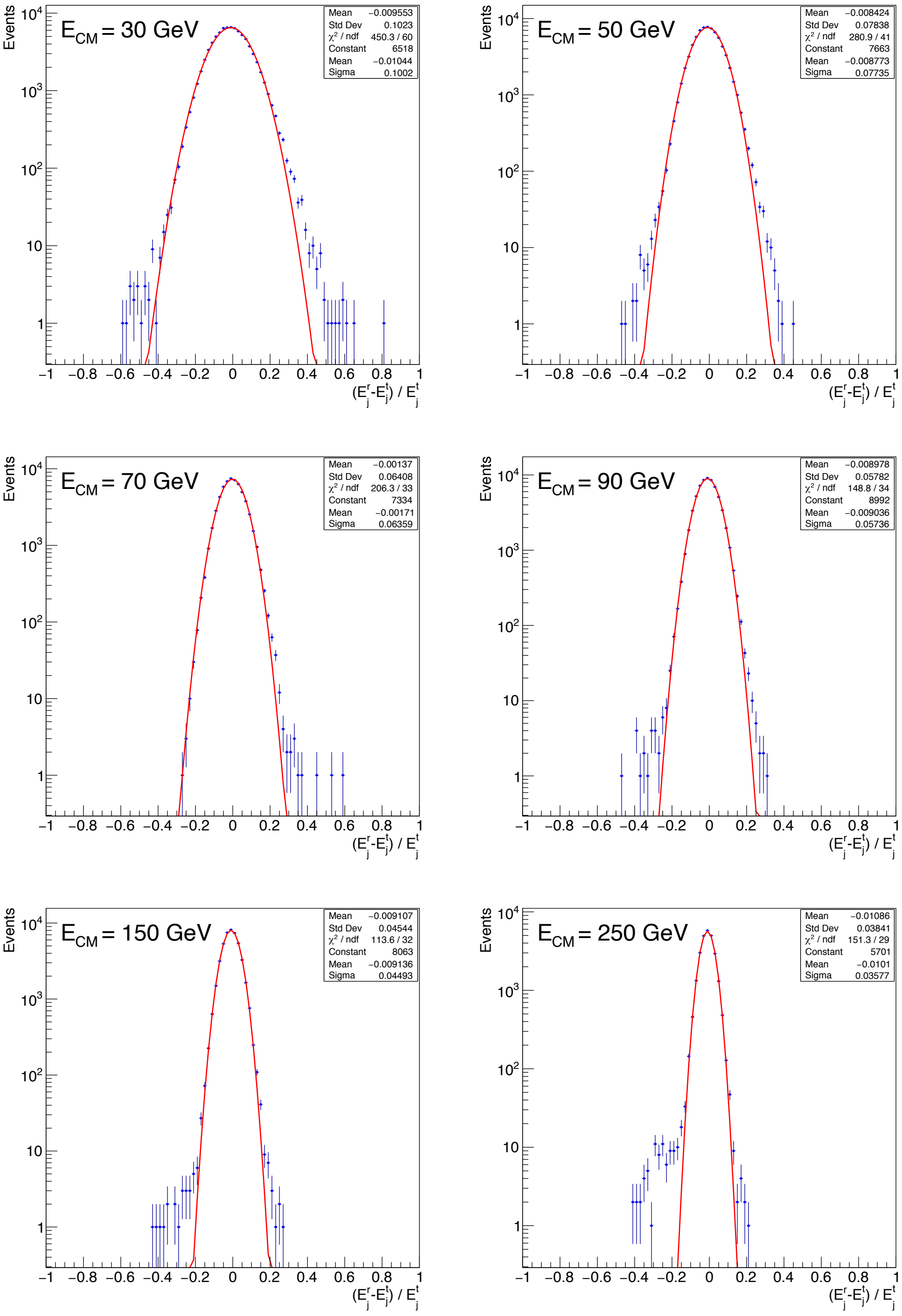

Figure 3.42: Distributions of the difference between the reconstructed and true energy of the jet, divided by the true energy of the jet, at different center-of-mass energies using $\chi = 0.43$.

- $e^+e^- \to ZH$, $H \to \chi_1^0\chi_1^0$, $Z \to jj$
  The Z is required to decay only in u,d,s,c quark pairs. The events are cleaned requiring that no neutrinos or muons enter the calorimeter, that the two reconstructed jets are within 2 in pseudorapidity, and that the energy leaked behind the calorimeter is smaller than 1 GeV.

- $e^+e^- \to W^+W^-$, $W^+ \to \mu\nu$, $W^- \to jj$
  The cleaning requirements are the same as for the Z, except that one muon and one neutrino are admitted, and, given the presence of the muon, the requirement on the leakage is modified into the requirement that the difference between the energy of the muon, as assumed to be measured in the inner detector, and the sum of the leaked energy and the scintillating-fiber energy deposited in the calorimeter, in a cone of $\Delta R = 0.1$ around the muon direction, is smaller than 1 GeV.

- $e^+e^- \to ZH$, $H \to b\bar{b}$, $Z \to \nu\nu$
  The cleaning requirements are the same as for the Z, except that no neutrinos beyond the ones from the Z decay are accepted. Since the Higgs decay into $b\bar{b}$ has a large semileptonic branching ratio, the requirement of no neutrinos strongly reduces the statistics. We also looked at the distribution obtained while including the semileptonic decays.

The distributions of the difference between the reconstructed and the true mass of the jet-jet resonances for the three masses are shown in Fig. 3.43. The residual miscalibration of the masses is within $\simeq$ 200 MeV, a remarkable result considering that no advanced calibration and no correction on what is provided by the dual-readout method has been used. In Fig. 3.44 (up), we plot the distributions of the measured masses for the three considered resonances, for the H mass no semileptonic decays have been included. Fig. 3.44 (down) shows the case when semileptonic decays are accepted in the analysis. A good discrimination power between the peaks of the W and the Z can be observed. As explained in Chap. 2, this is likely the most stringent requirement for hadronic calorimetry at future e^+e^- colliders.

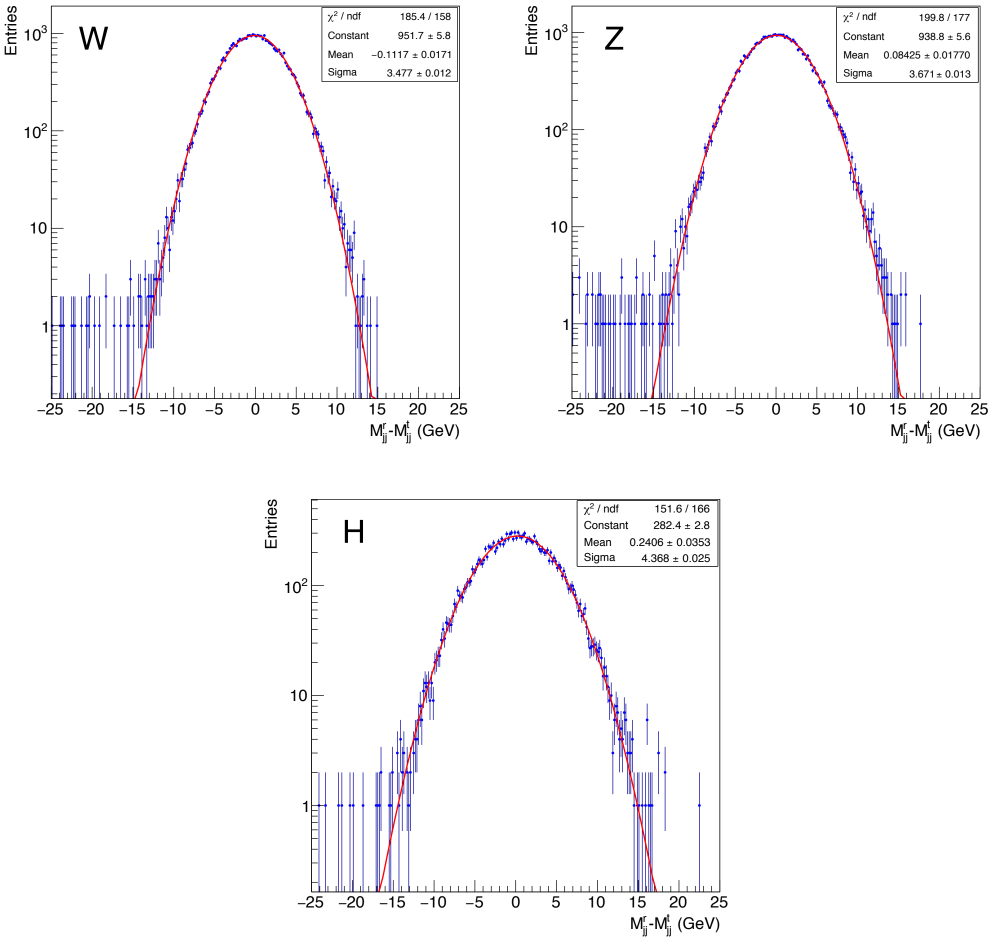

Figure 3.43: Distribution of the difference between the reconstructed and the true mass of the jet-jet resonances for the calo-only algorithm. Top left: W, top right: Z, bottom: H. See text for details.

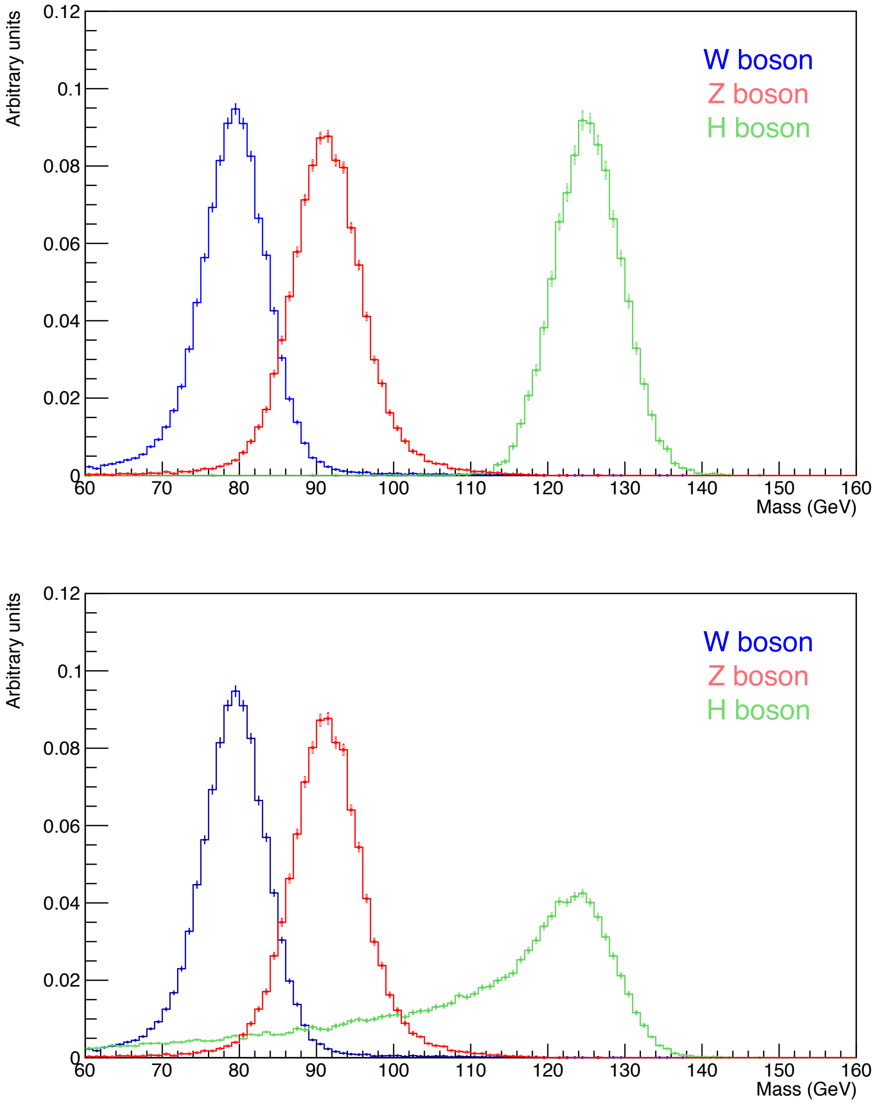

Figure 3.44: Distribution of the reconstructed mass for three jet-jet resonances for the calo-only algorithm. Top: excluding b semileptonic decays; bottom: including b semileptonic decays. See text for details.

Chapter 4

Dual-readout calorimetry with SiPM light sensors

The chapter describes the R&D work addressing the adoption of silicon photomultipliers as dual-readout fiber calorimeter light sensors. The work started in 2017 and is still evolving towards new detector prototypes. We review the main results up to 2019 that have been extensively documented in [91, 95, 96, 97]. Eventually the path for new detector construction and beam testing will be discussed. The author of the thesis participated in the prototype design, testing and data analysis, with particular attention given on the test-beam-data-to-simulation agreement.

4.1 Silicon photomultipliers

Silicon PhotoMultipliers (SiPMs) are solid state light sensors with countless applications thanks to their single photon sensitivity, high and tunable photon detection efficiency and photon number resolving capability. Unlike standard PhotoMultiplier Tubes (PMTs), they are compact, magnetic field insensitive and operate under low voltages with a low power consumption.

A SiPM is a matrix of independent Avalanche PhotoDiodes (APDs), packed in microcells, operating under a common load, and connected in parallel to a single readout output. Cells are positioned on a common monolithic silicon crystal with standard dimensions ranging from 1×1 mm^2 to 6×6 mm^2. The cell density kept increasing enormously during the last decades reaching 10^4 cells per mm^2 for recent large scale productions.

The photodiodes are operated in a limited Geiger-Müller regime, biased few volts above the breakdown voltage. Any charge carrier produced by photon absorption in

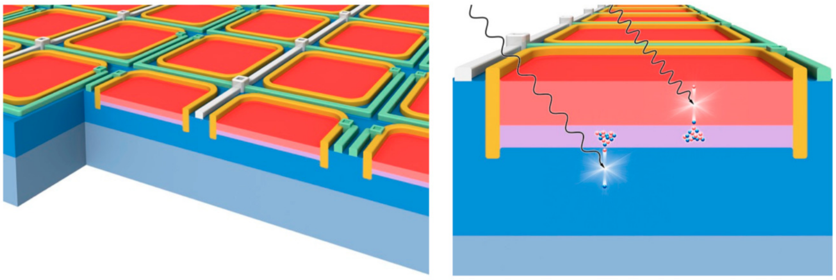

Figure 4.1: Artistic view of a SiPM structure and operating principle.

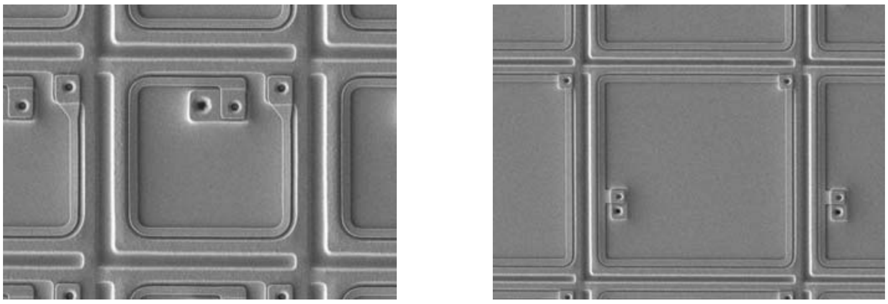

Figure 4.2: Individual SiPM pixels with metal-composite quenching resistor fabricated around each cell. Left: 25 μm pixel pitch. Right: 50 μm pixel pitch. Image from [98].

the depletion region drifts towards the photodiode junction, where the high electric field induces a self-sustained charge amplification, the avalanche. The avalanche is eventually stopped by a quenching resistor put in series, which induces a voltage drop and restores the initial bias condition. Fig. 4.1 shows an artistic representation of an SiPM structure and operation and Fig. 4.2 shows typical SiPM cells.

The output charge of an APD is the product of the junction capacitance and the applied operating overvoltage. The gain (M) is measured by dividing the output charge by the fundamental charge of an electron:

$$M = \frac{C \cdot \Delta V}{q_e} \tag{4.1}$$

Considering a typical ΔV value of 3-5 V, and a capacitance (C) of tens of fF, we find that standard values of M are of the 10^6 order. This single-cell high gain is the origin of the SiPMs single photon sensitivity.

SiPMs are binary (digital) devices where any cell releases, in average, the same amount of charge despite the number of charge carriers produced in the depletion region. The SiPM response to photons or thermally induced events is identical.

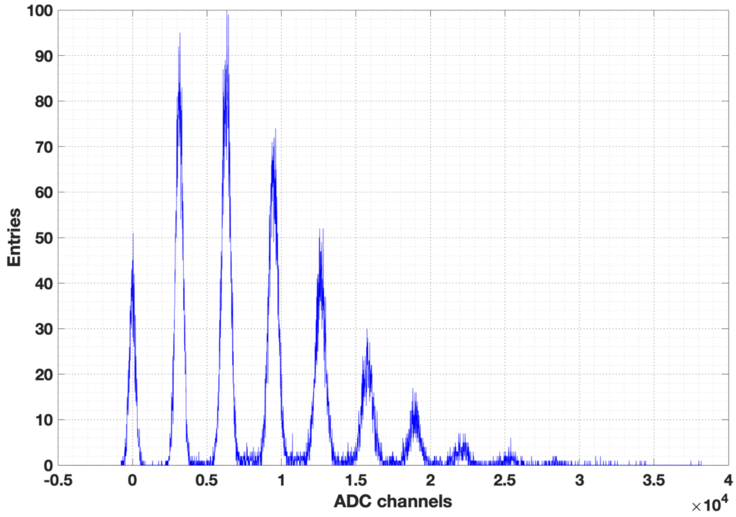

Figure 4.3: Integrated and digitized response of a 1.3×1.3 mm^2 Hamamatsu MPPC (SiPM) 13360-1350CS with a 50 μm cell pitch when exposed to differently populated light bunches.

Fig. 4.3 shows the convoluted response of an SiPM when stimulated with differently populated photon bunches. Every entry corresponds to the digitized charge produced, obtained by integrating the current over a predefined time gate. Each peak corresponds to events with the same number of fired cells. Thanks to the high gain, the charge signal intensity dominates over the signal noise and peaks are effectively separated providing an unprecedented photon number detection capability.

The peak at 0 ADC-counts corresponds to events with no photons, hence its width (σ_0) is a direct measurement of the system noise, *i.e.* the signal stochastic fluctuations in the absence of light. Interestingly, the width (σ_i) of the peak corresponding to one photoelectron, is slightly bigger ($\sigma_1 > \sigma_0$). This is due to event-by-event fluctuations in the avalanche formation process and to cell-to-cell differences in the charge produced.

As fired cells are randomly distributed among the SiPM matrix, and their fluctuations in the avalanche charge are independent, the peak width (σ_i) is expected to scale with the square root of the number of fired cells. This feature eventually limits the maximum number of photons that can be resolved and the SiPM signals, for events with a photon number above this limit, form a continuous distribution. An analog behavior arises from the digital response to highly populated light samples.

The possibility to resolve discrete peaks makes the SiPM calibration procedure straightforward. Once the readout electronics parameters are known, it is possible to relate the peak-to-peak distance to the sensor gain and the gain is eventually used to estimate the number of fired cells even when peaks are no longer resolved. This could also greatly facilitate the calibration monitoring of a SiPM-read-out calorimeter at future collider experiments once a known source of light impinging the sensor is provided.

4.1.1 Signal time evolution

The SiPM signal evolution with time is driven by the sensor design and the powering circuit. The equivalent circuit of a Geiger APD and the corresponding conceptual output pulse are sketched in Fig. 4.4.

When the APD is ready for light detection, its capacitance (C_d) is biased at V_{bias} and the switch is open. When a photon interacts in the depleted region and generates through photoelectric effect an electron-hole pair, the switch closes and C_d discharges through R_s. This provides a surge in the current and an exponential decrease of V_d, the potential difference across C_d.

The net current through C_d is:

$$I_d = (V_d - V_{bd})/R_S + (V_{bias} - V_d)/R_q \tag{4.2}$$

with V_{bd} being the breakdown voltage. The two currents are flowing in opposite directions and the net flow is dictated by the most intense one. When V_d is so small that $V_d - V_{bd} = V_{bias} - V_d$, if R_q is large enough that the current flow from V_{bias} cannot sustain the C_d discharge, the avalanche process is quenched. Once the conceptual switch is reopened, the current flowing into C_d through R_q increases the voltage across C_d up to V_{bias} and the cell recovers for the next avalanche.

The recovery time of a single APD follows an exponential law characterized by a time constant $R_q \cdot C_d$. The time needed for a cell to fully recover ranges between 20 and 250 ns. On the other hand, the brief exponential charge multiplication period, known as the rise time, follows the much shorter time constant $R_s \cdot C_d$, typically of the order of hundreds of ps. The signal rise has no dependence on the bias voltage applied. When connecting each APD in parallel to a common output line, the signal rise does not depend on the number of fired cells.

4.1.2 Photon detection efficiency

The SiPM Photon Detection Efficiency (PDE) is the probability of producing an output signal in response of an incident photon. It depends on the overvoltage (ΔV), the light wavelength, and the temperature. The PDE is factorizable into

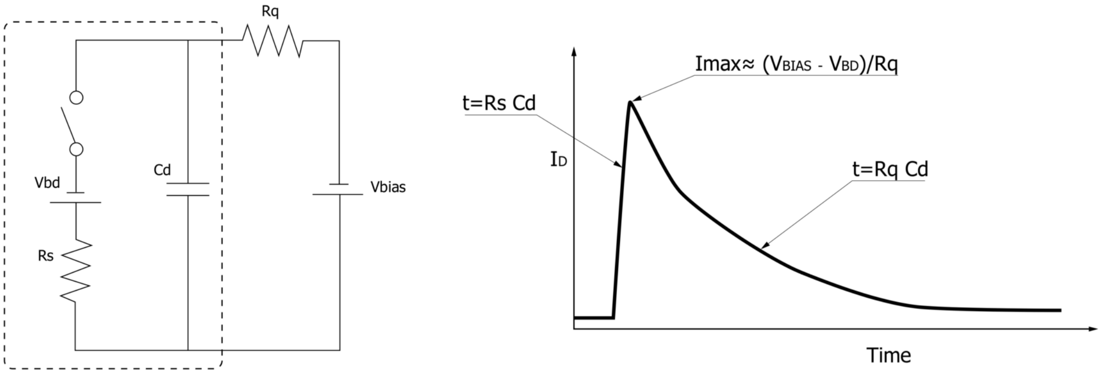

Figure 4.4: Sketch of the equivalent circuit of a single Geiger APD (left) and the corresponding conceptual output pulse (right). Image from [98].

three terms:

$$PDE = G_F \times QE(\lambda) \times P_T(\lambda, \Delta V, T) \tag{4.3}$$

G_F is the geometrical fill factor defined as the ratio between the light-sensitive area and the total sensor area. Each cell is surrounded by auxiliary passive elements: the guard ring structure, the bias line, the quenching resistor and the trenches preventing optical crosstalk (explained in Sec. 4.1.3). The cell design is optimized for each application and the fill factor changes accordingly. It ranges from 90% to 30% and typically increases with the cell size.

The quantum efficiency, QE, is the probability for a photon impinging the sensor on the active area to produce an electron-hole pair in the high-field region. It depends on the transmittance of the dielectric layer on top of the sensor and on the probability for a photon to generate an electron-hole. To increase the photon absorption, the dielectric layer is usually treated with an anti-reflective coating. Once a photon passes through the dielectric layer, its probability of creating an electron-hole pair depends on the absorption depth and the collection properties of the photo-generated carriers. The absorption depth in silicon increases with the wavelength. It is about ten nanometers for UV light and few tens of micrometers in the near IR. Depending on the wavelength used in the application, the thickness of the active silicon layer has to be chosen according to the absorption depth.

The probability for any carrier to trigger an avalanche is called trigger probability (P_T). Both electrons and positive holes are associated to a trigger probability, P_e and P_h, respectively, and the trigger probability P_T is given by $P_e + P_h - P_e P_h$. P_e and P_h increase with the overvoltage and P_e is greater than P_h as a consequence of the higher electron ionization power. The P_T dependence on the carrier generation position directly translates in a dependence on the light absorption depth dictated

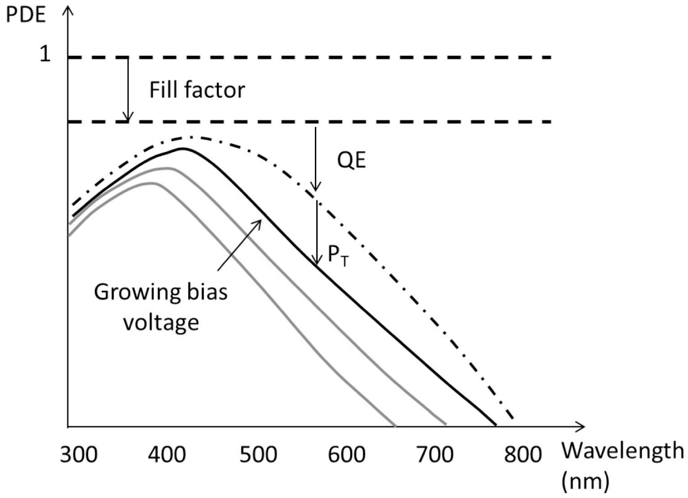

Figure 4.5: Contributions of Eq. 4.3 terms to the PDE of a blue sensitive device. Image from [99].

by the light wavelength. For instance, in a n+/p junction, electrons drift towards the n electrode and holes towards the p one, so the maximum P_T is expected for light absorbed in the region where the electrons can cross the whole high-field zone before reaching the n electrode [99]. When the absorption depth is optimized to maximize P_e, then the P_T dependence on the overvoltage is as little as possible.
The SiPM PDE is the combination of the tree terms described above, as reported in Eq. 4.3 and illustrated in Fig. 4.5 for a blue light sensitive detector. The geometrical fill factor acts as a constant reduction of the perfect PDE (PDE=1) and is, with good approximation, wavelength independent. The quantum efficiency further reduces the PDE and introduces a strong dependency on the wavelength; for instance, blue sensitive SiPMs have few micrometers thick active layers and the QE drops quickly above 500 nm. Finally, the triggering probability adds a strong dependence on the applied overvoltage. For blue-sensitive SiPMs and short wavelengths, its correction is almost negligible as avalanches are electron initiated and almost no dependence on the applied overvoltage is present. For wavelengths above the blue peak (450 nm), the triggering probability grows with the overvoltage. At present, SiPMs optimized for blue light detection can reach a PDE of $\simeq 80-90\%$ at the 450 nm peak.

4.1.3 Intrinsic noise sources

The high signal-to-noise ratio of SiPMs is the key feature for both single photon sensitivity and photon number counting capability. However, intrinsic noise sources might compromise the performance. Among them there are dark counts, optical crosstalk and after pulses.

Optical crosstalk Reversely biased junctions have an emission spectrum in three energy ranges: the region below the band-gap energy, the near-band edge region and the high-energy region peaking in the visible-light range. High-energy photons arise from the transitions of energetic electrons within the conduction bands. The probability for a photon emission with energy above 1.14 eV (the band gap of silicon) is $2.9 \cdot 10^{-5}$ per charge carrier crossing the junction. Assuming a SiPM gain of 10^6, on average about 30 optical photons are generated during a single discharge, each of them can reach a neighboring cell and trigger an avalanche discharge. This intrinsic source of noise is simultaneous to the primary discharge and cannot be deconvoluted from it. It is an inter-pixel correlated noise, known as Optical CrossTalk (OCT). Fig. 4.6 shows an example of SiPM waveforms during optical crosstalk events. At present, SiPM cells are surrounded by deep trenches coated with reflective material to minimize the OCT without affecting seriously the fill factor. This technique recently reduced the OCT probability to 1-2%.

Dark count rate Avalanches triggered by any carriers in the depletion region in the absence of light are called *dark counts*. The rate for these spurious avalanches to occur is know as the Dark Count Rate (DCR). Most often they are triggered by thermally generated free carriers, hence reducing the temperature mitigates the DCR. Also, lowering the bias voltage reduces both the active area and the triggering probability, and consequently the DCR. Being an uncorrelated, randomly triggered, source of noise, the DCR depends on the sensor area and, using up-to-date technologies, it ranges from a few MHz to tens of kHz for the $6{\times}6$ mm^2 and the $1{\times}1$ mm^2 sensors, respectively. A single dark count event can induce simultaneous and identical signals by activating neighbouring cells through optical crosstalk, an example is shown in Fig. 4.7.

Afterpulsing Electrons produced in an avalanche can be trapped in the silicon lattice and be released after an amount of time ranging from nanoseconds to microseconds, inducing an afterpulse from a previously fired cell. The charge released during the afterpulse depends on the delay time (Δt) between the two signals and the cell recovery time constant (τ_r). The charge ratio between the afterpulse and the original pulse is approximately $1 - exp(-\frac{\Delta t}{\tau_r})$ and a standard-amplitude signal is produced if $\Delta r \ll \tau_r$. Fig. 4.8 shows waveforms followed by amplitude-suppressed afterpulses. These signals cannot be separated from the original one and constitute an intrinsic source of noise, especially important for signal correlation measurements and coincidence analysis. The afterpulsing probability increases with the overvoltage, a clear consequence of the higher gain. The trapped-carrier lifetime becomes longer with lower temperatures. Therefore, lowering the temperature has the effect of suppressing the DCR and the OCT but increases the afterpulsing probability. The afterpulse induced noise can be reduced with higher quality silicon lattices and with the present technologies amounts to 1-3%.

4.2 Tests of a dual-readout calorimeter prototype with SiPMs

The first dual-readout calorimeter prototype tested with SiPMs consists of brass (Cu260) with embedded scintillating and Cherenkov fibers positioned in a chess-board-like geometry. It is 112 cm long and 15×15 mm^2 wide. It was built out of ten brass plates housing ten grooves. In total 64 fibers, equally divided between scintillating and Cherenkov, were inserted, covering an active volume of 12×12 mm^2. The fiber diameter is 1 mm. The metal absorber made 49% of the calorimeter volume, fibers occupied 35% of the volume and air accounted for the remaining 16%. The radiation length (X_0) and the Moliere radius (R_M) were 29 mm and 31 mm respectively. The calorimeter was 39 X_0 deep. Fibers defined an active region of only 0.22 R_M. Geant4 simulations were used to estimate an average energy containment of 45% for electrons entering in the calorimeter center region. Fig. 4.9 shows a sketch of the brass absorber structure and fibers arrangement and a picture of the detector front face.

Up to 2017, dual-readout fiber calorimeters were instrumented with PMTs reading out bunches of fibers. Fibers were extended of about 30 cm out of the calorimeter back-end to allow their separation and grouping into bunches. This procedure leads to a forest of optical fibers at the calorimeter end that, in a collider experiment, might sample particles not originating from the interaction point or oversample particle showers developing very deep inside the detector. Solid state light sensors may offer a simple solution if coupled directly and independently to each fiber. Moreover, SiPMs are magnetic field insensitive and typically have a larger quantum efficiency for photon detection that might lead to an increase in the calorimeter Cherenkov light yield whose statistical fluctuations affect both the electromagnetic and the hadronic energy resolution. On the other hand, SiPMs are digital devices prone to signal saturation. One more thing to take into account is the potential crosstalk arising from having readout sensors operating close to each other while sampling signals (Scintillation (S) and Cherenkov (C)) differing of more than an order of magnitude in intensity. For instance, if the two light yields differ of a factor

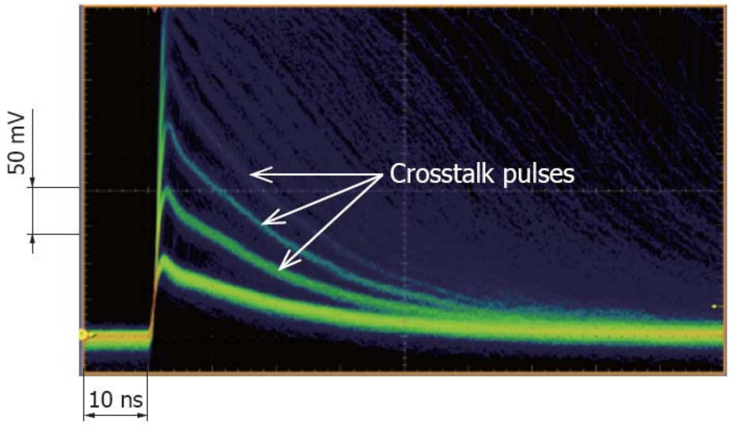

Figure 4.6: SiPM waveforms under the occurrence of prompt crosstalk. Image from [98].

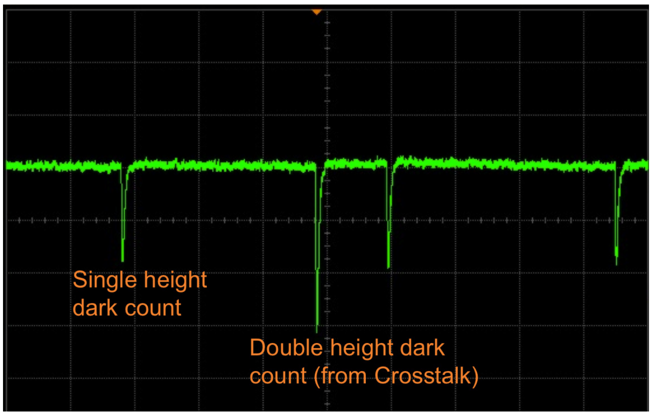

Figure 4.7: SiPM waveforms under the occurrence several dark count events. Image from [100].

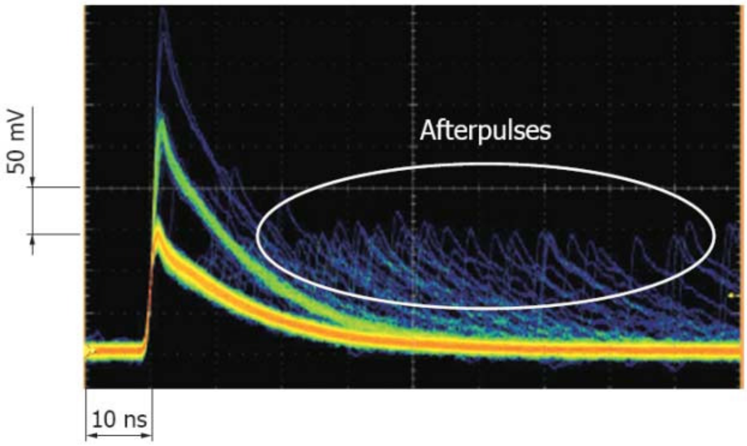

Figure 4.8: SiPM waveforms under the occurrence of afterpulses. Image from [98].

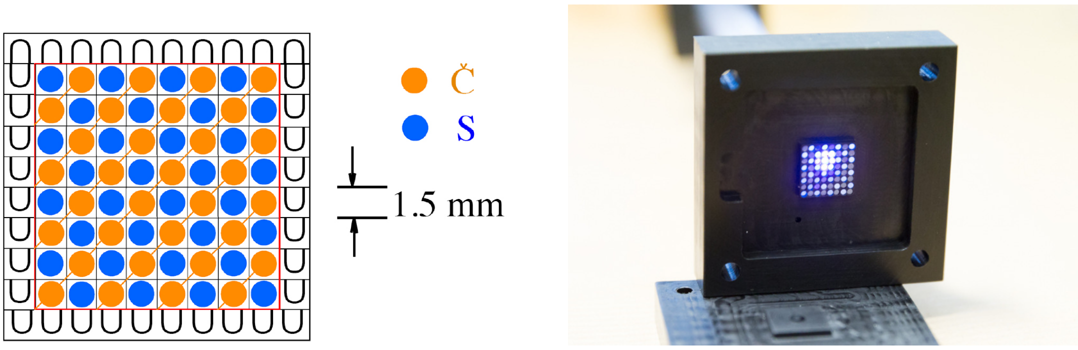

Figure 4.9: Sketch of the detector brass structure and fiber arrangement (left) and picture of the prototype (right). Left image from [91].

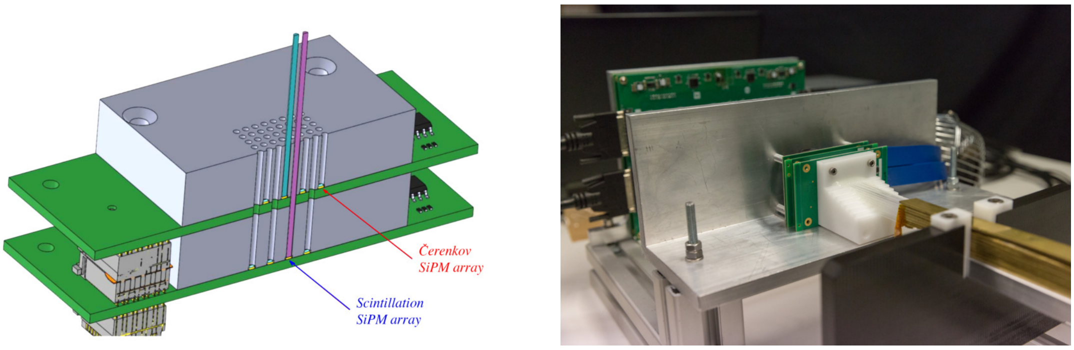

Figure 4.10: Schematic readout of the calorimeter with two arrays of SiPMs (left). Picture from the rear end of the calorimeter prototype (right). Left image from [91].

50, as observed, then the Cherenkov signal would increase by 50% if only 1% of the scintillation light is detected by the SiPMs that read out the Cherenkov fiber signals. Quantifying these aspects is the goal of this work.

4.2.1 Light readout system

In the new prototype each fiber is independently read out by a dedicated sensor. SiPMs are mounted on a two tier structure, sketched in Fig. 4.10 together with a picture of the prototype instrumented back-end. Cherenkov fibers were readout by SiPMs on the front tier while scintillating fibers were guided through holes to the second tier. This mechanical separation of the readout was intended to minimize the optical cross talk between the S and C photons. The sensors used were HAMAMATSU S13615-1025 with an active area of 1×1 mm^2 and a cell pitch of 25 μm for a total of 1584 cells/sensor. Tab. 4.1 summarizes their main parameters.

HAMAMATSU S13615-1025	
Sensitive area	1×1 mm^2
Cell pitch	25 μm
Pixels	1584
Peak photon detection efficiency	25%
Breakdown voltage V_{br}	53 V
Recommended operational voltage V_{op}	V$_{br}$+5 V
Gain at V_{op}	7×10^5
Dark count rate at V_{op}	50 kps
After pulse rate at V_{op}	2%-3%
Optical crosstalk at V$_{op}$	1%

Table 4.1: Main parameters of the SiPM used. The peak sensitivity reported is obtained at the recommended operational voltage at the 450 nm peak. The breakdown voltage was determined by measuring the gain-voltage dependence.

The SiPM readout was performed with a DC preamplifier with a 1 μm shaping time and an AC-coupled differential amplifier to match the digitizer dynamic range. The two-tier board also provided individual bias and on-board temperature measurements.

The calibration of the readout system is a strong point in favor of SiPMs. We exploited the signal distribution structure when the sensors are exposed to a small number of photons. Fig. 4.11 (left) shows two typical signal distribution spectra for light samples used for calibration purposes. The peaks arise from different numbers of fired cells. Once the DAQ system parameters are know, the peak-to-peak distance is turned directly into the SiPM gain and its value is the gauge to translate any digitized signal into the number of fired cells.

The goal of any calorimeter light readout is to measure the light produced in the active elements, however SiPMs provide a direct measurement of the number of fired cells. When dealing with large photon samples the probability of two photons interacting almost simultaneously in the same cell is not negligible and leads to an occupancy saturation effect for which the number of photons is not directly proportional to the number of fired cells. To correct for this effect a simple solution is to infer the number of detected photons ($N_{photons}$) from the number of fired cells via the equation:

$$N_{fired} = N_{cells} \times \left[1 - exp[-\frac{N_{photons} \times PDE}{N_{cells}}] \right] \tag{4.4}$$

where N_{fired} is the raw number of fired cells, N_{cells} is the number of cells in the sensor and PDE is the Photon Detection Efficiency at the operational voltage. In the following Eq. 4.4 is used to restore the calorimeter linearity.

The PDE strongly depends on the applied bias voltage, related measurements are

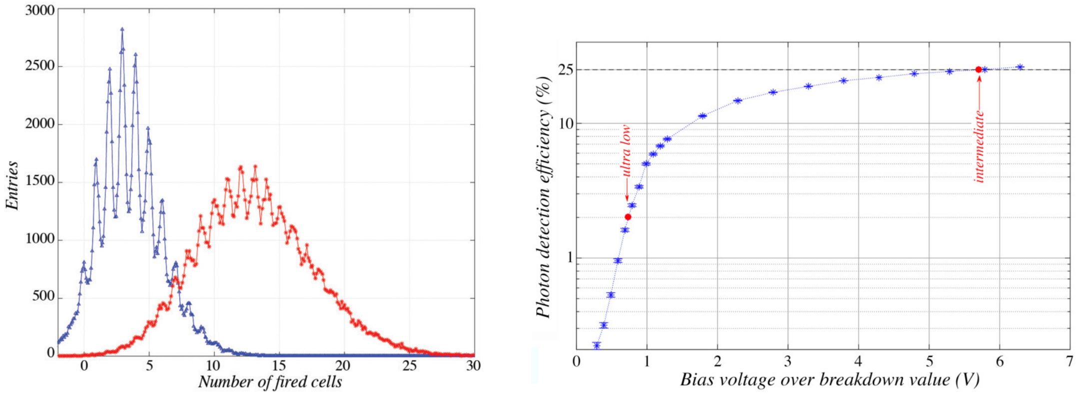

Figure 4.11: Signal distributions of the SiPMs while sampling calibrating signals (left). The SiPM PDE as a function of the bias voltage applied (right). Result for light with wavelength of 523 nm. Operational voltages applied in the following are marked (ultra-low and intermediate). Image from [91].

shown in Fig. 4.11 (right). To avoid saturation of the scintillation light, the corresponding SiPMs were operated at the *ultra-low* regime (PDE $\simeq 2\%$) while SiPMs reading out Cherenkov fibers were operated at the *intermediate* regime (PDE $\simeq 25\%$). The corresponding gains at these voltages were measured to be $9.9 \cdot 10^4$ and $8.0 \cdot 10^5$, respectively. The ratio of the two readout-system PDEs, operating at the same temperature, was 12.5.

Each of the two boards digitized 32 channels at a rate of 80 MS/s and a 14-bit ADCs performed real-time charge integration on FPGAs. Signals from the two-tier boards were sent through 64-channel coaxial cables into a mother board, eventually they were read out using a Multi-channel Analog to Digital Acquisition system (MADA). The imaging capabilities of such a detector are well represented in Fig. 4.12 showing event displays for 10 GeV particles measured with the scintillating fibers only. Result for an electron showering in the central region (a) or slightly off-centered (b) and for a muon (c) are clearly recognizable.

4.2.2 Test-beam setup

The detector was beam tested using secondary and tertiary beams from the 400 GeV proton beam delivered by the CERN SPS accelerator. We used the H8 experimental line. Either 60 GeV and 180 GeV secondaries, produced by SPS protons on a target, were selected for highly energetic events. Low energy tertiary beams were produced starting from the 60 GeV beam and energies above 60 GeV were derived from the 180 GeV secondaries. Run with tertiary beams were carried out for the following

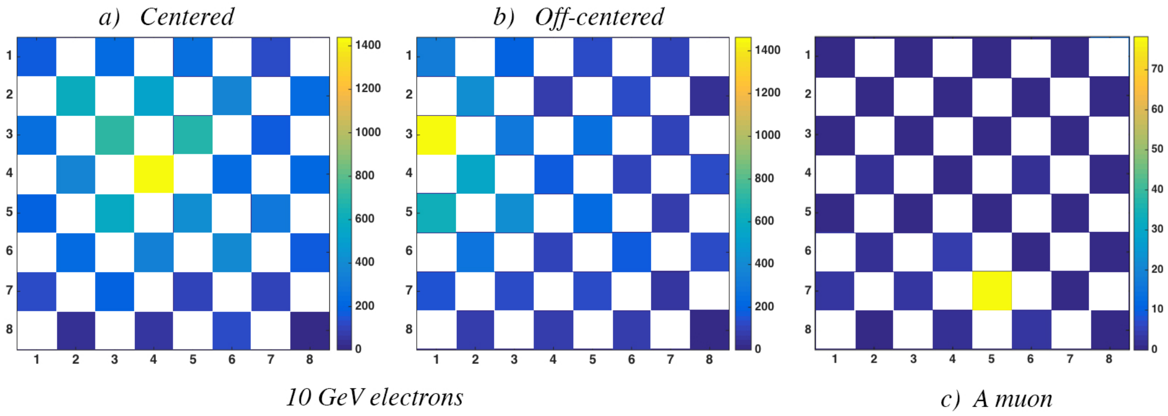

Figure 4.12: Event displays for the 8×8 scintillating fibers for 10 GeV electrons and a muon showering inside the calorimeter. Cherenkov signals are left blank to illustrate energy depositions more clearly. Image from [91].

beam energies (GeV): 6, 10, 20, 30, 40, 50, 60, 80, 100 and 125.
Auxiliary detectors were used for triggering, identification and tracking purposes. The experimental setup is sketched in Fig. 4.13. We used

- Three 2.5-mm-thick scintillating counters for triggering purposes. The third one, closest to the calorimeter, has a 10 mm radius hole. The triggering signal was then built out of the logic $(T_1 \cdot T_2 \cdot \overline{T_3})$.

- A small Delay Wire Chamber (DWC) was used to locate the beam impact position at the calorimeter surface with a precision of few millimeters, depending on the beam energy.

- 20 cm upstream of the calorimeter, a preshower detector made of a 5-mm-thick lead plate followed by a 5-mm-thick plastic scintillator was used to identify electrons as beam particles. The signal was required to be three times larger than the signal of a minimum ionizing particle (*mip*). Muons and hadrons produce a signal characteristic of a *mip*.

- After an additional 8 λ worth of absorber, at 20 m downstream of the calorimeter, a scintillation counter was used to identify muons among the beam particles.

Signals from the preshower and the muon counter were integrated and digitized, with a sensitivity of 100 fC/count and a 12-bit dynamic range, in a charge ADC (CAEN V862AC). The signals from the DWC were recorded with a 140 ps resolution in a 16-channel CAEN V775N TDC and converted in a two-dimensional position.

Figure 4.13: Scheme of the experimental setup (not to scale). Image from [91].

All information was collected using gate widths of about 100 ns and readout, event by event, through the V2718 CAEN optical link with a dead time of $\simeq 300\ \mu$s. The data taking was focused on muons and electrons. Muon events were selected on the basis of the signals in the muon counter by requiring a signal not compatible with pedestal fluctuations. Electrons were tagged as particles producing a signal in the PSD larger than 150 ADC counts above pedestal, corresponding to the signal induced by 3 *mips*, and no signal incompatible with electronic noise in the muon counter. Off-line, the DWC information was used to select events within a small beam spot located in the central region of the calorimeter front face (radius < 3 mm).

4.2.3 Crosstalk results

Designing a readout system with minimal crosstalk between light sensors is a mandatory aspect to achieve excellent electromagnetic and hadronic energy resolution. The optical crosstalk of the prototype was measured before the test beam data taking. The measurement was performed in an optical laboratory. At the front face of the calorimeter, each fiber tips, except one, was masked. A pulsed LED was then used to illuminate the uncovered fiber and all the 64 SiPMs were simultaneously readout. A typical signal distribution, averaged over 10^5 events, is shown in Fig. 4.14. A clear signal contamination is evident in the close surrounding of the stimulated fiber, for both types of fibers. When a scintillating fiber was illuminated, the sum of the fired cells for the Cherenkov fibers was on average 0.3% of the scintillating signal and the corresponding rms value was 0.1%. This is considered a crosstalk upper limit because we cannot exclude that some light from the LED directly entered in the neighboring Cherenkov fibers.

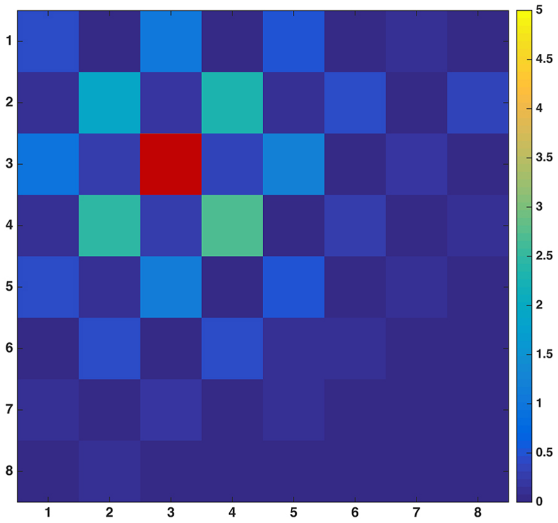

Figure 4.14: Signal distribution of the 64 SiPMs after a single fiber was illuminated with a light pulse corresponding to $\simeq$ 1400 fired cells. Colors indicated the raw number of fired cells. Numbers are averaged over 10^5 events. Image from [91].

4.2.4 Light yields results

To study the light yield, *i.e.* the absolute response in photoelectrons per GeV of deposited energy at the electromagnetic scale, it is mandatory to know the energy containment for electron induced showers. We used Geant4 simulations (version 10.3.p01, with physics list FTFP_BERT) for this purpose. The simulated average fraction of the shower energy deposited in the calorimeter, as a function of the impact point for 10 GeV and 100 GeV electrons is shown in Fig. 4.15. The study was performed for electrons entering the calorimeter along the fiber direction or at an angle of 0.2° in both the horizontal and the vertical plane. Because of the incomplete lateral containment of the showers, the effects of the rotation are clearly visible. However, if we select only electrons with an impact point within a region of a 3 mm radius around the geometrical center of the detector, the contained fraction is almost constant to 45% for both sets of data. Another aspect investigated with simulations turned out to be crucial for the following results, *i.e.* the fact that the shower containment is identical for 10 and 100 GeV electrons. This is a known feature of electromagnetic showers: the lateral shower containment is largely independent of the energy. The small difference observed in the tilted configuration is likely due to the difference in the longitudinal shower shape. Fig. 4.16 shows a simulated event for a 50 GeV electron induced shower, the lego-plot corresponds to the energy depositions in scintillating fibers. The red area corresponds to the one sampled by our prototype, while the surrounding area (marked as blue) was added replicating in simulation the same calorimeter structure.

The Cherenkov signal The average number of Cherenkov fired cells, for electron induced showers, divided by the beam energy, as a function of the beam energy, is shown in Fig. 4.17. It is approximately constant at $\simeq$ 28.6 Cpe/GeV over the range 6-125 GeV. The standard deviation is 0.4 Cpe/GeV. The found constant value indicates that there was no saturation and the average shower containment is independent of the electron-beam energy. As principle, it is possible that a saturating readout coupled to a non-constant shower containment leads to a constant light yield. However, this is ruled out by our simulations, see Fig. 4.15. We conclude that the Cherenkov response was $\simeq$ 2% linear in the energy range considered. Taking into account the shower containment, the Cherenkov light yield amounts to 64±2 photoelectrons per GeV deposited energy. After correcting for the light crosstalk, the Cherenkov light yield becomes 54±5 photoelectrons per GeV deposited energy. This value is almost a factor two higher than the previous one found, for a similar calorimeter, using a PMTs-based readout [67], a clear consequence of the higher SiPM PDE with respect to standard PMTs.

The scintillation signal If light saturation was absent in the Cherenkov signal, it highly affected the scintillation one. Its effect was noticeable even in the ultra-low PDE regime and at low energies. Fig. 4.18 (a) shows the average measured signal (expressed in arbitrary units) for electron showers divided by the beam energy. In the energy range 10-50 GeV, it decreases by more than a factor of 2 in the mostly stimulated fiber while the signal measured by all the remaining fibers shows a reduction of about 25%. Fig. 4.18 (b) shows the ratio of these quantities, that is a measurement of the relative contribution of the hottest fiber to the total signal. Since the lateral shower profile does not depend on the energy, the ratio decrease indicates that light saturation was indeed causing this behavior.

Signals were corrected for the occupancy saturation effect using Eq. 4.4 considering 1584 cells per SiPM. The linearity greatly improved. The average signals, divided by the beam energy, against the beam energy is shown in Fig. 4.19. The non-linearity for the sum of the 31 fibers is almost completely recovered, but the hottest fiber still exhibits some saturation effect. This is also evident if we look at the ratio of the two quantities.

The signals shown in this figure were eventually converted in photoelectrons, using the calibration at the ultra-low bias voltage. To minimize the impact of the remaining saturation effect, the scintillation light yield was measured with 10 GeV electrons. Taking into consideration a 45% shower containment and a PDE that

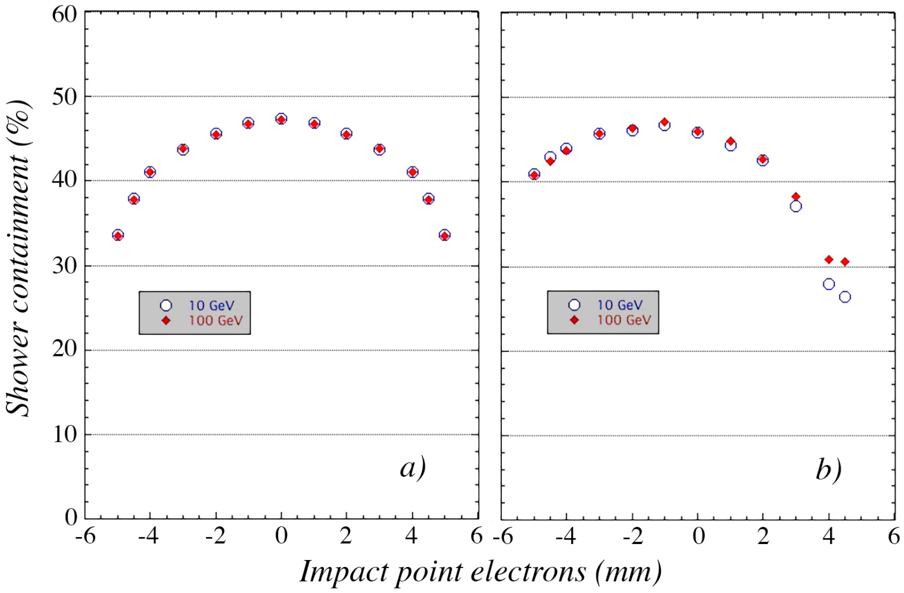

Figure 4.15: Average fraction of shower energy deposited in the calorimeter as a function of the impact point for 10 GeV and 100 GeV electrons. Results from Geant4 simulation obtained with the beam impinging parallel to the fiber axis (a) or 0.2° tilted in both the vertical and the horizontal plane (b). Image from [91].

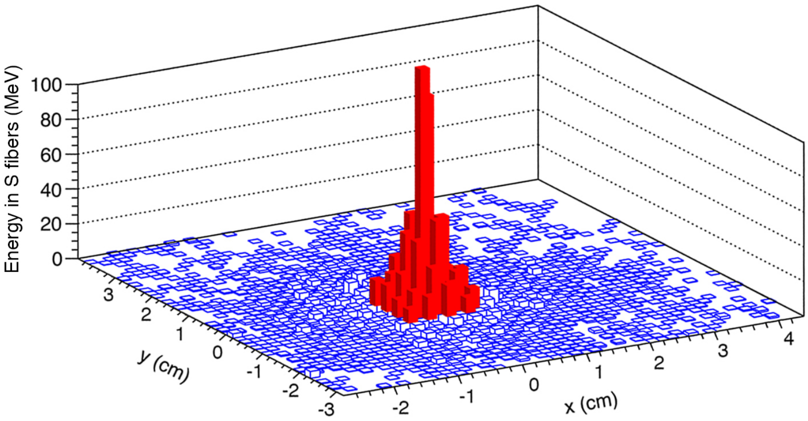

Figure 4.16: Event display for a simulated 50 GeV electron induced shower developing in an extended calorimeter structure identical to the prototype one. Shown are energy depositions in scintillating fibers. Fibers in the area covered by the prototype considered are marked in red. The shower fraction sampled by these fibers is, in this event, 46%. Results from Geant4 simulation. See text for details.

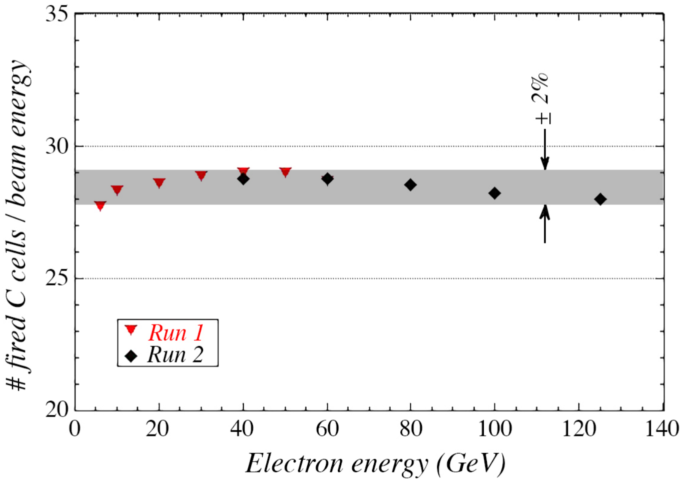

Figure 4.17: Average number of Cherenkov photoelectrons from the SiPM readout divided by the beam energy (Cpe/GeV). Results obtained with a bias voltage of 5.7 V above the breakdown level.

is 12.5 times lower than the Cherenkov one, we found 108 photoelectrons for the sum of the 32 scintillating fibers. The light yield is given by 108×12.5/0.45 ≃ 3000 photoelectrons per GeV deposited energy. If one uses only the sum of the 31 fibers, for which saturation effects seem to be absent, then the shower fraction sampled by these fibers reduce to 29% and the light yield becomes 80×12.5/0.29 ≃ 3400 photoelectrons per GeV deposited energy. It is possible to conclude that the scintillation light yield at the bias voltage 5.7 V above breakdown was 3200±200 photoelectrons per GeV deposited energy. It is roughly 50 times higher than the Cherenkov one. This number was used to correct for the crosstalk effect while calculating the Cherenkov light yield before. We conclude that the S/C light yield ratio of this calorimeter is (3200±200)/(54±5) = 59±8.

4.2.5 Measuring electromagnetic shower profiles

This highly granular two-dimensional readout opened the possibility to sample shower profiles, close to the shower axis, with great detail. The profiles were measured selecting a clean sample of electron induced showers, for each event the impact point

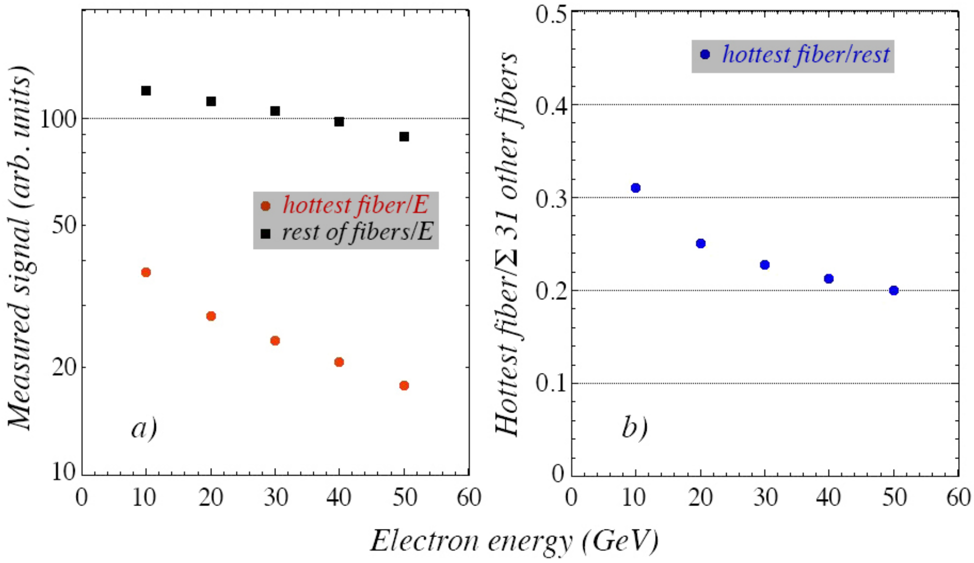

Figure 4.18: Average scintillation signal (arbitrary units) divided by the beam electron energy. Results obtained in the ultra-low PDE regime. Results shown separately for the hottest fiber and the sum of the signals from the other fibers (a) and for the ratio of these quantities (b). Image from [91].

on the calorimeter $(\overline{x}, \overline{y})$ was calculated as the barycenter of the signals, *i.e.*

$$\overline{x} = \frac{\sum_i x_i E_i}{\sum_i E_i} \tag{4.5}$$

$$\overline{y} = \frac{\sum_i y_i E_i}{\sum_i E_i} \tag{4.6}$$

and the radial distance (r_i) between each fiber i and the shower axis as given by

$$r_i = \sqrt{(x_i - \overline{x})^2 + (y_i - \overline{y})^2} \tag{4.7}$$

It is then possible to calculate the average signal of a fiber as a function of the distance r from the shower axis, that represents the lateral shower profile. Moreover, in a dual-readout calorimeter it is possible to measure it for the Cherenkov and the scintillation signals independently. This exercise was performed using 40 GeV electrons for the Cherenkov signal and 10 GeV electrons and the ultra-low bias voltage for the scintillation signal in order to minimize the saturation effect. Therefore, the shower barycenter was calculated using 32 signals. The profiles can be compared because the lateral shower profile of high-energy electron showers does not depend on the electron energy.

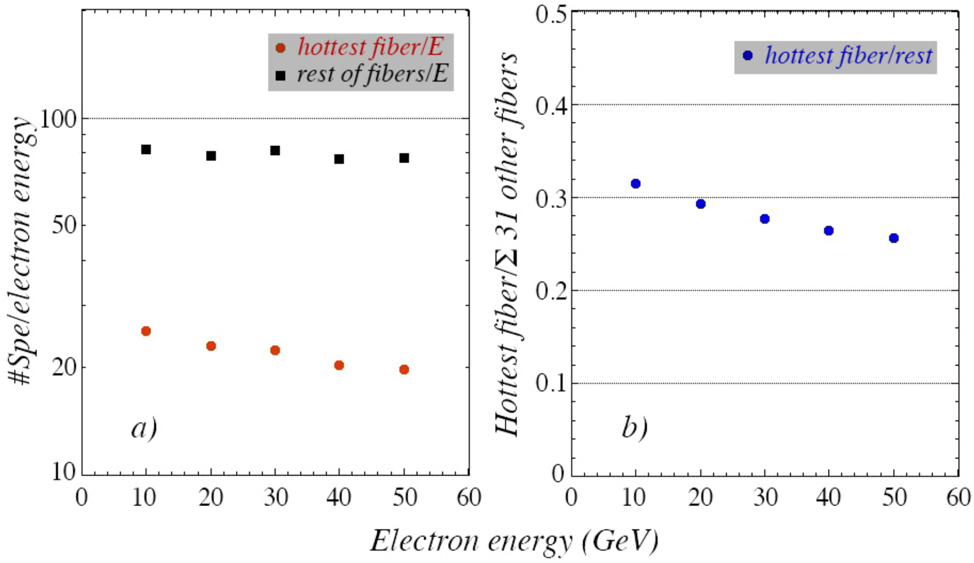

Figure 4.19: Average scintillation signal (arbitrary units) divided by the beam electron energy. Results obtained in the ultra-low PDE regime after the occupancy saturation correction. Results shown separately for the hottest fiber and the sum of the signals from the other fibers (a) and for the ratio of these quantities (b). Image from [91].

The lateral profiles are shown in Fig. 4.20 that compares test-beam data (a) with Geant4 simulated data (b). Fig. 4.20 (c) shows the relative difference between test beam data and simulated data against the distance from the shower axis.
Another important figure of merit is obtained by summing the signals from fibers located in the same $r-$bin and the average value is plotted against r. We call this the radial shower profile. Fig. 4.21 (a) shows the result by normalizing the integral of the signal to 45% that is the calorimeter energy containment. Fig. 4.21 (b) is obtained from the same experimental data and shows what fraction of the total energy is deposited within a distance r from the shower axis.
We found remarkable differences in the profiles measured with the scintillation and the Cherenkov signals, with the Cherenkov profile being less concentrated very close to the shower axis. To our understanding, this is due to the fact that the highly energetic component of electromagnetic showers, very close to the shower axis, is suppressed because, in this region, the emitted Cherenkov light falls outside the numerical aperture of the clear fibers. Signs of this effect were already observed while studying the electromagnetic energy resolution of the RD52 dual-readout fiber calorimeter [67]. It is also remarkable how well Geant4 describes both signal profiles in great detail.

This extremely collimated nature of electromagnetic showers poses new constraints on the design of future highly granular calorimeters. The fact that the hottest fiber carries $\simeq 25\%$ of the total recorded signal, combined with the shower containment, indicates that $\simeq 10\%$ of the entire energy is deposited within one millimeter from the shower axis thus contributing to the signal of one fiber only. This is confirmed by Fig. 4.21 (b).

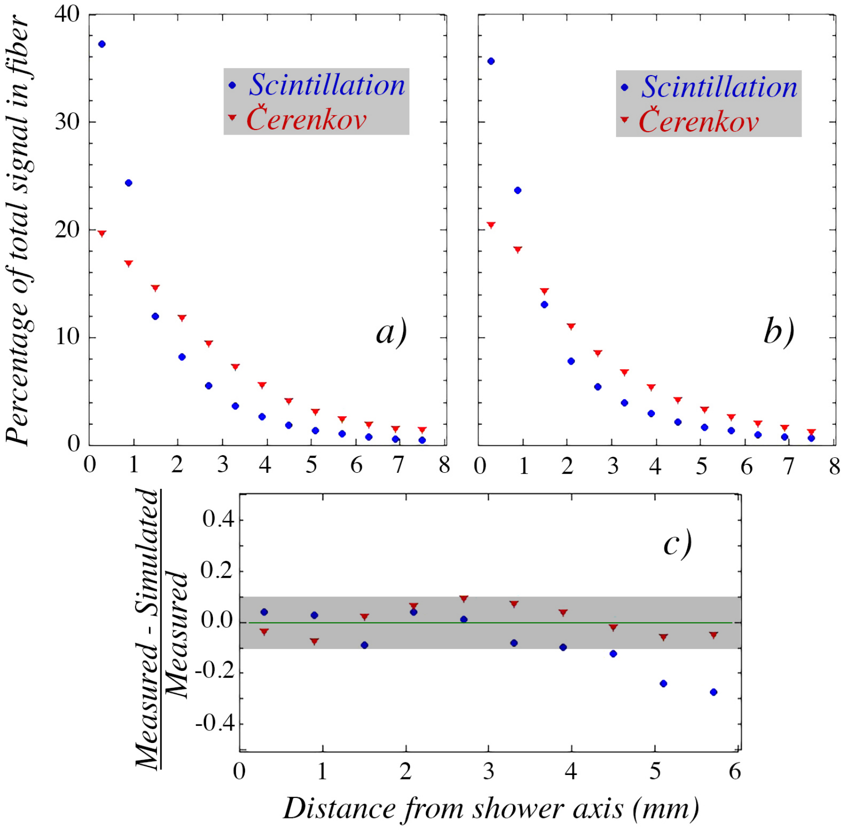

Figure 4.20: Lateral profiles of electromagnetic showers in the brass-fiber calorimeter for the scintillation and Cherenkov signals. Results for test-beam data (a) and for Geant4 simulated data (b). Fractional difference between the measured and simulated data (c). Image from [91].

4.2.6 Additional information from simulations

The tests described before were obtained with a very small calorimeter. The light yield, the light crosstalk and the shower profiles were obtained under the hypothesis of a 45% shower energy containment, as indicated by Geant4 simulations. We also considered that the light signals were on average 45% of the total light that would be

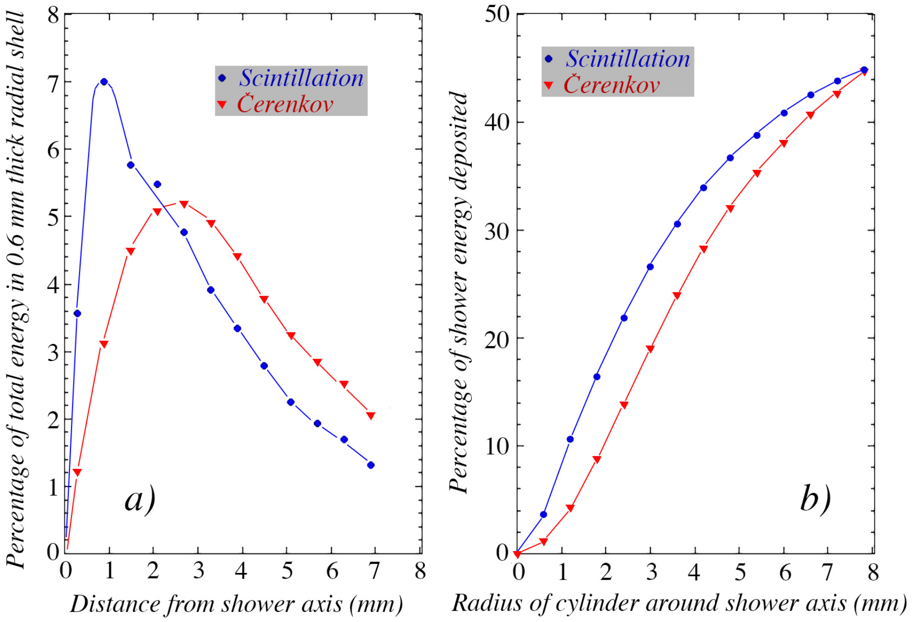

Figure 4.21: Radial profiles of electromagnetic showers in the brass-fiber calorimeter for the scintillation and the Cherenkov signals (a). Fraction of the signal deposited in a cylinder around the shower axis (b) for the scintillation and the Cherenkov signals. Both signals normalized to 45% containment. Image from [91].

produced by a same-structure calorimeter fully containing electromagnetic showers. While this assumption is certainly correct for the scintillation light, it might well not be the case for the Cherenkov light.

To address this issue we performed additional Geant4 simulations by enlarging the calorimeter volume, replicating the same structure, to fully contain electromagnetic showers and we recorded the totally produced signals (S and C). The scintillation signal, being proportional to the energy deposited in scintillating fibers, is in very good agreement with the shower energy containment: 45% of the scintillation signal come from the area covered by our calorimeter. However, the small prototype calorimeter area accounted for only 36% of the total signal. This means that the results obtained before must be further investigated with prototypes that can properly contain electromagnetic showers and this is one of the goal of the new prototype design discussed here after. Using this additional information from simulation the Cherenkov light would be 28.6/0.36=79 photoelectrons per GeV in a fully containing calorimeter. After correcting for the optical crosstalk, (10±4 photoelectrons), the Cherenkov light yield becomes to 69±5 photoelectrons per GeV deposited energy. The S/C light yields ratio is reduced to 46±6. Eventually, the radial shower pro-

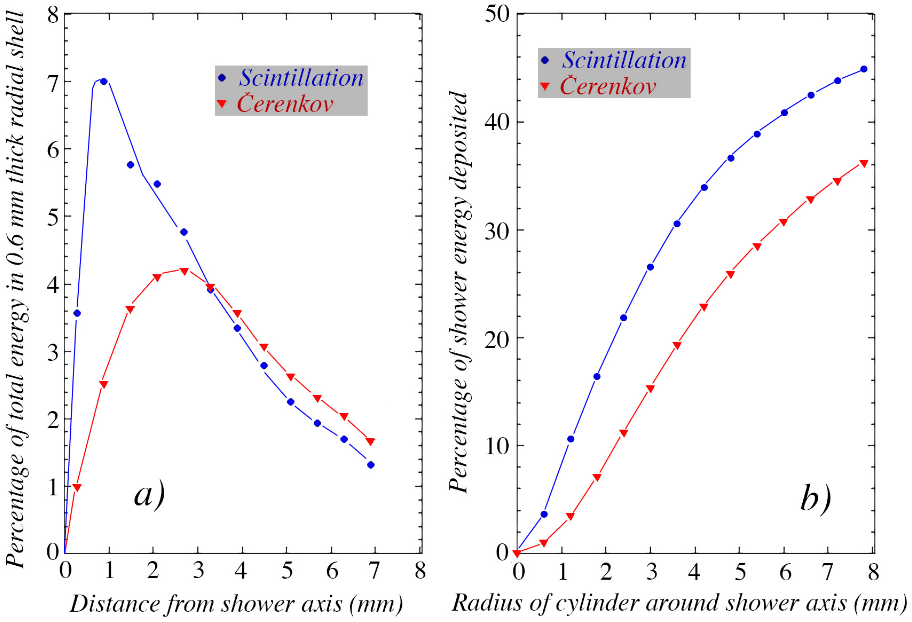

Figure 4.22: Radial profiles of electromagnetic showers in the brass-fiber calorimeter for the scintillation and the Cherenkov signals (a). Fraction of the signal deposited in a cylinder around the shower axis (b) for the scintillation and the Cherenkov signals. Scintillation signal normalized to 45% containment and Cherenkov signal normalized to 36% containment. See text for details. Image from [91].

files for the Cherenkov signal changes with this additional information, the updated results are shown in Fig. 4.22.

4.2.7 Restoring signal linearity

One of the main problems discussed above is a significant scintillation light saturation. Even with an ultra-low PDE of $\simeq 2\%$, a non-linear response was evident, especially true for the hottest fiber. One of the goals of the future dual-readout calorimeter prototypes will be a mitigation of this problem by using SiPMs with smaller pixel sizes. A second solution might come by attenuating the intensity of the scintillation light with filters positioned between the fiber ends and the light sensors. The final solution will most likely be a combination of the two.
The light-filtering approach was studied using the same prototype equipped with yellow-filters. The filter used is a Kodak gelatine Wratten 2 nr. 21 featuring a cut-off wavelength at $\simeq 550$ nm and a thickness of 0.1 mm that makes the light divergence negligible and the filter easily stickable on the mechanical support of the sensors. A measurement of the radiation spectrum of scintillating fibers was

performed by using a 350 nm UV lamp at 1 m from a fluorometer. The light distribution was convoluted with the SiPM PDE as a function of the light wavelength and eventually with the measured transmission curve of the filter. Fig. 4.23 (left) shows the unfiltered light spectrum of the fibers (blue dashed line), the SiPM PDE as a function of the light wavelength (black dotted line) and the filter transmission spectrum (red line). The convolution of these functions corresponds to the expected spectrum of the scintillation light chain and is shown as well (black dashed line and zoomed box). The effective attenuation factor of the filter can be measured as the ratio of the areas under the curves. It corresponds to $\simeq 77$.

The prototype equipped with yellow filters was tested using the same test-beam setup described before. The prototype was tested with pure electron beams with energies ranging from 10 to 40 GeV. This time the SiPMs reading out scintillating fibers were operated at the optimal bias voltage (57.5 V, +5 V_{Ov}) providing a high and stable PDE of 25%. Fig. 4.23 (right) shows the average scintillation signal (p.e.), corrected for the containment, per unit of deposited energy (GeV), as a function of the beam energy. Indeed, the calorimeter achieved 3% signal linearity and the hottest fiber had a mean value of $\simeq 9.8$ Sp.e./GeV, linear within 1%. The scintillation light amounted to 93 ± 3 Spe/GeV.

The benefit of adopting yellow filters in scintillating fiber calorimeters were studied in [101] and it is twofold. The response of a projective fiber calorimeter should depend as less as possible on the shower starting point. The attenuation of the light traveling inside the optical fibers is the main parameter involved. Electromagnetic showers are always contained in the first $20-25$ X_0 with minimal variations on the showering starting point, so all the produced light approximately travels the same distance before reaching the readout and signal fluctuations induced by light attenuation are negligible. On the other hand, hadrons produce particle showers with non negligible shower shape differences and the showering starting point follows the stochastic nature of the first inelastic nuclear interaction to occur. The typical length scale to describe hadronic showers is the calorimeter nuclear interaction length, λ_{int}. Assuming an exponential light attenuation into fibers, governed by an average light attenuation λ_{att}, the key parameter to reduce signal fluctuations due to light attenuation in fibers is $\lambda_{int}/\lambda_{att}$. It has been shown, [101], that yellow filters produce an higher effective light attenuation constant λ_{att} by cutting off the short wavelength component of the scintillation spectrum that is affected by shorter λ_{att}.

Moreover, the possibility to combine a filter with SiPMs with different cell sizes let us choose the best light yield configuration with great flexibility. For instance, keeping the same PDE while using 10 μm pixels, *i.e.* 10^4 cells, and using a filter attenuating light by a factor 18, we could achieve a scintillation light yield of 400 Sp.e./GeV.

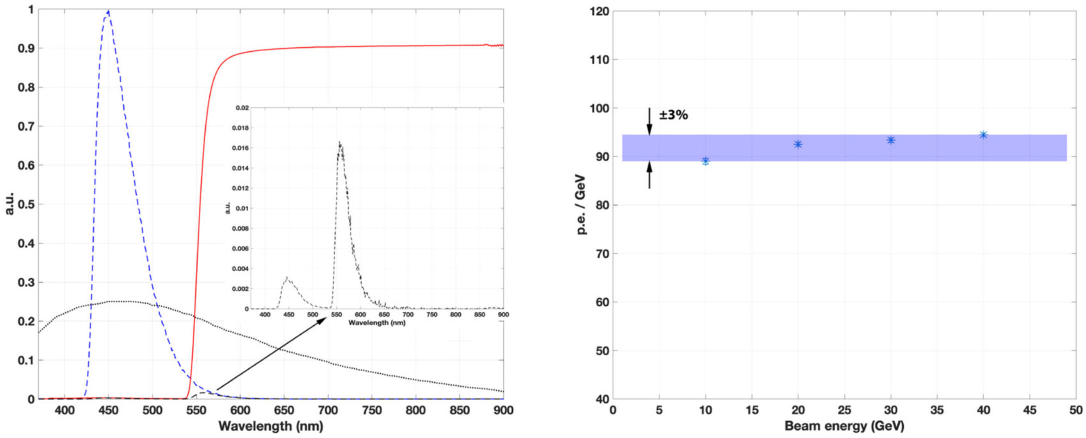

Figure 4.23: The measured scintillation spectrum (blue dashed), the Wratten 21 transmittance spectrum (red), the SiPM PDE curve (black dotted) and the expected spectrum (black dashed and zoomed box) (left). Average scintillation signal (photoelectrons) divided by the beam energy, as a function of the electron beam energy (GeV) (right). Image from [97].

While sampling electromagnetic showers, the stochastic term on the energy resolution is dictated by the sampling fluctuations and the photo-statistical fluctuations on light emission following the Poissonian nature of the scintillation light emission. Usually, these contributions are independent and contribute to the energy resolution term as follow:

$$\frac{a}{\sqrt{E}} = \frac{\sigma_{Npe} \oplus \sigma_{samp}}{\sqrt{E}} \tag{4.8}$$

while σ_{samp} can only be reduced by increasing the sampling fraction and the sampling frequency, σ_{Npe} can be reduced by increasing the light output per unit of deposited energy, *i.e.* the light yield. According to simulation, the sampling fluctuations term in scintillating fibers amounts to $\simeq 10\%$ in the geometry considered. The photo-statistical term, considering 93 Sp.e./GeV, amounts to 10%, hence the two terms contribute to the energy fluctuations with similar intensities. Assuming a scintillating light yield of 400 Sp.e./GeV the photo-statistical term would be pushed down to 5%.

4.3 Conclusions and path towards the 2021 test beam

The last test beams pointed out the advantages and drawbacks of using SiPMs as dual-readout calorimetry light sensors. The crosstalk between signals can be kept low by mechanically disentangling the two readout systems, the Cherenkov light yield is enhanced with respect to traditional PMT-based readout systems and the scintillation light yield can be tuned by choosing the proper combination of SiPM cell size and filter attenuation. Eventually, SiPMs provide an extremely high two-dimensional spatial resolution. On the other hand, a prototype capable of fully containing electromagnetic showers is needed to properly estimate the radial development of the two signals and additional work is required to design the best large scale application of SiPMs on dual-readout calorimeters. These are the features to be investigated with a new prototype, built in 2020, that will likely be beam-tested in 2021. As no data exists at present, the following is a brief introduction to the prototype design and construction.

Usually, fiber calorimeters are built starting from absorber plates in which grooves are mechanically created with the rolling technique. The calorimeter structure is obtained by stacking extruded grooves on top of each other. This technique easily works for ductile metals, like lead, but becomes tiresome and not very precise for hard absorber, like copper or copper-based alloys. A possible solution studied with the new prototypes uses absorber capillary tubes that are cheap and easily produced by industries. We only add here that 3D metal printing techniques are an interesting new possibility to build highly precise copper structures for fiber calorimeters.

The 2020 prototypes is made of nine identical modules, as shown in Fig. 4.24 (b), while each module is made of 16×20 tubs, as shown in Fig. 4.24 (a). Single modules dimensions are 32 mm wide and 32 mm height with a standard deviation within 80 μm. The nine modules are packed to create a 96×96 mm^2 electromagnetic calorimeter. According to simulations the average energy containment for electromagnetic showers amounts to 95%.

Each tube has an outer diameter of 2 mm with and an inner diameter of 1.1 mm. Both raddii have a tolerance of (-0 mm, +0.1 mm). 1 mm diameter fibers are inserted in each tube (160 fibers per type in each module). While the inner tube radius is bound to the fiber one, the outer radius might in future be reduced to increase both the calorimeter sampling fraction and sampling frequency. Tubs are 1 m long. Each module was built on a dedicated assembly station using six adjustable stations to pack capillaries in the correct positions. Micrometric screws were used for the fine tuning of capillaries positions. Between each layer, glue was deposited to fix the tube inter-positions.

The eight modules surrounding the central one will be readout using 2 PMTs each, one for the Cherenkov fibers and one for the scintillation fibers. The central one will be entirely readout by 320 SiPMs. To facilitate the fiber grouping and routing, each tubs raw is filled with the same type fibers (S or C), see Fig. 4.24. The SiPM chosen are HAMAMATSU S14160-1315PS with a pixel size of 15 μm over a 1.3×1.3 mm^2 area for a total of 7296 cells per sensor. Coupled to the same yellow filters described

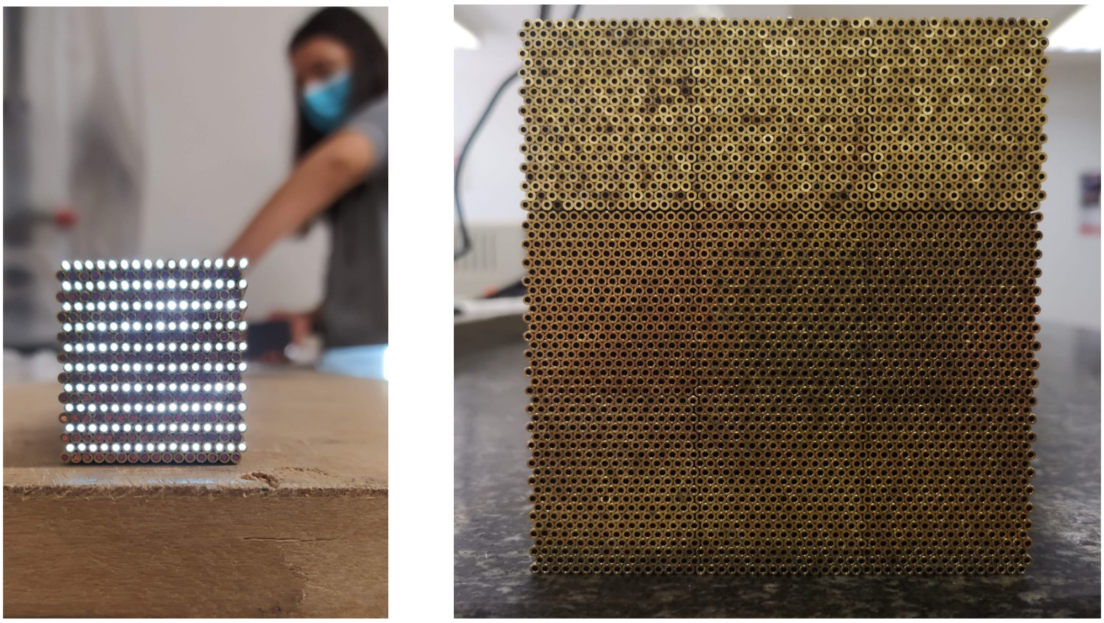

Figure 4.24: Front face of a single 16×20 tubs module when Cherenkov fibers are stimulated with light from the rear end (left). Front face of the 3×3 modules prototype (right).

above, this readout should be completely free from saturation effects when operating at the high PDE regime. To minimize the crosstalk, the readout is longitudinally staged: the fibers for the PMT readout are shorter than the fibers for SiPM readout. The central (SiPM) module is prolonged of about 20 cm, passing through the PMT readout stage and bringing the fibers to two independent SiPM readout structure for the scintillation and Cherenkov signals. Fig. 4.25, 4.26 shows a preliminary sketch of the readout system, and a picture of the 2020 prototype back-end before the readout mounting.

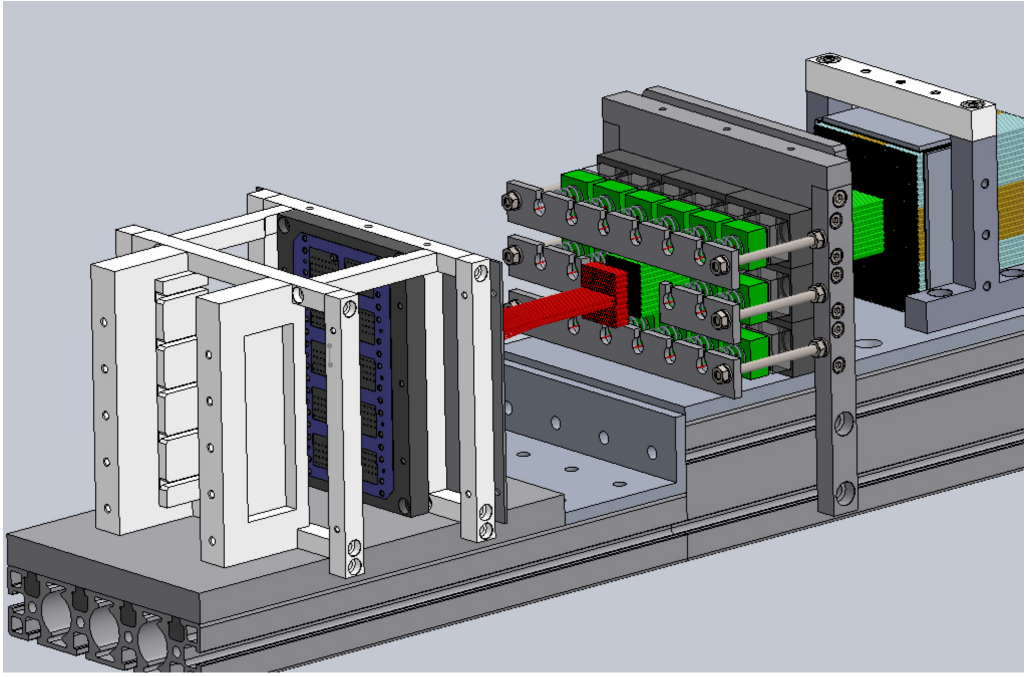

Figure 4.25: Sketch of the new calorimeter prototype light readout system. The eight modules surrounding the central one are shorter and are readout by PMTs on a first layer (green blocks). The central module is prolonged (red elements) through the first readout layer and its 320 fibers are individually brought to a second layer with an optical collector connecting each fiber to a dedicated SiPM (SiPMs not displayed).

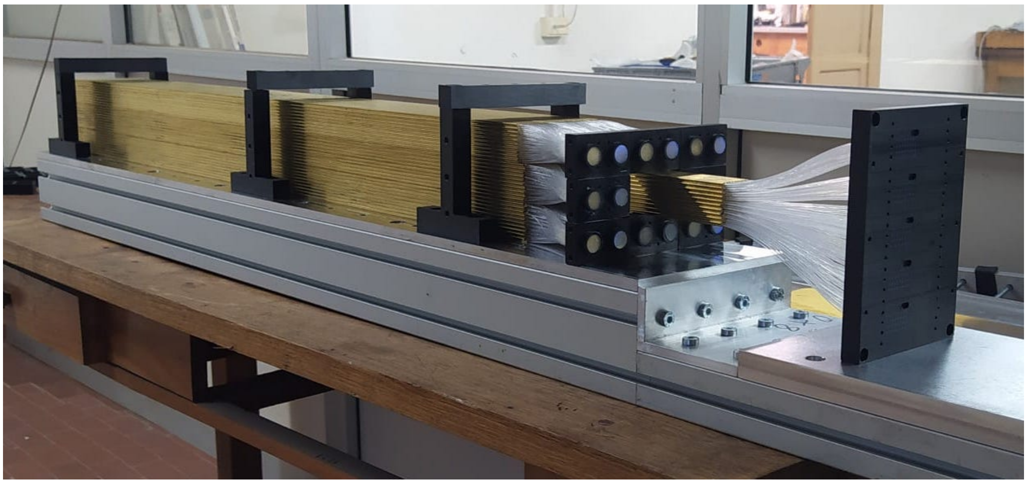

Figure 4.26: The 2020 prototype. Picture taken before the readout mounting. Fibers to be readout by PMTs are grouped into bunches. For the SiPM-readout central module, each fiber is extended out of the absorber tubes and routed to a dedicated hole on a plastic holder where a SiPM will be placed.

Chapter 5

Axion like particles search with the FCC-ee IDEA Detector

The chapter delineates the physics reach of the future e^+e^- circular collider (FCC-ee) for axion-like-particles production in the decay of heavy Standard Model resonances. The detector simulation is performed with a fast-simulation toolkit, Delphes 3, tuned on the IDEA Detector expected performance. The author of the thesis is the main author of this work.

5.1 Axion like particles search through 3-photon final states

Axion-Like Particles (ALPs) are gauge-singlet pseudoscalar particles with direct couplings to Standard Model (SM) particles. ALPs are predicted by any theory with spontaneously broken global symmetry. Their masses and couplings to SM particles are unpredicted and range over orders of magnitudes. Depending on these parameters ALPs can be non-thermal candidates for Dark Matter [102], or mediators to a dark sector. Since the leading ALP couplings to SM particles scales as the inverse of the scale of new physics (Λ^{-1}), ALPs become weakly coupled for large new-physics scales. Accessing the smallest possible couplings is thus crucial to reveal non-trivial information about a whole new physics sector.

ALP searches depend on the ALP mass(es) and couplings, and the most stringent constraints usually come from searches of ALPs decaying into photons. For masses below twice the electron mass, ALPs only decay into photons and the corresponding decay rate scales like the third power of the ALP mass. Hence, light ALPs are usually long lived and travel long distances before decaying. Their search is performed by helioscopes such as CAST [103] and SUMICO [104, 105] as well as through observations of the evolution of red giant stars [106, 107, 108] and the Supernova SN1987a [109, 110]. Further cosmological constraints exclude a large region of this parameter space being sensitive to very small ALP-photon couplings [111, 112]. ALP masses up to the GeV scale were considered by collider experiments such as BaBar, CLEO, the LEP and LHC experiments, searching for missing-energy signals as probes for long-lived ALPs with non-negligible couplings to SM particles [113, 114]. Beam-dump searches are also sensitive to ALPs with masses below $\simeq 1$ GeV radiated off photons and decaying outside the target [115, 116, 117, 118]. The different ALP production mechanisms at high-energy colliders allow to probe a large range of ALP masses and couplings. Beyond resonant production, ALPs can be produced in decays of heavy SM particles or in association with electroweak gauge bosons, Higgs bosons or jets. Depending on the ALP mass and coupling structure, ALPs produced at colliders can decay into photons, charged leptons, light hadrons or jets.

At the FCC-ee the most relevant production mechanism is the associated ALP production. Fig. 5.1 shows the Feynman diagram considering the ALP being radiated by a Z boson or a photon and being produced in association with a photon. This signature is the one investigated in the following. A theoretical explanation of the model can be found in [119].

The differential cross section for the process $e^+e^- \to \gamma a$ is given by:

$$\frac{d\sigma(e^+e^- \to \gamma a)}{d\Omega} = 2\pi\alpha\alpha^2(s)\frac{s^2}{\Lambda^2}\left(1 - \frac{m_a^2}{s}\right)^3 (1 + \cos^2\theta)(|V_\gamma(s)|^2 + |A_\gamma(s)|^2) \tag{5.1}$$

where

$$V_\gamma(s) = \frac{C_{\gamma\gamma}^{eff}}{s} + \frac{g_V}{2c_\omega^2 s_\omega^2}\frac{C_{\gamma Z}^{eff}}{s - m_Z^2 + i m_Z \Gamma_Z}, \tag{5.2}$$

$$A_\gamma(s) = \frac{g_A}{2c_\omega^2 s_\omega^2}\frac{C_{\gamma Z}^{eff}}{s - m_Z^2 + i m_Z \Gamma_Z} \tag{5.3}$$

with $g_V = 2s_\omega^2 - 1/2$ and $g_A = -1/2$. $\sqrt{s}$ is the center-of-mass energy, θ denotes the scattering angle of the photon relative to the beam axis, Γ_Z is the total width of the Z boson, s_ω and c_ω are $\sin\theta_w$ and $\cos\theta_w$ with θ_w being the weak mixing angle. $C_{\gamma\gamma}^{eff}$ and $C_{\gamma Z}^{eff}$ are the Wilson coefficients described in [119]. The cross section becomes independent of s in the energy limit $m_a^2 \ll s < \Lambda$.

The $e^+e^- \to \gamma a \to 3\gamma$ process only depends on the photon coupling $|C_{\gamma\gamma}^{eff}|/\Lambda$ once a specific relation with $C_{\gamma Z}$ is assumed. The projected reach can therefore be expressed in terms of m_a and $C_{\gamma\gamma}^{eff}$. In the following, being consistent with [119], we assume

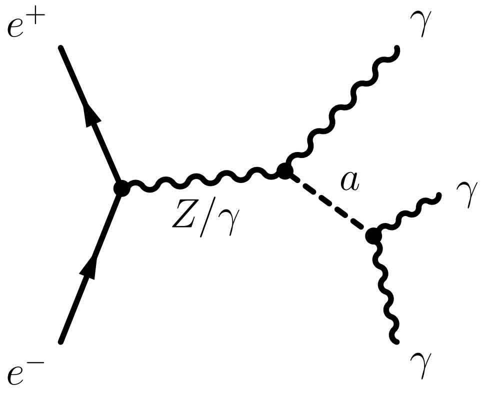

Figure 5.1: Feynman diagram for the ALP being radiated by a Z boson or a photon and produced in association with a photon.

$C_{\gamma Z} = -s_w^2 C_{\gamma\gamma}$. The relevant ALP branching ratio into the observed final state is set to 100%.

5.2 The Delphes 3 software and the IDEA fast simulation

The Delphes 3 software [120] is designed to simulate the response of a simplified and generic collider detector composed of an inner tracker, electromagnetic and hadron calorimeters, and a muon system. It is mostly used for phenomenological studies for which a parameterized detector response is in general good enough. Recently, the IDEA Collaboration adopted it as its fast-simulation framework.

All sub-detectors are cylinders organized concentrically around the beam axis. The user can specify the dimensions, the calorimeter cell segmentation and the strength of the (uniform) magnetic field. The sub-detectors performance, like the tracker momentum resolution and the calorimeter energy resolution, are provided by the user through dedicated detector description cards.

The input is made of the collection of stable particles from the most common event generators. Long-lived particles are propagated in the magnetic field inside the inner tracker volume. Charged particles follow an helicoidal trajectory up to the calorimeter volume, while neutral particles reach the calorimeter through straight lines. Charged particles are reconstructed as tracks according to a user-defined probability and a smearing on the norm of the transverse momentum vector is applied at the stage of particle propagation.

The simplified calorimeter system has a finite user-defined segmentation in pseudorapidity and azimuthal angle (η, ϕ) with dimensions specified by the user. The coordinate of the resulting calorimeter energy deposit, the tower, is computed as the geometrical center of the cells. Long-lived particles reaching the calorimeters deposit a fixed fraction of their energy in the corresponding ECAL (fECAL) and HCAL (fHCAL) cells. Since ECAL and HCAL are perfectly overlaid in ϕ, each particle reaches one ECAL and one HCAL cell. The resulting ECAL and HCAL cells are grouped in a calorimeter tower. Muons and neutrinos do not deposit energy in the calorimeter system.

The energy resolution of the ECAL and the HCAL are independently defined with the function:

$$\left(\frac{\sigma}{E}\right)^2 = \left(\frac{S(\eta)}{\sqrt{E}}\right)^2 + \left(\frac{N(\eta)}{E}\right)^2 + C(\eta)^2 \tag{5.4}$$

where S, N and C are defined by the user. The electromagnetic and hadronic energy deposits are accordingly smeared by a log-normal distribution and the final tower energy is computed as the sum of the corresponding energies. Calorimeter towers are, together with tracks, the ingredients used to reconstruct high-level objects.

Muons have an user-defined probability of being reconstructed, this probability vanishes outside the tracker acceptance and for momenta below some threshold to reject looping particles. Once a muon is reconstructed, its momentum is obtained by a parameterized Gaussian smearing of the initial 4-momentum as described before for the tracks. Also electrons are reconstructed according to a user-defined probability as a function of the energy and pseudorapidity. As for muons, the electron reconstruction efficiency vanishes outside the tracker acceptance and below some energy threshold. The reconstructed electron energy is given by a combination of the ECAL and tracker resolution: at low energy, the tracker resolution dominates, while at high energy, the ECAL energy resolution dominates. On the other hand, photons are reconstructed on the basis of the ECAL information only: true photons and electrons with no reconstructed track that reach the ECAL are reconstructed as photons. The reconstructed photon energy is obtained by applying the ECAL resolution function presented before.

For each reconstructed muon, electron or photon ($P = e, \mu, \gamma$), the isolation variable I is defined:

$$I(P) = \frac{\sum_{i \neq P}^{\Delta R < R, p_T(i) > p_{min}} p_T(i)}{p_T(P)} \tag{5.5}$$

The denominator is the transverse momentum of the particle of interest P and the numerator is the sum of all the p_T above p_{min} of the particles that lie within a cone of radius R around the particle P, except P. Typically values of $I \simeq 0$ indicate

Pole/threshold	E_{CM} (GeV)	Integrated luminosity (ab^{-1})
Z	91.6	150
W	160	10
H	240	5.0
t	365	1.5

Table 5.1: The FCC-ee center-of-mass energies and integrated luminosities.

that the particle is isolated. P is said to be isolated if $I(P) < I_{min}$ and the user can specify via the configuration file the three isolation parameters p_{min}, R and I_{min}.
In Delphes 3, jets can be reconstructed starting from different input collections, in particular there are *Generated Jets* clustered from generator level long-lived particles obtained after parton-shower and hadronization, *Calorimeter Jets* from the calorimeter towers and *Particle-flow Jets* from the clustering performed on both the particle-flow tracks and particle-flow towers. As jets are not of interest for this analysis we will not cover this part here.
For the analysis considered we parameterized the IDEA fast-simulation as follows. The calorimeter has an inner radius of 2.5 m, the tracker radius is 2 m and a straight magnetic field of 2 T is considered. The ECAL energy resolution is the one studied in Chap. 3 with Geant4 simulations. The ECAL cell size chosen is 6 cm × 6 cm; given the electromagnetic shower energy containment studied with Geant4, such a cell size would correspond to an energy containment close to 90%. The final state we are considering is made of three photons. To make sure that photons reaching three different ECAL cells are reconstructed as isolated objects, the photon isolation variable I_{min} was deliberately increased to 999.

5.3 Analysis strategy

The e^+e^- future circular collider, FCC-ee, is proposed to run at four different center-of-mass energies (E_{CM}), corresponding to the Z pole and the W, H and top-quark thresholds. In Tab. 5.1 we report the FCC-ee energies and integrated luminosities considered in the following.
The signature of interest corresponds to a three photons final state (Fig. 5.1), hence the associated standard model background is the *t-channel* process $e^+e^- \to 3\gamma$. The Feynman diagram is sketched in Fig. 5.2.

Monte Carlo simulation Both the signal and the background processes were generated for each proposed E_{CM}. For the signal process, different axion masses were considered, ranging from 0.2 GeV to 360 GeV. In total 31 signal samples were pro-

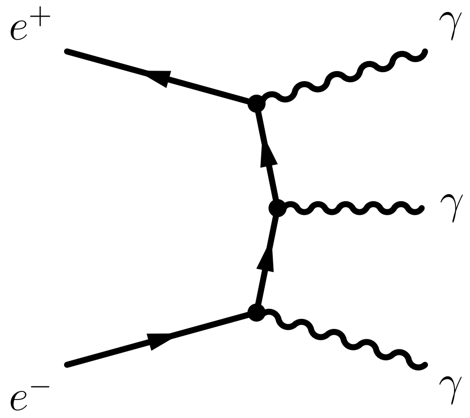

Figure 5.2: Feynman diagram for the FCC-ee 3-photon final state Standard Model background.

duced, varying both the axion mass and the center-of-mass energy. All samples were generated at LO with MadGraph5 [121] interfaced with PYTHIA 8.2 [93] for the showering. We are thankful to the authors of [119] for having provided the ALP UFO model for event simulation. For every sample, the photons were generated within the pseudorapidity range $|\eta| < 2.6$. Stable particles were then fed into the Delphes 3 detector simulation described above.

Some numbers might be useful to explain the experimental challenges posed by this search. The cross section for the background process at $E_{CM} = 91.6$ GeV, considering only photons with $|\eta| < 2.6$ and with energies above 1 GeV, amounts to 5.63 pb. While for the signal process, considering the same generation parameters, an axion mass of 20 GeV and a coupling of 0.01, the cross section is equal to 2.095 $\cdot\ 10^{-4}$ pb. At the foreseen luminosity, the FCC-ee will thus produce $840 \cdot 10^6$ background events and only 31400 signal events. The goal of this work is to exploit the different final states kinematics to define a cut-based Signal Region (SR) where the signal process becomes observable over the background. The strength of the signal depends on the coupling of the axion, and the minimal coupling for which a statistical significance of 2 is expected defines the expected sensitivity of the FCC-ee IDEA Experiment to the signature under study.
The statistical analysis is performed considering different values of the systematic uncertainty for the total background events evaluation. Details about the statistical analysis will be given in the following.
The analysis starts from the high-level objects reconstructed by the IDEA Delphes 3 simulation. Events with no tracks and exactly three reconstructed photons with

energy above 1 GeV are selected. The fraction of generated signal events passing these cuts is 90% or higher, depending on both E_{CM} and the axion mass considered. Out of the three reconstructed photons it is then mandatory to identify the two from the axion decay. For an axion of mass M, the energy of the photon produced in association to the axion is related to the known value of E_{CM} by the formula

$$E_\gamma = \frac{E_{CM}^2 - M^2}{2E_{CM}} \tag{5.6}$$

In the following the photon with energy nearest to E_γ is dubbed γ_3. The third photon (γ_3) is identified as the one being produced in association with the axion, while the other two photons (γ_1, γ_2) are considered originating from the axion decay. In this process no error on E_{CM} is considered. While in this phenomenological study M can be assumed to be the axion mass used in the event generation, in an actual experiment its value can be considered as ranging over the whole experiment physics reach.

The reconstructed 4-momenta from γ_1 and γ_2 are used to build the axion invariant mass, M_a. The discriminating variable M_{cut} is then built as

$$M_{cut} = \sqrt{(M_a - M)^2/\sigma_{M_a}^2 + (E_{\gamma_3} - E_\gamma)^2/\sigma_{E_{\gamma_3}}^2} \tag{5.7}$$

The usefulness of selecting events on the basis of the M_{cut} variable is well depicted in Fig. 5.3 that shows the $(E_{\gamma_3} - E_\gamma)^2/\sigma_{E_{\gamma_3}}^2$ variable versus the $(M_a - M)^2/\sigma_{M_a}^2$ variable for 10^5 signal events generated at $E_{CM} = 160$ GeV and an axion mass of 120 GeV (left) and the corresponding variables for the associated background process (right). Fig. 5.4 shows the distribution of the M_{cut} variable for the same signal and background events.

The SR definition proceeds by selecting only events with $M_{cut} < 1.5$. Between 55% and 60% of the signal events pass this selection regardless the center-of-mass energy and the axion mass. On the other hand, between 1% and 5% on the background events pass this cut depending on the test value M considered.

The event selection continues by looking at two other variables for events passing the M_{cut} cut. The two tagged photons from the axion decay are ordered by energy so that the relation $E_{\gamma_1}/E_{\gamma_2} < 1$ is always true. $E_{\gamma_1}/E_{\gamma_2}$ is the first variable considered. The second variable is the angular distance between these two photons, $\Delta R_{\gamma_1\gamma_2}$. Fig. 5.5 shows a scatter plot of the two variables for events of Fig. 5.3 passing the M_{cut} cut, results for the signal (left) and the background (right) are compared. An upper limit on $\Delta R_{\gamma_1\gamma_2}$ and on $E_{\gamma_1}/E_{\gamma_2}$, dependent on the explored axion mass and E_{CM}, provides an additional background rejection. The applied selections for each axion mass are given in Tab. 5.2. The signal and background yields, corresponding

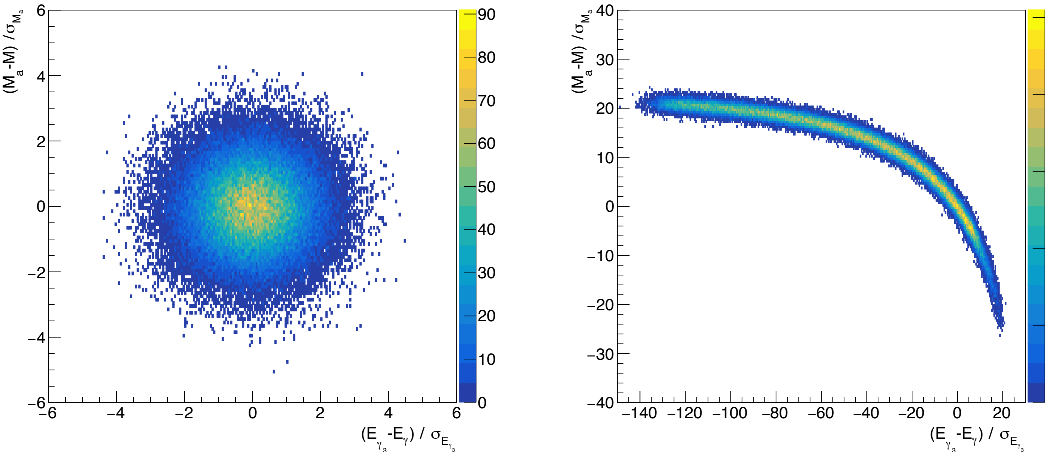

Figure 5.3: The $(E_{\gamma 3} - E_{\gamma})^2/\sigma^2_{E_{\gamma 3}}$ variable versus the $(M_a - M)^2/\sigma^2_{Ma}$ one for 10^5 signal events generated with $E_{CM} = 160$ GeV and an axion mass of 120 GeV (left) and for the associated background process (right).

to 10^5 event samples, after this selection, for three axion masses, a coupling value of 0.01, at $E_{CM} = 160$ GeV, are shown in Tab. 5.3. The fraction of events passing the signal region requirements is used to predict the actual number of events that would pass the event selection at the FCC-ee IDEA Detector, using the known production cross-section and machine integrated luminosity. Two numbers are thus needed: the number of observed events n under the axion existence hypothesis, given by the sum of the signal and background events passing the SR selection at the FCC-ee, and the number of expected background SM events b.

The formula used for estimating the significance (Z) of observing n events given a prediction of $b \pm \sigma$ events is

$$Z = \begin{cases} +\sqrt{2\Big(n \ln[\frac{n(b+\sigma^2)}{b^2+n\sigma^2}] - \frac{b^2}{\sigma^2}\ln[1+\frac{\sigma^2(n-b)}{b(b+\sigma^2)}]\Big)} & \text{if } n \geq b \\ -\sqrt{2\Big(n \ln[\frac{n(b+\sigma^2)}{b^2+n\sigma^2}] - \frac{b^2}{\sigma^2}\ln[1+\frac{\sigma^2(n-b)}{b(b+\sigma^2)}]\Big)} & \text{if } n < b \end{cases} \tag{5.8}$$

The origin of this formula is discussed in [122], and is consistent with a Poisson-counting likelihood where the background rate nuisance parameter is constrained by an auxiliary Poisson measurement.

The significance was calculated per each signal sample considered. While calculating the significance, different systematic error values (σ) over the expected number of events (b) were used: $\sigma = 1‰$, 1% and 5% of b. The significance estimation was performed several times over a loop while changing the coupling value affecting the

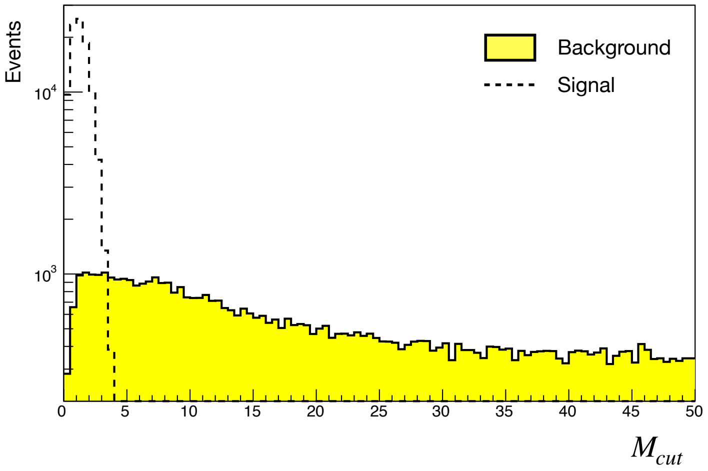

Figure 5.4: The M_{cut} variable distribution for 10^5 signal events generated with $E_{CM} = 160$ GeV and an axion mass of 120 GeV (dashed line) and for the associated background process (yellow filled area).

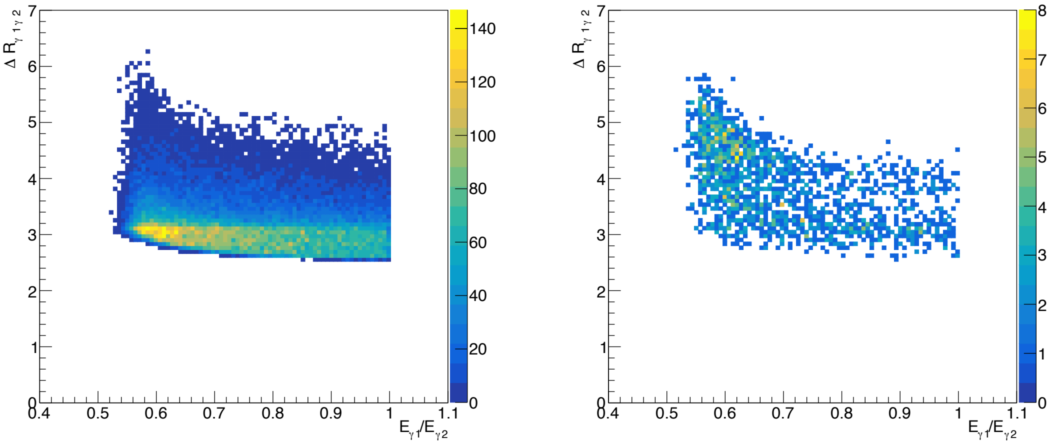

Figure 5.5: The $E_{\gamma_1}/E_{\gamma_2} < 1$ variable versus the $\Delta R_{\gamma_1\gamma_2}$ one for events of Fig. 5.3 passing the M_{cut} selection. Signal and background samples, left and right respectively.

E_{CM} (GeV)	M_A (GeV)	Cut
90	0.2	$(E_{\gamma_1}/E_{\gamma_2} > 0.20$ and $\Delta R_{\gamma_1\gamma_2} < 0.06)$
90	0.5	$(E_{\gamma_1}/E_{\gamma_2} > 0.20$ and $\Delta R_{\gamma_1\gamma_2} < 0.08)$
90	1	$(E_{\gamma_1}/E_{\gamma_2} > 0.20$ and $\Delta R_{\gamma_1\gamma_2} < 0.12)$
90	5	$(E_{\gamma_1}/E_{\gamma_2} > 0.20$ and $\Delta R_{\gamma_1\gamma_2} < 0.60)$
90	10	$(E_{\gamma_1}/E_{\gamma_2} > 0.20$ and $\Delta R_{\gamma_1\gamma_2} < 1.00)$
90	20	$(E_{\gamma_1}/E_{\gamma_2} > 0.25$ and $\Delta R_{\gamma_1\gamma_2} < 1.30)$
90	30	$(E_{\gamma_1}/E_{\gamma_2} > 0.20$ and $\Delta R_{\gamma_1\gamma_2} < 1.60)$
90	40	$(E_{\gamma_1}/E_{\gamma_2} > 0.20$ and $1.60 < \Delta R_{\gamma_1\gamma_2} < 2.50)$
90	50	$(E_{\gamma_1}/E_{\gamma_2} > 0.30$ and $\Delta R_{\gamma_1\gamma_2} < 2.70)$
90	60	$(E_{\gamma_1}/E_{\gamma_2} > 0.70)$
90	70	$(E_{\gamma_1}/E_{\gamma_2} < 0.75$ and $\Delta R_{\gamma_1\gamma_2} < 3.14)$ or $(\Delta R_{\gamma_1\gamma_2} < 3.05)$
90	80	$(E_{\gamma_1}/E_{\gamma_2} < 0.65$ and $\Delta R_{\gamma_1\gamma_2} < 3.10)$ or $(\Delta R_{\gamma_1\gamma_2} < 3.05)$
90	85	$(E_{\gamma_1}/E_{\gamma_2} < 0.85$ and $\Delta R_{\gamma_1\gamma_2} < 3.14)$ or $(\Delta R_{\gamma_1\gamma_2} < 3.15)$
160	30	$(0.10 < E_{\gamma_1}/E_{\gamma_2} < 0.20$ and $\Delta R_{\gamma_1\gamma_2} < 3.00)$ or $(E_{\gamma_1}/E_{\gamma_2} > 0.20$ and $\Delta R_{\gamma_1\gamma_2} < 1.80)$
160	80	$(0.20 < E_{\gamma_1}/E_{\gamma_2} < 0.40$ and $\Delta R_{\gamma_1\gamma_2} < 3.20)$ or $(e > 0.40$ and $\Delta R_{\gamma_1\gamma_2} < 2.40)$
160	100	$(0.40 < E_{\gamma_1}/E_{\gamma_2} < 0.50$ and $\Delta R_{\gamma_1\gamma_2} < 3.20)$ or $(e > 0.50$ and $\Delta R_{\gamma_1\gamma_2} < 3.00)$
160	120	$(E_{\gamma_1}/E_{\gamma_2} > 0.30$ and $\Delta R_{\gamma_1\gamma_2} < 3.00)$
160	140	$(E_{\gamma_1}/E_{\gamma_2} > 0.77$ and $\Delta R_{\gamma_1\gamma_2} < 3.10)$
160	155	$(E_{\gamma_1}/E_{\gamma_2} > 0.96$ and $\Delta R_{\gamma_1\gamma_2} < 3.10)$
240	100	$(E_{\gamma_1}/E_{\gamma_2} > 0.25$ and $\Delta R_{\gamma_1\gamma_2} < 2.00)$
240	150	$(0.38 < E_{\gamma_1}/E_{\gamma_2} < 0.45$ and $\Delta R_{\gamma_1\gamma_2} < 3.30)$ or $(E_{\gamma_1}/E_{\gamma_2} > 0.45$ and $\Delta R_{\gamma_1\gamma_2} < 3.00)$
240	180	$(E_{\gamma_1}/E_{\gamma_2} > 0.55$ and $\Delta R_{\gamma_1\gamma_2} < 3.30)$
240	220	$(E_{\gamma_1}/E_{\gamma_2} > 0.85$ and $\Delta R_{\gamma_1\gamma_2} < 3.10)$
240	235	$(E_{\gamma_1}/E_{\gamma_2} > 0.96$ and $\Delta R_{\gamma_1\gamma_2} < 3.15)$
365	50	$(E_{\gamma_1}/E_{\gamma_2} > 0.25$ and $\Delta R_{\gamma_1\gamma_2} < 0.90)$
365	100	$(E_{\gamma_1}/E_{\gamma_2} > 0.20$ and $\Delta R_{\gamma_1\gamma_2} < 1.40)$
365	150	$(0.20 < E_{\gamma_1}/E_{\gamma_2} < 0.40$ and $\Delta R_{\gamma_1\gamma_2} < 2.00)$ or $(E_{\gamma_1}/E_{\gamma_2} > 0.40$ and $\Delta R_{\gamma_1\gamma_2} < 1.90)$
365	200	$(0.30 < E_{\gamma_1}/E_{\gamma_2} < 0.40$ and $\Delta R_{\gamma_1\gamma_2} < 3.00)$ or $(E_{\gamma_1}/E_{\gamma_2} > 0.40$ and $\Delta R_{\gamma_1\gamma_2} < 2.50)$
365	240	$(E_{\gamma_1}/E_{\gamma_2} > 0.55$ and $\Delta R_{\gamma_1\gamma_2} < 2.50)$ or $(E_{\gamma_1}/E_{\gamma_2} < 0.55$ and $\Delta R_{\gamma_1\gamma_2} < 3.30)$
365	300	$(E_{\gamma_1}/E_{\gamma_2} > 0.65$ and $\Delta R_{\gamma_1\gamma_2} < 3.30)$
365	360	$(E_{\gamma_1}/E_{\gamma_2} > 0.96$ and $\Delta R_{\gamma_1\gamma_2} < 3.40)$

Table 5.2: The event selection applied, after the $M_{cut} < 1.5$ selection, on $E_{\gamma_1}/E_{\gamma_2}$ and $\Delta R_{\gamma_1\gamma_2}$.

axion process cross section. For every coupling value considered the number of observed events n was changed accordingly to the rule $\sigma(e^+e^- \to \gamma a \to 3\gamma) \propto |C^{eff}_{\gamma\gamma}|^2$. The scan was stopped when a significance of 2 was found and the corresponding coupling is considered as the minimal one within the reach of the FCC-ee IDEA Detector.

5.4 Results

This work represents the first attempt to evaluate the FCC-ee IDEA sensitivity to axion-like-particles through the 3-photon final state, considering axion masses from 0.2 GeV to 360 GeV. Results for the four FCC-ee center-of-mass energies are shown in Fig. 5.6.

Sample	Axion mass (GeV)	Cleaning cuts	M_{cut}	$\Delta R_{\gamma_1\gamma_2}$ & $E_{\gamma_1\gamma_2}$
Signal	100	92947	58446	37850
Background	-	100000	2078	384
Signal	120	92983	58331	22888
Background	-	100000	1923	149
Signal	140	93048	58026	18152
Background	-	100000	2249	145

Table 5.3: The signal and background events after the three step event selection presented. Result for 10^5 signal samples with $E_{CM} = 160$ GeV, a coupling of 0.01, and three axion masses and for the corresponding SM background samples.

The extremely high statistics at the Z pole leads to lower excluded minimal couplings. On the other hand, the higher center of mass energies of the W, H and top thresholds allow to probe higher ALP masses. We underline that the very-low axion-mass range ($M_a < 5$ GeV) is particularly challenging for the detector. Indeed, while reconstructing the axion invariant mass, the impact of the position resolution of the two observed photons on σ_{M_a} starts to be comparable with the one provided by the energy resolution. Therefore, a detailed detector description is needed instead of the simplified one from Delphes 3. In the present study, we included a smearing on the photon impact position driven by the ECAL cell size (6 cm × 6 cm), however, as described in Chap. 3, the high granularity of the IDEA dual-readout calorimeter is likely to provide a better position resolution. Moreover, as the axion mass reduces, the two photons originating from the axion become more collimated thus increasing the difficulty in reconstructing them as two isolated photons. In the present description, they are reconstructed as two if they reach the ECAL at two different cells, otherwise they are reconstructed as a single photon and the event is discarded. We believe that a more realistic detector description, as the one provided by the IDEA calorimeter full simulation, is needed to validate the estimated sensitivity in the low energy range.

The existing limits for the ALP-photon coupling, as a function of the ALP mass, were originally computed in [123, 124]. Fig. 5.7 illustrates a subset of these bounds for ALP masses between 10^{-3} GeV and 2 TeV and coupling values from 10^{-3} to 10^{1} TeV^{-1}, it can be compared to Fig. 5.6. ALPs have been constrained in beam dump experiments at SLAC, probing resonant production of neutral pseudoscalar mesons in photon interactions with nuclei, corresponding to the area in yellow. Upsilon meson decays searched by the CLEO and BaBar Experiments excluded the region shaded in green. Collider experiments constraints have been derived by recasting results on mono-photon, diphoton and tri-photon searches at LEP (light blue corresponds to Run 2 of LEP whereas dark blue corresponds to Run 1 of LEP), the Tevatron (magenta, by CDF) and the LHC. Projections for p-p collisions ($pp \to p(\gamma\gamma \to \gamma\gamma)p$) drawn from [125] are also marked (grey area). Fig. 5.7 also shows the more recent results on light-by-light scattering by the ATLAS and CMS collaborations in Pb-Pb collisions (bluish green area) [126, 127]. We note that collider-based constrains assume $\mathrm{Br}(a \to \gamma\gamma) = 1$.

Fig. 5.7 also includes the recent projections for ion-ion and proton-ion collisions, derived in [128]. They consider p-Pb collisions at 8.16 TeV per nucleon pair and a luminosity of 5 pb^{-1}, Pb-Pb collisions at 5.02 TeV per nucleon pair and a luminosity of 10 nb^{-1} and Ar-Ar collisions at 7 TeV per nucleon pair and a luminosity of 3 pb^{-1}, corresponding to the future opportunities of the heavy-ion program at the LHC [129]. Interestingly, Ar-Ar collisions could constrain the ALP-photon coupling for masses between 100 GeV to about 400 GeV, covering a region of parameter space that is also accessible by the FCC-ee running at the W, H and top thresholds. Below 100 GeV, Pb-Pb collisions reach the lowest couplings possible among the ion and proton-ion collisions. They should be compared with the sensitivity expected for the FCC-ee Z-pole running where similar bounds, if not tighter, on the lowest accessible couplings are found. Moreover, the FCC-ee will provide the possibility to effectively search for ALPs with masses below $\simeq 5$ GeV, a region that, at present, looks inaccessible to other probes. Following what stated above, we believe that a detailed simulation of the IDEA Detector and the FCC-ee beam background is needed to better constrain that region.

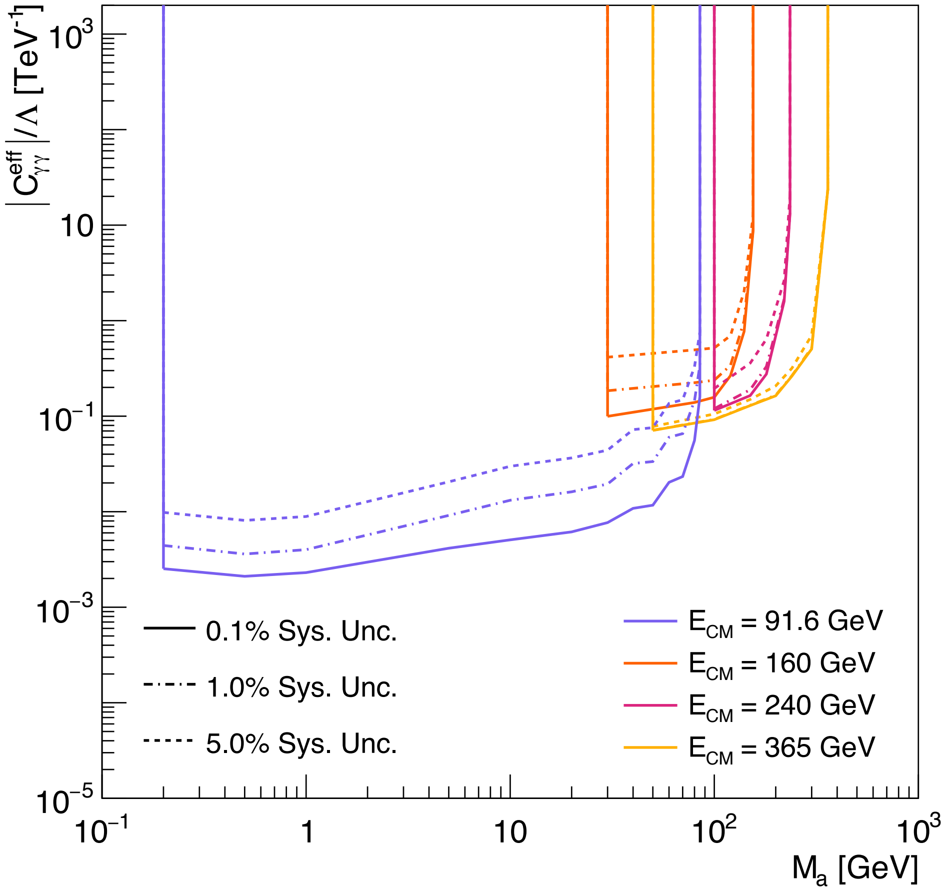

Figure 5.6: Projected sensitivity regions for searches for $e^+e^- \to \gamma a \to 3\gamma$ at the FCC-ee IDEA Detector assuming $\mathrm{Br}(a \to \gamma\gamma) = 1$.

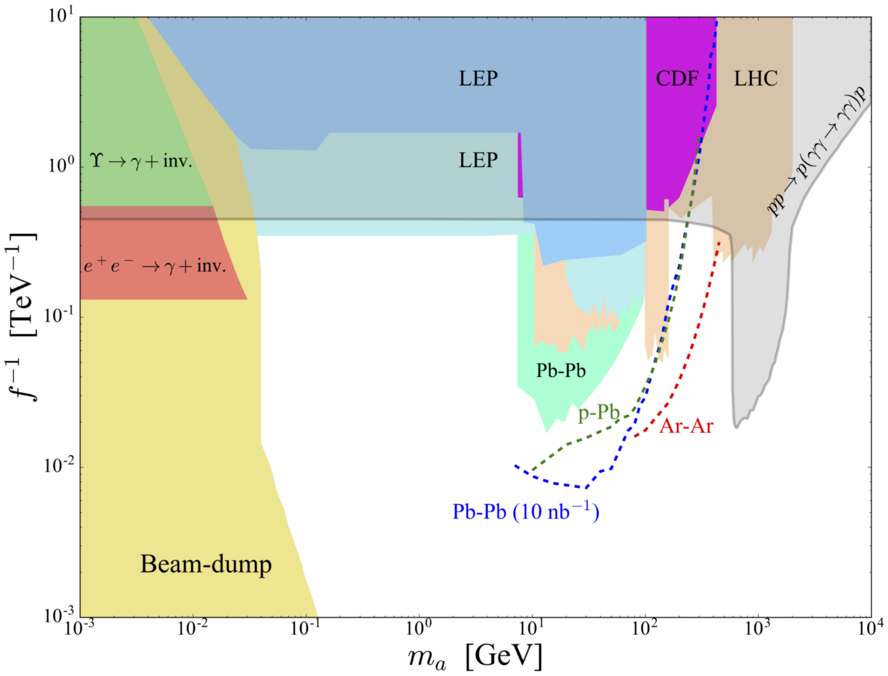

Figure 5.7: Exclusion bounds on the ALP-photon coupling as a function of the ALP mass (see text and [123, 124]). Projections for p-p collision ($pp \to p(\gamma\gamma \to \gamma\gamma)p$ are drawn from [125]. Projections derived in [128] for future p-Pb, Pb-Pb and Ar-Ar collisions at the LHC (under the assumption $\text{Br}(a \to \gamma\gamma) = 1$) are shown as well (dashed lines). Image from [128, 130].

Part II

Construction and testing of the ATLAS New Small Wheel MicroMegas chambers

Chapter 6

The ATLAS Experiment

The chapter is an introduction to the ATLAS Detector, one of the four big experiments at the Large Hadron Collider. The detector description is needed to frame the ATLAS Phase-I upgrade work presented in the next chapter.

6.1 The ATLAS Detector

ATLAS [131, 132] is a multi-purpose experiment operating at the Interaction Point 1 (IP-1) on the LHC ring. The ATLAS Detector is cylindrical in shape, and is approximately 44 meters long with a radius of 12 meters. The total weight is more than 7000 ton. It is the largest of the four big LHC experiments. Given the large variety of particles and energies produced by $p-p$ collisions, the design of the experiment was driven by the necessity to precisely measure and identify as many collision products as possible.

The detector structure exploits a series of concentrical layers surrounding the interaction point. The detector closest to the IP, known as Inner Detector (ID), is a tracking detector with the task of measuring the trajectory of charged particles and reconstructing the interaction vertex. To bend the path followed by charged particles, the ID is surrounded by a thin solenoid providing an axial magnetic field of 2 T. The solenoid is followed by the calorimeters that measure the energies of electromagnetic and hadronic particle cascades.

The muon system surrounds the calorimeters and reconstructs muon track bending thanks to three very large air-core toroid magnets. A cut view of the ATLAS detector is shown in Fig. 6.1. The cylindrical part in the central region is referred to as the barrel region and the detectors at both ends form the end caps.

ATLAS uses a right-handed coordinate system with its origin at the nominal IP in

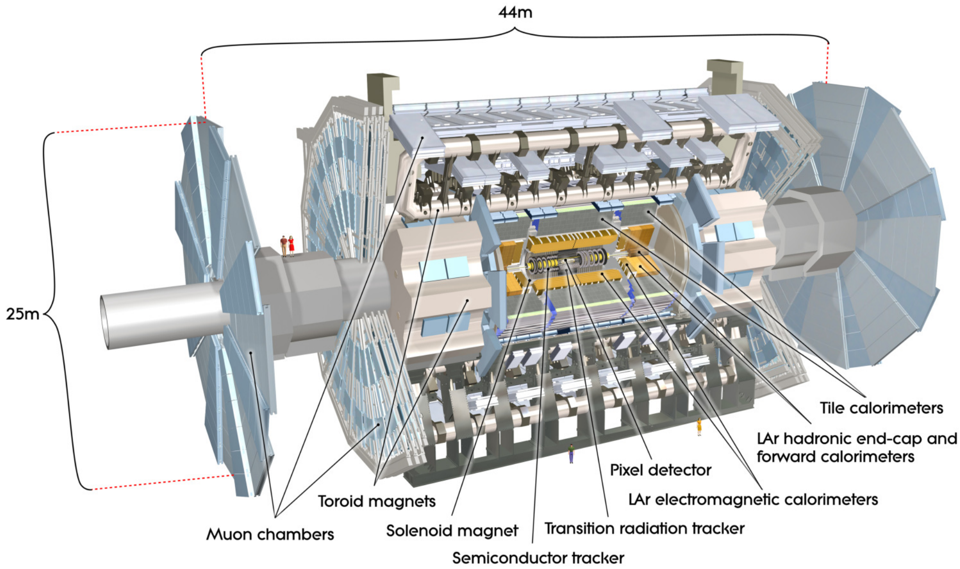

Figure 6.1: Drawing of the ATLAS detector showing the different sub-detectors and the magnet systems. Image from [132].

the center of the detector and the z-axis along the beam pipe. The x-axis points from the IP to the center of the LHC ring, and the y-axis points upward. Cylindrical coordinates (r, ϕ) are used in the transverse plane, with ϕ being the azimuthal angle around the beam pipe. The pseudorapidity is defined in terms of the polar angle θ as $\eta = -\ln(\tan(\theta/2))$. The pseudorapidity η has been chosen because of its Lorentz-invariant property. A large absolute value of η ($\eta \rightarrow \infty$) indicates a direction close to the beam line, while a small value indicates a direction close to the xy-plane.

When using the angular coordinates η and ϕ, it is useful to express the angular separation between two particles in terms of ΔR, defined as $\Delta R = \sqrt{\Delta\eta^2 + \Delta\phi^2}$. It is also useful to define, for every reconstructed particle, the transverse momentum measured in the xy-plane, *i.e.* $p_T = \sqrt{p_x^2 + p_y^2}$. Protons interacting at the IP have momenta largely parallel to the beam axis and the initial transverse momentum is zero. Therefore, due to momentum conservation and neglecting the contribution carried out by particles escaping within the beam pipe, the sum of the transverse momenta of the event particles should be zero. A large total transverse momentum (also called "missing transverse momentum") can be generated in the presence of invisible particles like neutrinos or Beyond Standard Model (BSM) weakly-interacting particles. The missing transverse momentum is usually one of the most important discriminating variables of physics analyses.

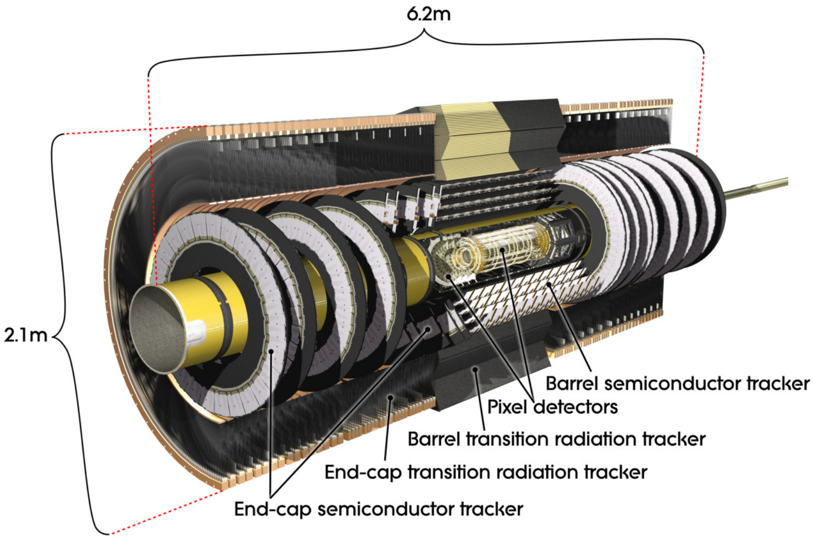

Figure 6.2: Schematic view of the ATLAS inner detector. The IBL (not shown here) is located between the beam pipe and the innermost layer of the Pixel Detector. Image from [132].

6.2 Inner detector

The ATLAS Inner Detector [132] is 6.2 m long and has a diameter of 2.1 m. It covers the pseudorapidity region with $|\eta| < 2.5$. The ID offers a precise measurement of track impact parameters, with resolution down to 80 μm along the z-axis and 20 μm in the transverse plane. It also performs transverse momentum measurement in the range 0.5 - 150 GeV within $|\eta| < 2.5$ and electron identification within $|\eta| < 2.0$.
The ID exploits four complementary sub-systems, located at different radii from the beam pipe: three high-resolution silicon detectors - the new Insertable B-Layer (IBL), the Pixel Detector and the Semi-Conductor Tracker (SCT) - and a gaseous straw-tube tracking device, the Transition Radiation Tracker (TRT). Fig. 6.2 shows the ID sub-detectors made of cylindrical concentric barrel modules in the central region and disk-shaped end-cap modules in the forward regions. A cut view of the ATLAS ID is shown in Fig. 6.3.

Insertable B-layer The Insertable B-Layer (IBL) [133, 134] is the tracking sub-detector closest to the beam pipe, at a radial distance of only 3.3 cm from the beam axis. Its installation took place during the long shutdown between Run 1 and Run 2. The upgrade reason was the radiation damage of the innermost Pixel layer, which was expected to spoil vertex reconstruction precision in Run 2 and 3. The IBL is a very-high-resolution semiconductor pixel detector, with a spatial hit resolution

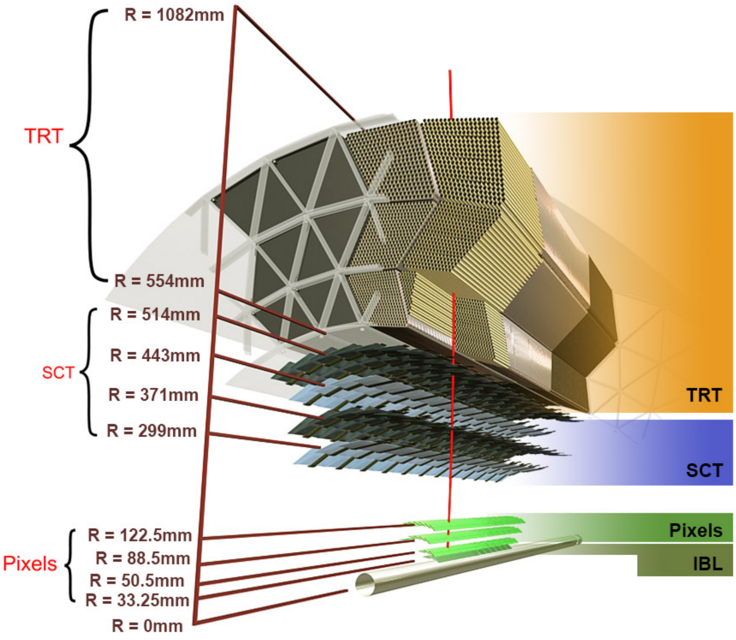

Figure 6.3: Cut-away view of the ATLAS Inner Detector. Image from [132, 133, 134].

of 8 μm in the $r\phi$-plane and 40 μm along the z-axis, and covers the barrel region up to $|\eta| < 2.9$. The installation of the IBL improved the track reconstruction, providing more precise vertex and impact parameter measurements. The latter is extremely important for efficient b-jet identification, the so-called b-tagging, to which the detector owes its name.

Pixel detector The Pixel Detector consists of three concentric cylinders around the beam axis, at average radii of 5.05, 8.85 and 12.2 cm, and three end-cap disks located between 9 and 15 cm from the interaction point. The pixel sensors are made of oxygenated 250-μm-thick n-type wafers with readout pixels on the n^+ implanted side of the detector. The pixel size is 50×400 μm^2 and is dictated by the size of the corresponding readout cell on the readout chip. This cell-size determines the intrinsic resolution of the detector. The high granularity of the pixel system is the crucial element to achieve a robust pattern recognition in the challenging environment of ATLAS, dominated by high occupancy and pile-up. Exploiting more than 80 million readout channels, a spatial resolution of 10 μm in the $R\phi$-plane and 115 μm along z is obtained in the barrel. It changes to 10 μm in the $R\phi$-plane and 115 μm along z in the end-cap regions.

Semiconductor tracker The SemiConductor Tracker (SCT) is radially the next sub-detector of the ID. It is made of four concentric barrel layers positioned between radii 30 cm and 52 cm and nine disks in each end cap, providing coverage up to $|\eta| < 2.5$. It uses semiconducting silicon technology, but its sensors are segmented into strips with a 80 μm pitch. In the end-cap disks, the strip pitch ranges from 56.9 to 90.4 μm to accommodate the more complex geometry. The strip geometry was chosen to deal with the larger surface to be covered. To measure two coordinates per hit, each SCT module exploits two layers of strips with a relative rotation (stereo angle) of 40 mrad. The SCT has around 6.3 million of readout channels and a resolution of 17 μm in the azimuthal direction and 580 μm along the z-axis.

Transition radiation tracker The outermost ID sub-detector is the Transition Radiation Tracker (TRT). It uses straw tubes filled with a Xe-based gas mixture and interleaved with transition radiation material (polypropylene fibers in the barrel and foils in the end caps). It enables electron identification through the detection of transition-radiation photons emitted during the passage of the electrons in the transition-radiation material. The detector geometry is divided into a barrel region ($|\eta| \leq 0.8$) and two end-cap sections, made of multi-plane wheels ($|\eta| < 2.0$). To compensate the lower resolution compared to silicon detectors, the TRT exploits a large number of hits per track. The barrel has a total of 73 layers of 144-cm-long straw tubes, parallel to the beam axis, covering from 56 to 107 cm in the radial direction. The two end caps consist of 18 wheels of radially oriented straw tubes, located at a distance between 0.8 m and 2.7 m along the z-axis. The first 14 nearest to the interaction point cover a radius of 64 to 102 cm, while the last four wheels extend down to a radius of 48 cm to provide coverage of the full pseudorapidity range. The TRT detector provides typically 36 measurements per track (except in the barrel-end-cap transition region, where this number decreases to a minimum of 22 crossed straws) with a spatial resolution of 130 μm.

6.3 Calorimeter system

The calorimeter system [132] is sketched in Fig. 6.4 (an introduction to calorimetry is given in Chap. 2). It makes use of different technologies across the different regions of pseudorapidity, absorbing particles up to $|\eta| = 4.9$. In general, the calorimeter system is made of an Electromagnetic CALorimeter (ECAL), placed right after the solenoid, and a Hadronic CALorimeter (HCAL), surrounding the ECAL. Nevertheless a three-layer Forward CALorimeter (FCAL) is located on both end-cap sides at the highest values of $|\eta|$, performing both electromagnetic and hadronic energy

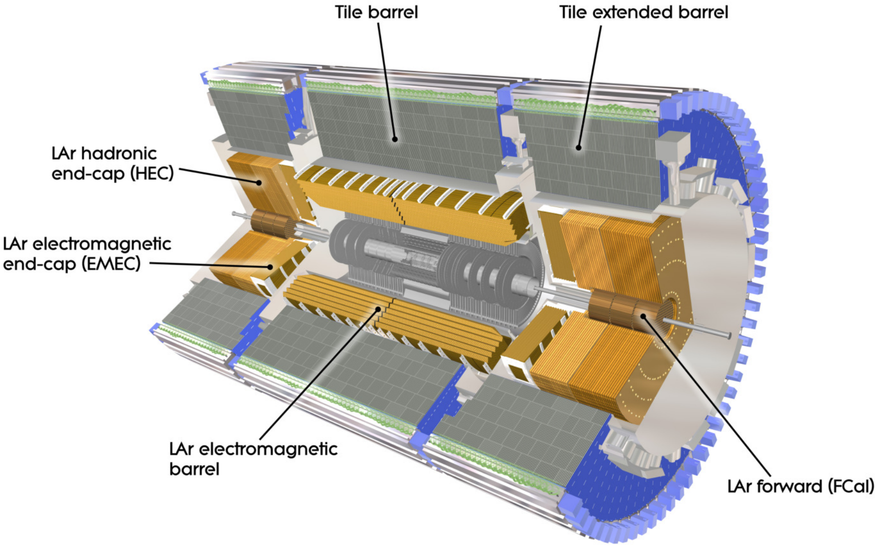

Figure 6.4: Schematic illustration of the calorimeter system of the ATLAS detector. Image from [132].

measurements. ATLAS uses only sampling calorimeters.
To avoid longitudinal particle leakage, the calorimeter system is designed to contain jets up to the TeV scale. The ECAL (electromagnetic) thickness is 22 radiation lengths for the barrel and 24 for the end caps, and the total (hadronic) thickness of the combined ECAL+HCAL system amounts to 11 interaction lengths. This choice efficiently reduces the longitudinal leakage and the probability of punch-through events in which charged pions pass through the calorimeter without inducing a nuclear reaction and end up into the muon system.

Electromagnetic calorimeter The ECAL is divided into a barrel part ($|\eta| < 1.475$) and two end caps ($1.375 < |\eta| < 3.2$). The barrel extends in the radial direction from 2.8 m to 4 m and is made of 32 modules. The end caps are constituted by two coaxial wheels: the outer one covers the region from $|\eta| = 1.375$ to $|\eta| = 2.5$, while the inner wheel extends the coverage up to $|\eta| = 3.2$. In total, they extend over radii from about 0.3 m to 2.1 m, and are segmented into eight wedge-shaped modules each. The ECAL is composed of different layers of lead, used as absorber, interleaved with Liquid Argon (LAr) as active material. LAr is chosen because of its intrinsic radiation hardness. It is held in a liquid state at 89 K thanks to cryostats (one for the barrel and one for each end cap). The absorber plates and electrodes are arranged in an accordion geometry, which allows a full azimuthal coverage without cracks and a good energy and space resolution.

The ECAL is longitudinally segmented. In the region $|\eta| < 2.5$, dedicated to precision physics, the calorimeter is divided into three sections. The strip section, $\simeq 6$ X_0 thick (upstream material included), is composed of narrow strips with a pitch of $\simeq 4$ mm in the η direction. This high segmentation allows particle identification and precise position measurements in η. The middle section extends up to 24 X_0 and is transversely segmented into square towers of size $\Delta\eta \times \Delta\phi = 0.025 \times 0.025$ ($\simeq 4\times4$ cm^2 at $\eta = 0$). It is designed to contain most of the energy of the showers created by photon and electrons with energy up to 50 GeV. The back section has a granularity of 0.05 in η and a thickness varying between 2 X_0 and 12 X_0, and it is used to estimate the energy leakage in the hadronic cells. Outside the precision physics region ($2.5 < |\eta| < 3.2$), the calorimeter is segmented in only two longitudinal sections and has a coarser granularity of 0.1×0.1 in $\Delta\eta \times \Delta\phi$. Due to transitions between different detector layout, some regions of the ECAL have a worst performance, in particular for $\eta = 0$, for η between 1.37 and 1.52, and at $|\eta| = 2.5$.

In the region $0 < |\eta| < 1.8$, a pre-sampler detector is placed inside the solenoid in order to study the shower development before the calorimetry system and estimate the energy loss inside the ID. It consists of a liquid argon active layer of thickness 1.1 cm in the barrel region and 0.5 cm in the end caps.

Hadronic calorimeter The HCAL measures hadronic showers up to $|\eta| = 3.2$. It is composed of two different detectors: the Tile Hadronic Calorimeter (TileCal) and the liquid-argon Hadronic End Cap calorimeter (HEC). The TileCal active elements are plastic polystyrene scintillator tiles interspersed by steel plates. It is divided into three parts: a barrel, covering the region up to $|\eta| < 1.0$, and two extended barrels, which cover the region between $|\eta| > 0.8$ and $|\eta| < 1.7$. The TileCal has an inner radius of 2.28 m and an outer radius of 4.25 m, corresponding approximately to 7.4 λ. The HEC, which covers the region $1.5 < |\eta| < 3.2$, is a copper-LAr sampling calorimeter with a flat-plate design. It consists of two wheels per end cap with an outer radius of 2.03 m, each of them containing two longitudinal sections, for a total of four layers per end cap.

Forward calorimeter The Forward Calorimeter (FCal) covers the $3.1 < |\eta| < 4.9$ region. It is made of three calorimeter modules per end cap, one electromagnetic and two hadronic ones. All modules consist of a metal matrix containing the electrode structures in longitudinal channels, with liquid argon as active medium. The electromagnetic layer uses copper as absorber, whereas tungsten is used in the hadronic ones. The FCal goal is to provide information for the reconstruction of the missing transverse momentum and of very forward jets. It has a high resistance to radiation, which is extremely important due to the high particle flux in the forward region.

6.4 Muon spectrometer

The Muon Spectrometer (MS) [132] is the outermost sub-detector of the ATLAS Experiment. Its main goal is to trigger on high-p_T muons and di-muon pairs and to measure the muon transverse momentum with a resolution of 10% at $p_T = 1$ TeV up to $|\eta| < 2.7$.

A magnetic field, provided by a toroidal magnetic system and perpendicular to the muon tracks, bends them in the Rz-plane, thus allowing momentum measurements. The system is composed of three sets of eight flat superconducting coils, one for the barrel region ($|\eta| < 1.4$) and two for the end-cap regions ($1.6 < |\eta| < 2.7$). The latter are inserted into the central toroid with a rotation of 22.5°, in order to optimize the bending power in the transition region between the two systems. The magnetic field is 0.5 T in the barrel and 1 T in the end caps.

The layout of the MS is shown in Fig. 6.5. The barrel region is formed by three concentric cylinders equipped with Monitor Drift Tube chambers (MDTs) at radii of about 5, 8 and 10 meters. Each MDT chamber is made of six layers of drift tubes in the middle and outer stations and eight layers in the innermost one. The middle and the outer stations are also instrumented with Resistive Plate Chambers (RPCs) for triggering purposes. Two RPCs are installed in the middle stations and a single one in the outer stations. In the end-cap regions, the MS consists of three independent wheels per side, at a distance of 7.5, 14 and 22.5 meters from the interaction point. The first wheel, called Small Wheel, uses Cathode Strip Chambers (CSCs) close to the beam pipe and MDTs in the outer part for tracking purpose, while Thin Gap Chambers (TGCs) are installed close to the MDTs to measure the track coordinate in the direction perpendicular to the MDT wires. The Phase-I Small Wheel upgrade is presented in Chap. 7. The two outermost wheels, known as Big Wheels, rely, for track reconstruction, only on MDT chambers. Finally, the central wheel includes two TGC doublets and one triplet for providing trigger signals.

Monitor drift tube chambers Monitor Drift Tubes (MDTs) are cylindrical aluminum tubes, with a 3 cm diameter and a 50 μm tungsten-rhenium wire at high voltage at the cylinder center. They are filled with Ar:CO$_2$ (93:7) gas mixture and are operated at a pressure of 3 bar (absolute). The tube length ranges between 0.9 m and 6.2 m. Three or four layers of tubes form a multi-layer and two multi-layers separated by an aluminum spacer form a chamber. The hit resolution of each tube is 80 μm, for a chamber resolution of about 50 μm. The large drifting length and

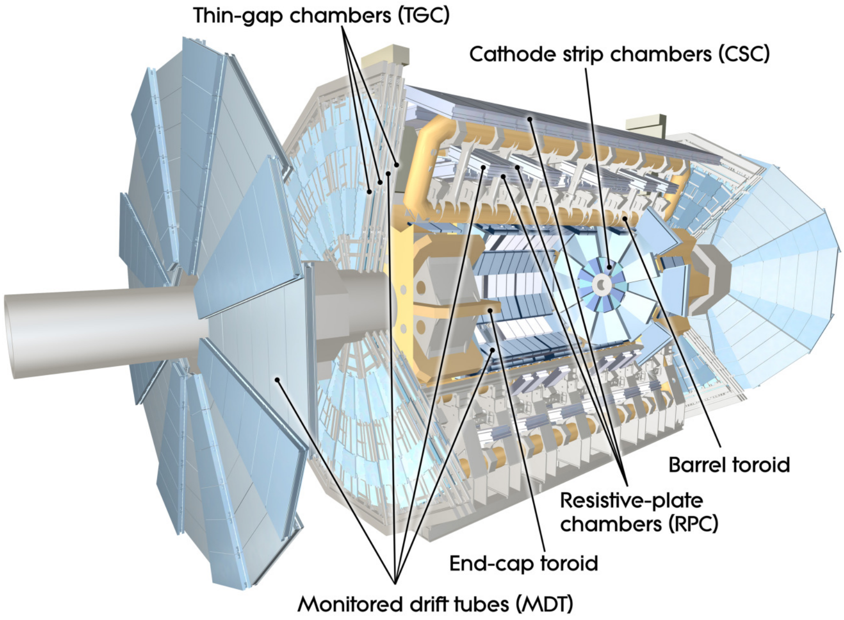

Figure 6.5: Layout of ATLAS Muon Spectrometer. Image from [132].

the high gas pressure make MDTs slow with respect to standard Micro-Pattern Gas Detectors (MPGDs). Therefore, MDTs can be successfully operated up to a rate of about 200 Hz/cm^2 and CSCs are used in the region $|\eta| > 2$ of the innermost end-cap layer, where the flux exceeds this rate.

Cathode strip chambers Cathode Strip Chambers (CSCs) are multi-wire proportional chambers made of four planes. Each plane consists of a layer of anode wires placed between two layers of cathode strips, one with strips parallel to the wires and the other one perpendicular. It provides independent measurements of η and ϕ. The strip segmentation in η is finer than in ϕ, giving a resolution of about 60 μm in the precise coordinate and 5 mm in the other one. An Ar:CO$_2$:CF$_4$ gas mixture (30:50:20) is fluxed in these chambers.

Resistive plate chambers Resistive Plate Chambers (RPCs) are fast detectors used for triggering purposes. A single module is composed of two parallel plastic resistive plates, with a 2 mm gas gap filled with a freon-based gas mixture. The signal is read out via capacitive coupling to metallic strips. Readout strips are placed on the outer faces of the resistive plates. An RPC chamber is composed of two detectors, next to each other, called units. Each unit consists of two independent detector layers, each one read out by two perpendicular sets of strips.

Thin gap chambers Thin Gap Chambers (TGCs) are multi-wire proportional chambers with a wire-to-cathode distance smaller than the one between the wires (1.4 mm vs 1.8 mm). The signal read from the wires provides a position resolution in the η coordinate of a few mm, while copper strips provide a measurement of the ϕ coordinate with a similar precision. The chambers are operated in a quasi-saturated mode, leading to a typical signal rising time of 5 ns. The gas used is a mixture of 45% n-Pentane and 55% CO_2.

6.5 Trigger

Fig. 1.2 (in Chap. 1) is usually used to explain the need of a trigger system. At center-of-mass energies of $\simeq$ 13 TeV the integrated cross section for $p - p$ collisions is 10^8 nb. Given an instantaneous luminosity of $\simeq 10^{34}$ cm^{-2} s^{-1}, it implies an event rate of about 1 GHz inside the ATLAS detector. To cope with such a tremendous event rate, only a small fraction of the events can be recorded. The ATLAS Trigger System performs a run-time event selection, recognizing and saving only events interesting for the analyses. A first hardware level identifies the (potentially interesting) events to be read out. A second selection, fully implemented on a standard computing farm, further reduces the number of events, to be permanently collected, down to a rate of approximately 1 kHz.

The trigger system operating during Run 2 [135] exploits two different trigger technologies: a Level-1 (L1) hardware-based trigger and a software-based High-Level-Trigger (HLT). The L1 trigger purpose is to use the information provided by the calorimeters and by the muon spectrometer to determine Regions of Interest (RoIs) in the detector, searching for high transverse-momentum leptons, photons, hadrons and jets . Electrons and photons are triggered using energy deposits in the EM calorimeter, while hadron and jet candidates are selected through the hadronic calorimeter information. Muons are instead triggered based on coincidences of hits among multiple layers of the Muon Spectrometer trigger chambers. The L1 trigger reduces the event rate down to 100 kHz.

The HLT uses a staged selection (starting from the RoIs) for a final output rate of about 1 kHz. The first pass uses a finer granularity (with respect to the L1 trigger system) and includes the ID measurements within the RoIs. The last stage, instead, performs a fully event reconstruction, using (online) the ATLAS offline software. On top of the events that pass the selection requirements, directly written to the main analysis stream(s), events requiring longer processing time are saved to a debug stream for later reprocessing.

Chapter 7

The ATLAS New Small Wheel Micromegas chambers

The chapter describes the Micromegas detector construction and the high-voltage testing for the ATLAS New Small Wheel Phase-I upgrade. A quarter of the chamber construction was performed by an INFN consortium (the units of Roma Tre, Roma La Sapienza, Pavia, Napoli, Cosenza, Lecce and the National Laboratory of Frascati) in the period 2017-2020. The Pavia group took the responsibility of the readout-panel construction and of the printed circuit board QA/QC testing. Micromegas chambers were later assembled at the Laboratori Nazionali di Frascati and then shipped to CERN for the integration within the ATLAS detector. The chamber acceptance test consists of high-voltage testing with and without irradiation. The author of the thesis participated in the construction and QA/QC of the readout panels in Pavia and spent the whole of 2019 at CERN, with an INFN Simil-Fellowship position, working on the Micromegas high-voltage testing. Related results have been published in [136] and [137].

7.1 The ATLAS New Small Wheel upgrade

The New Small Wheel (NSW) project [138] consists in the construction and installation of two new innermost stations of the ATLAS forward muon spectrometer, replacing the current Small Wheels, with the final integration scheduled for the end of the Long Shutdown 2 (LS2) of LHC. The project is dictated by the need to adopt tracking and triggering detectors with stable performances during the Large Hadron Collider High-Luminosity operation (HL-LHC), for which a luminosity up to 7.5×10^{34} cm^{-2}s^{-1} is expected. The NSW will operate in the ATLAS pseudorapi-

tidy region $1.3 < \eta < 2.7$ under a high hit rate (up to 15 kHz/cm^2), reconstructing tracks with high precision and providing additional information with respect to the original muon trigger system. The whole project is part of the ATLAS Phase-I upgrade focusing on the Level-1 trigger. The goal is to maintain the low-transverse momentum (p_T) trigger threshold for single leptons (e and μ) while keeping the Level-1 trigger rate at a manageable level. Without the planned upgrades for the muon and the calorimetry trigger system, for the single-lepton Level-1 triggers, either the p_T threshold would have to be raised, or the trigger rate pre-scaled, leading to acceptance losses for several interesting physics processes.
The ATLAS muon spectrometer uses three stations, both in the barrel and end-cap regions, and reconstructs the muon momentum through the measurement of the track curvature in the ATLAS toroid magnetic field. At the high luminosity foreseen, especially in the end-cap regions, the spectrometer performance could degrade due to the reasons explained in the following.

- The efficiency of the muon tracking chambers degrades with the increasing background rate. This degradation is more evident in the end-cap first stations, the current Small Wheels, where the cavern background is higher. Fig. 7.1 shows the current Small-Wheel Monitored Drift Tubes (MDT) hit efficiency and segment-finding efficiency as a function of the hit rate. The first one decreases linearly with the hit rate. Due to the linear dependence of the hit rate on the instantaneous luminosity, a linear decrease of the MDT efficiency is expected after an increase of the instantaneous luminosity. Already at a luminosity of 3×10^{34} cm^{-2}s^{-1}, a big fraction of the Small Wheel MDTs will have to operate at rates much above 300 kHz with a poor segment-finding efficiency. The muon momentum resolution critically depends on the segment presence in the first stations of the muon spectrometer because that is the only segment measured before the magnetic-field track bending. Therefore, a lower efficiency there would drastically compromise the muon momentum resolution.

- The original Level-1 muon trigger in the end-cap regions is based on track segment reconstruction in the Thin Gap Chambers (TGC) of the middle muon station. The variable of interest is the track p_T determined with the measurement of the track momentum, from the angle of the segment with respect to the direction linking the hit to the interaction point. Low energy particles, originating from the interaction with the material located between the Small Wheel and the Middle Station, interact with the Middle Station with no preferential angle and produce a high component of fake high-p_T triggers. This problem is well depicted by the fact that the Level-1 muon trigger in the end-cap regions is eight to nine times higher than the barrel one. Fig. 7.2

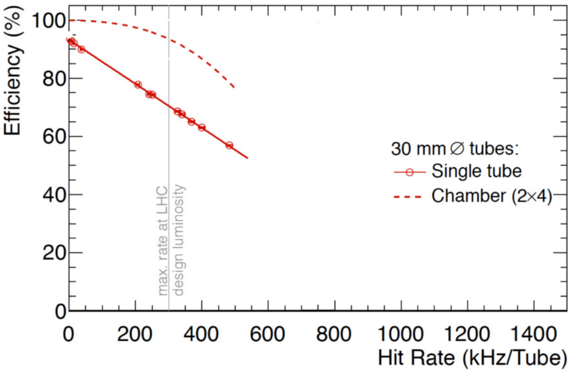

Figure 7.1: MDT tube hit (solid line) and track-segment efficiency (dashed line) for an MDT chamber with 2 × 4 tube layers, as a function of the tube hit rate. The design luminosity refers to 1×10^{34} cm^{-2}s^{-1}. Image from [138].

shows the L1 ($p_T > 10$ GeV) trigger distribution and compares it to a subset of matched muon candidates with the reconstructed muon (with either $p_T > 3$ GeV or $p_T > 10$ GeV). Already at a luminosity of 3×10^{34} cm^{-2}s^{-1}, triggering on muons with $p_T > 20$ GeV, a Level-1 trigger rate of approximately 60 kHz is expected, dominated by triggers from the end caps. This number has to be compared with the total available 100 kHz Level-1 trigger rate budget.

Both these issues demand for specific solutions before the HL-LHC ATLAS operation. Moreover, pattern recognition will become more challenging, the higher the pile-up and the backgrounds are, hence the need to design a detector with a higher hit redundancy.

The chosen solution is to replace the Small Wheels with new detectors that can provide the Level-1 muon trigger system with redundant track-segment information to reject tracks not originating from the IP (fake triggers). The goal is to keep the low-p_T muon trigger rate (usually $p_t > 20$ GeV) applicable during the HL-LHC operation. It has been shown [138] that a 20 kHz Level-1 muon trigger (targeting $p_T > 20$ GeV) can be achieved at a luminosity of 3×10^{34} cm^{-2}s^{-1} if the NSW will provide, to the current trigger system, track segments with an angular resolution of 1 mrad, a granularity better than 0.04×0.04 in the $\eta\phi$-plane and an online track-segment reconstruction efficiency larger than 95%. On the tracking side, the new detector must have a stable single-layer hit efficiency up to a 15 kHz/cm^2 hit rate to provide muon p_T measurements with a precision of 10% for 1 TeV muons. This requirement calls for a tracking detector with a single-layer hit resolution better that 100 μm and a segment-finding efficiency better than 97% for muons with p_T greater than 10 GeV.

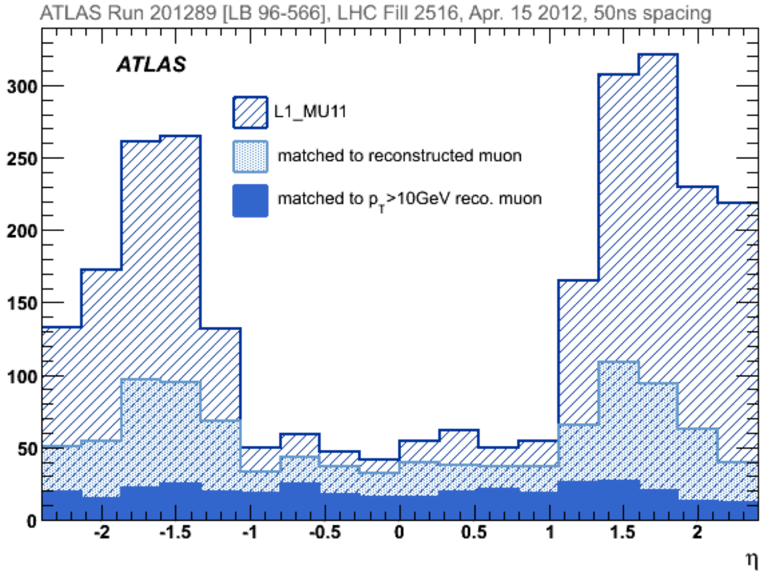

Figure 7.2: Level-1 muon trigger ($p_T > 10$ GeV) as a function of η. Also shown results for the subset of candidates with a match to an offline reconstructed muon with $p_T > 3$ GeV or $p_T > 10$ GeV. Image from [138].

7.2 The New Small Wheel layout

The NSW adopts two detector technologies for planar gaseous detectors: the small-strip Thin Gap Chambers (sTGC), mostly devoted to triggering purposes thanks to their single bunch crossing identification capability, and the Micro Mesh Gaseous Structure (MicroMeGaS or MM) detectors, providing highly precise hit information given their small gas gap and strip pitch. For a complete description of the sTGC chambers refer to [138].

Each NSW consists of 16 multi-layer sectors. Each sector is made of six sTGC and four MM detectors arranged in order to maximize the distance between the sTGCs (sTGC-MM-MM-sTGC). Each MM chambers provides four hits so that a muon passing through the NSW produces eight tracking hits. The 16 sectors are divided into 8 small and 8 large. Small sectors are mounted on the mechanical structure side that will be closer to the IP and large sectors behind them. The detectors weight is transferred to the supporting structure through a cylindrical plug connected to the internal shielding, the *new JD*, to be placed after the end-cap calorimeter system. The NSW diameter is about 9 m. Fig. 7.3 shows the structure of the NSW (left) and the detector composition for a single sector (right). Fig. 7.4 shows a picture of the installation of the first (small) sector on the NSW-A mechanical structure from December 2019.

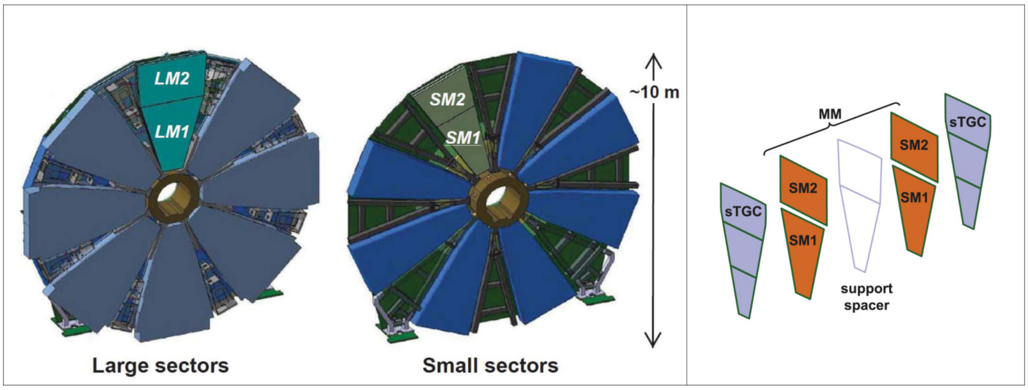

Figure 7.3: Two side structure of the NSW with sectors (left). Sketch of a single sector made of four MM and six sTGC chambers (right). Image from [136].

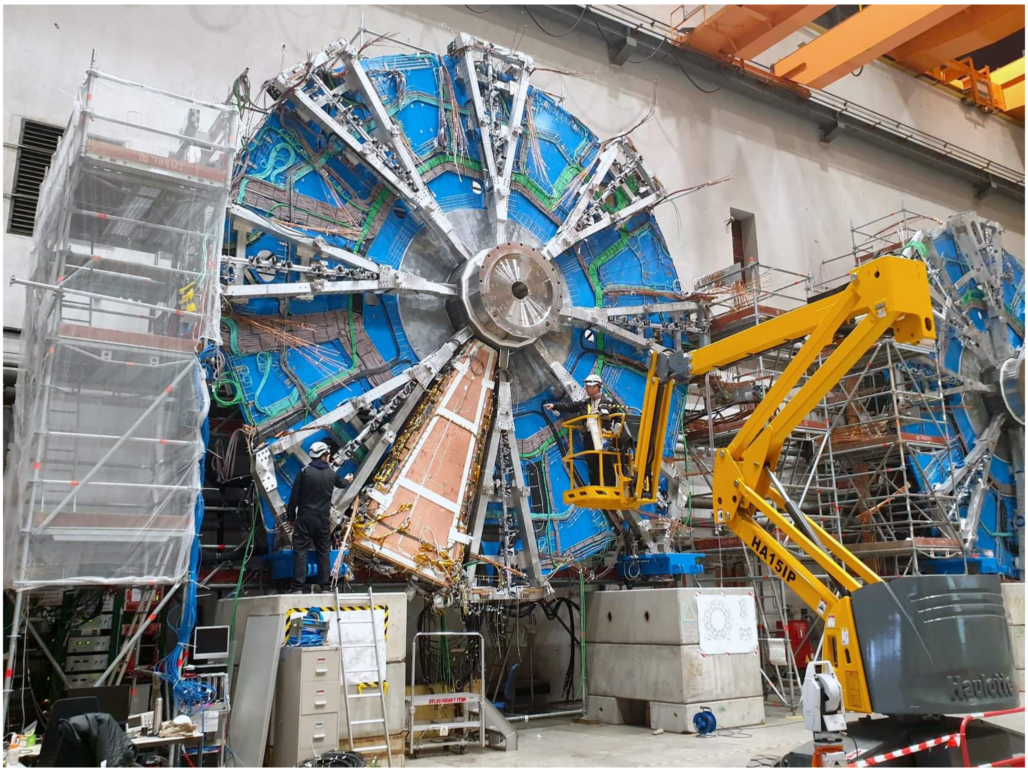

Figure 7.4: Picture from December 2019 showing the installation of the first small sector on the NSW-A mechanical structure. The NSW-C mechanical structure is also visible on the right side of the picture.

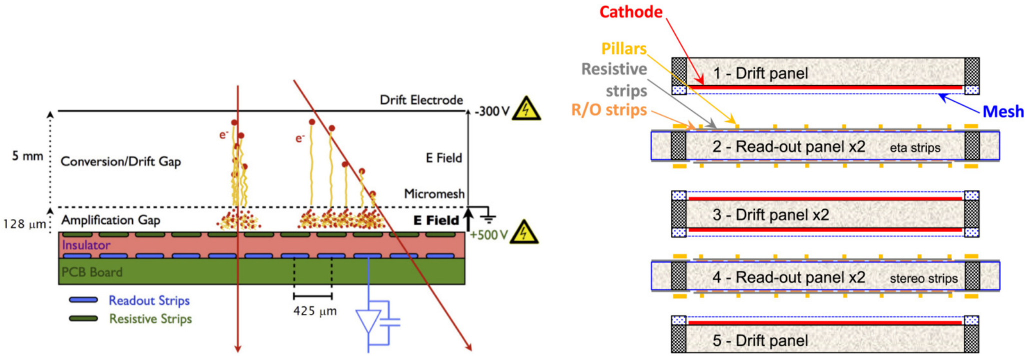

Figure 7.5: Scheme of the working principle of a single-layer MM chamber (left) and the 4-readout-layer configuration of the ATLAS MM chambers (right). Image from [136].

7.3 Micromegas chambers

A single layer of a Micromegas detector is sketched in Fig. 7.5 (left). The readout Printed Circuit Board (PCB), held at 500-600 V depending on the gas mixture, is followed by a grounded stainless steel mesh which defines the 128-μm-wide avalanche region. The mesh is followed by a 5 mm drift gap ending with a cathode plane held at -300 V. The drifting electric field is 600 V/cm and the typical avalanche electric field is 40-50 kV/cm. The standard gas mixture is Ar:CO_2 (93:7). The mesh, designed to be transparent to drifting electrons, is stretched over the readout PCB area and supported by 128-μm-high pillars glued on the PCB surface. The readout PCB consists of resistive strips deposited on a kapton® layer and the actual signal is carried by capacitively coupled copper strips below the insulator. Copper strips are printed on a 500 μm thick FR4 layer. They are 17 μm thick and 300 μm wide. To increase the hit precise coordinate resolution, the strip pitch is reduced down to 425 μm. Resistive strips are 300 μm wide and their strip pitch is 425 μm as well. Their design resistivity is $\sim$ 10 MΩ/cm.

Charged particles traversing the drift region ionize the gas and the electrons liberated drift towards the mesh. The charge amplification happens in the avalanche region with a typical gain of $\sim 10^4$. The electrons drift is a slow process that takes tens of nanoseconds. The amplification step instead happens in a fraction of nanosecond, inducing a fast pulse on the readout strips. Most of the ions are produced in the last avalanche steps, close to the readout strips, and their evacuation approximately takes $\sim$ 100 ns, still very short compared to other gaseous detectors. This fast positive charge evacuation makes MM chambers suited for high-rate operation.

The week point of MM detectors is the spike/spark problem. Typically, sparks occur when the number of electrons in the avalanche reaches $\sim 10^7$ (Raether limit [139]).

For a high single-layer detection efficiency, for muons at the minimum of ionization power, a gas amplification factor of 10^4 is needed. Therefore, ionization processes producing more than 1000 electrons linked to a single avalanche might induce sparks, see for instance [140]. Moreover, any detector imperfection leading to a localized higher electric field can induce spikes, even without ionization from traversing charged particles. Sparks may damage the readout layers and electronics and, depending on the current intensity, might lead to a large dead time after a High-Voltage (HV) breakdown. The resistive strips on top of the readout PCB are a spike protection system. The benefit of including resistive strips is twofold. As spikes deposit a large charge on few resistive strips, the localized charge counterbalances the electric field, thus acting as a quencher and reducing the spike intensity. Moreover, the readout strips are not directly exposed to the charge created in the amplification region, so that the spike-induced damaging effects are highly reduced.

The resistive quenching mechanism critically depends on the actual resistivity. Spikes can occur at any point on the active area, hence the need to design a resistive layout with minimal dependence on the path towards the HV distribution line. To achieve that, resistive strips are interconnected at several points on the readout area so that the actual resistivity resembles the one of a resistive plane.

To achieve four tracking hits per MM chamber, four readout planes per detector are needed. The detector configuration chosen is shown in Fig. 7.5 (right), called a *quadruplet*. Each quadruplet is made of five panels, two readout panels and three drift panels, defining four gas gaps. A quadruplet must measure two coordinates, X and Y, for each charged muons. To measure two coordinates, two types of readout panels are used, the eta panels for reconstructing the precision coordinate, X (readout strips almost orthogonal to the bending tracks), and the stereo panels, with a $\pm 1.5°$ strip inclination, for reconstructing both coordinates (X and Y).

The NSW will integrate four types of quadruplets called Small Modules 1 (SM1) and Small Modules 2 (SM2), to be used in the small sectors, and Large-Modules-1 (LM1) and Large-Modules-2 (LM2), for the large sectors, as shown in Fig. 7.4. Quadruplets are trapezoidal in shape. In the case of SM1 quadruplets, the dimensions are 2210 mm high, 368 mm and 1187 mm wide at the two bases. The readout panels have an extra border to host the front-end electronic boards and services, such that their dimensions extend to 500 mm and 1320 mm at the two sides. Fig. 7.6 shows a sketch of a Small-Module-1 Micromegas chamber (left) and a picture of a real SM1 quadruplet (right).

The SM1 and SM2 quadruplet surface is ~ 2 m^2 while it reaches ~ 3 m^2 for LM1 and LM2 quadruplets. Each layer of SM1- and LM1-type chambers is divided in 5 readout PCBs and each PCB is powered by two HV lines, so that the whole detector is piloted by 40 HV lines. SM2 and LM2 chambers have 3 PCBs per layer, for a total of 24 HV lines.

Two SM1 and two SM2 type quadruplets are integrated to form a small *double wedge* as sketched in Fig. 7.3. Fig. 7.7 shows a small double wedge under assembly with the last SM2 quadruplet still missing. Two (small) quadruplets embedded in two layers of sTGC chambers form a NSW small sector. The same is true with LM1 and LM2 quadruplets for NSW large sectors. Overall, each NSW will adopt enough Micromegas chambers to cover an active area of $\sim$ 640 m^2. SM1, SM2, LM1 and LM2 detectors are built in Italy, Germany, France and Greece/Russia, respectively.

7.4 Micromegas chambers construction and QA/QC

The SM1 Micromegas quadruplet components are built in parallel at different production sites. The readout PCBs are produced by the ELTOS company, tested at CERN and then shipped to the INFN Sezione di Pavia for the readout panels construction, the detector most critical part. The readout panels are prepared in a class 10000 clean room using a *stiff-back* technique. From September 2017 to October 2020 the 64 production panels for NSW-A and NSW-B have been assembled (plus 7 for prototyping and backup).

SM1 readout panels use five types of PCBs as sketched in Fig. 7.6 (left). A single PCB is shown in Fig. 7.8 (left), together with the HV distribution line powering the resistive strips, the *silverline* (right). Fig. 7.9 shows a zoomed part of the active area where the copper strips are visible, together with the resistive strips interconnected at several points on the surface. Fig. 7.10 shows the pillar layout on the readout PCB surface (left) and a single pillar on top of the resistive strips (right).

The quality of the chambers critically depends on the readout panels construction accuracy. For instance, the alignment of the readout-panel strips directly affects the precision in the measured coordinates. The precision requirements in X (on the strip plane, perpendicular to them) and Y (along the strips) are:

- 20 μm in X for the average strip alignment in a single layer (40 μm tolerance);
- 35 μm in X for the average layer-to-layer alignment (60 μm tolerance);
- 150 μm tolerance in Y for the single layer alignment;
- 300 μm tolerance in Y for the layer-to-layer alignment.

Moreover, in order to achieve a uniform electric field, a good planarity of the readout and drift panels is required, together with a correct grounding. The values used for the planarity along Z are:

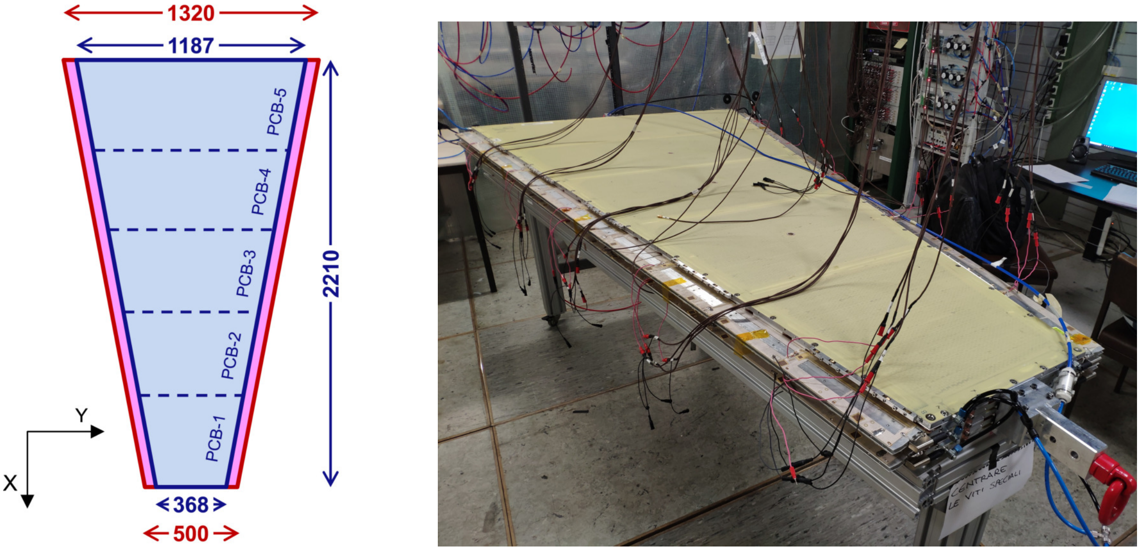

Figure 7.6: Sketch of a Small-Module-1 type Micromegas chamber (left) (dimensions in mm) and a picture from a real one (right). Left image from [136].

Figure 7.7: A small sector under assembly at the CERN BB5 building. The last chamber is still missing and cables to connect front-end boards are visible.

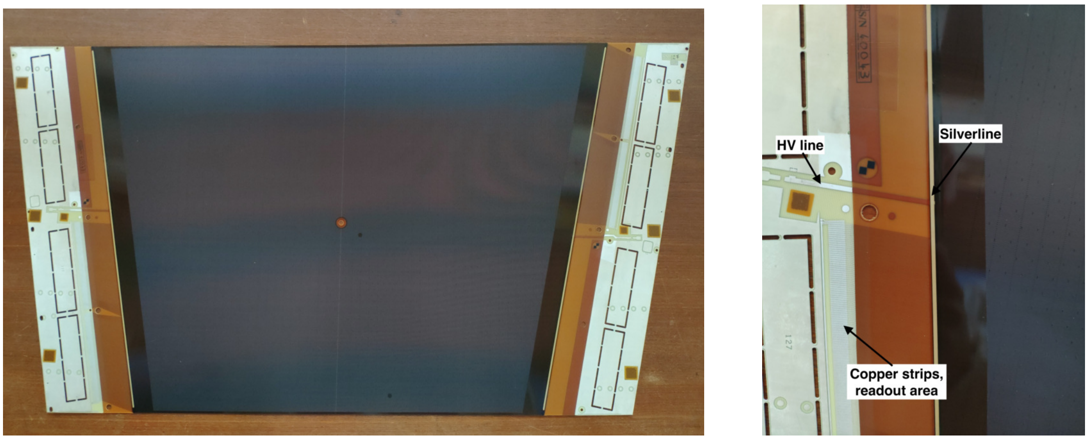

Figure 7.8: The Micromegas readout PCB (left). The main parts of the electrical scheme are labeled (right).

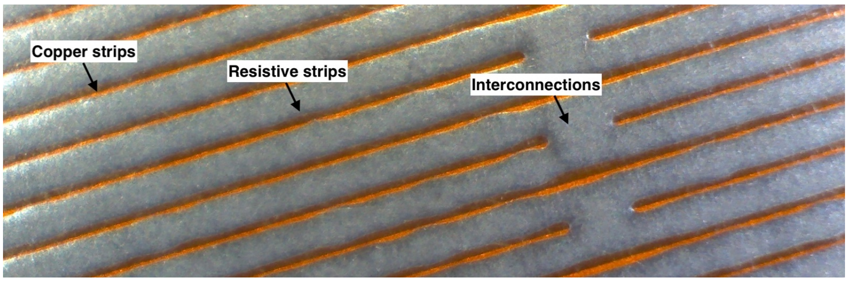

Figure 7.9: A zoomed picture of the PCB active area showing the resistive and readout strip geometry.

- 50 μm tolerance for the bars and for the honeycomb before mounting;
- ± 110 μm mechanical tolerance with respect to the nominal value, with 37 μm allowable RMS, for both readout and drift panels after assembly;
- 100 μm in RMS for both readout and drift panels after final module assembly under gas pressure.

In order to match the requirements, during and after construction, the panels have to pass a QA/QC procedure. Summary results are reported after the description of the readout-panel construction procedure.
The clean room is equipped with a $3500 \times 2000 \times 350$ mm^3 granite table, on which a measurement system and the construction tools are placed. A device for dimensional measurements, the CMM (Coordinate Measuring Machine), that can reach an accuracy of 3 μm over the entire table surface, is exploited for the panel-planarity measurements. The construction of the panels is based on reference plates

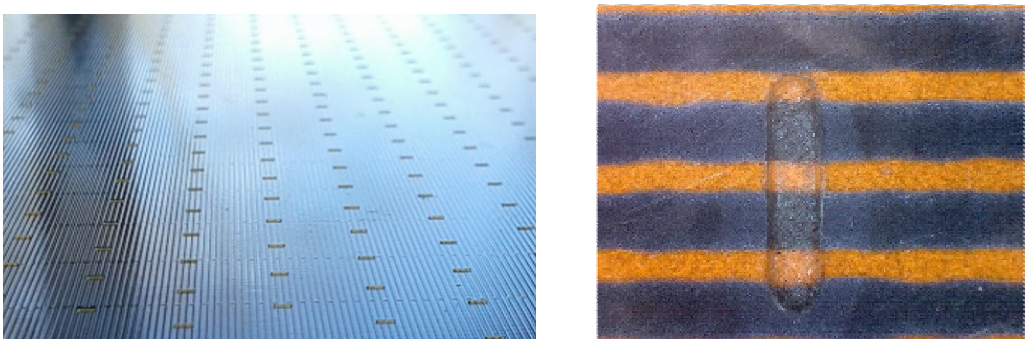

Figure 7.10: Picture of a Micromegas resistive-strip readout panel (left). Picture of a single pillar (about 1 mm × 330 μm) (right).

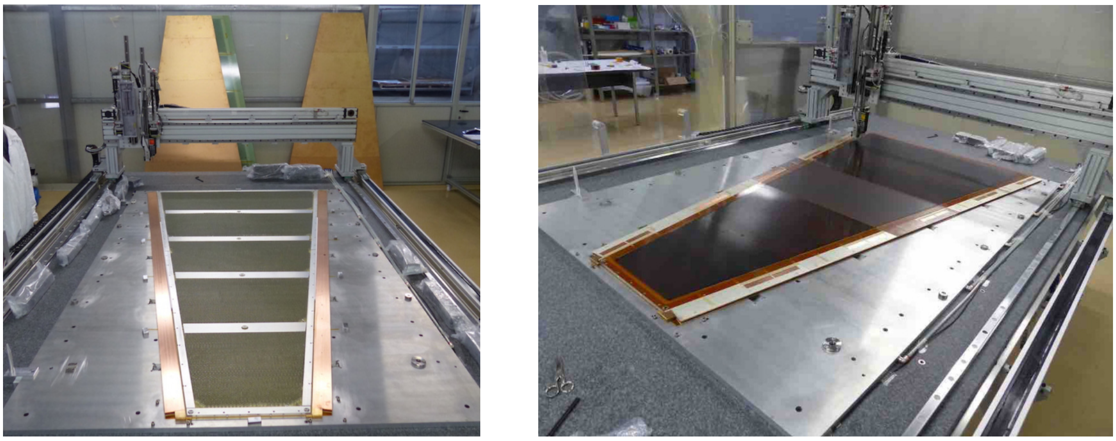

Figure 7.11: A readout panel during (left) and after (right) construction. Image from [136].

located on the granite table and the stiff-back. A set of 5 rectified aluminum plates is placed on the granite table, parallel to its short side, and used as reference plane. During construction, each of the five readout PCBs is blocked and aligned by means of reference pins positioned with precision holes in the granite table. A set of pass-through holes and grooves are machined at the bottom side of all the plates in order to place the PCBs under vacuum. Vacuum is used to block in position on the reference plates the 5 PCBs (one on each reference plate), composing the lower surface of each panel for gluing.

The stiff-back is composed of 5 similar reference plates, 20 mm thick, mounted on a support made of two aluminum skins with a 60 mm aluminum honeycomb sheet inside. The stiff-back is attached to a crane and can be moved horizontally, vertically, and rotate to allow for an upward or downward facing of the readout plane on it, depending on the assembly phase.

To build a panel, 5 PCBs are placed on the granite table reference plates with an underpressure of 300 mbar and their thickness is measured using the CMM machine. The same measuring procedure is followed for the 5 PCBs to be positioned on the stiff-back plates. Internal and external frames, honeycomb and cooling bars are placed on top of the five PCBs on the granite table. A dry-run (full closure operation but the glue deposition) is performed to check the coupling of the stiff-back with the table reference plates and spot possible interference of the internal structure of the panel: the stiff-back is rotated upside down (PCBs facing down) and moved over the table, then lowered on top of the reference plates. The plates on the table and on the stiff-back are precisely matched by using a tapered interlock and a V-shaped interlock, which allow for the correct positioning of the two PCB layers in a XY-plane. In addition, 18 steel flat supports are used to guarantee the correct Z distance between the reference plates of the stiff-back and those of the table. Once the stiff-back is placed on the table, reference measurements of the gap between the table reference plates and the stiff-back plates are taken along the perimeter with a bore meter.

The stiff-back is then removed, and turned upside down once again (PCBs facing up). At this point, the gluing of the two readout planes, frames, honeycomb and cooling bars takes place. The glue is automatically disposed by a motor-controlled machine both on the PCBs on the table and those on the stiff-back. The panel is closed by rotating the stiff-back upside down (PCBs facing down), moving it over the table, and finally lowering it on top of the reference plates. The system is left untouched for the rest of the day (18 h), for glue curing. Later on, the stiff-back vacuum is turned off and the stiff-back removed from the table, leaving the glued panel still sucked on the reference plates of the table to allow a planarity measurement. The planarity of the panel is then measured again with vacuum off, to verify possible

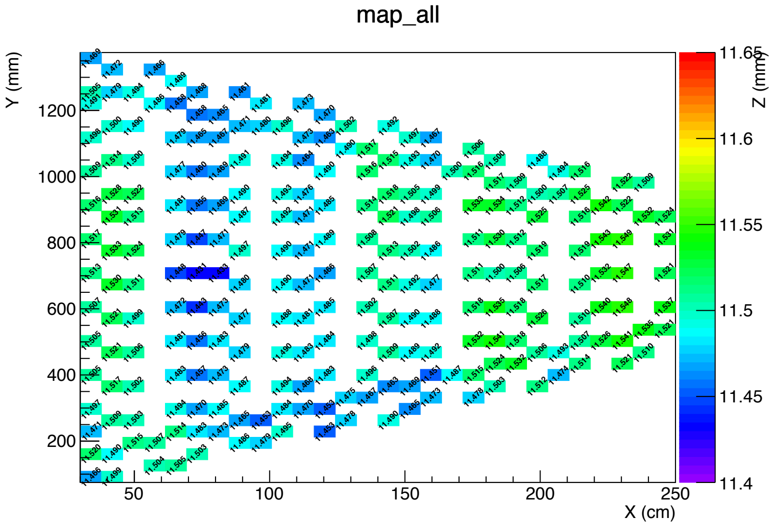

Figure 7.12: Typical planarity measurement results after a single-panel QA/QC test. The absolute thickness is reported (mm).

distortions due to internal tensions of the panel. Fig. 7.11 shows a NSM MM readout panel during (left) and after (right) construction at INFN Sezione di Pavia.

The panel planarity is measured by means of the CMM at 242 points on the panel surface. Fig. 7.12 shows a typical map from a panel-planarity test, where the absolute thickness (mm) is displayed. The average thickness, the RMS and the max-to-min difference for each panel are shown in Fig. 7.13. Eta panels are measured on both sides (up and down) while stereo panels on the up side only. The max-to-min thickness value is always within ±110 μm and the overall RMS is never larger than 37 μm.

Once the readout panels are built, they undergo the electrical inspection. For each PCB, on both sides (left and right), the following test are performed:

- The resistivity of the resistive strips. The measurement is performed with a multimeter measuring the resistance between the HV distribution line and the resisitive strips at several point on the PCB surface. Particular attention was given at the resistivity close to the HV distribution line ($\simeq$ 1 cm from the resistive strip starting point).

- The insulation between the resistive strips and the readout strips is measured with an Megger BM25 insulation tester, which is able to measure resistances up to 1 TΩ, connected to the HV distribution line and the end of the readout strips.

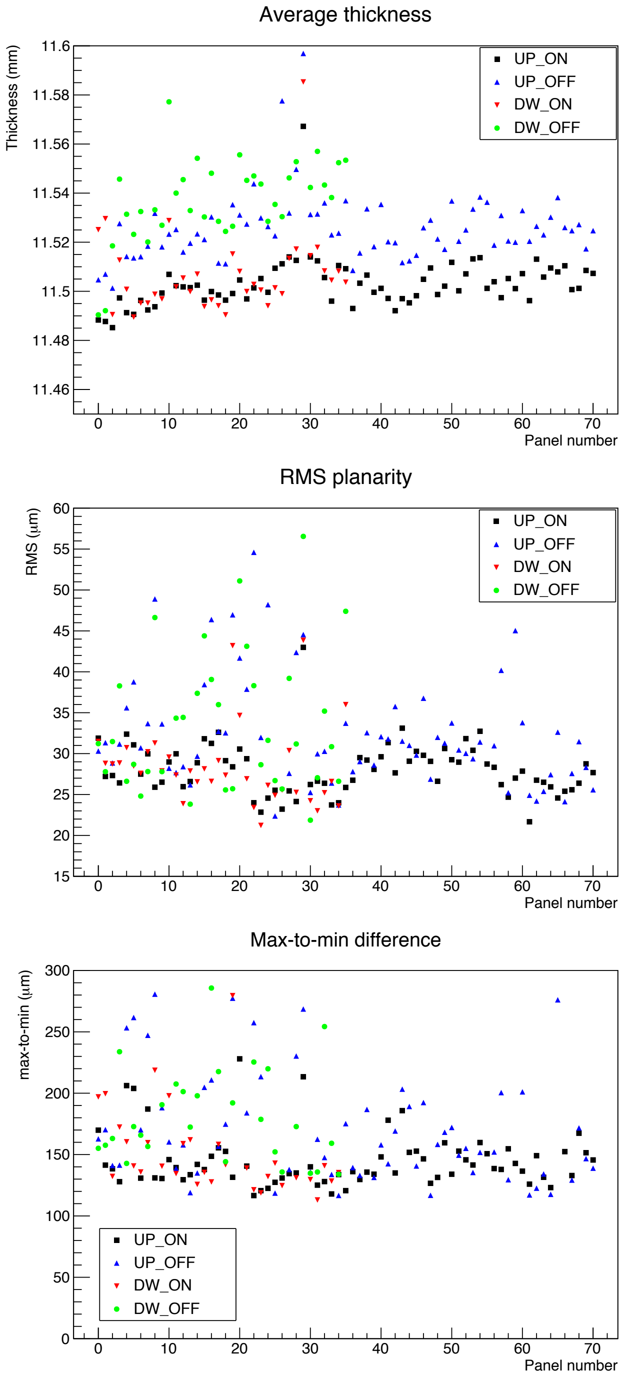

Figure 7.13: Summary results for planarity measurements of NSW SM1 readout panels. Average thickness, RMS and max-to-min height difference for each panel. Results for measurements vacuum off/on. First 36 panels are eta, the others are stereo. Eta panels are measured on both sides (up/down) while stereo panels are measured on the up side only.

- The silverline insulation was tested with a Megger BM25 insulation tester. The measurement was performed between the HV line and the coverlay on top of the silverline.

Summary results concerning all the QA/QC electrical measurements are shown in Fig. 7.14. Other QA/QC test, such as strip alignment measurements and panel gas tightness are performed, along with the panel finalization. Details about these steps are reported in [136]. The SM1 Micromegas chambers construction also consists of the drift panel construction and the final assembly. For a detailed explanation of the other construction steps refer to [136]. An additional article describing the whole production of Small-Module-1 chambers is in preparation. After the construction, the Micromegas chambers are shipped to CERN for the high-voltage testing, the front-end electronics mounting, the cosmic-ray testing and the final integration within the NSW mechanical structure. For a review on the Micromegas chambers integration work-flow see [141]. The following section describes the detectors high-voltage testing.

7.5 Micromegas chambers high-voltage testing

Upon the arrival at CERN, each MM chamber undergoes a first HV test at the CERN BB5 workshop to spot any HV instability or spiking behavior. About 70% of the production chambers are also tested to check the HV behavior under irradiation with doses greater than (or comparable to) the ones foreseen for the HL-LHC operation. To reach this extremely-high radiation doses, chambers are tested at the CERN Gamma Irradiation Facility (GIF++). The first chambers arrived at CERN in January 2019 and the last are expected within March 2021. Up to October 2020, about 80 Micromegas detectors have been characterized for HV behavior, corresponding to two-thirds of the full (NSW-A and NSW-C) production.

7.5.1 The CERN Gamma Irradiation Facility

The Gamma Irradiation Facility (GIF++), built during the LHC Long Shutdown 1 (LS1) at the CERN SPS North Area, is mainly used for the characterization of large-area gaseous detectors. It exploits a single $\simeq$ 14 TBq ^{137}Cs radioactive source with a half-time of 30.08 years. ^{137}Cs decays by beta emission to a metastable nuclear isomer of barium, ^{137m}Ba, with a branching ratio of 94.6%. The remainder directly populates the ground (stable) state of ^{137}Ba. Meta-stable barium decays to the ground state by emission of 662 keV photons, with a half-life of about 153 s, and is responsible for all the gamma ray emissions in samples of ^{137}Cs, .

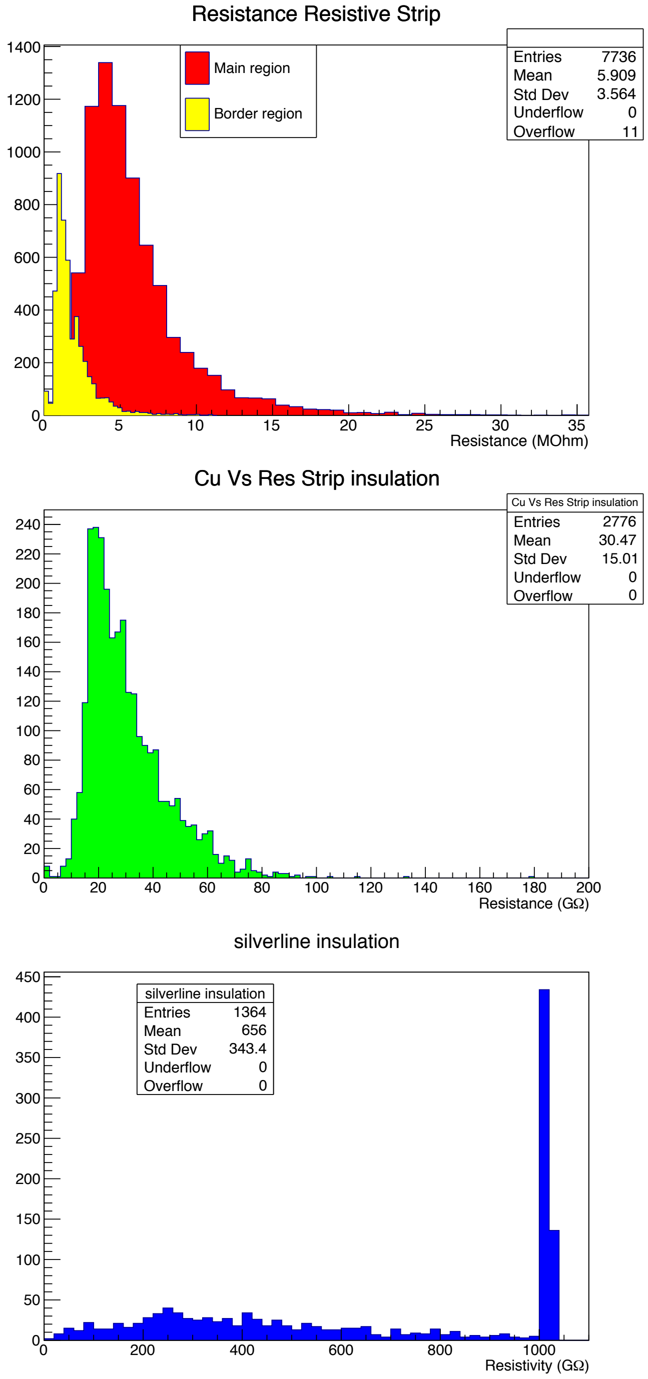

Figure 7.14: Summary results for readout PCB electrical inspections. Displayed are the resistivity of the resistive strips, close to the HV distribution line or in the main active region, the insulation between resistive strips and readout strips and the silverline insulation.

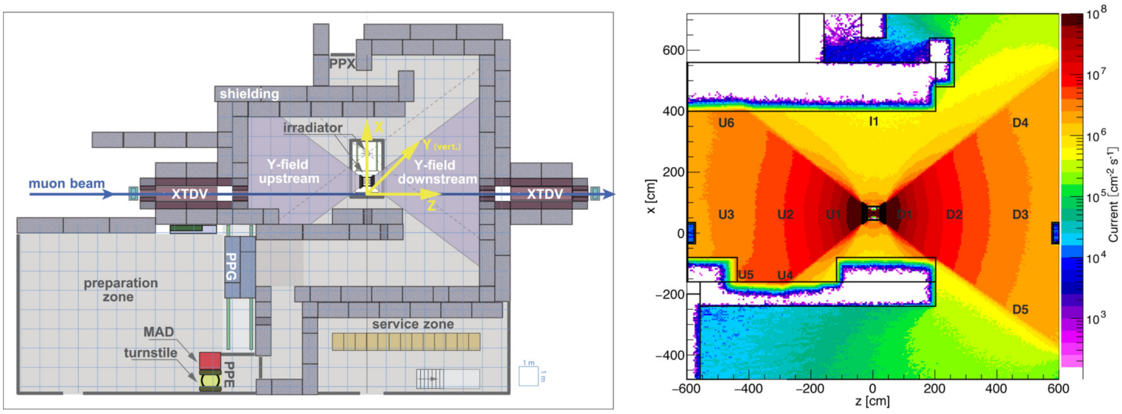

Figure 7.15: The GIF++ bunker (left) and simulated total photon current (cm^{-2}s^{-1}) inside the GIF++ bunker. Images from [142].

The GIF++ bunker has two independent irradiation areas named *upstream* and *downstream*, as shown in Fig. 7.15 (left). Without any correction, the photon emission would be isotropic and almost point-like. Both irradiator outlets are equipped with a len shaped angular correction filter in order to guarantee a uniform photon field at any XY-plane for 662 keV photons. This is beneficial for large area detectors testing. Fig. 7.15 (right) shows the simulated maximal irradiation current within the GIF++ bunker, as calculated in [142]. It can reach 10^8 photons/cm^{-2}s^{-1} next to the irradiator walls. Two independent sets of lead attenuation filters are available to tune the photon flux intensity. In total, 24 nominal attenuation factors are available, ranging from 1, *i.e.* no attenuation, to 46415. The attenuation factor does not depend on the photon emission angle, *i.e.* photons from the source traverse the same lead thickness regardless their emission angle. It is important to note that the nominal attenuation factor is defined as the attenuation for 662 keV photons. Superimposed to the 662 keV photons there is a broad low-energy spectrum component due to the scattering on the lens-shaped filters and the source capsule.

To understand the actual field intensity at the Micromegas chambers surface, we performed a study based on both simulated and measured data. Readapting data from [142], we mapped the simulated gamma field at point *upstream* 1 and *downstream* 1 (U1/D1 in Fig. 7.15), corresponding to a distance of $\simeq$ 1 m from the source. Photon energies are divided in 100 keV bins and the 662 keV peak component is identified as the one in the 661-662 keV bin. Results, expressed in 10^6 photons/cm^{-2}s^{-1}, are given in Tab. 7.1.

The intensity of the photons with an energy of 661-662 keV is indeed reduced by a factor compatible with the nominal attenuation. On the other hand, the 400 keV to

Nominal filter	0-100 keV	100-200 keV	200-300 keV	300-400 keV	400-500 keV	500-600 keV	600-662 keV	0-662 keV	661-662 keV
									10^6 cm^{-2}s^{-1}
1.0	0.36	2.92	2.44	3.29	5.18	5.88	23.8	43.9	20.0
2.2	0.30	0.40	0.43	1.57	3.32	3.79	11.78	21.59	9.43
4.6	0.16	0.22	0.18	0.77	1.85	2.19	5.82	11.26	4.44
6.8	0.11	0.16	0.13	0.56	1.42	1.68	4.12	8.18	3.06
10.0	0.07	0.15	0.13	0.37	1.10	1.31	2.90	6.03	2.10
21.5	0.04	0.06	0.04	0.19	0.56	0.72	1.43	3.04	1.01

Table 7.1: Simulated photon current expressed in 10^6 cm^{-2}s^{-1} at position D1/U1 for several attenuation filters.

600 keV photons are attenuated less than the nominal factor, whereas the 100 keV to 300 keV ones are attenuated more.
The composition of the irradiation field at different attenuation factors was studied as well, by dividing the amount of photons in each energy bin by the total amount of photons (0-662 keV). Results are given in Tab. 7.2. Different attenuation filters lead to small deviations on the field spectrum from filter 1 to filter 21.5. The 100 keV to 300 keV component changes from 12.3% to 3.5%: this discrepancy arises almost completely in the passage from filter 1.0 to filter 2.2, *i.e.* when the first lead slab is installed. The 300 keV to 500 keV component changes from 19.3% to 25.4% while the high energy component, from 500 keV to 662 keV, changes from 67.6% to 73.2%. Overall, it was found that for any irradiation study close to position U1/D1, with the only exception of filter 1.0, the photon spectrum composition is barely affected by the chosen attenuation filter up to filter 21.5.

Nominal filter	0-100 keV	100-200 keV	200-300 keV	300-400 keV	400-500 keV	500-600 keV	600-662 keV	0-662 keV	661-662 keV
									%
1.0	0.8	6.7	5.6	7.5	11.8	13.4	54.2	1.0	45.6
2.2	1.4	1.9	2.0	7.3	15.4	17.6	54.6	1.0	43.0
4.6	1.4	1.9	1.6	6.8	16.4	19.5	51.7	1.0	39.5
6.8	1.3	2.0	1.6	6.9	17.4	20.5	50.4	1.0	37.6
10.0	1.2	2.5	2.2	6.1	18.2	21.7	48.1	1.0	35.1
21.5	1.3	2.0	1.3	6.3	18.4	23.7	47.0	1.0	30.9

Table 7.2: Simulated photon energy spectrum for several attenuation filters normalized to the total photon current at position U1/D1.

7.5.2 Photon field mapping

To measure the actual Micromegas hit rate, the readout electronics is needed. Unluckily, Micromegas readout boards are only mounted after the HV tests and the tight integration schedule did not allow for any electronics-equipped chamber testing at GIF++. Therefore, we decided to measure the rate with an auxiliary Thin Gap Chamber (TGC). The structure of the TGC chamber is similar to the one of a Multi-Wire Proportional Chamber where the cathode to anode distance is much shorter than the anode to anode one. The anode consists of 50 μm diameter gold-plated tungsten wires spaced by 1.8 mm. The cathode planes are made of 1.6 mm G-10 plate covered with a 100 μm thick graphite layer on the inner side. The distance between the anode planes and the cathode is 1.4 mm. The flushed gas was n-pentane (n-C_5H_{12} 55:45) and the active area was 14 cm × 16 cm. The anode wires were polarized at +2800 V while the cathode planes were kept at 0 V by grounding connections. The chamber was operated in a limited proportional mode, by drifting towards the wires electrons released by the incident photons. Wire signals were processed by custom onboard ASICs and fed into an ADC converter. The dynamic range of the pulses, to be digitized, was 0-1 V. Eventually, the digitized signals were used as input of a scaler to count the number of detected electrons. The current carried by TGC wires was sampled with a sensitivity of 0.4 μA.
To perform a hit-rate measurement over an entire MM detector surface, the TGC was placed over the surface of an LM2-type Micromegas chamber positioned at 2 m distance from the source. The hit rate was estimated as the average count over 10 s long counts. Fig. 7.16 shows the TGC detector, close to the Micromegas one, inside the GIF++ bunker. The TGC chamber sensitivity to the GIF++ photon spectrum, *i.e.* the fraction of photons that interact with the detector and are detected, has been studied with data and simulations in [143]. By exposing the detector to a ^{137}Cs source, the sensitivity to 662 keV photons was measured to be 0.264%. Detailed simulation studies were performed with photon energies ranging from few keV to 20 MeV and were found to be in good agreement with measurements performed with several radioactive sources. In the energy range 100-662 keV, the dominating interaction is by Compton scattering on the gas mixture or on the cathode planes, whereas below 100 keV the photoelectric effect dominates.
The Micromegas chamber sensitivity to photons has been studied in [144], for each of the four gas gaps, over the range from 10 keV up to 10 GeV. Both the MM and the TGC sensitivity exhibits a strong dependence over the photon energy. Their sensitivity to the GIF++ photon spectrum was measured by convoluting its value with the photon spectrum given in Tab. 7.2. Results for the effective sensitivity for different attenuation filters are reported in Tab. 7.3. The Micromegas sensitivity

Figure 7.16: Picture of the LM2 M7 Micromegas chamber in the GIF++ bunker and the auxiliary TGC chamber mounted next to it. In the picture right side the GIF++ radiator wall is visible as well.

was calculated as the average value for the four layers and the error as the difference between the most and the less sensitive gap. Over the attenuation filter range considered, the average MM and TGC sensitivity is almost constant, clearly a consequence of the constant photon spectrum studied before with simulations.
Results for the rate measurements using the TGC are shown in Tab. 7.4. Per each filter, we report the charge per electron (the primary electron scattered by the incident photon) and the effective rate on the Micromegas chamber. The error due to the different sensitivity of the Micromegas gas gaps amounts to $\simeq$ 25% of the average rate value.
Many tests were performed to verify the result correctness. The TGC anode charge per electron is compatible within the errors from filter 21.5 to filter 2.2. This guarantees that the counted electrons correctly account for the whole negative charge produced within the TGC chamber. The discrepancy for filter 1.0 can be explained by an expected saturation of the readout electronics for high rates which leads to an underestimation of the counts. This effects amount to a $\sim$ 10% of counts lost by

Nominal filter	MM	MM error	TGC
			%
1.0	0.486	0.124	0.217
2.2	0.505	0.128	0.229
4.6	0.503	0.127	0.228
6.8	0.502	0.126	0.227
10.0	0.498	0.125	0.225
21.5	0.500	0.125	0.226

Table 7.3: Sensitivity to the GIF++ photon field of the TGC chamber and the Micromegas chamber. Results for different attenuation factors expressed as percentage values.

the TGC detector.

Moreover, dividing the rate measured with filter 1.0, 16.8 kHz/cm^2, by the corresponding TGC sensitivity, 0.217 %, we can estimate a photon flux of 7.7×10^6 cm^{-2}s^{-1}, in very good agreement with the simulated data, see Fig. 7.15. This exercise demonstrates that at GIF++ it is possible to test the MM chambers high-voltage behavior up to rates more than two times higher than the one foreseen at the High-Luminosity operation of the LHC.

Nominal filter	Rate (TGC) kHz/cm^{-2}	Charge per e^- pC	Error pC	Rate (MM) kHz/cm^{-2}	Error kHz/cm^{-2}
1.0	16.8	9.2	± 0.1	37.6	± 9.5
2.2	8.9	8.4	± 0.1	19.6	± 5.0
4.6	4.6	8.1	± 0.2	10.2	± 2.6
6.8	3.5	7.9	± 0.3	7.7	± 2.6
10.0	2.4	8.1	± 0.7	5.3	± 1.3
21.5	1.2	8.1	± 0.7	2.7	± 0.7

Table 7.4: Measured rate with the TGC chamber at a 2 m distance from the source, integrated charge per electron on the anode wires and estimated rate for the Micromegas chamber.

This exercise also showed an important feature of the GIF++ photon field, *i.e.* its uniformity over XY-planes. The rate at the Micromegas surface was measured on each of the six sectors, in such a way the photon field was mapped over a surface of $\simeq 3$ m^2 in the XY-plane. Fig. 7.17 shows the rate over each sector, as well as the

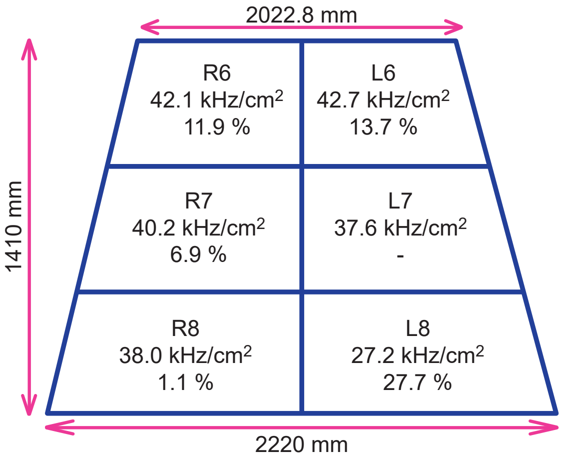

Figure 7.17: Measured rate with filter 1.0 for each Micromegas sector and percentage variations with respect to sector L7.

variations with respect to the rate measured at sector L7. The maximal variation appears on sector L8 and is due to the presence of upstream material between the chamber and the source.

7.5.3 Results

Micromegas chambers were typically positioned between 1 m and 3 m distances from the source, where a photon flux between 10^6 cm^{-2}s^{-1} and 5×10^7 cm^{-2}s^{-1} is expected. The goal was to measure the current produced at the amplification stage with respect to the high-voltage applied and the incident flux. Particular attention was given to the current (in)stability problems and the spiking effects that might compromise the detector performance during the long-term operation within the ATLAS Detector. Gas mixtures were provided by pre-mixed bottles stored in the service zone and fed to the detector through copper pipes. Each Micromegas sector was independently powered through an HV line of a CAEN A7030 HV board. The whole detector was controlled with a dedicated Detector Control System (DCS), from the GIF++ control room. For each sector the current and voltage values during a given time slot were acquired and stored for later analysis. A typical picture of the DCS during operation is given in Fig. 7.18. The following are selected results from HV tests performed from January 2019 to October 2020.

The first Micromegas chambers tested showed severe spiking issues. An example from a Large-Module-1 type chamber, LM1 M8, is showed in Fig. 7.19. The current at the amplification stage (red line) is plotted with the detector operated at the working point and exposed to different fluxes by changing the GIF++ source filters.

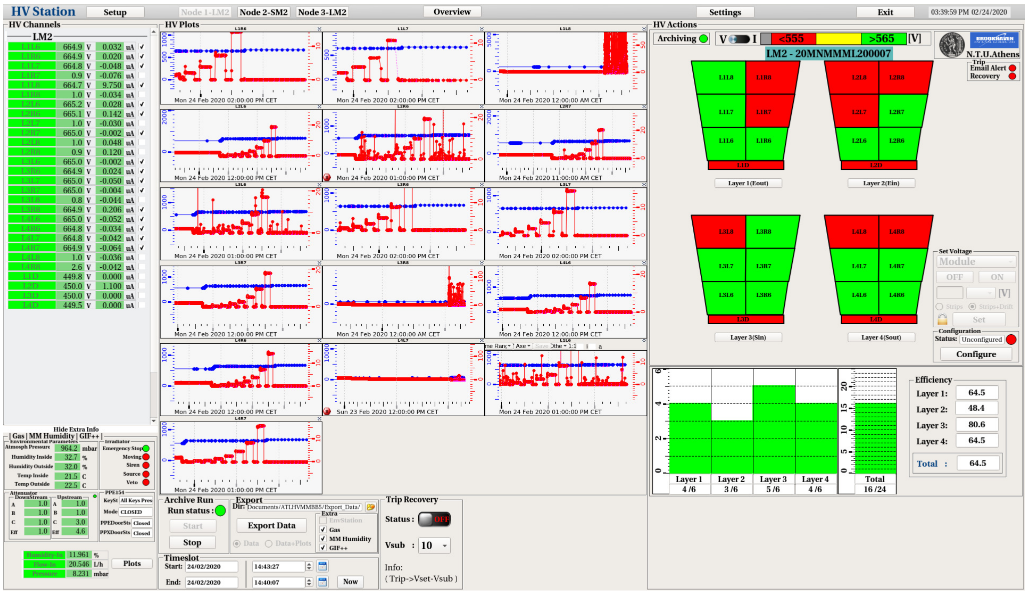

LM2

L1L6	664.9	V	0.032	uA	✓
L1R6	664.9	V	0.020	uA	✓
L1L7	664.8	V	-0.048	uA	✓
L1R7	0.9	V	-0.076	uA	
L1L8	664.7	V	9.750	uA	✓
L1R8	1.0	V	-0.034	uA	
L2L6	665.2	V	0.028	uA	✓
L2R6	665.1	V	0.142	uA	✓
L2L7	1.0	V	-0.030	uA	
L2R7	665.0	V	-0.002	uA	✓
L2L8	1.0	V	0.048	uA	
L2R8	0.9	V	0.120	uA	
L3L6	665.0	V	-0.002	uA	✓
L3R6	664.9	V	0.024	uA	✓
L3L7	665.0	V	-0.050	uA	✓
L3R7	665.0	V	-0.004	uA	✓
L3L8	0.8	V	-0.044	uA	
L3R8	664.9	V	0.206	uA	✓
L4L6	665.0	V	-0.052	uA	✓
L4R6	664.8	V	-0.034	uA	✓
L4L7	664.8	V	-0.042	uA	✓
L4R7	664.9	V	-0.064	uA	✓
L4L8	1.0	V	-0.036	uA	
L4R8	2.6	V	-0.042	uA	
L1D	449.8	V	0.000	uA	
L2D	450.0	V	1.100	uA	
L3D	450.0	V	0.000	uA	
L4D	449.5	V	0.000	uA	

Configuration Status: Unconfigured

Layer 1	Layer 2	Layer 3	Layer 4	Total
4 /6	3 /6	5 /6	4 /6	16 /24

Efficiency
Layer 1: 64.5
Layer 2: 48.4
Layer 3: 80.6
Layer 4: 64.5
Total : 64.5

Figure 7.18: The Micromegas chambers Detector Control System during operation.

The nominal attenuation value is plotted as well (blue line). While for sector L1L4 (layer 1, left side of PCB4) the current perfectly changes with the hit rate (left), for sector L3R5 the current is completely dominated by spikes originating at the amplification stage (right).

The only solution for problematic sectors was to lower the HV, that limits the spike formation but leads also to a lower detector efficiency. A MM chamber is accepted for integration if its average efficiency is above 90% and the spike rate is less than six per minute. These values are calculated as average values over the chamber sectors. An average efficiency of 90% occurs when operating the chamber sectors at an average HV of 560 V. The nominal working point with the standard gas mixture is 570 V. In the first months of 2019 about 7%, 15%, 30% and 12% of the sectors were found below this specification, respectively for SM1, SM2, LM1 and LM2 chambers. The detector production was delayed at every construction site while trying to understand the origin of the spiking behavior. Several features were considered, among which there were the humidity correlation, the non-perfect mesh stretching and the ionic contamination. The first hint of the real cause came after a Small-Module-1 type chamber, SM1 M3, was irradiated for three months at GIF++ and spikes were not dumped by lowering the HV. The chamber was then shipped back to the assembly workshop at LNF (Laboratori Nazionali di Frascati) and re-opened. Strong signs of damaging of the readout PCBs were found close to the HV distribution line and the resistive strip interconnections closer to the HV distribution line, see Fig. 7.20.

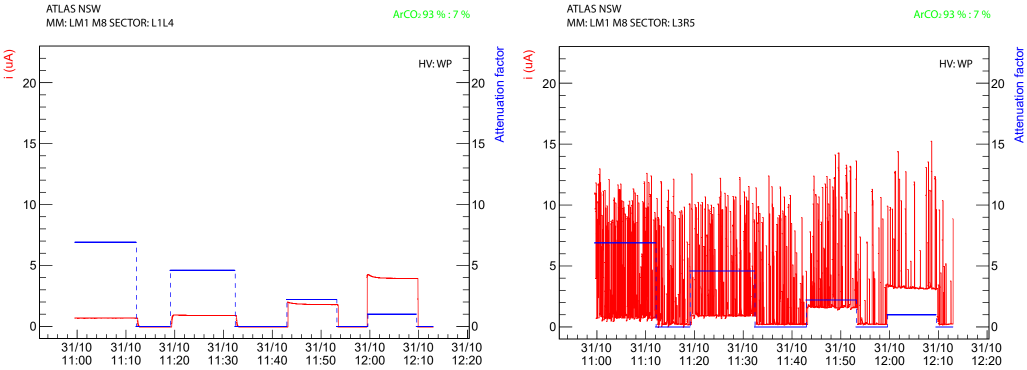

Figure 7.19: Monitored current at the amplification stage of chamber LM1 M8, sector L1L4 (left) and L3R5 (right).

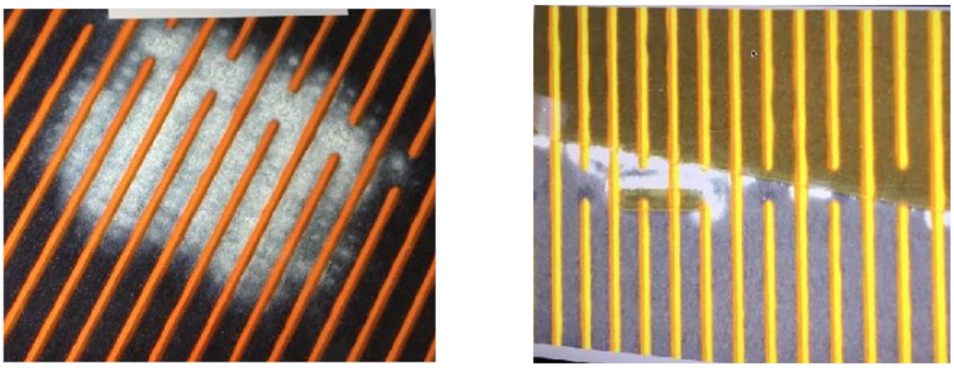

Figure 7.20: Zoomed pictures of a SM1 M3 readout panel after a three months irradiation period at GIF++. Visible are discharge residuals at strip interconnection zones (left) and close to the HV distribution line covered by a piralux coverlay (right).

This triggered the idea that spikes occur where the local resistance of the resistive layer is below a given threshold.

To validate this hypothesis, the maximal HV reachable by each sector without exceeding the nominal spike threshold was correlated to the minimal resistivity measured between the HV distribution line and the resistive layout. The result for a subset of SM1 type chambers is shown in Fig. 7.21. Indeed, the HV found was minimal for those sectors experiencing the minimal resistance between the resistive strips and the HV distribution line. That is because, if the resistance is too low, the spikes quenching mechanism does not work anymore and the only way to lower the spike intensity is to lower the HV.

A technique to mitigate this problem was developed at LNF and later adopted by all construction sites. It is known as *passivation*. The resistance of the resistive strips is measured per each sector close to the HV distribution line and, if it is found to be lower than 0.8 MΩ, an araldite layer is deposited over that region to electrically insulate the area. The technique helped in mitigating the spiking problems, sometimes with dramatic effects. Fig. 7.22 shows the monitored current of a Small-Module-2 type detector, sector L1R7, tested at GIF++ before (left) and after (right) the passivation technique.

Starting from the second half of 2019 all problematic chambers were treated with the passivation technique. The fraction of good sectors tested at CERN reached 98% for SM1 and SM2 type chambers, 90% for LM1 type chambers and 92% for LM2 type chambers.

The HV testing of Micromegas chambers for the first New Small Wheel (NSW-A) started in January 2019 and ended at the end of 2020. A summary of the HV testing for NSW-A is given in Fig. 7.23. The picture refers to the NSW-A configuration as of October 2020. Each sector is considered as independently powered. Red sectors are the ones for which the HV was lowered below 559 V to mitigate spikes or sectors that, while operated at the nominal working point (570 V), showed a spike frequency greater than six spikes per minute. Chambers marked with bold lines are passivated.

It is clear that a non-negligible fraction of sectors still shows some out-of-specifications behavior, especially among the non passivated chambers. To further mitigate the HV instabilities afflicting NSW-A, the ATLAS Muon Collaboration decided to test the Micromegas chambers HV behavior with new gas mixtures. The first chamber used is a Large-Module-2 type, LM2 M7, the same used for the photon field mapping described before and depicted in Fig. 7.16. The detector did not went through any passivation treatment. The chamber was placed in the downstream irradiation area close to point D1 at 2 m distance from the source and was not moved for the entire data taking period. It was mounted on a trolley keeping the chamber vertically with respect to the bunker floor with the *eta* side facing the irradiation source. Three different gas mixtures were considered: $ArCO_2$ (93:7), which is the baseline one, $ArCO_2$ (80:20) and $ArCO_2C_4H_{10}$ (93:5:2).

To compare the HV behavior for the three gas mixtures, we recorded the current at different amplification voltages and particle rates. Drift voltages were selected by maximizing the drift transparency for each gas mixture. Results for the sectors L1L6 and L3R7 are shown in Fig. 7.24. It is clear that the three gas mixtures defines three different high-voltage operation ranges. The current obtained with $ArCO_2$ (93:7) at the working point (570 V) is used as reference to extract the working points for the other gas mixtures. We considered an error of (±10 V) on the working points. Tab. 7.5 summarizes the drift and amplification working points found.

The current values *vs.* the amplification voltage is well described by an exponential fit to data up to a certain current value. To highlight this point, an exponential fit

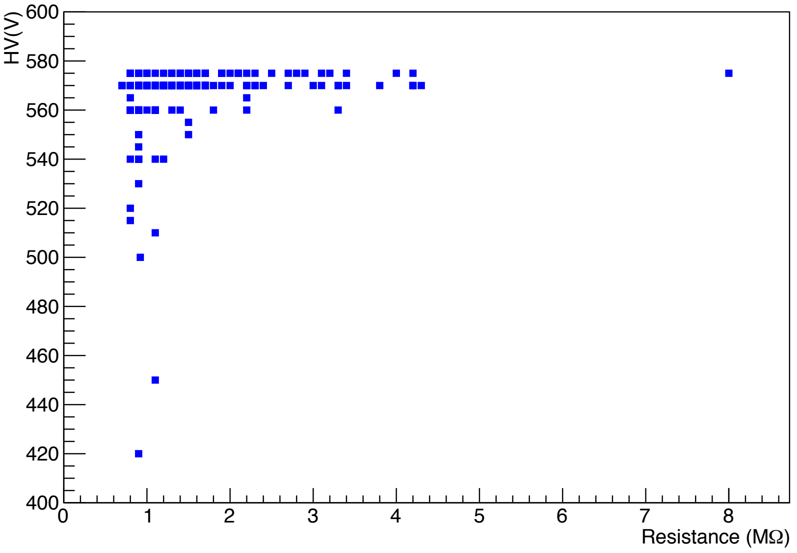

Figure 7.21: Correlation between the maximal HV reached and the minimal resistance between the resistive layout and the HV distribution line. Result for a subset of SM1 chambers.

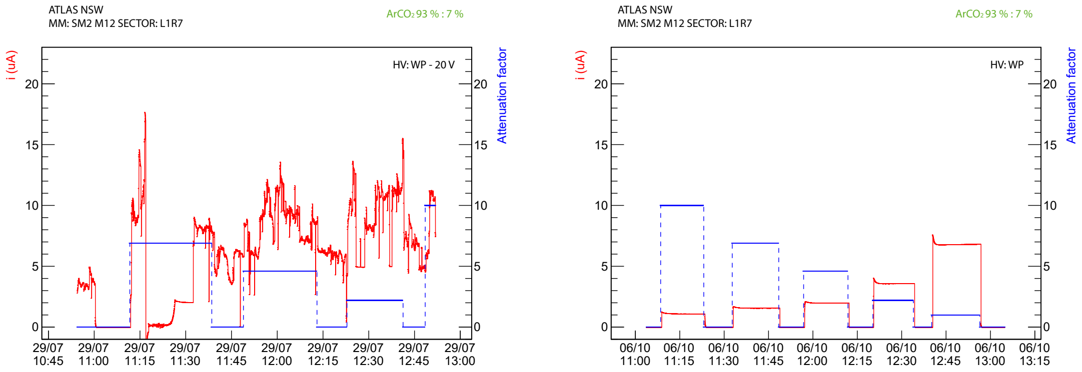

Figure 7.22: Monitored current at the amplification stage of chamber SM2 M12, sector L1R7, irradiated at GIF++ before (left) and after (right) passivation.

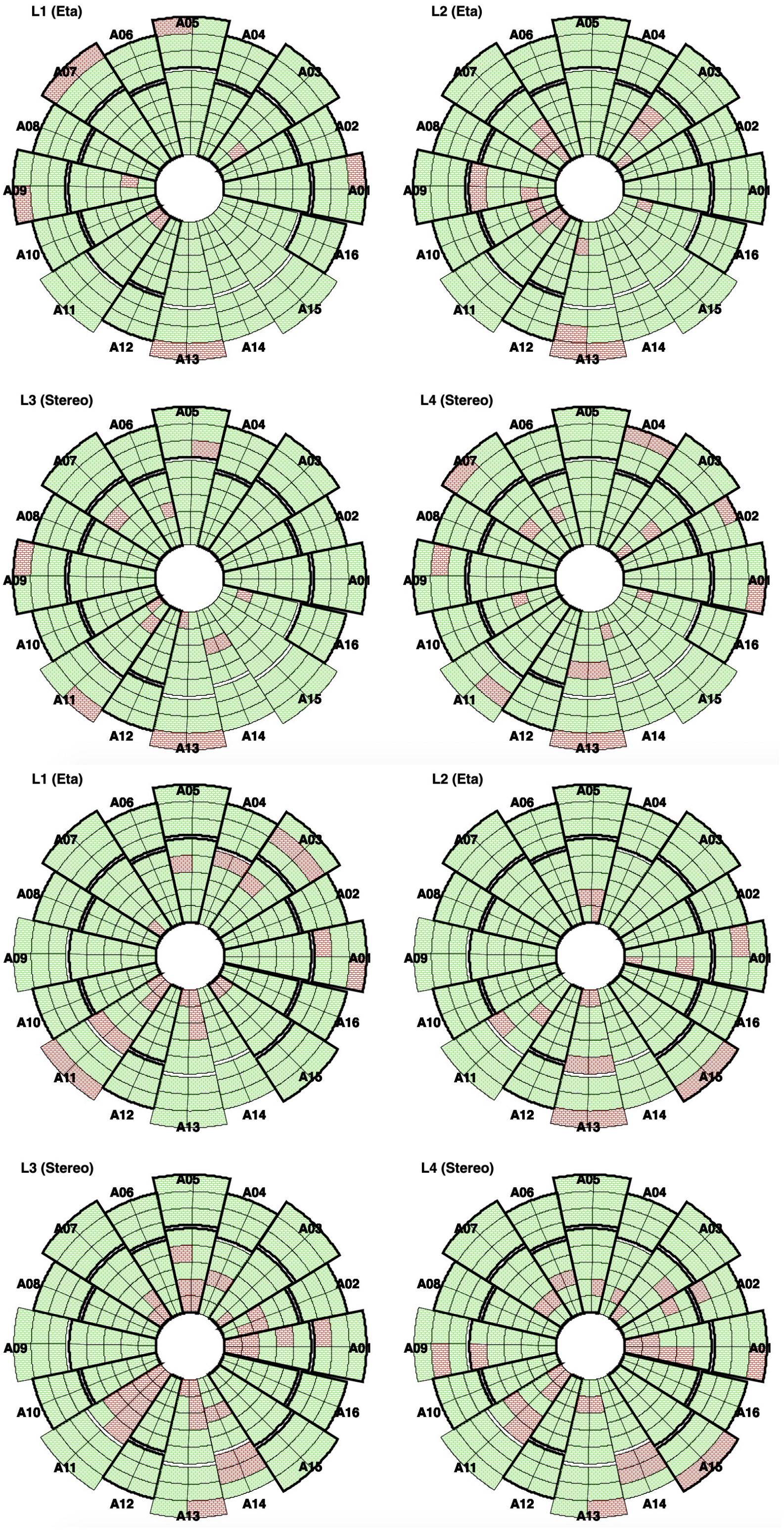

Figure 7.23: Summary of NSW-A Micromegas chamber HV testing as on October 2020. The first four pictures refer to the first quadruplets and the second four to the second quadruplets. Both small and large sectors are displayed. All sectors are considered as independently powered. Passivated chambers are marked with bold lines. See text for details.

to data was performed up to 20 V below the working point (colored lines) and the functions found were extrapolated till the maximum voltage values. In the very high current regions, all current values lie below the exponential prediction. This effect is caused by a voltage drop at the amplification stage when very high currents are produced. Fig. 7.25 shows the ratio between the fitted function and the measured current value. It is clear that, for any gas mixture, the voltage drop reduces the gain and this effect increases with the hit rate.

Gas mixture	Drift V	HV V
$ArCO_2$ (93:7)	300	570
$ArCO_2$ (80:20)	450	635-655
$ArCO_2C_4H_{10}$ (93:5:2)	250	490-510

Table 7.5: Drfit voltage value and amplification voltage working point for the three gas mixtures.

The aim of testing different gas mixtures was to find the optimal one in terms of current stability. Typically, gas detectors exploit quenchers to suppress spikes. To achieve low working voltages in gaseous detectors, noble gasses are used, as they require the lowest electric field for avalanche formation. Argon is by far the mostly used. Pure argon, however, cannot be used in detectors with gains of 10^4 without discharges. This is due to the high excitation energy of argon (11.6 eV), as excited argon atoms de-excite giving rise to high energy photons which cause further avalanches. This problem is usually fixed by adding polyatomic gasses that act as quenchers by absorbing the radiated photons and dissipating this energy through dissociation or elastic collisions. Two typical quenchers are isobutane (C_4H_{10}) and methane (CH_4).

We found dramatic improvements in spike suppression when flushing the $ArCO_2C_4H_{10}$ (93:5:2) mixture. Fig. 7.26 shows the current at the amplification stage of sector L1L8 for several voltages when the chamber is not exposed to irradiation. Isobutane is indeed very effective in suppressing any spike formation (right side) with respect to the standard gas mixture (left side). Same improvement was found when comparing the isobutane enriched mixture with $ArCO_2$ (80:20): Fig. 7.27 shows the current profile for sector L3L6 with the chamber operated at the working point plus 20 V and flushed with $ArCO_2$ (80:20) (left side) or $ArCO_2C_4H_{10}$ (93:5:2) (right side). The same improvement was also found on a *passivated* chamber, SM1 M31. Fig. 7.28 shows the current for sector L3R5 with the chamber operated at the working point and several attenuation filters (blue line) applied to the GIF++ source. The spik-

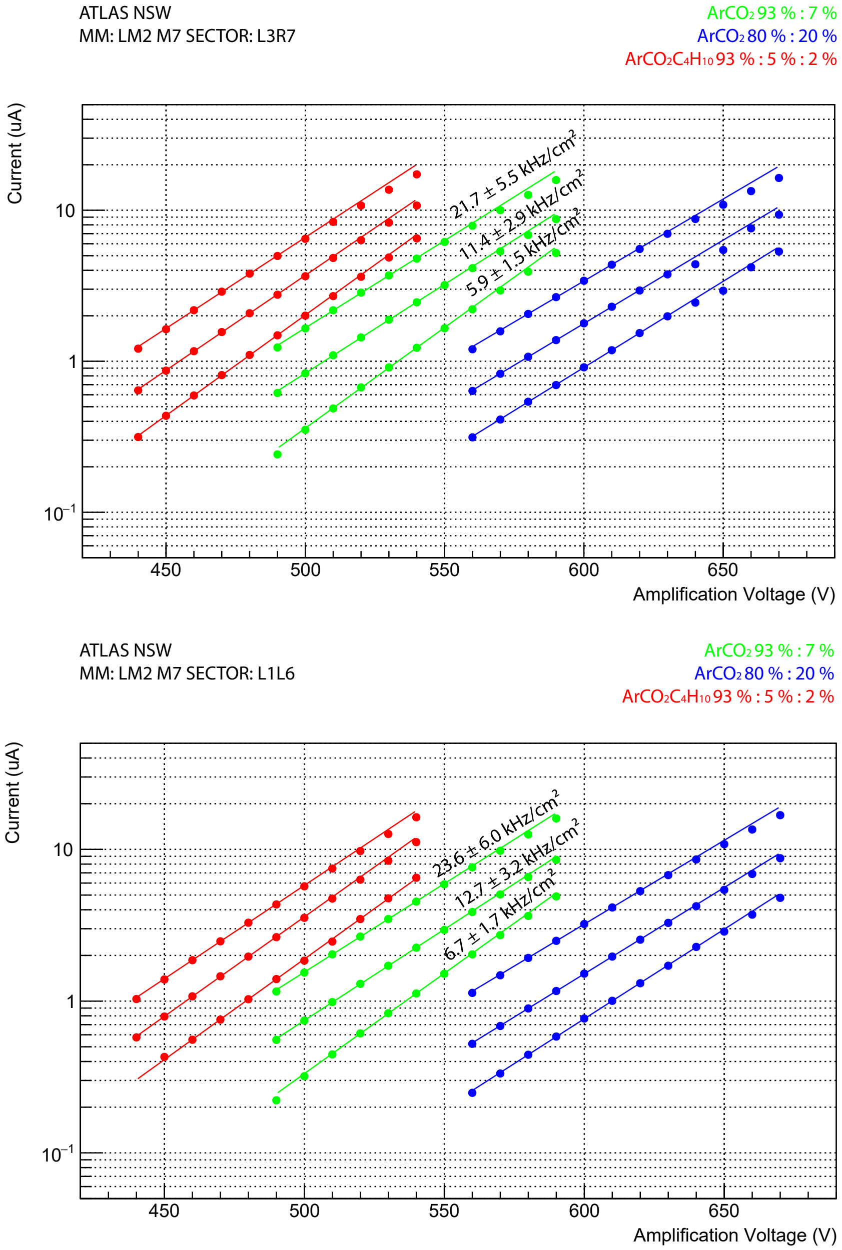

Figure 7.24: Current drawn at the amplification stage *vs.* the amplification voltage for different gas mixtures and particle rates. Results for chamber LM2 M7, sector L3R7 (up) and L1L6 (down).

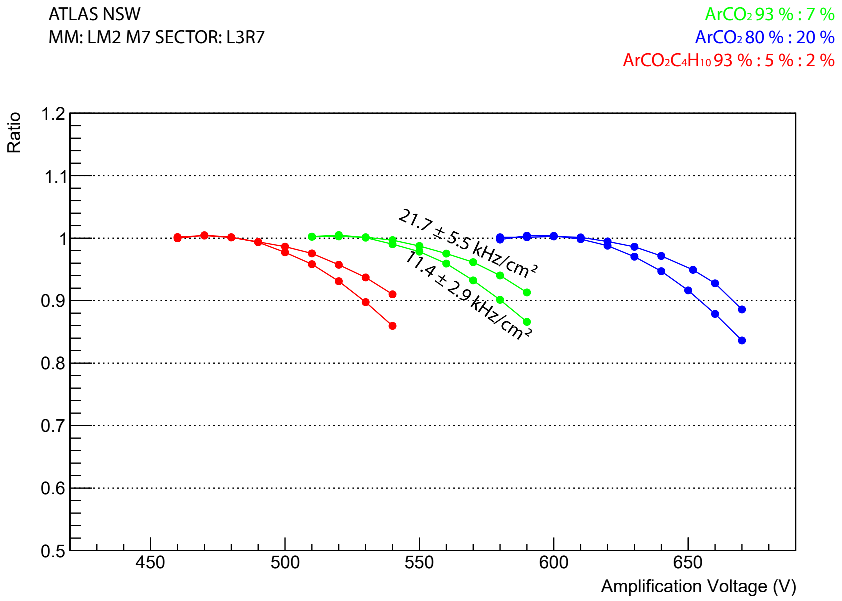

Figure 7.25: Ratio between the expected current value and the measured current value. Result for chamber LM2 M7, sector L3R7, for three gas mixtures and the two highest hit rates.

ing and streaming issues found with $ArCO_2$ (93:7) (left) completely disappeared by using the isobutane mixture (right).

To compare gas mixtures operating at different working points, we scaled each HV value by subtracting the working point and monitored the current per each voltage value. Results showing the average current *vs.* the applied voltage, for three spiking sectors, are shown in Fig. 7.29. By adding a relative volume of 2% of isobutane, it becomes possible to operate very problematic sectors up to 20 V over the working point without detecting any spike. On the other hand, using $ArCO_2$ (93:7) and (80:20), the same sectors showed an average current of 5-10 μA, only due to the spike activity, already at the working point.

Some other results might help for confirming this effect. The current of each sector was monitored for $\simeq$ 60 minutes at an amplification voltage equal to the working point +20 V when no irradiation was present. It was also monitored for about 12 hours under an effective incident rate of $\simeq$ 40 kHz/cm^2. In the latter case the amplification voltage was reduced to the working point -20 V to limit the current value to $\simeq$ 10 μA. Fig. 7.30 shows the distribution of the current values. With both no irradiation and a high irradiation flux, isobutane leads to a much more stable current, avoiding high current values due to spikes. After these studies, the NSW Collaboration started considering the possibility to use isobutane-enriched gas mixtures to mitigate residual spiking issues. In particular, long-term irradiation studies are ongoing to evaluate the micromegas aging effects while operating within the ATLAS Detector.

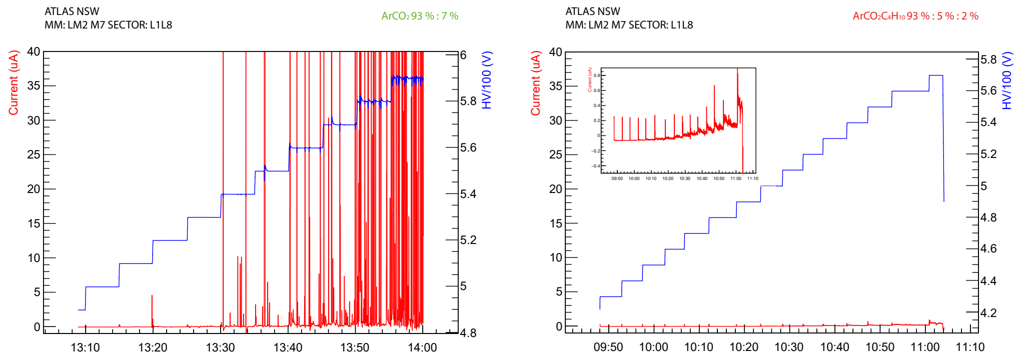

Figure 7.26: Monitored current at the amplification stage of sector L1L8, chamber LM2 M7, for several voltages when the chamber is not exposed to irradiation. Left side corresponds to the chamber flushed with $ArCO_2$ (93:7), right side corresponds to the chamber flushed with $ArCO_2C_4H_{10}$ (93:5:2).

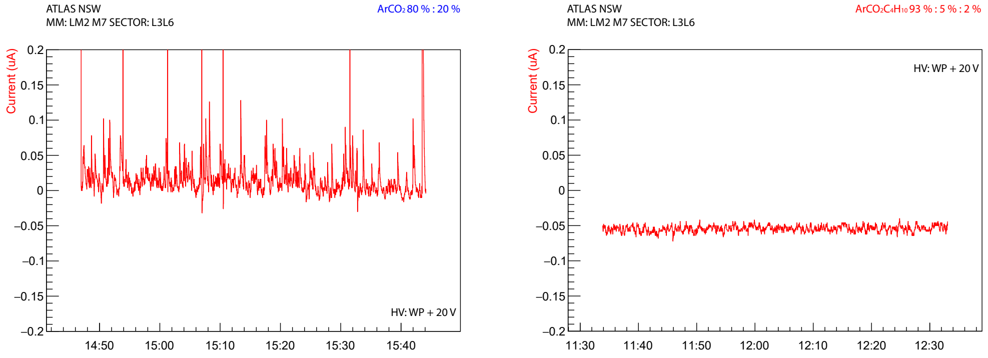

Figure 7.27: Monitored current at the amplification stage of sector L3L6, chamber LM2 M7, when the chamber is operated at the working point +20 V and is not exposed to irradiation. Left side corresponds to the chamber flushed with $ArCO_2$ (80:20), right side corresponds to the chamber flushed with $ArCO_2C_4H_{10}$ (93:5:2).

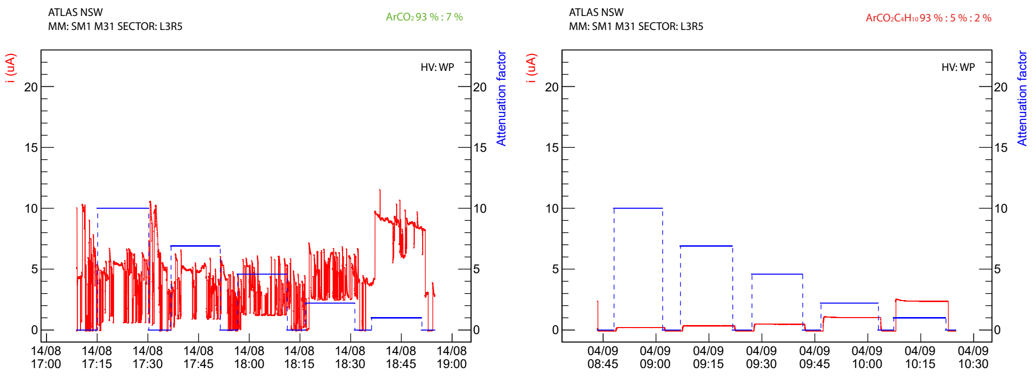

Figure 7.28: Monitored current at the amplification stage of sector L3R5, chamber SM1 M31 (passivated), when the chamber is operated at the working point and is exposed to different irradiation rates. Left side corresponds to the chamber flushed with $ArCO_2$ (93:7), right side corresponds to the chamber flushed with $ArCO_2C_4H_{10}$ (93:5:2).

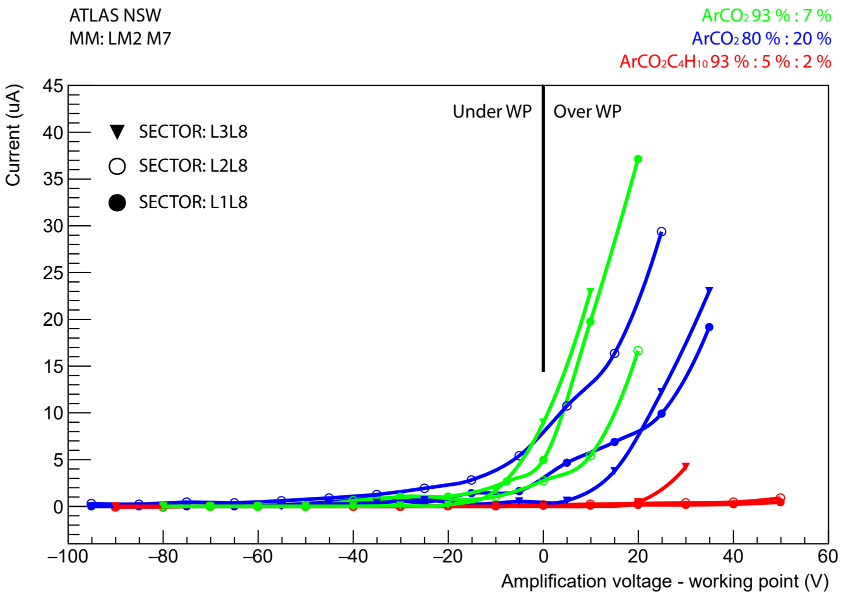

Figure 7.29: Monitored current at the amplification stage *vs.* the applied voltage for three spiking sectors when being flushed with three gas mixtures. Result for chamber LM2 M7.

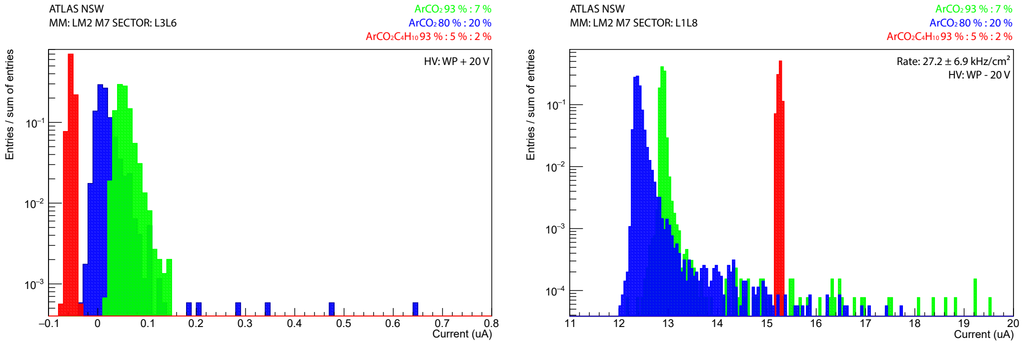

Figure 7.30: Distribution of the current values, without irradiation (left side) and under a irradiation flux of $\simeq 40$ kHz/cm^2 (right side). Results for the three gas mixtures flushing into chamber LM2 M7.

Conclusions

The thesis presented my contribution on the development of particle detectors for present and future experiments in high energy physics. It was crafted on the work carried out within the INFN RD_FCC Collaboration and the ATLAS Collaboration in the three-years period from October 2017 to October 2020.
The first part was dedicated to calorimeter design, both software and hardware, for application at future electron-positron circular colliders. It was demonstrated that the dual-readout technique could bring a significant contribution to the precision physics program envisaged. Through a detailed and original work of full-simulation of the calorimeter for the IDEA Experiment, it was shown that a dual-readout fiber calorimeter can satisfy the most stringent requirements on hadronic calorimetry, by exploiting calibration and reconstruction approaches that are unique among future detectors. Several results, such as the discrimination of the W/Z bosons by reconstructing the invariant masses of two-jet final states, were reported here for the first time. The development of the Monte Carlo description of the IDEA calorimeter resulted to be extremely accurate in reproducing the detector features, and constitutes the basis for all future studies on the subject.
A dual-readout fiber calorimeter operating at future multi-purpose experiments would require a new scalable readout system for both Cherenkov and scintillation light. To cope with this need, the use of Silicon PhotoMultipliers was pioneered, demonstrating a substantial improvement in the collection of Cherenkov light with respect to previous prototypes, and opening up the possibility of sampling particle showers with an unprecedented granularity. Also in this case, the obtained results are original and chart the activities for next years, whose path is drawn in the document. Given their importance and being ahead of the times, these activities contributed to the dawn of the IDEA Experiment.
Exploiting the study performed, I have investigated the sensitivity of the IDEA Detector, in the context of its possible operation at the future circular electron-positron collider at CERN, for Beyond-Standard-Model Axion-Like-Particles (ALPs) search. ALPs have been considered as produced in the decays of heavy Standard Model resonances and decaying into two photons. The possibility of distinguishing the weak

signal with respect to the expected background has been analyzed and the result demonstrated the uniqueness of the experiment compared to the current and future probes.

The second part was focused on the ATLAS Experiment and its Phase-I upgrade of the muon spectrometer, the New Small Wheel (NSW). From 2017 to 2020 all the needed SM1-type MicroMegas chambers have been built, in a huge collaboration among Italian Universities and INFN. The readout panels construction and testing at the University of Pavia and INFN Sezione di Pavia was described, and the results found to fulfill the ATLAS requirements. Particular attention was given to the detector high-voltage instability problems that severely affected the first phase of the project. The origin of the high-voltage instabilities was understood thanks to a long detector characterization through irradiation at the CERN Gamma Irradiation Facility. Once an ad-hoc solution was found, the monitored detector quality substantially improved, as described in the thesis. At present, the first NSW station installation within the ATLAS Detector is scheduled at the end of 2021.

Bibliography

[1] L. Evans and P. Bryant, *LHC Machine*, `http://dx.doi.org/10.1088/1748-0221/3/08/S08001`, JINST 3 (2008)

[2] F. Marcastel, *Cern's accelerator complex*, `https://cds.cern.ch/record/1621583` (2013)

[3] J. Stirling, *Parton luminosity and cross section plots*, `http://www.hep.ph.ic.ac.uk/~wstirlin/plots/plots.html` (2012)

[4] ATLAS Collaboration, Run2 Luminosity Public Results, `https://twiki.cern.ch/twiki/bin/view/AtlasPublic/LuminosityPublicResultsRun2`

[5] Future Circular Collider Study. Volume 1: Physics Opportunities. Conceptual Design Report, preprint edited by M. Mangano et al. CERN accelerator reports, CERN-ACC-2018-0056, Geneva, December 2018. Published in Eur. Phys. J. C

[6] Future Circular Collider Study. Volume 2: The Lepton Collider (FCC-ee) Conceptual Design Report, preprint edited by M. Benedikt et al. CERN accelerator reports, CERN-ACC-2018-0057, Geneva, December 2018. Published in Eur. Phys. J. ST.

[7] Future Circular Collider Study. Volume 3: The Hadron Collider (FCC-hh) Conceptual Design Report, preprint edited by M. Benedikt et al. CERN accelerator reports, CERN-ACC-2018-0058, Geneva, December 2018. Published in Eur. Phys. J. ST.

[8] J. de Blas, *Higgs Boson Studies at Future Particle Colliders*, arXiv:1905.03764 [hep-ph]

[9] The CEPC Study Group, CEPC Conceptual Design Report: Volume 1 - Accelerator, arXiv:1809.00285 [physics.acc-ph]

[10] The CEPC Study Group, CEPC Conceptual Design Report: Volume 2 - Physics & Detector, arXiv:1811.10545 [hep-ex]

[11] The CEPC Accelerator Study Group, The CEPC input for the European Strategy for Particle Physics - Accelerator, arXiv:1901.03169 [physics.acc-ph]

[12] F. An et al., *Precision Higgs Physics at CEPC*, arXiv:1810.09037 [hep-ex], DOI:10.1088/1674-1137/43/4/043002

[13] T. Behnke et al., The International Linear Collider Technical Design Report - Volume 1: Executive Summary, (2013), arXiv:1306.6327 [physics.acc-ph]

[14] L. Evans and S. Michizono (Linear Collider Collaboration), The International Linear Collider Machine Staging Report 2017, (2017), arXiv:1711.00568 [physics.acc-ph]

[15] H. Abramowicz et al., The International Linear Collider Technical Design Report - Volume 4: Detectors, (2013), arXiv:1306.6329 [physics.ins-det]

[16] J. Brau and et al., *The international linear collider: A global project*, `https://ilchome.web.cern.ch/sites/ilchome.web.cern.ch/files/ILC_European_Strategy_Document-ILCGeneral.pdf` (2018)

[17] T. Barklow et al., *Improved Formalism for Precision Higgs Coupling Fits*, Phys. Rev. D97, 053003 (2018), arXiv:1708.08912 [hep-ph]

[18] A. Robson et al., *The Compact Linear e^+e^- Collider (CLIC): Accelerator and Detector*, arXiv:1812.07987 [physics.acc-ph]

[19] M. Aicheler et al., A Multi-TeV Linear Collider Based on CLIC Technology: CLIC Conceptual Design Report, CERN-2012-007, 2012, DOI: 10.5170/CERN-2012-007

[20] L. Linssen et al., CLIC Conceptual Design Report: Physics and Detectors at CLIC, CERN-2012-003, 2012, DOI: 10.5170/CERN-2012-003

[21] P. Lebrun et al., CLIC Conceptual Design Report: The CLIC Programme: Towards a Staged e^+e^- Linear Collider Exploring the Terascale, CERN-2012-005, 2012, DOI: 10.5170/CERN-2012-005

[22] A. Robson et al., *The Compact Linear e^+e^- Collider (CLIC): Physics Potential*, arXiv:1812.07986 [hep-ex]

[23] J. de Blas et al., eds., *The CLIC Potential for New Physics*, 2018, arXiv: 1812.02093 [hep-ph]

[24] A. Robson, P. Roloff, *Updated CLIC luminosity staging baseline and Higgs coupling prospects*, CLICdp-Note-2018-002, 2018, `https://cds.cern.ch/record/2645352`

[25] H. Abramowicz et al., *CLICdp Collaboration, Higgs physics at the CLIC electron-position linear collier*, Eur. Phys. J. C77 (2017) 475, DOI: 10.1140/epjc/s10052-017-4968-5

[26] European Strategy Group, *Update of the European Strategy for Particle Physics*, CERN-ESU-013 2020

[27] A. Blondel, P. Janot, *Circular and Linear* e^+e^- *Colliders: Another Story of Complementarity*, arXiv:1912.11871

[28] Future Circular Collider Study. Volume 4: The High Energy LHC (HE-LHC) Conceptual Design Report, preprint edited by F. Zimmermann et al. CERN accelerator reports, CERN-ACC-2018-0059, Geneva, 2018. Published in Eur. Phys. J. ST.

[29] European Strategy Group, *Supporting note for briefing book 2020*, CERN/ESG/05 2019

[30] CLIC Physics Analysis, OPEN-PHO-ACCEL-2019-020, `http://cds.cern.ch/record/2683760`

[31] ALICE Collaboration, *Expression of Interest for an ALICE ITS Upgrade in LS3*, ALICE-PUBLIC-2018-013, 2018

[32] M. Adinolfi et al., *The tracking detector of the KLOE Experiment*, Nucl. Instr. and Meth. A 488 (2002) 51

[33] A. M. Baldini et al., *MEG Upgrade Proposal*, arXiv:1301.7225 [physics.insdet]

[34] A. M. Baldini et al., *Single-hit resolution measurement with MEG II drift chamber prototypes*, 2016 JINST 11 P07011, arXiv:1605.07970 [physics.ins-det]

[35] G. Bencivenni et al., *The micro-Resistive WELL detector: a compact spark-protected single amplification-stage MPGD*, in JINST 10 P02008 (2015)

[36] R. Wigmans, Calorimetry - Energy Measurement In Particle Physics, second ed., in: International Series of Monographs on Physics, vol. 168, Oxford University Press, 2017

[37] C. W. Fabjan, F. Gianotti, *Calorimetry for particle physics*, Rev. Mod. Phys. 75 (2003) 1243-1286

[38] R. Wigmans and M. Zeyrek, *On the differences between calorimetric detection of electrons and photons*, Nucl. Instr. and Meth. A485 (2002) 385

[39] R. Wigmans, *New developments in calorimetric particle detection*, Prog. Part. Nucl. Phys. 103 (2018) 109-161

[40] D. Gingrich et al., *Performance of a large scale prototype of the ATLAS accordion electromagnetic calorimeter*, Nucl. Instr. and Meth. A364 (1995) 290

[41] D. Acosta et al., *Lateral shower profiles in a lead/scintillating fiber calorimeter*, Nucl. Instr. and Meth. A316 (1992) 184

[42] N. Akchurin et al., *Beam test results from a fine-sampling quartz fiber calorimeter for electron, photon and hadron detection*, Nucl. Instr. and Meth. A399 (1997) 202

[43] C. Patrignani et al. (Particle Data Group), *Review of Particle Physics*, Chin. Phys. C, 40, 100001 (2016)

[44] ATLAS Collaboration, *Response and Shower Topology of 2 to 180 GeV Pions Measured with the ATLAS Barrel Calorimeter at the CERN Test-beam and Comparison to Monte Carlo Simulations*, ATL-CAL-PUB-2010-001

[45] P. Adragna et al., *Testbeam studies of production modules of the ATLAS Tile Calorimeter*, Nucl. Instr. and Meth. A606 (2009) 362

[46] N. Ackhurin et al., *On the differences between high-energy proton and pion showers and their signals in a non-compensating calorimeter*, Nucl. Instr. and Meth. A408 (1998) 380

[47] G. Gaudio, M. Livan and R. Wigmans, *The Art of Calorimetry*, Proceedings of the International School of Physics “Enrico Fermi”, DOI 10.3254/978-1-60750-630-0-31

[48] S. Lee, M. Livan, R. Wigmans, *On the limits of the hadronic energy resolution of calorimeters*, Nucl. Instr. and Meth. A882 (2018) 148

[49] S. Lee, M. Livan, R. Wigmans, *Dual-readout calorimetry*, Rev. Mod. Phys. 90 (2018) 025002

[50] N. Akchurin et al., *Hadron and jet detection with a dual-readout calorimeter*, Nucl. Instr. and Meth. A537 (2005) 537

[51] N. Akchurin et al., *Dual-readout calorimetry with a full-size BGO electromagnetic section*, Nucl. Instr. and Meth. A610 (2009) 488

[52] J. Hauptman, *The importance of high-precision hadronic calorimetry to physics*, Int. J. Mod. Phys. A31 (2016) 33, 1644023

[53] U. Behrens et al., *Test of the Zeus forward calorimeter prototype*, Nucl. Instr. and Meth. A289 (1990) 115

[54] M. Livan, V. Vercesi, R. Wigmans, *Scintillating-fibre Calorimetry*, CERN Yellow Report, CERN 95-02

[55] N. Akchurin et al., *Neutron Signals for Dual-Readout Calorimetry*, Nucl. Instr. and Meth. A598 (2009) 422

[56] E. Garutti, *Overview on calorimetry*, Nucl. Instr. and Meth. A628 (2011) 31-39

[57] A. Andresen et al., *Response of a uranium-scintillator calorimeter to electrons, pions and protons in the momentum range 0.5–10 GeV/c*, Nucl. Instr. and Meth. A290 (1990) 95

[58] M. Albrow et al.,*The CDF plug upgrade electromagnetic calorimeter: test beam results*, Nucl. Instr. and Meth. A480 (2002) 524

[59] Galaktionov Y. et al., *The performance of a uranium gas sampling calorimeter*, Nucl. Instr. and Meth. A251 (1986) 258

[60] N. Ackhurin and R. Wigmans, *Hadron Calorimetry*, Nucl. Intr. and Meth. A666 (2012) 80

[61] M. Ruan, *Performance requirement from the hadronic event/jet*, talk at the LCWS 2019, Sendai, Japan

[62] R. Aleksan, S. Jadachb, *Precision measurement of the Z boson to electron neutrino coupling at the future circular colliders*, Phys. Lett. B Vol. 799, 2019, 135034

[63] M. T. Lucchini et al., *New perspectives on segmented crystal calorimeters for future colliders*, 2020 JINST 15 P11005

[64] S. Agostinelli et al., *GEANT4 - A simulation toolkit*, Nucl. Instr. and Meth. A506 (2003) 250.

[65] DREAM Collaboration, 2013 Internal report CERN-SPSC-2013-012

[66] N. Ackhurin et al., *Electron detection with a dual-readout calorimeter*, Nucl. Instr. and Meth. A536 (2005) 29

[67] N. Akchurin et al., *The electromagnetic performance of the RD52 fiber calorimeter*, Nucl. Instr. and Meth. A735 (2014) 130

[68] S. Lee et al., *Hadron detection with a dual-readout fiber calorimeter*, Nucl. Instr. and Meth. A866 (2017) 76

[69] N. Akchurin et al., *Lessons from Monte Carlo simulations of the performance of a dual-readout fiber calorimeter*, Nucl. Instr. and Meth. A762 (2014) 100

[70] N. Akchurin et al., *Particle identification in the longitudinally unsegmented RD52 calorimeter*, Nucl. Instr. and Meth. A735 (2014) 120

[71] D. Buskulic et al., *Performance of the ALEPH detector at LEP*, Nucl. Instr. and Meth. A360 (1995) 481

[72] A. Bocci et al., *Study of jet energy resolution at CDF*, Int. J. Mod. Phys. A16, suppl. 1A, 255 (2001)

[73] CMS Collaboration, *Particle-Flow Event Reconstruction in CMS and Performance for Jets, Taus, and MET*, Note CMS-PAS-PFT-09-001 (2009)

[74] ATLAS Collaboration, *Jet reconstruction and performance using particle flow with the ATLAS Detector*, Eur. Phys. J. C77 (2017) 466

[75] CMS Collaboration, *Technical proposal for the phase-II upgrade of the Compact Muon Solenoid*, CERN-LHCC-2015-10

[76] N. Bacchetta et al., CLD - A Detector Concept for the FCC-ee, LCD-Note-2019-001

[77] F. Sefkow et al., *Experimental tests of particle flow calorimetry*, Rev. Mod. Phys. 88 (2016) 015003

[78] J. Repond et al., *Design and electronics commissioning of the physics prototype of a Si-W electromagnetic calorimeter for the International Linear Collider*, JINST 3 (2008) P08001

[79] C. Adloff et al., *Response of the CALICE Si-W electromagnetic calorimeter physics prototype to electrons*, Nucl. Instr. and Meth. A608 (2009) 372

[80] C. Adloff et al., *Construction and commissioning of the CALICE analog hadron calorimeter prototype*, JINST 5 (2010) P05004

[81] C. Adloff et al., *Hadronic energy resolution of a highly granular scintillator-steel hadron calorimeter using software compensation techniques*, JINST 7 (2012) P09017

[82] G. Drake et al., *Resistive Plate Chambers for hadron calorimetry: Tests with analog readout*, Nucl. Instr. and Meth. A578 (2007) 88

[83] J. Repond, *Imaging hadron calorimetry for future Lepton Colliders*, Nucl. Instr. and Meth. A732 (2013) 466

[84] C. Adloff et al., *Electromagnetic response of a highly granular hadronic calorimeter*, JINST 6 (2011) P04003

[85] J. Repond et al., *Analysis of Tungsten-DHCAL Data from the CERN Test Beam*, https://twiki.cern.ch/twiki/pub/CALICE/CaliceAnalysisNotes/CAN-039.pdf

[86] A. Steen et al., *Results of the SDHCAL technological prototype*, arXiv:1403.8097 [physics.ins-det] (2014).

[87] Z. Deng et al., *First results of the CALICE SDHCAL technological prototype*, JINST 11 (2016) P04001

[88] M. A. Thompson, *Particle flow calorimetry and the PandoraPFA algorithm*, Nucl. Instr. and Meth. A611 (2009) 25

[89] M. Antonello, et al., *Dual-readout calorimetry, an integrated high-resolution solution for energy measurements at future electron–positron colliders*, Nucl. Instr. and Meth. A958 (2020) 162063

[90] M. Antonello, et al., *Expected performance of the IDEA dual-readout fully projective fiber calorimeter*, 2020 JINST 15 C06015

[91] M. Antonello et al., *Test of a dual-readout fiber calorimeter with SiPM light sensors*, Nucl. Instr. and Meth. A899 (2018) 52

[92] F. Chollet et al., (2015). Keras. GitHub. Retrieved from https://github.com/fchollet/keras

[93] T. Sjostrand et al., An Introduction to PYTHIA 8.2, Comput. Phys. Commun. 191 (2015) 159–177, [1410.3012]

[94] M. Cacciari, G.P. Salam and G. Soyez, *FastJet user manual*, Eur. Phys. J. C72 (2012) 1896 [arXiv:1111.6097]

[95] L. Pezzotti et al., *Dual-readout fibre-sampling calorimetry with SiPM light sensors*, 2019 J. Phys. Conf. Ser. 1162 012014

[96] M. Antonello et al., *Development of a Silicon Photomultiplier based dual readout calorimeter: The pathway beyond the proof-of-concept*, Nucl. Instr. and Meth. A936 (2019) 127-129

[97] M. Antonello et al., *Linearity response measurement of a SiPM-based dual-readout calorimeter for future leptonic colliders*, Nucl. Instr. and Meth. A958 (2020) 162136

[98] A. Ghassemi, K. Sato, K. Kobayash,*Technical Note: MPPC*, `https://www.hamamatsu.com/resources/pdf/ssd/mppc_kapd9005e.pdf`

[99] C. Piemonte, A. Gola, *Overview on the main parameters and technology of modern Silicon Photomultipliers*, Nucl. Instr. and Met. A926 (2019) 2–15

[100] Sense Light, *An Introduction to the Silicon Photomultiplier*

[101] F.J. Hartjes, R. Wigmans, *Scintillating plastic fibers for hadron calorimetry*, Nucl. Instr. and Meth. A277 (1989) 379-385

[102] J. Preskill, M. B. Wise and F. Wilczek, *Cosmology of the Invisible Axion*, Phys. Lett. 120B (1983) 127–132.

[103] CAST collaboration, E. Arik et al., *Probing eV-scale axions with CAST*, JCAP 0902 (2009) 008, [0810.4482].

[104] Y. Inoue et al., *Search for solar axions with mass around 1 eV using coherent conversion of axions into photons*, Phys. Lett. B668 (2008) 93–97, [0806.2230].

[105] P. W. Graham et al., *Experimental Searches for the Axion and Axion-Like Particles*, Ann. Rev. Nucl. Part. Sci. 65 (2015) 485–514, [1602.00039].

[106] G. G. Raffelt, *Astrophysical axion bounds diminished by screening effect*s, Phys. Rev. D33 (1986) 897.

[107] G. G. Raffelt and D. S. P. Dearborn, *Bounds on Hadronic Axions From Stellar Evolution*, Phys. Rev. D36 (1987) 2211.

[108] G. G. Raffelt, *Astrophysical axion bounds*, Lect. Notes Phys. 741 (2008) 51–71, [hep-ph/0611350].

[109] A. Payez et al., *Revisiting the SN1987A gamma-ray limit on ultralight axion-like particles*, JCAP 1502 (2015) 006, [1410.3747].

[110] J. Jaeckel, P. C. Malta and J. Redondo, *Decay photons from the ALP burst of type-II supernovae*, [1702.02964].

[111] D. Cadamuro and J. Redondo, *Cosmological bounds on pseudo Nambu-Goldstone bosons*, JCAP 1202 (2012) 032, [1110.2895].

[112] M. Millea, L. Knox and B. Fields, *New Bounds for Axions and Axion-Like Particles with keV-GeV Masses*, Phys. Rev. D92 (2015) 023010, [1501.04097].

[113] CLEO collaboration, R. Balest et al., *Upsilon (1s) → gamma + noninteracting particles*, Phys. Rev. D51 (1995) 2053–2060.

[114] BaBar collaboration, P. del Amo Sanchez et al., *Search for Production of Invisible Final States in Single-Photon Decays of Y(1S)*, Phys. Rev. Lett. 107 (2011) 021804, [1007.4646].

[115] E. M. Riordan et al., *A Search for Short Lived Axions in an Electron Beam Dump Experiment*, Phys. Rev. Lett. 59 (1987) 755.

[116] J. D. Bjorken et al., *Search for Neutral Metastable Penetrating Particles Produced in the SLAC Beam Dump*, Phys. Rev. D38 (1988) 3375.

[117] S. Alekhin et al., *A facility to Search for Hidden Particles at the CERN SPS: the SHiP physics case*, Rept. Prog. Phys. 79 (2016) 124201, [1504.04855].

[118] B. Dobrich et al., *ALPtraum: ALP production in proton beam dump experiments*, JHEP 02 (2016) 018, [1512.03069].

[119] M. Bauer, M. Heiles, M. Neubert et al., *Axion-like particles at future colliders*, Eur. Phys. J. C79, 74 (2019). https://doi.org/10.1140/epjc/s10052-019-6587-9

[120] J. de Favereau, C. Delaere, P. Demin et al., *DELPHES 3: a modular framework for fast simulation of a generic collider experiment.*, JHEP. 2014, 57 (2014)

[121] J. Alwall, M. Herquet, F. Maltoni et al., *MadGraph 5: going beyond.*, JHEP. 2011, 128 (2011)

[122] W. Buttinger, M. Lefebvre, *Formulae for Estimating Significance*, ATL-COM-GEN-2018-026

[123] M. Bauer, M. Neubert, A. Thamm, *Collider Probes of Axion-Like Particles*, JHEP. 12 (2017) 044, arXiv:1708.00443

[124] J. Jaeckel, M. Spannowsky, *Probing MeV to 90 GeV axion-like particles with LEP and LHC*, Phys. Lett. B 753 (2016) 482, arXiv:1509.00476 [hepph]

[125] C. Baldenegro, S. Fichet, G. von Gersdorff, C. Royon, *Searching for axion-like particles with proton tagging at the LHC*, JHEP. 1806 (2018) 131, *Probing the anomalous $\gamma\gamma\gamma Z$ coupling at the LHC with proton tagging*, JHEP 1706 (2017) 142

[126] ATLAS Collaboration, *Evidence for light-by-light scattering in heavy-ion collisions with the ATLAS detector at the LHC*, Nat. Phys. 13 (9) (2017) 852, arXiv:1702.01625 [hep-ex]

[127] A.M. Sirunyan, et al., CMS Collaboration, *Evidence for light-by-light scattering and searches for axion-like particles in ultraperipheral PbPb collisions at* $\sqrt{s_{NN}} = 5.02\ TeV$, arXiv:1810.04602 [hep-ex]

[128] C. Baldenegro, S. Hassani, C. Royon, L. .Schoeffel, *Extending the constraint for axion-like particles as resonances at the LHC and laser beam experiments*, Phys. Lett. B 795, (2019) 339

[129] Z. Citron et al., *Future physics opportunities for high-density QCD at the LHC with heavy-ion and proton beams*, arXiv:1812.06772 [hep-ph]

[130] L. Schoeffel, C. Baldenegro, H. Hamdaoui et al., *Photon-photon physics at the LHC and laser beam experiments, present and future*, arXiv:2010.07855 [hep-ph]

[131] ATLAS collaboration, *ATLAS detector and physics performance: Technical Design Report*, `https://cds.cern.ch/record/1291633` (1999)

[132] ATLAS collaboration, *The ATLAS Experiment at the CERN Large Hadron Collider*, JINST 3 (2008) S08003

[133] ATLAS collaboration, *ATLAS Insertable B-Layer Technical Design Report*, `https://cds.cern.ch/record/391176` (2010)

[134] ATLAS collaboration, *Production and integration of the ATLAS Insertable B-Layer*, JINST 13 (2018) T05008

[135] ATLAS collaboration, *Performance of the ATLAS Trigger System in 2015*, http://dx.doi.org/10.1140/epjc/s10052-017-4852-3, Eur. Phys. J. C 77 (2017)

[136] T. Alexopoulos et al., *Construction techniques and performances of a full-size prototype Micromegas chamber for the ATLAS muon spectrometer upgrade*, Nucl. Instr. and Meth. A955 (2020) 162086.

[137] L. Pezzotti, on behalf of the ATLAS Muon Collaboration, *Irradiation and gas studies of Micromegas production chambers for the ATLAS New Small Wheel*, PoS (ICHEP2020) 766 (ATL-MUON-PROC-2020-019, `https://cds.cern.ch/record/2744037`)

[138] New Small Wheel Technical Design Report, CERN-LHCC-2013-006; ATLAS-TDR-020

[139] H. Raether, *Die Entwicklung der Elektronenlawine in den Funkenkanal*, Z. Phys. 112 464

[140] V. Peskov, M. Cortesi, R. Chechik, and A. Breskin, *Further evaluation of a THGEM UV-photon detector for RICH - comparison with MWPC*, JINST 5 (2010) P11004

[141] T. Vafeiadis, on behalf of the ATLAS Muon Collaboration, *Integration and commissioning of ATLAS New Small Wheel Micromegas detectors with electronics at CERN*, ATL-MUON-PROC-2020-021, `https://cds.cern.ch/record/2746096/` - Prepared for submission to the ICHEP2020 Conference Proceedings

[142] D. Pfeiffer et al., *The radiation field in the Gamma Irradiation Facility GIF++ at CERN*, Nucl. Instr. and Meth. A866 (2017) 91-103

[143] S. Tsuno et al., *Gamma-ray sensitivity of a thin gap chamber*, Nucl. Instr. and Meth. A482 (2002) 667-673

[144] H. Cai et al., *Sensitivity of MicroMegas to Photons and Neutrons in the ATLAS New Small Wheel*, ATLAS NOTE, ATL-COM-MUON-2017-04

List of Figures

1.1 The CERN accelerator complex. Image from [2]. 12

1.2 Production cross section for different processes as a function of the center-of-mass energy. Image from [3]. 14

1.3 Peak instantaneous luminosity delivered to ATLAS for each LHC fill during stable beams for pp collisions at 13 TeV as a function of time in 2018. Image from [4]. 15

1.4 Integrated luminosity versus time delivered to ATLAS (green), recorded by ATLAS (yellow), and certified to be good quality data (blue) during stable beams for pp collisions at 13 TeV center-of-mass energy in 2015-2018. Image from [4]. 16

1.5 The FCC-ee baseline luminosity against $\sqrt{s}$ and compared to other e^+e^- colliders (left) and the integrated FCC-ee luminosity during 15 years of operation (right). Image from [6]. 18

1.6 (Left) Sample diagrams illustrating the dependence on the Higgs self-coupling of single Higgs production at the FCC-ee.(Right) Standalone FCC-ee precision in the model-independent determination of the Higgs self-coupling ($\delta\kappa_\lambda$) and the HZZ coupling (δc_Z) deviations at 240 GeV (black), 350 GeV (purpled dashed), 365 GeV (green dashed) and by combining data at 240 and 350 GeV (purple), and at 240, 350 and 365 GeV (green). Image from [6]. 21

1.7 The FCC-hh mass discovery reach for several BSM s-channel resonances. Image from [5]. 22

1.8 Schematic view of the FCC-ee. Image from [6]. 23

1.9 Schematic view of the CEPC. Image from [10]. 23

1.10 Expected relative precisions of the Higgs boson property measurements at the CEPC, with an integrated luminosity of 5.6 ab^{-1} at $\sqrt{s} = 240$ GeV, and the comparison with the LHC/HL-LHC. In the left panel, a constrained 7-parameter fit (chosen to facilitate a comparison with the LHC) in the $\kappa - framework$ is presented. In the right panel, a model-independent 10-parameter fit is presented. Image from [12]. 24

1.11 Expected ILC Higgs boson coupling uncertainties considering $\sqrt{s} =$ 250 GeV and an energy upgrade to 500 GeV, using the highly model-independent analysis presented in [17]. This analysis makes use of data of $e^+e^- \to W^+W^-$ in addition to Higgs boson observables and incorporates the projected LHC results. Results from integrated luminosities of 2 ab^{-1} at 250 GeV and 4 ab^{-1} at 500 GeV. The scenario S1* refers to analyses with the current detector understanding; the scenario S2* refers to more optimistic assumptions in which experimental errors decrease with experience. For a detailed explanation see [16]. Image from [16]. 26

1.12 Schematic layout of the ILC250. Image from [16]. 27

1.13 Schematic layout of the CLIC 380 GeV stage. Image from [18]. 27

1.14 CLIC projection for the model-independent measurement of the Higgs coupling to SM particles [24, 25]. Image from [22]. 29

1.15 Possible timelines of future colliders including e^+e^- (ILC, CLIC, CEPC and FCC-ee), pp (FCC-hh and HE-LHC) and e^-p (LHeC and FCCeh) machines. Non discussed in the text is the HE-LHC, *i.e.* the possibility to extends the current energy frontier by almost a factor 2 by exploiting 16 T magnets while reusing the LHC tunnel [28]. Image from [29]. 31

1.16 Artistic view of the IDEA detector concept (left). The structure and dimensions of the IDEA detector concept (right). 33

1.17 Cross-section (fb) for the $e^+e^- \to X$ process as a function of $\sqrt{s}$ (GeV). Image from [30]. 34

1.18 Schematic view of the DCH separation between gas containment and wire extension relief. In evidence the wire cage and the gas envelope (left). Schematic view from the MEG2 DCH: printed circuit boards (in green) to which wires are soldered, are stacked radially alternating with spacers (in red). 36

1.19 The arrangement of the DCH stereo wires. 37

1.20 Momentum and angular resolution of the IDEA DCH as a function of the particle transverse momentum for $\theta = 90°$ assuming 100 μm spatial resolution. 38
1.21 Particle type separation power of the IDEA DCH, in terms of number of standard deviations, as a function of the particle momentum. . . . 38

2.1 The energy deposited as a function of depth for 1, 10, 100 and 1000 GeV electron showers developing in a block of copper. The integral of the profiles has been normalized to the same value (a). The radial distributions of the energy deposited by 10 GeV electron showers in copper, at various depths (b). Results of EGS4 calculations. Image from [36]. 45
2.2 Distribution of the energy fraction deposited in the first 5 X_0 by 10 GeV electrons and photons showering in lead. Results of EGS4 calculations. Image from [38]. 46
2.3 Longitudinal profiles of 10 GeV e^- showers developing in aluminum ($Z = 13$), iron ($Z = 26$) and lead ($Z = 82$). Image from [36]. 47
2.4 The em energy resolution of several sampling calorimeters as a function of $\sqrt{d/f_{samp}}$, where d is the thickness (in mm) of an active sampling layer and f_{samp} the sampling fraction for mips. The energy E is expressed in units of GeV. Image from [39]. 48
2.5 The em energy resolution and the separate contributions to it, for the ATLAS EM calorimeter as reported in [40]. 50
2.6 The e/mip ratio as a function of the thickness of the absorber layers, for uranium/PMMA and uranium/LAr calorimeters. The thickness of the active layers is 2.5 mm in all cases. Results from EGS4 simulations. Image from [36]. 51
2.7 Measured average value of f_{em} as a function of energy, for showers developing in lead or copper (a), and the distribution of f_{em} values measured for 150 GeV, π^- showers developing in lead (b). The curves in graph (a) represent Eq. 2.5. Experimental data and images from [41, 42]. 53
2.8 Mean energy for pions at beam momenta of 2–180 GeV showering in the ATLAS calorimeter. Result for both for data and Monte Carlo simulations. Image from [44]. 55
2.9 The hadronic energy resolution for a non-compensating calorimeter up to 400 GeV (solid line) and calculated with a sole stochastic term with a slightly larger scaling constant. Image from [36]. 58

2.10 The f_{em} (a) and the total kinetic energy carried by neutrons (b) plotted *vs.* the total nuclear binding energy loss (invisible energy) when 100 GeV π^- are absorbed in lead. Results from GEANT Monte Carlo simulations. Image from [48]. 62
2.11 Distribution of the total Cherenkov signal for 100 GeV π^- (a) and the distributions for three subsets of events selected on the basis of the electromagnetic shower fraction (b). Data from [50]. Distribution of the total Cherenkov signal for 200 GeV multi-particle events (c) and the distributions for three subsets of events selected on the basis of the fractional contribution of neutrons to the scintillator signal (d). Data from [55]. Image from [39]. 65
2.12 The ratio of the responses of the (compensating) ZEUS calorimeter to electrons and (low-energy) hadrons. Data from [57]. Image from [36]. 66
2.13 Distribution of the fraction of the energy released by hadronically decaying Z (a) and H (b) bosons at rest that is carried by charged final-state particles with a momentum less than 5 GeV/c. Image from [36]. 67
2.14 Signal distributions from the L3 ^{238}U/gas calorimeter, for 6 GeV electrons (a) and 6 GeV pions (b), using Ar/CO$_2$ or isobutane. Data from [59]. Image from [36]. 68
2.15 The CMS barrel calorimeter response to electrons and pions as a function of energy. The pion events are subdivided into two samples according to the starting point of the shower, and the pion response is also shown separately for these two samples. Image from [60]. . . . 69
2.16 Production of flavor-untagged ν through the process $e^+e^- \to Z\gamma \to \nu\nu\gamma$ (top row). Production of flavor-tagged ν_e through the process $e^+e^- \to \overline{\nu_e}\nu_e\gamma$ with W exchange (middle and bottom rows). Image from [62]. 71
2.17 Examining difference of the photon spectrum for the electron neutrino and muon neutrino channels due to the t-channel W exchange (see text for details). Result considering 10 ab^{-1} at 161 GeV center-of-mass energy. Image from [62]. 72
2.18 The structure of the DREAM calorimeter, the RD52 calorimeter and, for comparison, the SPACAL calorimeter. Image from [65]. 74
2.19 The DREAM calorimeter front face (top). The DREAM calorimeter front face when fibers were illuminated from the rear end (middle). The DREAM calorimeter fibers grouped into bunches readout by PMTs (bottom). 75

2.20 Signal distribution for 100 GeV π^- for the scintillation (a) and the Cherenkov (b) signals of the DREAM calorimeter. Both signals are calibrated with electrons. Scatter plot correlating the two signals. Image from [50]. 76

2.21 The average reconstructed energy for several subsamples of f_{em}. Results from 200 GeV multi-particle events (see text for details), for the scintillation (a) and the Cherenkov (b) signals. Image from [50]. . . . 77

2.22 Energy distribution for the Cherenkov signal (a) and the dual-readout combination of the two signals (b) for 200 GeV multi-particle jets. The DREAM energy resolution (c) for multi-particle jets and linearity in the $10 - 300$ GeV range (d) for multi-particle jets and single-charged-pion events. Image from [50]. 78

2.23 Front face of a single RD52 copper module. Scintillating fibers from two of the four towers were illuminated at the calorimeter rear end. . 79

2.24 The em energy resolution of the RD52 copper calorimeter. Results for the scintillation and Cherenkov signals and for the linear combination of the two. Image from [67]. 80

2.25 The RD52 lead calorimeter at the CERN SPS H8 beam line and the calorimeter front face made of 3×3 modules. 82

2.26 The RD52 lead calorimeter scintillation and Cherenkov signal distributions for 20, 60 and 100 GeV π^- (top row). The corresponding energy distributions obtained with Eq. 2.13 (bottom row). Image from [65]. 82

2.27 The effect of including the tracker and the shower max detector information on the jet energy measurement, for jets detected in the CDF barrel region. Image from [72]. 84

2.28 The effect of including the tracker information on the jet energy measurement, for jets detected in the CMS barrel region. Results from CMS simulation. Image from [73]. 84

2.29 A plastic-scintillatior plane of the scintillator-based CALICE hadron calorimeter. The active tiles featuring different sizes are visible. Image from [80]. 86

2.30 Recorded event display from the CALICE digital calorimeter detecting 120 GeV π^-. Image from [77, 83]. 87

2.31 Average signal as a function of electron energy for the W/Si ECAL built by CALICE (a). Residual signals from this detector, before and after taking out a 360 MeV offset (b). Image from [79]. 88

2.32 Reconstructed energy distribution with the binary mode (red dashed line) and the three-threshold mode (solid black line), for pions of 20 GeV (a) and 70 GeV (b), in the CALICE semi-digital hadron calorimeter. Image from [87]. 89

3.1 Sketch of a single slice of the IDEA calorimeter. 93
3.2 Sketch of the IDEA calorimeter (left) and end-cap geometry (right). . 94
3.3 Energy containment of single tower (E_{cont}/E_{tot}) for 40 GeV electrons entering at the geometrical center of each tower, from tower 1 (first tower of the barrel region) to tower 75 (last tower of the end-cap region). 94
3.4 Scintillation response of the IDEA Calorimeter when 40 GeV electrons enter the calorimeter at the geometrical center of the tower inner face, from tower 1 to tower 75. Color bans represents deviation of ±1% to the mean response. 97
3.5 Cherenkov response of the IDEA Calorimeter when 40 GeV electrons enter the calorimeter at the geometrical center of the tower inner face, from tower 1 to tower 75. Color bans represents deviation of ±1% to the mean response. 97
3.6 Response of the IDEA Calorimeter for 40 GeV electrons as a function of θ, scintillation signal (left) and Cherenkov signal (right). The highest points correspond to electrons entering the calorimeter at the geometrical center of the first three towers with no beam inclination. 98
3.7 Equalization constants *vs.* tower number for the scintillation signal. See text for details. Color bans represents deviation of ±1% to the mean value. 100
3.8 Equalization constants *vs.* tower number for the Cherenkov signal. See text for details. Color bans represents deviation of ±1% to the mean value. 100
3.9 Reconstructed electron energy divided by the energy deposited *vs.* tower number for scintillation signal. See text for details. 101
3.10 Reconstructed electron energy divided by the energy deposited *vs.* tower number for Cherenkov signal. See text for details. 101
3.11 Reconstructed 40 GeV electron energy divided by the contained energy *vs.* tower number for the scintillation signal after the application of the calibration constants. See text for details. 102
3.12 Reconstructed 40 GeV electron energy divided by the contained energy *vs.* tower number for the Cherenkov signal after the application of the calibration constants. See text for details. 103

3.13 Reconstructed 50 GeV electron energy with the scintillation signal (X-axis) and the Cherenkov signal (Y-axis). 107
3.14 Reconstructed 50 GeV electron energy with the scintillation signal (top-left), the Cherenkov signal (top-right) and the combined signals (bottom). 108
3.15 Electromagnetic energy resolutions of the IDEA dual-readout Calorimeter. See text for details. 108
3.16 Reconstructed energy for electrons in the 10-250 GeV energy range *vs.* the beam energy. 109
3.17 Average reconstructed energy, for 40 GeV electrons, divided by the beam energy *vs.* the tower number (left) and corresponding resolution *vs.* the tower number (right). 109
3.18 Kinetic energy of particles escaping the calorimeter outer surface. All particles (left) and neutrino particles only (right). 110
3.19 Reconstructed energy for 100 GeV π^- when the calibration at the electromagnetic scale is applied to the scintillation (up left) and the Cherenkov signal (up right). Scatter plot of the two variables (bottom left). Graphical representation of Eqs. 3.24, 3.25 (bottom right). . . . 111
3.20 χ factor distribution for 100 GeV π^-. 113
3.21 Profile of S/E (blue dots) and C/E (red dots) as a function of f_{em}, result for 100 GeV π^-. 113
3.22 S/E *vs.* C/E scatter plots for 100 GeV π^- (blue dots), k^- (pink dots), neutrons (green dots) and protons (red dots). 115
3.23 Reconstructed energy distribution with the same χ factor for 100 GeV π^- (blue), k^- (pink), neutrons (green) and protons (red). The energy has not been corrected for the hadronic energy containment of $\simeq 98.8\%$.116
3.24 Reconstructed energy distribution for 100 GeV π^- (up) and fit to energy resolution points from 10 to 150 GeV (down). 118
3.25 Linearity plot for $10 - 150$ GeV π^- energies reconstructed with the dual-readout method. 119
3.26 Average reconstructed energy *vs.* the χ factor, the resolution *vs.* the χ factor and the reduced χ^2 of the Gaussian fit to the energy distribution *vs.* the χ factor, for 100 GeV π^-. 119
3.27 MSE of the NN prediction evaluated on the training set (red line) and the evaluating set (blue line) *vs.* the epochs. 120
3.28 ML prediction *vs.* true energy for the evaluating set after 400 training epochs. 122
3.29 100 GeV π^- energy distribution obtained with the NN. 122

3.30 Energy resolution for 100 GeV π^- reconstructed with the deep learning approach (up) and corresponding linearity in the energy range 10-150 GeV (bottom). 123
3.31 Average number of activated elements for e^- and π^- at several energies. Results for e^- and π^- (up and down, respectively), for the scintillating and Cherenkov signals, (left and right, respectively). . . . 124
3.32 Event displays for 40 GeV e^- (upper plots), π^0 (central plots) and π^- (lower plots). Results for the scintillation and the Cherenkov signals, left and right, respectively. See text for details. 126
3.33 Signal containment *vs.* cone ΔR for showers induced by 30 GeV (blue points) and 150 GeV (red points) e^-. Results for scintillation and Cherenkov signals, left and right respectively. Results obtained with the beam setup described in Sec. 3.5.2. 127
3.34 Angular resolution, σ (mrad), for e^- events in the energy range $10-150$ GeV. Result for the Cherenkov signal (red points), the scintillation signal (blue points) and their combination (black line). 128
3.35 Scatter plot for the θ angle barycenter for 10 GeV e^- induced events measured with the scintillation and the Cherenkov signals independently. 129
3.36 Angular resolution, σ (mrad), for π^- events in the energy range $10-150$ GeV. Results for the Cherenkov signal (red points), the scintillation signal (blue points) and their combination (black line). . 130
3.37 $e^+e^- \rightarrow Z^*/\gamma \rightarrow jj$ at $E_{CM} = 90$ GeV event display from the IDEA calorimeter. Depicted are raw signals (p.e.) for the scintillation signal (left) and the Cherenkov signal (right). Results obtained with the tower granularity (up) and the fiber granularity (down). 131
3.38 Correlation between the energy deposition in the calorimeter (from GEANT4), and the sum of the energies measured in the scintillating fibers at $E_{CM} = 90$ GeV. E^s_{j1} and E^c_{j2} refer to the energy measured with the scintillation signal only for the first and the second reconstructed jets, respectively. 134
3.39 Difference between reconstructed and true energy for the first jet, versus the same difference for the second jet. Left side: first reconstruction method, right side: second reconstruction method. See text for details. 135
3.40 Gaussian means of the difference between the measured jet energy E^r_j and the true jet energy E^t_j as a function E_{nom} for different values of χ. 136
3.41 Energy resolution on the 2-jet energy measurement as a function of the reciprocal of the square root of the nominal jet energy. 137

3.42 Distributions of the difference between the reconstructed and true energy of the jet, divided by the true energy of the jet, at different center-of-mass energies using $\chi = 0.43$. 138
3.43 Distribution of the difference between the reconstructed and the true mass of the jet-jet resonances for the calo-only algorithm. Top left: W, top right: Z, bottom: H. See text for details. 140
3.44 Distribution of the reconstructed mass for three jet-jet resonances for the calo-only algorithm. Top: excluding b semileptonic decays; bottom: including b semileptonic decays. See text for details. 141

4.1 Artistic view of a SiPM structure and operating principle. 144
4.2 Individual SiPM pixels with metal-composite quenching resistor fabricated around each cell. Left: 25 μm pixel pitch. Right: 50 μm pixel pitch. Image from [98]. 144
4.3 Integrated and digitized response of a 1.3×1.3 mm^2 Hamamatsu MPPC (SiPM) 13360-1350CS with a 50 μm cell pitch when exposed to differently populated light bunches. 145
4.4 Sketch of the equivalent circuit of a single Geiger APD (left) and the corresponding conceptual output pulse (right). Image from [98]. . . . 147
4.5 Contributions of Eq. 4.3 terms to the PDE of a blue sensitive device. Image from [99]. 148
4.6 SiPM waveforms under the occurrence of prompt crosstalk. Image from [98]. 151
4.7 SiPM waveforms under the occurrence several dark count events. Image from [100]. 151
4.8 SiPM waveforms under the occurrence of afterpulses. Image from [98]. 151
4.9 Sketch of the detector brass structure and fiber arrangement (left) and picture of the prototype (right). Left image from [91]. 152
4.10 Schematic readout of the calorimeter with two arrays of SiPMs (left). Picture from the rear end of the calorimeter prototype (right). Left image from [91]. 152
4.11 Signal distributions of the SiPMs while sampling calibrating signals (left). The SiPM PDE as a function of the bias voltage applied (right). Result for light with wavelength of 523 nm. Operational voltages applied in the following are marked (ultra-low and intermediate). Image from [91]. 154
4.12 Event displays for the 8×8 scintillating fibers for 10 GeV electrons and a muon showering inside the calorimeter. Cherenkov signals are left blank to illustrate energy depositions more clearly. Image from [91].155

4.13 Scheme of the experimental setup (not to scale). Image from [91]. . . 156
4.14 Signal distribution of the 64 SiPMs after a single fiber was illuminated with a light pulse corresponding to $\simeq 1400$ fired cells. Colors indicated the raw number of fired cells. Numbers are averaged over 10^5 events. Image from [91]. 157
4.15 Average fraction of shower energy deposited in the calorimeter as a function of the impact point for 10 GeV and 100 GeV electrons. Results from Geant4 simulation obtained with the beam impinging parallel to the fiber axis (a) or 0.2° tilted in both the vertical and the horizontal plane (b). Image from [91]. 159
4.16 Event display for a simulated 50 GeV electron induced shower developing in an extended calorimeter structure identical to the prototype one. Shown are energy depositions in scintillating fibers. Fibers in the area covered by the prototype considered are marked in red. The shower fraction sampled by these fibers is, in this event, 46%. Results from Geant4 simulation. See text for details. 159
4.17 Average number of Cherenkov photoelectrons from the SiPM readout divided by the beam energy (Cpe/GeV). Results obtained with a bias voltage of 5.7 V above the breakdown level. 160
4.18 Average scintillation signal (arbitrary units) divided by the beam electron energy. Results obtained in the ultra-low PDE regime. Results shown separately for the hottest fiber and the sum of the signals from the other fibers (a) and for the ratio of these quantities (b). Image from [91]. 161
4.19 Average scintillation signal (arbitrary units) divided by the beam electron energy. Results obtained in the ultra-low PDE regime after the occupancy saturation correction. Results shown separately for the hottest fiber and the sum of the signals from the other fibers (a) and for the ratio of these quantities (b). Image from [91]. 162
4.20 Lateral profiles of electromagnetic showers in the brass-fiber calorimeter for the scintillation and Cherenkov signals. Results for test-beam data (a) and for Geant4 simulated data (b). Fractional difference between the measured and simulated data (c). Image from [91]. . . . 163
4.21 Radial profiles of electromagnetic showers in the brass-fiber calorimeter for the scintillation and the Cherenkov signals (a). Fraction of the signal deposited in a cylinder around the shower axis (b) for the scintillation and the Cherenkov signals. Both signals normalized to 45% containment. Image from [91]. 164

4.22 Radial profiles of electromagnetic showers in the brass-fiber calorimeter for the scintillation and the Cherenkov signals (a). Fraction of the signal deposited in a cylinder around the shower axis (b) for the scintillation and the Cherenkov signals. Scintillation signal normalized to 45% containment and Cherenkov signal normalized to 36% containment. See text for details. Image from [91]. 165

4.23 The measured scintillation spectrum (blue dashed), the Wratten 21 transmittance spectrum (red), the SiPM PDE curve (black dotted) and the expected spectrum (black dashed and zoomed box) (left). Average scintillation signal (photoelectrons) divided by the beam energy, as a function of the electron beam energy (GeV) (right). Image from [97]. 167

4.24 Front face of a single 16×20 tubs module when Cherenkov fibers are stimulated with light from the rear end (left). Front face of the 3×3 modules prototype (right). 169

4.25 Sketch of the new calorimeter prototype light readout system. The eight modules surrounding the central one are shorter and are readout by PMTs on a first layer (green blocks). The central module is prolonged (red elements) through the first readout layer and its 320 fibers are individually brought to a second layer with an optical collector connecting each fiber to a dedicated SiPM (SiPMs not displayed). . . 170

4.26 The 2020 prototype. Picture taken before the readout mounting. Fibers to be readout by PMTs are grouped into bunches. For the SiPM-readout central module, each fiber is extended out of the absorber tubes and routed to a dedicated hole on a plastic holder where a SiPM will be placed. 170

5.1 Feynman diagram for the ALP being radiated by a Z boson or a photon and produced in association with a photon. 173

5.2 Feynman diagram for the FCC-ee 3-photon final state Standard Model background. 176

5.3 The $(E_{\gamma 3} - E_{\gamma})^2/\sigma^2_{E_{\gamma 3}}$ variable versus the $(M_a - M)^2/\sigma^2_{Ma}$ one for 10^5 signal events generated with $E_{CM} = 160$ GeV and an axion mass of 120 GeV (left) and for the associated background process (right). . . 178

5.4 The M_{cut} variable distribution for 10^5 signal events generated with $E_{CM} = 160$ GeV and an axion mass of 120 GeV (dashed line) and for the associated background process (yellow filled area). 179

5.5 The $E_{\gamma_1}/E_{\gamma_2} < 1$ variable versus the $\Delta R_{\gamma_1\gamma_2}$ one for events of Fig. 5.3 passing the M_{cut} selection. Signal and background samples, left and right respectively. 179
5.6 Projected sensitivity regions for searches for $e^+e^- \to \gamma a \to 3\gamma$ at the FCC-ee IDEA Detector assuming $\text{Br}(a \to \gamma\gamma) = 1$. 183
5.7 Exclusion bounds on the ALP-photon coupling as a function of the ALP mass (see text and [123, 124]). Projections for p-p collision ($pp \to p(\gamma\gamma \to \gamma\gamma)p$ are drawn from [125]. Projections derived in [128] for future p-Pb, Pb-Pb and Ar-Ar collisions at the LHC (under the assumption $\text{Br}(a \to \gamma\gamma) = 1$) are shown as well (dashed lines). Image from [128, 130]. 184

6.1 Drawing of the ATLAS detector showing the different sub-detectors and the magnet systems. Image from [132]. 188
6.2 Schematic view of the ATLAS inner detector. The IBL (not shown here) is located between the beam pipe and the innermost layer of the Pixel Detector. Image from [132]. 189
6.3 Cut-away view of the ATLAS Inner Detector. Image from [132, 133, 134]. 190
6.4 Schematic illustration of the calorimeter system of the ATLAS detector. Image from [132]. 192
6.5 Layout of ATLAS Muon Spectrometer. Image from [132]. 195

7.1 MDT tube hit (solid line) and track-segment efficiency (dashed line) for an MDT chamber with 2 × 4 tube layers, as a function of the tube hit rate. The design luminosity refers to 1×10^{34} cm^{-2}s^{-1}. Image from [138]. 199
7.2 Level-1 muon trigger ($p_T > 10$ GeV) as a function of η. Also shown results for the subset of candidates with a match to an offline reconstructed muon with $p_T > 3$ GeV or $p_T > 10$ GeV. Image from [138]. . 200
7.3 Two side structure of the NSW with sectors (left). Sketch of a single sector made of four MM and six sTGC chambers (right). Image from [136]. 201
7.4 Picture from December 2019 showing the installation of the first small sector on the NSW-A mechanical structure. The NSW-C mechanical structure is also visible on the right side of the picture. 201
7.5 Scheme of the working principle of a single-layer MM chamber (left) and the 4-readout-layer configuration of the ATLAS MM chambers (right). Image from [136]. 202

7.6 Sketch of a Small-Module-1 type Micromegas chamber (left) (dimensions in mm) and a picture from a real one (right). Left image from [136]. 205

7.7 A small sector under assembly at the CERN BB5 building. The last chamber is still missing and cables to connect front-end boards are visible. 205

7.8 The Micromegas readout PCB (left). The main parts of the electrical scheme are labeled (right). 206

7.9 A zoomed picture of the PCB active area showing the resistive and readout strip geometry. 206

7.10 Picture of a Micromegas resistive-strip readout panel (left). Picture of a single pillar (about 1 mm × 330 μm) (right). 207

7.11 A readout panel during (left) and after (right) construction. Image from [136]. 207

7.12 Typical planarity measurement results after a single-panel QA/QC test. The absolute thickness is reported (mm). 209

7.13 Summary results for planarity measurements of NSW SM1 readout panels. Average thickness, RMS and max-to-min height difference for each panel. Results for measurements vacuum off/on. First 36 panels are eta, the others are stereo. Eta panels are measured on both sides (up/down) while stereo panels are measured on the up side only. . . . 210

7.14 Summary results for readout PCB electrical inspections. Displayed are the resistivity of the resistive strips, close to the HV distribution line or in the main active region, the insulation between resistive strips and readout strips and the silverline insulation. 212

7.15 The GIF++ bunker (left) and simulated total photon current ($\mathrm{cm}^{-2}\mathrm{s}^{-1}$) inside the GIF++ bunker. Images from [142]. 213

7.16 Picture of the LM2 M7 Micromegas chamber in the GIF++ bunker and the auxiliary TGC chamber mounted next to it. In the picture right side the GIF++ radiator wall is visible as well. 216

7.17 Measured rate with filter 1.0 for each Micromegas sector and percentage variations with respect to sector L7. 218

7.18 The Micromegas chambers Detector Control System during operation. 219

7.19 Monitored current at the amplification stage of chamber LM1 M8, sector L1L4 (left) and L3R5 (right). 220

7.20 Zoomed pictures of a SM1 M3 readout panel after a three months irradiation period at GIF++. Visible are discharge residuals at strip interconnection zones (left) and close to the HV distribution line covered by a piralux coverlay (right). 220

7.21 Correlation between the maximal HV reached and the minimal resistance between the resistive layout and the HV distribution line. Result for a subset of SM1 chambers. 222
7.22 Monitored current at the amplification stage of chamber SM2 M12, sector L1R7, irradiated at GIF++ before (left) and after (right) passivation. 222
7.23 Summary of NSW-A Micromegas chamber HV testing as on October 2020. The first four pictures refer to the first quadruplets and the second four to the second quadruplets. Both small and large sectors are displayed. All sectors are considered as independently powered. Passivated chambers are marked with bold lines. See text for details. 223
7.24 Current drawn at the amplification stage *vs.* the amplification voltage for different gas mixtures and particle rates. Results for chamber LM2 M7, sector L3R7 (up) and L1L6 (down). 225
7.25 Ratio between the expected current value and the measured current value. Result for chamber LM2 M7, sector L3R7, for three gas mixtures and the two highest hit rates. 226
7.26 Monitored current at the amplification stage of sector L1L8, chamber LM2 M7, for several voltages when the chamber is not exposed to irradiation. Left side corresponds to the chamber flushed with $ArCO_2$ (93:7), right side corresponds to the chamber flushed with $ArCO_2C_4H_{10}$ (93:5:2). 228
7.27 Monitored current at the amplification stage of sector L3L6, chamber LM2 M7, when the chamber is operated at the working point +20 V and is not exposed to irradiation. Left side corresponds to the chamber flushed with $ArCO_2$ (80:20), right side corresponds to the chamber flushed with $ArCO_2C_4H_{10}$ (93:5:2). 228
7.28 Monitored current at the amplification stage of sector L3R5, chamber SM1 M31 (passivated), when the chamber is operated at the working point and is exposed to different irradiation rates. Left side corresponds to the chamber flushed with $ArCO_2$ (93:7), right side corresponds to the chamber flushed with $ArCO_2C_4H_{10}$ (93:5:2). 229
7.29 Monitored current at the amplification stage *vs.* the applied voltage for three spiking sectors when being flushed with three gas mixtures. Result for chamber LM2 M7. 229
7.30 Distribution of the current values, without irradiation (left side) and under a irradiation flux of $\simeq$ 40 kHz/cm^2 (right side). Results for the three gas mixtures flushing into chamber LM2 M7. 230

List of Tables

1.1 Precisions determined in the κ framework [8] on the Higgs boson couplings and total decay width, as expected from the FCC-ee data, and compared to those from the HL-LHC. All numbers indicate 68% C.L. sensitivities, except for the last line which gives the 95% C.L. sensitivity on the exotic branching fraction, accounting for final states that cannot be tagged as SM decays. The fit to the HL-LHC projections alone (first column) requires some assumptions: here, the branching ratios into $c\bar{c}$ and into exotic particles (and those not indicated in the table) are set to their SM values. The FCC-ee accuracies are subdivided in three categories: the first sub-column gives the results of the fit expected with 5 ab^{-1} at 240 GeV, the second sub-column in bold includes the additional 1.5 ab^{-1} at $\sqrt{s} = 365$ GeV, and the last sub-column shows the result of the combined fit with the HL-LHC. Similar to the HL-LHC, the fit to the FCC-eh projections alone requires an assumption to be made: here the total width is set to its SM value, but in practice will be taken to be the value measured by the FCC-ee. 19
1.2 Target precision, at the FCC-hh, for the parameters relative to the measurement of various Higgs decays, ratios thereof, and of the Higgs self-coupling. Notice that Lagrangian couplings have a precision that is typically half that of what is shown here, since all rates and branching ratios depend quadratically on the couplings. 20
1.3 The IDEA sub-detectors main parameters. 33

3.1 Cuts applied for hadron event selection. 110
3.2 χ factor values estimated with π^- simulations ranging from 10 to 150 GeV. 114

3.3 Hyper-parameters of the NN to reconstruct hadrons energies. 120

4.1 Main parameters of the SiPM used. The peak sensitivity reported is obtained at the recommended operational voltage at the 450 nm peak. The breakdown voltage was determined by measuring the gain-voltage dependence. 153

5.1 The FCC-ee center-of-mass energies and integrated luminosities. . . . 175
5.2 The event selection applied, after the $M_{cut} < 1.5$ selection, on $E_{\gamma_1}/E_{\gamma_2}$ and $\Delta R_{\gamma_1\gamma_2}$. 180
5.3 The signal and background events after the three step event selection presented. Result for 10^5 signal samples with $E_{CM} = 160$ GeV, a coupling of 0.01, and three axion masses and for the corresponding SM background samples. 181

7.1 Simulated photon current expressed in 10^6 cm^{-2}s^{-1} at position D1/U1 for several attenuation filters. 214
7.2 Simulated photon energy spectrum for several attenuation filters normalized to the total photon current at position U1/D1. 214
7.3 Sensitivity to the GIF++ photon field of the TGC chamber and the Micromegas chamber. Results for different attenuation factors expressed as percentage values. 217
7.4 Measured rate with the TGC chamber at a 2 m distance from the source, integrated charge per electron on the anode wires and estimated rate for the Micromegas chamber. 217
7.5 Drfit voltage value and amplification voltage working point for the three gas mixtures. 224

Acknowledgements

I am grateful to the thesis reviewers, Prof. Chiara Roda and Dr. Zoltan Gecse, for their careful reading and suggestions. A heartfelt thanks go to them.

Among the New Small Wheel community, I want to thank my colleagues and friends Ivan Gnesi, Alan Peyaud, and George Glonti, with whom I shared the whole 2019 at CERN.

A sincere thanks also go to my collaborators within the future colliders community. In particular, I am honored of having worked with Massimiliano Antonello, Elisa Fontanesi, Lisa Borgonovi, Massimo Caccia, Romualdo Santoro, Stefano Giagu, Iacopo Vivarelli, Franco Bedeschi and all the members of the IDEA project. I am also indebted to Richard Wigmans for his life-long commitment to the art of calorimetry, without which my thesis would not exist. I would like to take the opportunity to also thank Alessandro Villa, whom I co-supervised for his master thesis. I hope the experience has been as profitable for him as it has been for me.

The most important thanks go to the University of Pavia, the National Institute of Nuclear Physics, and the ATLAS-Pavia Group, in which I grew up as a bachelor, master, and doctoral student. Thanks to them I have found a fruitful environment in which to grow, sometimes perhaps too quickly, to which I hope I have left something of mine. I feel particularly grateful to Giacomo Polesello, Gabriella Gaudio, and Roberto Ferrari for their mentorship.

A Silvana, Irene e Giulia, che non ho mai ringraziato, e mi pare pure sia arrivato il momento. Grazie.